

G E O L O G I C A U L T R A I E C T I N A

Mededelingen van de
Faculteit Aardwetenschappen
Universiteit Utrecht

No. 201

Deformation mechanisms and melt
nano-structures in experimentally
deformed olivine-orthopyroxene rocks
with low melt fractions

An electron microscopy study

René de Kloe

Deformation mechanisms and melt
nano-structures in experimentally deformed
olivine-orthopyroxene rocks
with low melt fractions

An electron microscopy study

Deformatiemechanismen en smelt nano-structuren in
experimenteel gedeformeerde olivijn-orthopyroxeen gesteenten
met een kleine smeltfractie

Een elektronenmicroscopische studie

(met een samenvatting in het Nederlands)

proefschrift

ter verkrijging van de graad van doctor aan de Universiteit Utrecht
op gezag van de Rector Magnificus, Prof. Dr H.O. Voorma
ingevolge het besluit van het College voor Promoties
in het openbaar te verdedigen op
maandag 5 maart 2001 des middags te 14.30 uur

door

Peter Antonie de Kloe

geboren op 22 september 1970 te Gameren

Promotor: Prof. Dr S.H. White
Faculteit Aardwetenschappen, Universiteit Utrecht, The Netherlands

Co-promotor: Dr M.R. Drury
Faculteit Aardwetenschappen, Universiteit Utrecht, The Netherlands

ISBN: 90-5744-058-x

The research reported in this thesis was carried out at the Faculty of Earth Sciences, Utrecht University and at EMSA, the Utrecht University centre for Electron Microscopy and Structure Analysis. The project was part of the PIONIER project 'Deformation mechanisms, rheology and tectonics of the Earth's upper mantle' funded by the Netherlands Organisation for Scientific Research *NWO*.

Project number 030-75-346

voor Maarten

Table of contents

Abstract	11
Samenvatting	13
Chapter 1	
General introduction and aim of the present study	17
1.1 Introduction	17
1.2 Previous work	17
1.2.1 Melt distribution	18
1.2.2 Effect of partial melt on rheology	22
1.3 Problem definition and scope of the thesis:	24
1.4 Organisation of the thesis	27
Chapter 2	
Electron microscopy techniques and set-up of the controlled oxygen fugacity furnace	29
2.1 Introduction	29
2.2 Electron microscopy techniques	29
2.2.1 Scanning electron microscopy (SEM) analysis	29
2.2.2 Transmission electron microscopy (TEM) analysis	30
2.3 EDX analysis	35
2.3.1 EDX quantification procedures	35
2.3.2 EDX K-value determination	37
2.3.3 Element loss during EDX analysis	38
2.4 Experiments in the controlled atmosphere furnace	39
2.4.1 Furnace set-up	39
2.4.2 Experimental procedure	42
Chapter 3	
Deformation, static annealing, and microstructural characterisation of the studied partially molten olivine and olivine-orthopyroxene rocks	43
3.1 Introduction	43
3.2 Deformation experiments	44
3.3 Results	48
3.3.1 Microstructural characterisation of selected deformed samples	48
3.3.2 Melt microstructures after annealing	62
3.4 Discussion	66
3.4.1 Mechanical data	66
3.4.2 Microstructures and melt distribution	67
3.4.3 Crystallographic preferred orientation	68
3.4.4 Implications for mechanical properties	68
3.5 Conclusions	69

Chapter 4	
Intracrystalline deformation microstructures in partially molten olivine and olivine-orthopyroxene rocks deformed in the dislocation creep field	71
4.1 Introduction	71
4.2 Background	72
4.3 Applied analytical methods	75
4.4 Results	80
4.5 Discussion	87
4.6 Conclusions	91
Chapter 5	
Evidence for stable grain boundary melt films in experimentally deformed olivine-orthopyroxene rocks	93
5.1 Introduction	93
5.2 Background	94
5.3 Results	95
5.3.1 Diffuse dark field imaging	95
5.3.2 Fresnel fringe imaging	98
5.3.3 High resolution lattice fringe imaging	98
5.3.4 EDX	99
5.3.5 Energy filtering imaging	101
5.4 Discussion	102
5.5 Conclusions	107
Chapter 6	
Subgrain controlled melt topology in experimentally deformed upper mantle rocks	109
6.1 Introduction	109
6.2 Imaging and measurement techniques	110
6.3 Results	111
6.4 Discussion	122
6.4.1 Morphology of subgrain boundary melt tubes	122
6.4.2 Distribution of defect related melt occurrences	125
6.4.3 Implications for the deformation of partially molten olivine-orthopyroxene rocks.	126
6.5 Conclusions	130
Chapter 7	
Summary and implications of the melt and deformation microstructures on the rheology of partially molten mantle rocks	131
7.1 Introduction	131
7.2 Melt and deformation microstructures reported in this thesis	131
7.2.1 Melt microstructures	131

7.2.2	<i>Deformation microstructures</i>	133
7.2.3	<i>Deformation mechanisms</i>	134
7.3	Implications of the observed microstructures on the properties and interpretation of partially molten mantle rocks	137
7.3.1	<i>Dislocation microstructures</i>	137
7.3.2	<i>Melt related effects on rheology in general</i>	140
7.4	Conclusions	144
7.5	Suggestions for further research	145
	References	149
	Appendix A	161
	Appendix B	165
	Appendix C	167
	Dankwoord	171
	Curriculum Vitae	173

Abstract

The major part of the Earth's upper mantle is thought to be solid, with some regions in the mantle where the rocks contain a small melt fraction. These partially molten rocks are associated with important geological processes such as magma production beneath mid-oceanic ridges and may also play an important role in the motion of lithospheric plates. For a better understanding of the physical properties of these rocks, it is essential to characterise the melt distribution and the effect of a partial melt on deformation for melt fractions representative for the upper mantle.

In this thesis, the distribution of the melt phase and its influence on the mechanical properties of olivine and olivine-orthopyroxene rocks with ~ 1 vol% melt deforming in the dislocation creep field are investigated. The melt phase in the studied rocks originated from *in situ* melting in the samples. The effects of the melt phase on rheology were examined using two sets of olivine and olivine-orthopyroxene materials that showed a different response to an applied stress at the experimental conditions ($P=300$ MPa, $T=1473$ - 1573 K), with some samples being significantly weaker than others. The melt and deformation microstructures in selected samples have been investigated in detail using scanning and transmission electron microscopy in order to determine the mechanisms that govern deformation in these materials.

The melt distribution in partially molten rocks, as established in earlier studies, mainly consists of melt tubes along grain edges, larger melt bodies that occur between several grains and layers or ellipsoidal inclusions along grain interfaces. In this study, two additional types of nanometer-scale melt occurrences that are present along grain interfaces are reported. Continuous 1 to 3 nanometer thin films of amorphous material with a melt-like composition were detected along olivine grain interfaces in both the olivine and olivine-orthopyroxene samples using high-resolution chemical analysis and imaging in the TEM. These thin films are relatively Si-rich and were characterised by the presence of Al and Ca. Amorphous films were only present along some boundaries in the hot-pressed starting material. After deformation and after long-term annealing tests, amorphous films were present along all boundaries investigated, suggesting that the films are stable features of the melt microstructure.

The second type of sub-micrometer melt occurrence along grain interfaces consisted of tubes with triangular cross-section and typical dimensions of 100×500 nm (height \times width). These tubes were associated with subgrain boundaries and the tube morphology was determined by the subgrain boundary misorientation and the composition of the melt phase. The aspect ratio (height/width) of the subgrain melt tubes increased with increasing subgrain misorientation. Ultimately, melt tubes similar to those along grain edges formed along intersections of subgrains with misorientations exceeding 4° , thereby allowing melt to penetrate into the rim of deforming crystals.

The ubiquitous occurrence of both ultrathin amorphous films and subgrain melt tubes in all studied samples indicates that such melt occurrences may be a uniform, but unrecognised, feature in many olivine-bearing materials studied at elevated temperature and pressure. As many samples from experimental deformation studies may contain amorphous films and subgrain melt tubes, the magnitude of melt-related weakening in rocks containing a small melt fraction ($<1\%$) with respect

to melt-free materials remains unknown.

A detailed microstructural characterisation of specimens from two sets of olivine-orthopyroxene samples showed minor variations in (local) melt content and in the distributions of melt pocket size, grain size, and grain boundary misorientation. None of these microstructural features, however, produced a consistent weakening in all the samples and a correlation between these features and the differences in mechanical properties could not be demonstrated. As the samples have been deformed in the dislocation creep field, it is feasible that strength differences were related to differences in activated dislocation slip systems, with intergranular misfits being accommodated by melt-enhanced grain boundary processes. This hypothesis was not supported by the dislocation microstructures in two studied samples. Dislocation densities were highly variable between individual grains and no dominance for dislocations with either Burgers vector $\mathbf{b}=[a]$ or $\mathbf{b}=[c]$ was observed. The variability in dislocation substructure was also present within individual grains, where regions could be identified in which different dislocation slip systems had been active. The occurrence of localised activation of dislocation slip systems inside crystals is interpreted to result from variations in local stresses due to interaction with adjacent grains. The main difference in dislocation microstructure was indicated by the orientation distribution of the rotation axes that describe the crystallographic misorientations accommodated by subgrain boundaries. This distribution, however, indicated a more abundant activation of the weakest olivine slip system in the stronger sample and is apparently not related to the observed weakening.

The characterisation of the melt and deformation microstructures was inconclusive in the identification of the (melt-related) mechanisms that caused the differences in rheological behaviour between the studied sample sets. Similarly, the differences in mechanical properties could not be attributed to the nanometer-scale melt bodies, as these were present in all samples. It is concluded that the observed rheological differences between the studied samples are most likely related to minor variations in the local melt distribution and differences in melt composition, which can influence the rheology through effects on diffusion kinetics and the grain boundary film thickness.

Samenvatting

Het grootste deel van de bovenmantel van de Aarde, de zone direct onder de aardkorst die zich uitstrekt van zo'n 40 tot circa 700 km diepte, bestaat uit vast gesteente. Tot een diepte van circa 400 km bestaan bovenmantel gesteenten vooral uit de mineralen olivijn en orthopyroxeen, met geringere hoeveelheden clinopyroxeen en aluminiumsilicaten als granaat. In bepaalde situaties kunnen deze gesteenten echter ook een kleine hoeveelheid gesmolten materiaal bevatten. Dergelijke gedeeltelijk ofwel partieel gesmolten gesteenten in de bovenmantel worden geassocieerd met belangrijke geologische processen zoals de vorming van magma onder vulkanen en onder mid-oceanische ruggen. Bovendien kunnen deze gesteenten een belangrijke rol spelen in de beweging van de continenten. De mechanische eigenschappen van partieel gesmolten gesteenten worden sterk beïnvloed door enerzijds de totale hoeveelheid smelt en anderzijds de verdeling van de smeltfase tussen de korrels. Om een beeld te krijgen van de processen die zich (kunnen) afspelen in de bovenmantel is het nodig om het effect van een partiële smelt op de vervorming van gesteenten te bepalen, en de verdeling van de smeltfase in gesteenten met smeltfracties, representatief voor de bovenmantel, in detail vast te stellen.

Het centrale thema van dit proefschrift betreft het onderzoek naar de distributie van de smeltfase, en het effect hiervan op de mechanische eigenschappen van olivijn en olivijn-orthopyroxeen monsters met circa 1 volume% smelt die vervormen in het dislocatie-kruip veld. De smeltfase in de monsters is tijdens de experimenten gevormd. Het effect van de aanwezigheid van een kleine hoeveelheid smelt op het vervormingsgedrag is bestudeerd in twee sets experimenteel vervormde olivijn en olivijn-orthopyroxeen monsters. Bij de experimentele omstandigheden (drukken van 300 megapascal en temperaturen tussen 1473 en 1573 K) reageerden de materialen uit de twee sets verschillend op een opgelegde spanning, waarbij enkele monsters beduidend zwakker waren dan de anderen. Om de mechanismen te identificeren die dit sterkteverschil veroorzaakten zijn de smelt- en deformatie-microstructuren in geselecteerde monsters in detail onderzocht met behulp van scanning en transmissie elektronenmicroscopie.

Uit eerdere studies van partieel gesmolten gesteenten was duidelijk dat de smeltverdeling gekarakteriseerd wordt door smeltkanalen langs korrelranden, grotere smeltvoorkomens die ingesloten zijn tussen meerdere korrels, en smeltlagen of ellipsvormige smelt insluitels langs korrelcontacten. Naast deze typen smeltvoorkomens zijn in dit proefschrift twee aanvullende typen nanometerschaal smeltstructuren geïdentificeerd die beiden voorkomen langs korrelcontacten. Continue, 1 tot 3 nanometer dunne films van een amorf materiaal zijn waargenomen langs olivijn korrelcontacten in zowel olivijn als olivijn-orthopyroxeen monsters met behulp van hoge resolutie chemische analyse en transmissie elektronenmicroscopie. De films hebben een samenstelling die lijkt op die van de smeltfase in de grotere voorkomens, en worden gekenmerkt door relatief hoge silicium gehalten en de aanwezigheid van aluminium en calcium. In het niet gedeformeerde uitgangsmateriaal komen de amorfe films slechts voor langs enkele olivijn korrelcontacten. Amorfe films komen echter consequent voor langs alle onderzochte korrelgrenzen in gedeformeerde monsters en in monsters die na deformatie zijn onderworpen aan langdurige statische 'herstel' experimenten. Dit suggereert dat de films stabiele fenomenen zijn van de smelt microstructuur.

Het tweede type sub-micrometer smeltvoorkomen langs korrelcontacten bestaat uit driehoekige

kanalen met karakteristieke afmetingen van 100 x 500 nm (hoogte x breedte). Deze smeltkanalen zijn geassocieerd met subkorrelgrenzen, waarbij de vorm van de kanalen in dwarsdoorsnede wordt bepaald door de misoriëntatie van de kristaldelen aan weerszijde van de subkorrelgrens en door de samenstelling van de smelt. De hoogte-breedteverhouding (h/b) van de subkorrel-smeltkanalen blijkt toe te nemen met toenemende subkorrel-misoriëntatie. Dit kan uiteindelijk leiden tot de vorming van smeltkanalen langs snijlijnen van subkorrels met misoriëntaties groter dan 4° waardoor de smelt in vervormde olivijnkristallen kan binnendringen.

Ultradunne, amorfe films en subkorrel-smeltkanalen langs olivijn korrelcontacten zijn aangetroffen in alle onderzochte monsters. Dit kan erop wijzen dat dergelijke smeltvoorkomens tot dusver niet herkende, universele onderdelen zijn van de smelt microstructuur zoals die zich ontwikkelt in olivijnhoudende materialen bij hoge druk en temperatuur. Het is daarom waarschijnlijk dat monsters uit eerdere experimentele studies van de vervorming van olivijnhoudende gesteenten eveneens amorfe films en subkorrel-smeltkanalen bevatten. Aangezien er geen studies zijn waarbij de afwezigheid van een smeltfase is aangetoond, is het nog niet mogelijk om het effect van een smeltfase op de sterkte van gesteenten met een kleine smeltfractie ($<1\%$) vast te stellen.

De gedetailleerde microstructurele studie van de twee sets olivijn-orthopyroxeen materialen beschreven in dit proefschrift laat kleine variaties zien tussen de monsters. De belangrijkste verschillen betreffen de hoeveelheid smelt in lokale smeltconcentraties, de distributie van de misoriëntatiehoeken van aangrenzende korrels en de verdelingen van de korrelgrootte en de grootte van de smeltlichamen. Geen van deze microstructuren leidt echter tot een consistente verzwakking, en een mogelijk verband tussen de waargenomen verschillen in microstructuur en verschillen in mechanisch gedrag kon niet worden aangetoond.

Aangezien de materialen zijn gedeformeerd in het dislocatie-kruiplveld is het mogelijk dat de waargenomen sterkteverschillen tussen de onderzochte monsters zijn veroorzaakt door activering van verschillende dislocatie slipsystemen. Eventueel hierdoor ontstane ruimteproblemen langs korrelcontacten zouden dan kunnen zijn opgevangen door korrelgrensprocessen die worden versneld door een aanwezige smeltfase. Deze hypothese wordt echter niet ondersteund door de dislocatie-microstructuur in twee onderzochte monsters. Dislocatiedichtheden in verschillende korrels variëren sterk, en een dominantie van dislocaties met ofwel Burgers vector $\mathbf{b}=[a]$ of Burgers vector $\mathbf{b}=[c]$ is niet waargenomen. Een dergelijke variabiliteit in de dislocatie-microstructuur treedt ook op binnen individuele korrels. Binnen olivijnkristallen konden gebieden worden geïdentificeerd waarin verschillende dislocatie-slipsystemen actief zijn geweest. Deze lokale activering van specifieke dislocatie-slipsystemen is waarschijnlijk het gevolg van variaties in plaatselijke spanningen, veroorzaakt door de interactie met naastliggende korrels. Het belangrijkste verschil in dislocatie-microstructuur tussen de onderzochte monsters betreft de richting van de rotatieassen die de kristallografische misoriëntatie beschrijven tussen aangrenzende subkorrels. Opmerkelijk bij deze analyse is dat de oriëntatie van deze assen erop wijst dat het zwakste olivijn slipsysteem het meest algemeen optreedt in het sterkere monster, en dus dat dit zwakste slipsysteem blijkbaar niet gerelateerd is aan de waargenomen verzwakking.

De karakterisering van de smelt- en deformatiemicrostructuren in dit proefschrift leidt helaas niet tot een eenduidige identificatie van de (smelt-gerelateerde) mechanismen die de verschillen in

mechanisch gedrag tussen de bestudeerde sets monsters veroorzaakten. De verschillen in mechanische eigenschappen konden ook niet worden toegeschreven aan de nanometerschaal smeltlichamen, omdat deze aanwezig waren in alle onderzochte monsters. Geconcludeerd kan worden dat de waargenomen rheologische verschillen tussen de bestudeerde monsters waarschijnlijk verband houden met kleine verschillen in smeltsamenstelling, welke de rheologie kunnen beïnvloeden door effecten op diffusiekinetiek en de dikte van de korrelgrensfilms, en variaties in de lokale smeltverdeling.

General introduction and aim of the present study

1.1 Introduction

The investigation of partially molten rocks is an integral part of the study of the properties of the Earth's mantle. It is the mantle that influences or controls many processes that form and deform the Earth's surface. The heat from the mantle drives volcanism and provides the energy for the movement of the continents. Where only 100 years ago the opinion of many geologists and geophysicists was still that the interior of the Earth was largely fluid, geophysical (seismic) evidence obtained since 1889 indicated that the major part of the Earth consists of solid rock (for a brief review see Bolt (1982)). However, there are distinct regions in the upper mantle and in the overlying crust where a melt phase occupies a few percent of the rock volume. These partially molten rocks are associated with geologically important processes like the formation of granitic material (migmatization) and the production of magma beneath volcanoes and mid-ocean ridges. On a global scale, small amounts of melt may also play an important role in the motion of the lithospheric plates. In the uppermost part of the upper mantle a zone of low seismic velocities and attenuation of seismic waves has been identified (Gutenberg 1954; Press 1959; Anderson & Spetzler 1970; Schmeling 1985; Green & Falloon 1998). As the presence of a liquid phase sometimes implies a weakening of the material (Carter *et al.* 1990), the presence of a small melt fraction in the upper mantle rocks just underneath the lithosphere (Shimozuru 1963; Anderson & Sammis 1970; Solomon 1972; Waff 1974) may cause this level to have a lower strength than the over- and underlying melt-free mantle regions (Goetze 1977). Therefore, such a weaker layer may act as decoupling horizon between the motion of the lithosphere with the continents at the surface and the underlying convecting mantle (Press 1959). While some of the physical properties of the rocks can be deduced using indirect geophysical methods, more direct observations of partially molten rocks are required to be able to model their strength and physical properties. For a better understanding of these partially molten rocks and the associated processes it is essential to know how the melt is distributed and to what extent the melt affects the deformation behaviour.

1.2 Previous work

The study of partially molten rocks has concentrated on two main topics. The first topic is the flow and extraction of a melt phase through a partially molten rock and the amount of melt that can be retained. Such studies were mainly concerned with the distribution of the melt phase and

the geometry and connectivity of the intergranular pore space in which the melt resides. The second topic is the deformation behaviour of partially molten rocks with particular interest on the weakening effect that may be caused by the presence of a melt phase. A brief review of previous work on these topics is given below. For more extensive reviews see Kohlstedt (1992), Kohlstedt & Zimmerman (1996), Daines (1997), Laporte & Provost (2000), and Kohlstedt *et al.* (2000).

1.2.1 Melt distribution

The distribution of a melt phase in a partially molten rock under hydrostatic stress is primarily controlled by the melt fraction, the melt composition and the interface energies for both the solid-solid and solid-liquid contacts (e.g. Kingery *et al.* 1976; Bulau *et al.* 1979; Watson 1982; Cooper & Kohlstedt 1986; McKenzie 1989; Wanamaker & Kohlstedt 1991). Migration of a melt through a partially molten rock is further influenced by the permeability of the host rock and the viscosities of both the melt phase and the (compacting) source rock (McKenzie 1984, 1989; Faul 1997). After a partial melt is formed by localised melting along grain interfaces or by melting of specific mineral phases, it will be dispersed throughout the rock in order to minimise the total energy of the system. This is achieved by distributing the melt into tubes along triple grain junctions, melt interserts, melt layers, and possibly thin melt films along grain interfaces (e.g. Vaughan *et al.* 1982; Toramaru & Fujii 1986; Bussod & Christie 1991; Faul 1994; Drury & FitzGerald 1996; Cmíral *et al.* 1998; Faul 2000). In this thesis the following terminology is used when referring to melt occurrences: melt tubes along three-grain intersections that can be imaged as triangular melt bodies in 2 dimensions are referred to as triple junction melt bodies (fig 1.1a), the term melt intersert (Cmíral *et al.* 1998) is used to describe larger melt occurrences that extend along multiple grain boundaries (fig 1.1b). Elongated melt bodies thicker than 5 nm along grain interfaces are described as melt layers (fig 1.1c) and continuous melt occurrences thinner than 5 nm along grain boundaries are referred to as melt films.

The morphology of melt occurrences along grain edges can be described by the dihedral angle at the crystal melt interfaces in triple junctions which is governed by the interaction of the

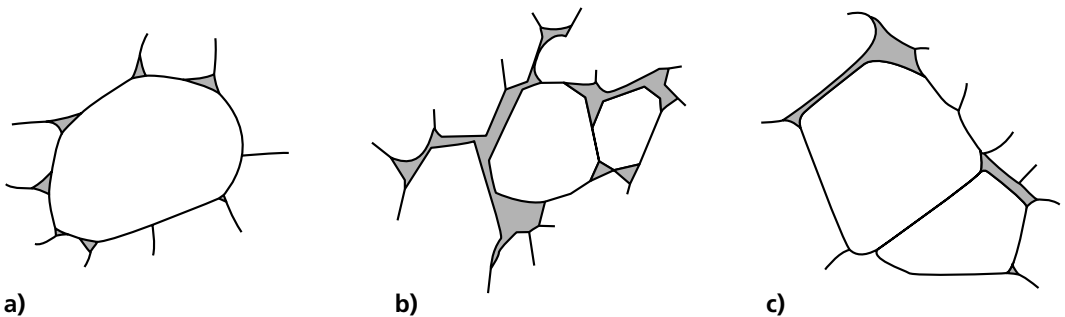


fig 1.1 Types of melt occurrences in partially molten olivine bearing rocks. Solid lines are grain interfaces, melt is indicated by shaded areas (a) grain edge tubes, triangular shaped triple junctions in cross-section (b) melt intersert that extends along several grains (c) continuous melt layers thicker than 5 nm along olivine grain interfaces. Nanometer-scale melt films may occur along all grain interfaces indicated by solid lines.

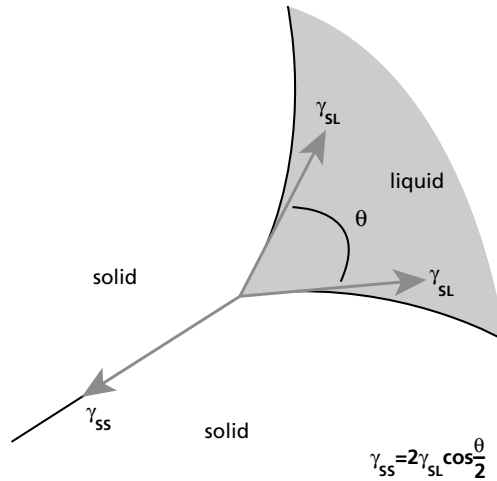


fig 1.2 Force balance of solid-solid (γ_{ss}) and solid-liquid (γ_{sl}) interface energies at an isotropic grain boundary-melt contact.

interface energies (Smith 1964; Beeré 1975; Kingery *et al.* 1976; Watson 1982; McKenzie 1984; Kohlstedt 1992) (fig 1.2). Until recently, the distribution and connectivity of the melt phase in partially molten rocks was modelled by assuming isotropic surface properties of the constituent minerals and limiting the melt occurrences to grain edge tubes and occasional melt interserts surrounded by several grains (Bulau *et al.* 1979; Raj 1981; Toramaru & Fujii 1986; Von Bargen & Waff 1986). This implied that for a given melt composition and grain surface energy the melt distribution within a partially system could be predicted when the dihedral angle and melt content are known. Experimental observations of dihedral angles in rocks however have shown that the dihedral angles actually exhibit a normal distribution about a mean value (Jurewicz & Jurewicz 1986; Bussod & Christie 1991; Laporte 1994). Jurewicz & Jurewicz (1986) assigned this variability to small variations in the surface energy due to crystallographic orientation, the presence of inclusions or variations in defect concentrations near the crystal-melt contact.

Recent studies (e.g. Waff & Faul 1992; Hirth & Kohlstedt 1995a; Faul 1997; Jung & Waff 1998; Cmíral *et al.* 1998; Faul & FitzGerald 1999) indicate that the melt distribution in olivine bearing rocks is further modified by the anisotropy of olivine surface energy. Where isotropic interface energies result in continuously curving crystal-melt interfaces (Bulau *et al.* 1979; Vaughan *et al.* 1982; Toramaru & Fujii 1986), crystalline anisotropy allows flat crystallographic faces to exist in contact with melt pockets (Waff & Faul 1992; Faul 1997; Cmíral 1998; Cmíral *et al.* 1998; Faul 2000). The presence of these flat faces results in a more crystallographically controlled melt microstructure for which dihedral angles that are based on isotropic continuously curving crystal melt interfaces are a poor representation (Cmíral *et al.* 1998). In olivine for example it is suggested that the low grain boundary energy of flat (010) faces may stabilise dihedral angles that are smaller than those expected if the grain boundary energy were isotropic (fig 1.3), thereby enlarging the surface area of such grain edge tubes (Waff & Faul 1992).

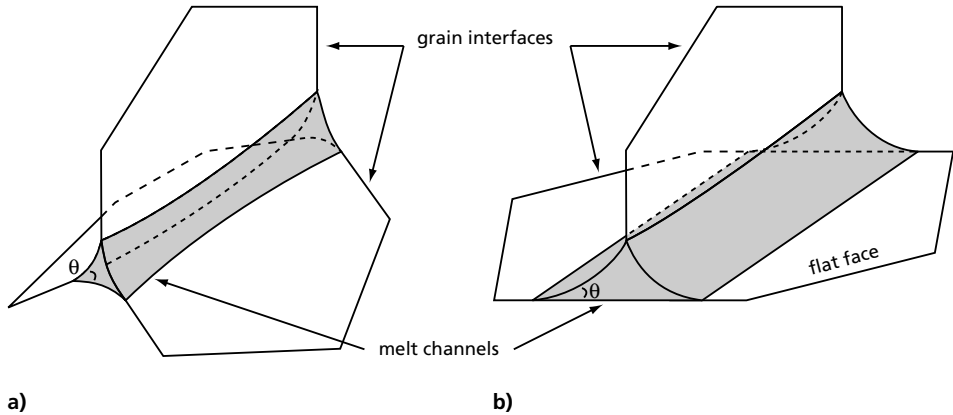


fig 1.3 Schematic representation of melt tubes along three-grain intersections: (a) symmetrical grain edge tube, (b) flattened melt tube along a crystallographic flat face characterised by smaller dihedral angles at the contact between the flat face and the melt phase. Note the larger cross-sectional area of the melt tube in (b).

When the dihedral angle at the triple grain junctions is less than 60° , a network of connected grain edge tubes is formed (Smith 1964; Bulau *et al.* 1979; Waff & Bulau 1979; Watson 1982; McKenzie 1984; Toramaru & Fujii 1986; Cooper & Kohlstedt 1986; Laporte 1994) (fig 1.4). As dihedral angles at olivine-olivine-melt contacts are typically below 60° (Bulau *et al.* 1979; Waff & Bulau 1982; Toramaru & Fujii 1986), an interconnected melt network is already established along randomly oriented triple junctions at melt fractions well below 1% (Waff & Bulau 1979; Von Bargen & Waff 1986; McKenzie 1987; Daines & Richter 1988; Riley *et al.* 1990; Bussod & Christie 1991; Riley & Kohlstedt 1991). Coexisting with these grain edge tubes are elongated disk-shaped inclusions along grain boundaries that contain a major portion of the melt phase ($\sim 75\%$) for melt contents ranging from 0.8 to 7 vol% (Faul *et al.* 1994; Bai *et al.* 1997; Faul 1997; Cmíral *et al.* 1998). The ellipsoidal melt inclusions may not interconnect at low melt fractions and therefore the permeability associated with these inclusions may be very low (Faul *et al.* 1994). Faul

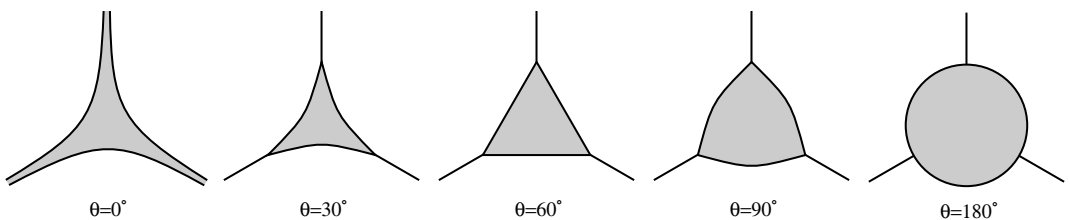


fig 1.4 Schematic representation of the cross-sectional shape of grain edge melt tubes for increasing solid-melt dihedral angles. Connectivity of melt-filled grain edge melt tubes is established at dihedral angles below 60° .

(1997) estimated that although a fully connected network is formed at melt fractions of 1%, effective extraction of the melt phase does not occur before the melt fraction has increased to 2–3% and the elongated grain boundary melt bodies become interconnected.

The distribution of the melt phase is modified when the host-rock is deformed. The study of Visser (1999) indicates that at differential stresses exceeding 10MPa, interface energies are replaced by the applied differential stress as main driving force for grain boundary diffusion. The change in driving force is illustrated by the formation of melt layers at differential stresses between 10 and 40 MPa in the study of Jin *et al.* (1994) who report that melt that resided in grain edge tubes under static conditions spreads out onto grain interfaces as the sample is being deformed. This suggests a decrease of the solid-liquid dihedral angle in the olivine-basalt system to 0° , which indicates that the solid-solid and solid-liquid interface energies no longer determine the melt distribution. Similar stress-induced grain boundary wetting was observed by Bai *et al.* (1997). Upon subsequent annealing the melt receded into grain edge tubes involving the formation of rolls and droplets along grain interfaces characteristic for healing of thin films driven by surface-energy minimisation (Smith & Evans 1984; Wanamaker & Evans 1985; Tullis *et al.* 1993; Jin *et al.* 1994; Bai *et al.* 1997). This dynamical wetting of grain boundaries in response to deformation followed by retreat of the melt phase from the grain interfaces is similar to that observed in salt-brine specimens where fluid inclusions along grain boundaries indicate the presence of a (semi)continuous fluid phase during deformation or recrystallisation (e.g. Urai 1985; Urai *et al.* 1987; Spiers & Schutjens 1990). In contrast, stress-induced wetting was not observed in the deformation experiments of Kohlstedt and co-workers (e.g. Cooper & Kohlstedt 1984b; Cooper & Kohlstedt 1986; Hirth & Kohlstedt 1995a, b; Kohlstedt & Zimmerman 1996).

Under low stress conditions (<100 MPa) little or no preferred orientation of melt pockets with respect to the compression direction was observed (Daines & Kohlstedt 1997). At differential stresses exceeding 100 MPa the melt phase tended to occur in larger interserts, often associated with clusters of small grains, that align subparallel to the compression direction (Zhang *et al.* 1995; Daines & Kohlstedt 1997; Cmíral 1998). Subsequent annealing resulted in redistribution of the melt from interserts with orientation (sub)parallel to the compression direction into melt bodies associated with specific low-index crystal faces with orientation irrespective of the previous stress conditions (Daines & Kohlstedt 1997). Such preferential wetting of low-index crystal faces, especially olivine (010) and (021) faces, can lead to alignment of elongated melt bodies when the rock exhibits a lattice preferred orientation (LPO) (Vaughan *et al.* 1982; Bussod & Christie 1991; Waff & Faul 1992; Kohlstedt & Zimmerman 1996; Daines & Kohlstedt 1997; Cmíral 1998). When a LPO is present, the grain edge melt tubes are not randomly oriented and can either focus melt transport in a specific direction (Daines & Kohlstedt 1997; Cmíral 1998) or isolate melt bodies and cause melt fractions up to 6% to remain trapped (Bussod & Christie 1991).

The presence of additional components in the melt phase can have a distinct effect on the wetting properties (Toramaru & Fujii 1986; Wanamaker & Kohlstedt 1991). Toramaru & Fujii (1986) found that the addition of small amounts of carbon effectively lowered the average dihedral angle in an olivine-basalt system. Similarly, water has been found to modify the melt tube morphology in partially molten rocks by lowering the average solid-melt dihedral angles thereby

increasing connectivity along grain edges (Fujii *et al.* 1986; Waff 1986). Furthermore, additional melt tubes may form along orthopyroxene grain edges as water has been found to reduce the dihedral angle at orthopyroxene–melt interfaces to values below the 60° connectivity threshold (Fujii *et al.* 1986). These observations indicate that the presence of orthopyroxene in a partially molten water-undersaturated mantle rock influences the connectivity of the melt phase and partly governs the melt fraction that can be detained in the system (Fujii *et al.* 1986; Toramaru & Fujii 1986). When the partially molten system is water-saturated, the connectivity of the different grain junctions is high and melt segregation may occur at lower melt content. This is supported by the conclusion of Tatsumi *et al.* (1983) that alkali–olivine basalt magmas with about 3 wt% H₂O in the north-eastern Japan arc separate at 4–5 times lower melt fraction than olivine–tholeiite magmas with less than 1 wt% H₂O from the same area.

1.2.2 Effect of partial melt on rheology

Studies that have concentrated on the rheological effect of the melt in partially molten olivine materials show that a persistent weakening occurs that is modest at melt fractions lower than 4%, but increases greatly when the melt fraction exceeds ~4–5% in both the dislocation and the diffusion creep field (Chopra & Kohlstedt 1983; Cooper & Kohlstedt 1984b; Cooper & Kohlstedt 1986; Cooper *et al.* 1989; Beeman & Kohlstedt 1993; Hirth & Kohlstedt 1995a, b; Kohlstedt & Zimmerman 1996; Bai *et al.* 1997). A viscosity reduction and corresponding strain rate increase by more than an order of magnitude may occur in partially molten rocks relative to melt-free aggregates (Pharr and Ashby 1983; Hirth & Kohlstedt 1995a, b; Bai *et al.* 1997). This substantial weakening is ascribed to the enhancement of grain boundary sliding and diffusion that occurs after complete wetting of a critical number of grain boundaries (Jin *et al.* 1994; Hirth & Kohlstedt 1995a, b) possibly accompanied by greatly enhanced grain boundary mobility (Bai *et al.* 1997) when the melt fraction exceeds ~4%. However, from studies of the connectivity of the melt phase in partially molten rocks, it follows that a fully interconnected melt network is present at melt fractions below 1% (e.g. Waff & Bulau 1979; Von Bargen & Waff 1986; McKenzie 1987; Daines & Richter 1988; Riley *et al.* 1990; Bussod & Christie 1991; Riley & Kohlstedt 1991) and that effective extraction of melt from the rock is established at melt fractions of 2–3% (Faul 1997). This may set a maximum melt content that can be retained within the host rock during partial melting in the upper mantle, thereby limiting the natural settings in which the substantial weakening reported for melt fractions exceeding 4–5% occurs.

The modest weakening at melt fractions lower than 4–5 vol% is characterised by an increase in strain rate by a factor 2 to 5 with respect to (nominally) melt-free specimens in the diffusion creep field (Chopra & Kohlstedt 1983; Cooper & Kohlstedt 1984b; Cooper & Kohlstedt 1986; Cooper *et al.* 1989; Hirth & Kohlstedt 1995a) and in the dislocation creep fields (Beeman & Kohlstedt 1993; Hirth & Kohlstedt 1995b; Bai *et al.* 1997). Note that the nominally melt-free specimens studied by Hirth & Kohlstedt (1995a, b) actually contained 0.5 to 1 vol% melt and the melt-free samples from Bai *et al.* (1997) showed microstructures suggestive of minor partial melting (<1 vol%), although melt could not be shown by light microscopy. For partially molten rocks deforming in the dislocation creep field, the modest weakening results in creep strength

similar to that of olivine single crystals deforming by creep on the weakest olivine dislocation slip system, [a]-slip (010)[100] (Durham & Goetze 1977a, Beeman & Kohlstedt 1993; Hirth & Kohlstedt 1995b; Bai *et al.* 1997). The exact mechanism that is responsible for this weakening is not known. It has been postulated that the presence of small melt fractions cause a transition in the active dislocation slip system from [c]-slip (010)[001] as the rate-limiting deformation mechanism to [a]-slip (010)[100] accommodated by grain boundary processes such as grain boundary sliding and grain boundary diffusion (Beeman & Kohlstedt 1993; Hirth & Kohlstedt 1995b).

The contribution of solution-precipitation mechanisms to the creep rate is directly related to the extent to which grain boundaries are wetted by a liquid phase (Cooper & Kohlstedt 1986; Jin *et al.* 1994). When deformation experiments are carried out in the diffusion creep field, deformation in both melt-free and melt-containing experiments is rate limited by Si-diffusion along apparently melt-free grain boundaries as long as the melt fraction does not exceed 5% (Cooper & Kohlstedt 1986). This result is consistent with theoretical models in which the melt phase is present at three grain junction tubes and four grain junction corners (Cooper & Kohlstedt 1986; Toramaru & Fujii 1986). The viscosity of these melts shows a direct correlation with oxygen diffusivity, suggesting that migration of larger, highly stable units like SiO_4 -tetrahedra which are apparently rate limited by oxygen diffusivity may actually control the kinetic processes in these melts (see Cooper & Kohlstedt 1986 and references therein). In addition to the weakening of partially molten rocks by promoting deformation by diffusion processes, melt may also have an effect in the dislocation creep field. When deformation involves dynamic recrystallisation in the presence of a fluid phase, interfaces between progressively misoriented subgrains may become wetted and thereby facilitate the final stages of the rotation process (Bussod & Christie 1991). The presence of flat faces results in a more crystallographically controlled melt microstructure, which subsequently has implications for the rheological behaviour of partially molten rocks. Rheology will especially be affected if there is a crystallographic preferred orientation present that concentrates the melt in specific directions and thereby forms local zones of low mechanical strength (Bussod & Christie 1991; Daines & Kohlstedt 1997; Grujic & Mancktelow 1998).

At the initiation of melting an additional effect may occur if water, which causes considerable intragranular weakening (Mackwell *et al.* 1985; Karato *et al.* 1986; Van der Wal 1993), is present. Karato (1986) argues that this water-induced weakening is reduced when melting starts, causing an increase in the strength of the rock. Such a strength increase can be explained by the fact that the solubility of water in basalt is three orders of magnitude greater than in olivine and virtually all the water that is present in the rock will become incorporated in the melt phase (Karato 1986; Hirth & Kohlstedt 1995a; 1996). Small amounts of melt may therefore have only a limited weakening effect on a 'wet' partially molten rock, irrespective of the amount of water that is dissolved in the melt phase. However, this melt-induced strengthening effect is in contrast to the profound weakening of nominally melt-free materials (which actually contain 0.1-1 % melt) produced by the addition of water (Chopra & Paterson 1984; Karato *et al.* 1986).

1.3 Problem definition and scope of the thesis:

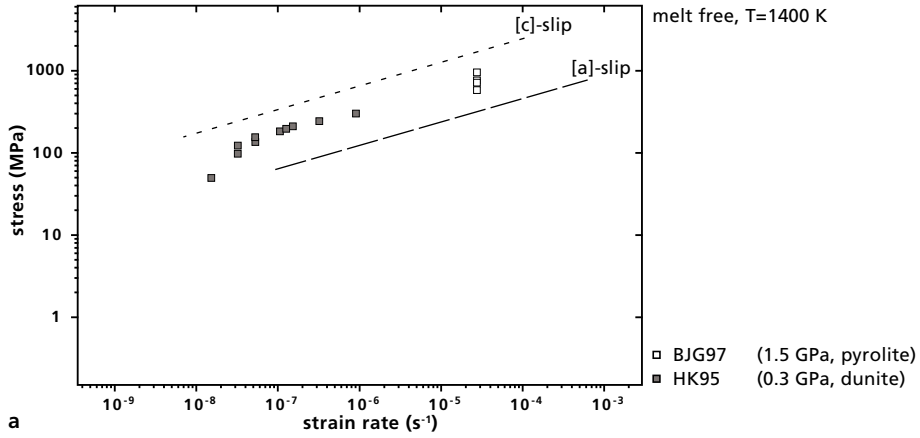
Two main subjects are studied in this thesis: –1– the detailed characterisation of nanometer-scale melt occurrences at grain interfaces and –2– the identification of the processes that govern the deformation of partially molten olivine and olivine-orthopyroxene rocks at low melt fractions (~ 1 vol%). The characterisation of the melt features is incorporated in the study of the deformation processes, because melt occurrences at grain interfaces are likely to affect the mechanical behaviour. A general microstructural analysis of the samples is presented in chapters 3 and 4. Details of the melt nano-structure will be presented after the microstructural analyses and are described in chapters 5 and 6.

From previous work, it has become clear that a rheological boundary exists between partially molten olivine-bearing rocks that contain more than 4–5 vol% melt and rocks containing less melt (fig 1.5). The substantial weakening for partially molten rocks with melt fractions exceeding 4–5% can be satisfactorily explained by complete wetting of a critical number of grain boundaries and subsequent loss of cohesion (Hirth & Kohlstedt 1995b), possibly accompanied by a large increase in grain boundary mobility (Bai *et al.* 1997). Connectivity studies, however indicate that the maximum melt fraction that can be retained in partially molten upper mantle rocks is on the order of 2–3 vol% (McKenzie 1984; Von Bargen & Waff 1986; McKenzie 1989; Salters & Hart 1989; Johnson *et al.* 1990; Jin *et al.* 1994; Faul 1997). Therefore the occurrence of weakening associated with melt fractions exceeding 4–5 vol% is expected to be uncommon under natural conditions.

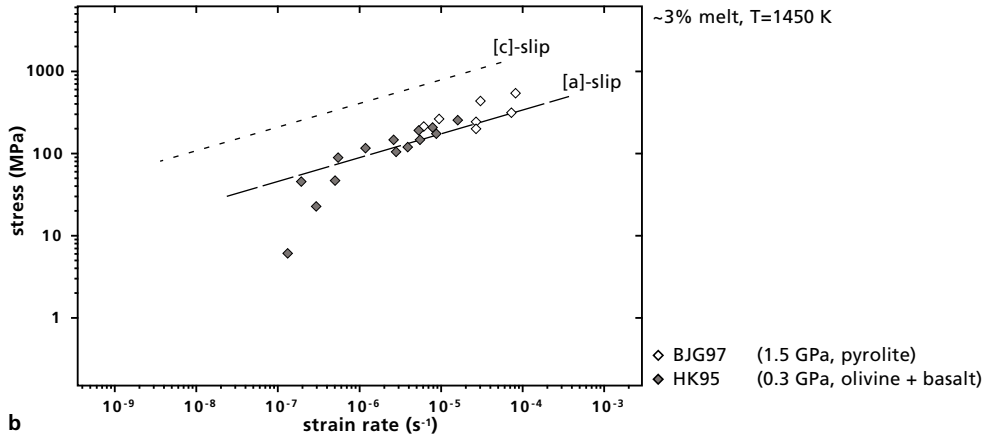
In contrast to weakening at high melt fractions, moderate weakening in the dislocation creep regime associated with melt fractions below 3 vol% may be a common process in partially molten upper mantle rocks. Unlike the weakening mechanism postulated for higher melt fractions, the mechanism(s) that cause(s) the observed 2 to 5 times increase in dislocation creep strain rate of partially molten rocks containing minor amounts of melt remain(s) unclear. A hint to the process that causes weakening at low-melt fractions is given by the creep strength reduction to the level of olivine-single crystal [a]-slip (Beeman & Kohlstedt 1993; Hirth & Kohlstedt 1995b). This strength reduction suggests replacement of stronger intracrystalline deformation mechanisms by weaker diffusion related grain boundary processes (Hirth & Kohlstedt 1995b). However, the change in deformation mechanism from dislocation creep limited by olivine [c]-slip to olivine [a]-slip accommodated by melt-enhanced grain boundary processes is based on indirect data obtained in creep experiments and has not been confirmed with microstructural observations. In this thesis, melt and deformation microstructures of olivine-orthopyroxene rocks containing ~ 1 vol% partial melt are investigated in detail in an attempt to discern the actual processes that govern deformation in the presence of small amounts of partial melt.

fig 1.5 Stress-strain rate data of experiments of BJG97 (Bai *et al.* 1997) and HK95 (Hirth & Kohlstedt 1995a, b) illustrating the magnitude of melt related weakening for increasing melt content (figure is modified after fig 2.4 from Bai *et al.* (1997)). Diffusion creep data from Hirth & Kohlstedt (1995a) were normalised by Bai *et al.* (1997) to a grain size of 30 μm using a grain size exponent 3.2

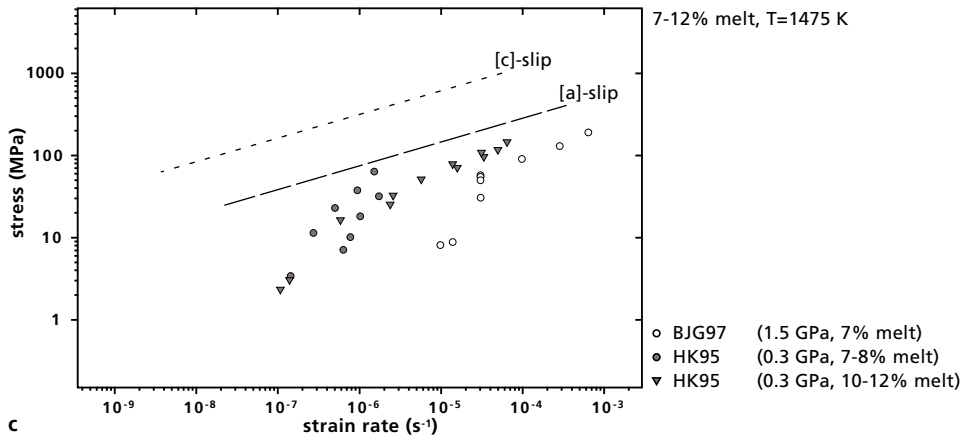
- (a) Nominally melt-free samples exhibit strength levels intermediate to olivine single crystal [a]- and [c]-slip.
- (b) Strength levels of samples containing 3% melt coincide with the strength of olivine single crystal [a]-slip.
- (c) Substantial weakening to levels below the strength of olivine single crystal [a]-slip occurs at melt fractions exceeding 5%.



a



b



c

The second goal of the research reported in this thesis, is to establish the grain-scale melt distribution in partially molten olivine and olivine-orthopyroxene rocks. Weakening related to low melt contents (<4 vol%) has been ascribed to the enhancement of grain boundary processes by enabling rapid diffusion through melt tubes along grain edges, melt interserts, and layers, effectively reducing the distance diffusing species must travel along melt-free grain contacts (e.g. Cooper & Kohlstedt 1984a, b; Cooper & Kohlstedt 1986; Farver *et al.* 1994; Hirth & Kohlstedt 1995a; Kohlstedt & Zimmerman 1996; Bai *et al.* 1997). The local grain-scale melt geometry will therefore influence the effectiveness of melt weakening.

Several types of melt occurrences along grain interfaces have been reported. Transitional wetting of olivine grain interfaces may occur when a differential stress is applied under specific chemical and physical conditions (Jin *et al.* 1994; and Bai *et al.* 1997). This is not a universal phenomenon as illustrated by the absence of such stress-induced melt layers along grain interfaces in studies of Kohlstedt and co-workers (e.g. Cooper & Kohlstedt 1984b; Cooper & Kohlstedt 1986; Hirth & Kohlstedt 1995a, b; Kohlstedt & Zimmerman 1996). A second type of melt body along grain interfaces appears to be related to the occurrence of subgrain intersections. These subgrain boundary-melt bodies have been reported by Cooper & Kohlstedt (1982), Drury & FitzGerald (1996), and Cmiral (1998), but their abundance and influence on the melt distribution have not been considered in detail. The presence of a third type of melt occurrence along olivine grain interfaces in both deformed and undeformed partially molten rocks is indicated by indirect chemical evidence. Drury and FitzGerald (1996) and Cmiral *et al.* (1998) reported chemical analyses of olivine grain boundaries that pointed to the presence of continuous nanometer-scale ultrathin melt films. From chemical analyses, however, it can not be shown if the chemical signal is derived from solid-state segregation of impurities to the grain boundary region or if it represents a distinct thin amorphous melt-like film. Furthermore, in the study of Drury & FitzGerald (1996) it was not clear whether or not the samples had reached structural and chemical equilibrium and it could not be excluded that the presence of a chemically distinguishable grain boundary phase was a transient feature. In this study, the morphology and stability of melt occurrences along olivine grain interfaces away from grain edge tubes, interserts, and melt layers at low melt fractions are investigated in detail. Emphasis will be on the nature and stability of melt films as indicated by chemical evidence and on the abundance, morphology, and stability of subgrain related melt bodies during deformation and subsequent static annealing.

The rock samples that are investigated in this study are subdivided into two sets. One sample set was taken from the study of Hitchings *et al.* (1989) and consists of experimentally deformed partially molten olivine and olivine-orthopyroxene rocks with ~1% melt. The expected moderate weakening to the level of single olivine crystal [a]-slip has been observed in one of the olivine-orthopyroxene samples but is absent in the olivine materials. The second set of samples was prepared by Martyn Drury in 1992 to reproduce the weakening observed in the olivine-orthopyroxene materials. Both experimental studies have been performed at the Australian National University in Canberra. The presence of samples that exhibit the anticipated melt-related weakening in combination with samples that do not seem to be affected by the presence of melt makes these sample sets especially suitable for the study of the melt microstructure and melt-

related changes in deformation behaviour. In addition, the stability of melt occurrences along olivine grain interfaces is tested in longer duration deformation experiments and by static annealing of previously deformed specimens for durations exceeding 100 hours.

1.4 Organisation of the thesis

After this introduction and brief literature review, a description of the analytical techniques used in this research and experimental set-up of the controlled oxygen fugacity furnace will be provided in chapter 2. Details on the deformation and annealing experiments together with a general microstructural characterisation of the materials are given in chapter 3. The subsequent chapters 4, 5, and 6 each concentrate on a specific part of the microstructure. Chapter 4 focuses on the intracrystalline deformation microstructures to investigate whether or not the stronger dislocation slip system, [c]-slip, has been replaced by other deformation mechanisms in favour of the weaker [a]-slip. In chapter 5 the presence and stability of continuous ultrathin melt films along olivine grain interfaces is investigated. Most of the results presented in chapter 5 are published in De Kloe *et al.* (2000). The occurrence and morphology of nm-scale melt tubes along the intersection of subgrain boundaries with high angle grain boundaries is described in chapter 6. In chapter 7, a summary of the results and a discussion on the implications of the observations on the deformation behaviour and melt microstructures in partially molten upper mantle rocks are presented together with general conclusions and some suggestions for further research. Because the chapters in which the results are presented have been prepared to be published as individual papers, some degree of repetition may occur.

Electron microscopy techniques and set-up of the controlled oxygen fugacity furnace

2.1 Introduction

The different aspects of the melt and deformation microstructure that have been investigated in this study required specific imaging and chemical analysis techniques. In the first section of this chapter, the principles of the EM imaging techniques used will be treated qualitatively. The basic characteristics and applications of each method are outlined, focussing attention on the specific application of each technique in this study. For more detailed descriptions of the imaging modes, the reader is referred to electron microscopy handbooks (e.g. Edington 1976; Loretto 1984; Williams 1984; McLaren 1991). In the second section of this chapter, the characterisation of the energy dispersive X-ray spectroscopy (EDX) chemical analysis system is presented. The EDX system is attached to the CM200FEG transmission electron microscope at EMSA, the Utrecht University centre for Electron Microscopy and Structure Analysis. This characterisation was carried out in collaboration with Dr H.L.M. van Roermund. In the final section, the experimental set-up for long-term annealing experiments in a controlled oxygen fugacity furnace is described.

2.2 Electron microscopy techniques

2.2.1 Scanning electron microscopy (SEM) analysis

SEM imaging was performed on a Philips XL30FEG (field emission gun) scanning electron microscope operating at 15–25 kV with typical beam currents of 0.15–2.5 nA. Standard SEM backscattered electron imaging and forward scattered orientation contrast imaging were used to determine the distribution of the mineral phases, the melt microstructure on a micron- to centimetre-scale and the grain size distributions (chapter 3). Specimens of the hot-pressed and deformed samples were prepared for SEM as standard polished petrological thin sections. The long-duration annealed samples were embedded in resin before polishing, because of their smaller dimensions (chapter 3). All sections were given a 1 hour final polish on a polyurethane lap using a suspension of 50 nm colloidal silicon in water (Syton™) and subsequently coated with a thin evaporative carbon layer to prevent charging.

The image intensity in backscatter electron imaging is primarily determined by differences in the composition of the constituent components. The intensity of the backscattered signal is directly proportional to the backscatter coefficient, η (White *et al.* 1984), where \bar{Z} is the average atomic number of the material and C_i is the weight fraction of component Z_i .

$$\eta_{\text{mineral}} = -0.0254 + 0.0162\bar{Z} - 0.000186\bar{Z}^2, \text{ with } \bar{Z} = \sum Z_i C_i \quad [1]$$

Backscatter coefficients of the different mineral phases present in the studied samples are given in tables 3.1 and 3.3 in chapter 3.

The variations in greyscale in backscattered electron images allowed quick determination of the distribution of the mineral and glass phases present with a spatial resolution of 1 μm . The backscattered electron signal is also weakly dependent on crystal orientation and small contrast variations, indicating the occurrence of subgrains, could occasionally be observed within grains. The contrast caused by orientation differences was too low to allow reliable identification of olivine-olivine and orthopyroxene-orthopyroxene grain boundaries, therefore backscattered electron imaging was not suitable for grain size measurements. Instead, grain size measurements were conducted using the forward scattering configuration (Prior *et al.* 1996). In forward scattering imaging, the specimen is tilted so that the specimen-normal is at an angle of 70° to the electron beam and the backscatter detector is placed below the specimen to collect the forward-scattered electrons. In this configuration, minor variations in crystal orientation ($<1^\circ$) can produce large contrast differences, because contrast variations between grains are critically dependent on the orientation of the crystal lattice and not on composition (Prior *et al.* 1996). This contrast difference allowed identification of individual grains and subgrains and determination of the grain size distributions in the specimens.

The forward scattering configuration is also used for the generation of electron backscattered diffraction patterns (EBSP, Van der Wal & Dingly 1996). In the forward scattering set-up, a fraction of the electrons that penetrate into the specimen is inelastically scattered. Within the interaction volume, such inelastically scattered electrons can again become (elastically) diffracted inside the sample and escape from the specimen. These electrons that are diffracted on specific sets of lattice planes generate a more intense cone-shaped distribution of electrons within the ‘cloud’ of inelastically scattered electrons. A fluorescent screen placed in forward scattering position intersects parts of these cones, thereby forming an EBSP pattern. The fluorescence is collected by a SIT camera, digitally enhanced and indexed using the Channel⁺ software package from HKL-technology software, Denmark (Schmidt & Olesen 1989). The electron backscatter diffraction patterns provide detailed information about the orientation of the crystal lattice with respect to the incident electron beam. This technique was used to determine the misorientation between (sub)grains and to analyse the crystallographic fabric of the samples reported in chapters 3 and 4. The accuracy of the orientation determination is estimated to be $\sim 1^\circ$ (Randle 1982).

2.2.2 Transmission electron microscopy (TEM) analysis

TEM imaging was performed on a Philips CM200FEG (field emission gun) transmission electron microscope operating at 200 kV. Specimens were prepared from standard petrological thin sections mounted with lakeside cement. Copper TEM sample grids were glued onto the thin sections before dissolving the lakeside cement in ethanol, separating the thin section from the glass slide. To prevent cracking of the brittle specimens a second copper sample grid was glued onto the back of the samples. Finally, the specimens were trimmed with a razorblade and thinned to

perforation by argon ion-beam thinning at an incident angle of 12° – 18° in a GatanTM dual mill 600 operating at 4 kV and 1 mA beam current. To remove most of the damaged material from both sides of the specimen after perforation was achieved, an additional 30 minutes of ion beam thinning was performed with a low energy 1 kV beam at 30° incident angle. In a last step the samples were coated with a thin layer of carbon to prevent charging. In the initial stages of this work coating was done by sputtering carbon from a target attached to a molybdenum substrate in the ion mill. This resulted in minor contamination of chemical analyses by molybdenum. In a later stage carbon coating was done in an EdwardsTM vacuum coater.

Standard bright field (diffraction contrast) imaging at relatively low magnifications (<50 kx, chapter 3) was used to image micrometer-scale melt occurrences along grain boundaries and triple junctions. With this imaging mode, contrast in the crystalline areas in the sample arises from interaction of the incident electrons with the crystal structure. This interaction makes the contrast highly dependent on the crystal orientation and enables easy discrimination of individual grains. As amorphous materials lack an ordered structure, contrast in amorphous areas is independent of orientation. The changing contrast of the crystalline areas on tilting the specimen can thus be used to distinguish amorphous material (solidified melt) from the crystals. The determination of the precise shape of melt pockets requires not only that there is contrast across all relevant crystal-melt interfaces but also that all of the crystal-melt interfaces are vertical.

Details of the dislocation microstructure (chapter 4) and the nanometer-scale melt distribution along grain boundaries (chapter 5) were imaged with six additional TEM imaging and analytical techniques (see also Clarke (1979b), Vaughan & Kohlstedt (1982), and Kohlstedt (1990)). Weak beam dark field imaging was used to measure the dislocation densities and to determine the Burgers vectors of individual dislocations. The techniques used to detect the nanometer-scale melt features along grain boundaries can be subdivided into two groups. The first three techniques, diffuse dark field imaging (DDF), Fresnel fringe imaging (FFI) and high-resolution transmission electron microscopy (HRTEM) are based on the electron scattering properties of the material and give structural information. The latter two techniques, energy filtering imaging (EFI) and energy dispersive X-ray spectroscopy (EDX), provide chemical information. These techniques are briefly outlined below.

2.2.2.1 *Weak beam dark field imaging (WBDF)*

Standard dark field images of crystals can be obtained using a two-beam diffraction condition. Two-beam conditions are produced by orienting a specimen such that besides the transmitted beam only one strongly diffracted beam occurs in the diffraction pattern (McLaren 1991). A dark field image can now be formed by allowing only the diffracted electron beam to contribute to the image while blocking the transmitted beam by the objective aperture. If an object of interest causes local diffraction, e.g. due to bending of the lattice planes around dislocations, the corresponding (two-beam) dark field image produces a (bright) image of the object, seen in a dark area as the surrounding crystal does not produce diffracted intensity. This makes the imaging method particularly useful to study the characteristics of crystal defects. However, the resulting images of lattice defects using two-beam imaging conditions will have widths of several tens of nanometers

(Kohlstedt 1985). This image width prohibits the imaging of narrowly spaced dislocations in subgrain boundaries.

Weak beam dark field imaging provides similar information about crystalline defects, but at a higher resolution of 2–10 nm (Kohlstedt 1985). Higher resolution is achieved by tilting the specimen away from the ideal two-beam condition used in dark field imaging such that only the lattice planes that are distorted next to a dislocation provide significant diffraction intensity. Because the distortion of the crystal lattice around to a dislocation will be highly localised, e.g. a few lattice planes from the dislocation core, the resulting weak beam image shows a very narrow image of the defect. The nature of the dislocation dictates the identity of the lattice planes that bend around its core. The crystallographic orientation and Burgers vector of each dislocation can be determined by selecting specific diffracted beams to form the weak beam dark field image. Details of the determination of Burgers vectors are described in chapter 4.

2.2.2.2 Diffuse dark field imaging (DDF)

The diffuse dark field imaging technique is based on the amorphous character of a melt phase and is applied to detect nanometer-scale melt films along grain boundaries (chapter 5). Inelastically scattered electrons in amorphous material are represented as a diffuse ring of background intensity around the central spot in the diffraction pattern. Inelastically scattered electrons can be used for dark field imaging by orienting a section of this ring along the optical axis of the microscope and centring the objective aperture. In order to collect enough electrons to reduce film exposure times to ~90 seconds, the transmitted beam was continuously rotated around objective aperture 2 (20 μm). The rotation of the transmitted beam around the optical axis just outside the objective aperture enabled all electrons that are inelastically scattered up to $\sim 0.33^\circ$ to contribute to the image while blocking the electrons that dynamically scattered in the crystalline areas in the specimen. In this way melt pockets and amorphous films along grain boundaries can be made visible (Clarke 1979b; Clarke 1987; Grant Norton 1990; Cinibulk *et al.* 1993b).

Ideally the resulting images only show intensity from locations where the sample is amorphous. However, under some circumstances elastically scattered electrons may locally contribute to the images. This occurs when diffraction spots that are generated by lattice planes with spacings exceeding 4.3 \AA are present in the diffraction pattern. As such lattice spacings occur both in olivine and in orthopyroxene, this may happen when several grains are present in the field of view. The background intensity of diffuse dark field images is formed by the scattering of electrons in the thin amorphous top and bottom layers of the sample that are formed during ion milling. Carbon coating of the specimens introduced an additional film of amorphous material that may also contribute to the background intensity.

2.2.2.3 Fresnel fringe imaging (FFI)

The Fresnel fringe technique is analogous to the Becke line method used in light microscopy to determine the relative refractive index of neighbouring mineral grains. Fresnel fringe imaging enables determination of both the presence and thickness of an intergranular phase (chapter 5). Fresnel fringes are produced in defocused bright-field images when there is a discontinuity in the

mean inner potential (which is the volume-averaged part of the crystal potential (Bethe 1928; Li *et al.* 1999)) at an interface (Ness *et al.* 1986). By taking a through focus series of bright-field electron micrographs, the phase contrast that results from the differences in mean inner potential between two chemically or structurally distinguishable phases produces Fresnel fringes along the boundary (Clarke 1980; Ness *et al.* 1986; McLaren 1991; Cinibulk *et al.* 1993b). The presence of two closely spaced interfaces, e.g. thin grain boundary films (Drury & FitzGerald 1996; Cmíral *et al.* 1998), produces a double set of fringes. When the mean potential of a grain boundary film is lower than that of the adjacent grains, in under focus conditions, bright fringes with alternating lower intensity dark and bright Fresnel fringes occur on either side of the boundary. In over focus conditions, the contrast will be reversed (Clarke 1980). The spacing of the fringes decreases with decreasing defocus until Gaussian focus is reached where the fringe spacing equals the film thickness. The grain boundary film width can be determined from extrapolation of a graph of the first fringe maxima separation versus defocus (e.g. chapter 5, fig 5.9) (Cinibulk *et al.* 1993b). The most accurate film widths can be determined if defocus is smaller than 300 nm (Ness *et al.* 1986), but the fringes often do not become visible until defocus exceeds 200 nm. In order to collect enough data points for accurate curve fitting, larger defocus values, giving rise to uncertainties, have to be used. The Fresnel fringe imaging method can also be used to orient the grain boundary parallel to the electron beam (Ness *et al.* 1986). When the mean inner potential of the two adjacent crystals is the same, the intensity of the fringes on both sides of the boundary will only be the same when the grain boundary is parallel to the electron beam. A grain boundary without an amorphous phase can either show no fringes (if the potentials of the grains are equal, i.e. if it is the same mineral), or a single set of Fresnel fringes if the neighbouring grains have a different composition.

The intensity of Fresnel fringes is greatly influenced by the diffraction conditions of the adjacent grains. Variations in diffraction intensity between grains may give rise to the appearance of fringes with different intensities on either side of the boundary and give the illusion that the boundary is not parallel to the beam (Ness *et al.* 1986). The appearance of Fresnel fringes with the same sign on both sides of a melt-film containing interface assumes that the mean inner potentials of both grains have the same (relative) sign with respect to the glass phase. If one of the grains has a higher potential and the other has a lower potential compared to the glass phase, it can be difficult to recognise an intergranular amorphous phase. Also, one should be cautious that Fresnel fringes are not only produced at interfaces of materials with different potential (i.e. different crystal structure or different composition), but also at abrupt thickness variations that may occur when a grain boundary is preferentially etched away in the ion beam thinner (Rasmussen *et al.* 1989).

2.2.2.4 High-resolution (lattice fringe) imaging

High-resolution lattice imaging can be used to study grain boundary microstructures, for instance to determine if a crystal-melt contact is atomically straight or jogged. In this work, the technique was used for investigating the structural width of grain boundaries and for determining whether or not an intergranular phase was present (chapter 5) (Clarke 1978; Clarke 1979a,b;

Carter & Sass 1981; Clarke 1985; Grant Norton & Carter 1990; Kleebe *et al.* 1992; Cinibulk *et al.* 1993a, b; Kleebe *et al.* 1993; Tanaka *et al.* 1994a; Kleebe *et al.* 1994a). At magnifications higher than 200 kx (Clarke 1979b) the lattice planes of adjacent grains can be imaged together with any intergranular amorphous film. Rigorous imaging conditions are required. For accurate measurement of the film thickness, the grain boundary should be exactly parallel to the electron beam. Furthermore, to be able to measure the thickness of an amorphous film between two grains, both crystals must show lattice fringes that terminate at the grain boundary, which requires that both grains are oriented in at least a two-beam diffracting condition. To prevent the occurrence of Moiré fringes (Edington 1976), the grain boundary has also to be flat over a certain distance. The maximum structure resolution in high resolution images is obtained at Scherzer defocus, but images were taken at Gaussian focus (McLaren 1991) to prevent lattice fringes extending into an amorphous film as an imaging artefact and so obscuring the actual film thickness. A major advantage of this technique is the availability of an internal magnification standard in the form of the lattice fringe spacing that corresponds to a known crystallographic d-spacing.

2.2.2.5 Energy-filtering imaging (EFI)

The energy-filtering method is based on the characteristic energy loss of electrons interacting with the atoms in the material (Egerton 1986). Energy-filtering is applied to the electron beam(s) that are selected to form the normal (unfiltered) image. When electrons that have lost a characteristic amount of energy are isolated from the main beam(s) and used to form an energy-filtered image, images can be made that show intensity variations representing the distribution of the element of interest (Egerton 1986).

Two main types of images that show chemical information can be obtained (Hofer & Warbichler 1996), elemental maps (three-window method) and jump-ratio maps (two-window method). In elemental maps, two energy-filtered images are produced at energy-loss intervals that do not contain element specific information before the energy-loss signal of the element of interest. These background images are used to extrapolate the background intensity curve to the energy-loss interval of interest. From this extrapolated signal a background image for the ionisation edge of the element of interest is calculated and subtracted from the actual energy-filtered image (Hofer & Warbichler 1996). This subtraction results in an image produced by electrons that have been inelastically scattered by the element of interest, showing its distribution. The three-window (elemental map) imaging mode is not suitable for situations where the element peak in the energy-loss spectrum is only slightly higher than the background intensity. The three-window method can then only be used if the fit of the background intensity is very accurate. Often the fit is poor due to the simple power-law approximation of the intensity curve, which does not allow for accurate background subtraction and produces noisy images and artefacts (Hofer & Warbichler 1996).

The two-window (jump-ratio map) imaging mode is an alternative method that can be applied when the signal from the elements of interest produces minor peaks in the energy-loss spectrum and background fitting and subtraction in the three-window method is too poor to produce good images. In the two-window method, the ionisation edge image that contains the signal from the

element of interest is filtered by subtracting one pre-edge background image, which enhances the areas where the element of interest occurs while adding minimum noise.

The TEM energy-filtering imaging was conducted by Dr M. Otten at Philips Electron Optics, Eindhoven on a Philips CM200FEG instrument equipped with a Gatan energy filter (GIF).

2.3 EDX analysis

In addition to TEM imaging techniques, chemical analyses of grain boundaries and olivine grain interiors were performed using EDX (energy dispersive X-ray spectroscopy) in the TEM to establish if grain boundary regions have a different chemical composition than olivine grain interiors. Chemical differences along grain boundaries were anticipated as a basaltic melt produced by *in situ* partial melting in olivine-orthopyroxene rocks is rich in Ca and Al and a melt phase that occurs at olivine-olivine grain boundaries is therefore expected to contain higher concentrations of Ca and Al (Kohlstedt 1990; Drury & FitzGerald 1996; Cmíral *et al.* 1998). EDX-analyses were carried out in nanoprobe mode using an EDAX DX4 system equipped with a super ultra-thin window (SUTW) detector with a 30 mm² active area. The beam diameter used was approximately 3 nm at an accelerating voltage of 200 kV. When possible, grain boundaries were oriented parallel to the incident electron beam to maximise the X-ray yield of atoms from the grain boundary.

The electron beam was positioned on the grain boundary using microdiffraction, the beam was shifted towards the boundary until the first appearance of a second diffraction pattern indicated that the electron beam covered the grain boundary region and a small area of both adjacent crystals. Because of this precise localisation of the beam on the grain boundary, the beam was held stationary during analysis. To minimise element loss, relatively short acquisition times (<100 seconds) were used. Preferably a maximum of 30000 counts were collected in each analysis, but the weak signal in the thinnest areas along the edge of the specimen sometimes produced less than 10000 counts before contamination influenced the relative peak heights of Mg, Al, and Si in the spectra. It is assumed that all the elements present in the melt phase equally contribute to the X-ray signal, but during X-ray analysis of TEM samples, certain elements may migrate from the beam position and thus alter the chemical composition of the studied area significantly (Champness & Devenish 1990).

Interpretation of the EDX results in a qualitative way, i.e. determining the presence of an atomic phase and comparing relative abundance, is readily done as the detection limit for EDX analysis lies at approximately 0.1–0.5 wt% (Peacor 1992). However, quantification of such low concentrations in an EDX spectrum obtained in the TEM is dubious. Details of the calibration procedure of the EDX system and the processing of olivine and grain boundary analyses are given below.

2.3.1 EDX quantification procedures

Quantification of the EDX spectra obtained in the TEM was performed using the techniques originally developed by Cliff & Lorimer (1975) (see also Van Cappellen *et al.* 1984; Sheridan 1989; Van Cappellen 1990; Williams *et al.* 1992; Eibl 1993a, b; Van Cappellen & Doukhan 1994). Spectra were processed using the EDAX DX4-mDX remote software (version 1.52). If it is

assumed that absorption or secondary fluorescence effects are negligible and the thin film criterion is satisfied (see Goldstein (1979) and references therein) which is often assumed to be the case for thin TEM foils, the atomic ratio of an element of interest (X) with respect to a reference element (R), C_X/C_R , equals their X-ray intensity ratio times a correction factor K_{XR} :

$$\frac{C_X}{C_R} = K_{XR} \frac{I_X}{I_R} \quad [2]$$

where I_X and I_R are the net peak integral in the EDX spectrum of element X and reference element R respectively. The K_{XR} factor in the Cliff-Lorimer equation is a proportionality term that, because of the thin film approximation, depends only on accelerating voltage and not on sample characteristics such as composition and thickness. The K-factors can be calculated using theoretical models or determined experimentally by analysing samples with a known composition (Sheridan 1989 and references therein). Detector characteristics, like the window thickness, have great influence on the detected X-rays intensities, particularly light elements with $Z < 14$ (i.e. lighter than Si) which have K_{α} -energies less than 2 kV. Therefore, for quantification of EDX spectra of minerals, it is best to use K-values that are experimentally determined on the specific instrument used for analysis (Van Cappellen, personal communication). This requires a calibration of the yield of the detector set-up of the elements of interest with respect to Si, which can be used as the reference element as it is present in all mineral and melt analyses.

Reliable quantification of the chemistry of an unknown grain or glass volume also needs a correction for absorption effects, which requires either extrapolation of a series of EDX-analyses to zero thickness or knowledge of the mass absorption coefficients, sample density, and sample thickness. Van Cappellen & Doukhan (1994) describe an alternative technique to obtain an absorption correction using the previously determined K-values. As in the Cliff-Lorimer ratio technique, the ratio of intensity attenuation factors for two elements gives an approximation of the actual absorption correction factor A:

$$A = \frac{f_X}{f_R} \approx 1 - \frac{1}{2}(\mu_X - \mu_R)\cos(\theta)\rho\Delta t \quad [3]$$

where f_X and f_R are the intensity attenuation factors for the element of interest and the reference element respectively, $(\mu_X - \mu_R)$ is the difference of the mass absorption coefficients, θ is the X-ray take off angle, ρ the density and Δt specimen thickness. When X-rays from both elements suffer similar absorption, A is close to unity and the absorption correction is small. However, when two elements whose mass absorption coefficients differ significantly are compared, even small variation of θ , ρ and Δt have a serious effect on the absorption correction factor A.

Because the absorption correction applied in EDX systems is approximated by a quadratic expression (Van Cappellen & Doukhan 1994) and θ and ρ are properties that do not change for individual analyses, processing a spectrum three times using appropriate K-values and arbitrary

thickness results in parabolic curves that represent the concentration in at% as a function of Δt . When the curve of each element is multiplied by the valence state of that element, cumulative parabolic curves are obtained for both the positive and negative ‘charges’. The intersection of these two parabolas represents the only value of the virtual thickness where the sample is electrically neutral. When the spectrum is analysed again and the absorption correction is applied for this virtual thickness, this yields the actual composition of the analysed area. If the density of the sample material is also known, the thickness of the probed area can be calculated (Van Cappellen & Doukhan 1994).

2.3.2 EDX K-value determination

The characterisation of the EDX system was performed together with Dr H.L.M. van Roermund. K-values have been determined for the main elements in the studied minerals using mineral standards for calibration (table 2.1). Calibration was done by performing 10 to 20 spot analyses along a profile with decreasing thickness for each determination and quantifying the spectra using an initial value of $K^X/R=1$. Extrapolation of the results with a linear or parabolic fit to zero thickness allowed calculation of the concentration ratio of the elements of interest with respect to Si without absorption correction. The extrapolated element ratios were then compared to the real ratio and K-values were calculated using equation [2] (table 2.1). The resulting K-values are average values of a number of calibration measurement series from each mineral sample with their standard deviations. The $K^{O/Si}$ -values determined for the different minerals show a large spread within each sample and also between the different standards. This suggests that absorption effects were insufficiently corrected. Therefore, to test if there is a relationship between the $K^{O/Si}$ -value and mineral composition, the average $K^{O/Si}$ -values were calculated for each mineral and plotted against the mean atomic weight of the minerals (fig 2.1). The large spread in calculated $K^{O/Si}$ -value within each standard and limited range in mean atomic weight indicate that the results have to be interpreted with caution, but there seems to be a correlation between the mean atomic weight and the average $K^{O/Si}$ -value. This finding has to be confirmed, but if true it would indicate that the thin film criterion on which the Cliff-Lorimer relationship is based is not satisfied for low energy oxygen X-rays. This has important implications for the use of the thickness estimation and the resulting absorption correction in the standardless quantification method proposed by Van Cappellen *et al.* (1984) that is based on charge neutrality - which depends upon a relatively accurate value for $K^{O/Si}$.

	used mineral standards	mean value	anorthite
O	olivine	$K^{O/Si} = 3.01$	4.05
O	olivine + all minerals below	$K^{O/Si} = 3.31 \pm 0.59$	
Mg	augite; diopside; olivine; enstatite; hyperstene	$K^{Mg/Si} = 1.11 \pm 0.11$	
Al	jadeite; albite; andalusite	$K^{Al/Si} = 0.94 \pm 0.07$	1.79
Ca	augite; titanite; diopside; hedenbergite; wollastonite	$K^{Ca/Si} = 1.31 \pm 0.19$	3.04
Fe	hedenbergite	$K^{Fe/Si} = 1.48 \pm 0.16$	

table 2.1 K^X_{Si} -values for the major elements in olivine and orthopyroxene grains obtained from different mineral standards. The high K^X_{Si} -values that were determined from an anorthite sample were probably influenced by radiation damage and were not included in the mean values.

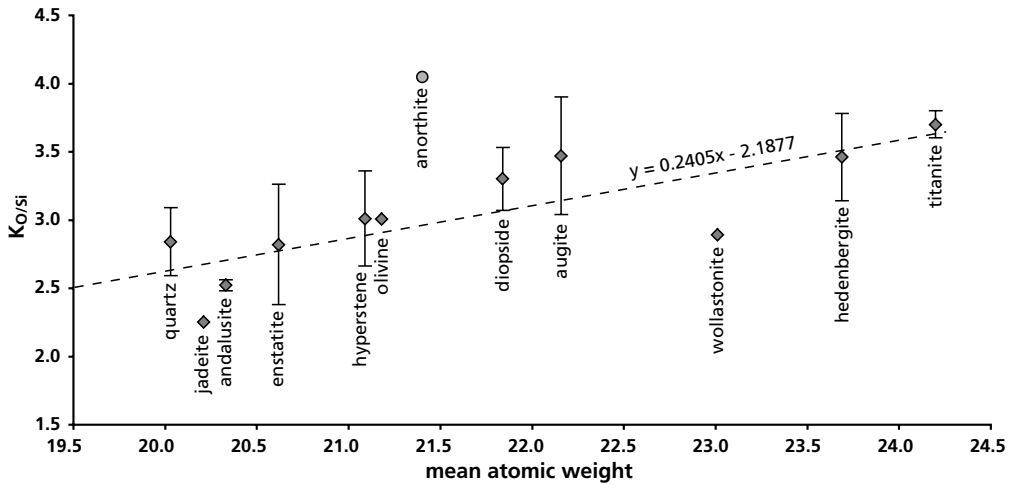


fig 2.1 Variation in $K^{O/Si}$ -values determined in different mineral standards plotted versus their mean atomic weight. The error bars in the figure are an indication of the spread in calculated $K^{O/Si}$ -values within each mineral standard. Values without error bars represent single $K^{O/Si}$ determinations.

2.3.3 Element loss during EDX analysis

In addition to uncertainties in determining the amount of absorption that occurs during analysis, beam interaction with the specimen can also introduce problems in reliably measuring the chemistry of small areas in thin TEM sections. Exposure of a specimen to a narrow (<10 nm) high intensity beam can cause element evaporation or migration away from the analysis spot. The conditions at which mass loss occurs depends on the current density of the electron beam (number of electrons per unit area), the element involved, and the mineral or glass phase involved. Champness & Devenish (1990) evaluated radiation damage and mass loss in silicate minerals in electron microscopes equipped with LaB_6 and field emission sources for a range of acceleration voltages (see also Champness & Devenish (1992) and Devenish & Champness (1992)). In the first few seconds of analysis, significant mass loss occurred in a variety of minerals, especially of the lighter elements, Na and Al. After the initial drop in measured relative X-ray intensity, the composition in the analysed area stabilised in the beam and the remaining (weak) X-ray signals seemed to stay constant; any further element loss was not apparent (Champness & Devenish 1990).

The loss or redistribution of elements during analysis may explain the high K-values calculated for minerals that easily damage in the electron beam, for example anorthite (table 2.1 and fig 2.1). These values were not used in the calculation of the average K-values in the present study. If an initial mass loss (which is dependent on the mineral involved (Champness & Devenish 1990; Champness & Devenish 1992)) is not recognised, K-values are calculated that are specific for a certain mineral and current density and not at all representative for the EDX system. This is another potential problem in the experimental determination of the K-values. When the K-value

for an element is measured in different mineral standards that have different initial mass losses under constant microscope conditions, this would result in different K-values for the same element. Because the mass loss occurs in the first few seconds of the analysis and the collection time is generally longer than 20 seconds it is hard to assess whether element loss has occurred and whether the determined K-value is representative.

For accurate quantitative chemical analysis it is therefore necessary to confirm that no initial mass loss occurs. For accurate monitoring of possible element loss, the incoming X-ray signal in the energy interval of the element of interest should be monitored with time. This was not possible with the EDX-software used. In the analyses of the olivine and orthopyroxene grains no significant element loss was observed, but in some cases element loss was observed on the computer monitor in the glass phase at low beam intensities, even when the beam intensity was so low that the exposure time exceeded 99 seconds (the maximum time indicated by the exposure meter). Lowering the beam current further to minimise element loss was impractical as the screen brightness becomes too low to allow for accurate positioning of the beam on the grain boundary. In order to minimise the uncertainties associated with the quantification procedure, the EDX analyses reported in this thesis were treated qualitatively. A possible method for the quantification of the chemistry of grain boundary regions is outlined in Appendix B.



fig 2.2 Controlled oxygen fugacity furnace set-up

2.4 Experiments in the controlled atmosphere furnace

2.4.1 Furnace set-up

Long-duration annealing experiments on olivine–orthopyroxene samples were carried out in a Carbolite™ Eurotherm 808P furnace at 1130°C with controlled oxygen fugacity at atmospheric pressure. Oxygen fugacity was monitored using a zirconia-based solid electrolyte oxide sensor (SIRO₂ C700⁺) from Ceramic Oxide Fabricators™. Annealing samples consisted of slices of hot-pressed and previously deformed olivine–orthopyroxene rocks. The furnace set-up is shown in fig 2.2. The furnace is centred around a vertical 110 cm long corundum tube with 5 cm inner

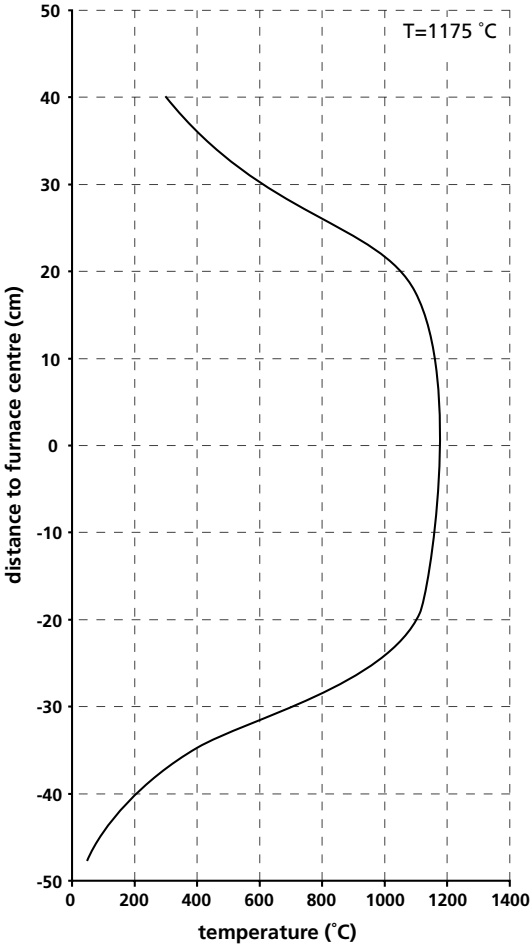


fig 2.3 Temperature profile within the furnace tube, determined for a hot-zone temperature of 1175°C.

diameter. Both ends of the tube were sealed and cooled with tap water. The central 10 cm of the corundum tube was uniformly heated and showed a total temperature variation of ~5°C (fig 2.3). The oxygen fugacity was controlled by a mixture of CO₂ and H₂ gas that flowed past the specimen with a flow rate of 70 ml/minute. The gas mixture was introduced at the top of the furnace and allowed to exit through a hose at the bottom

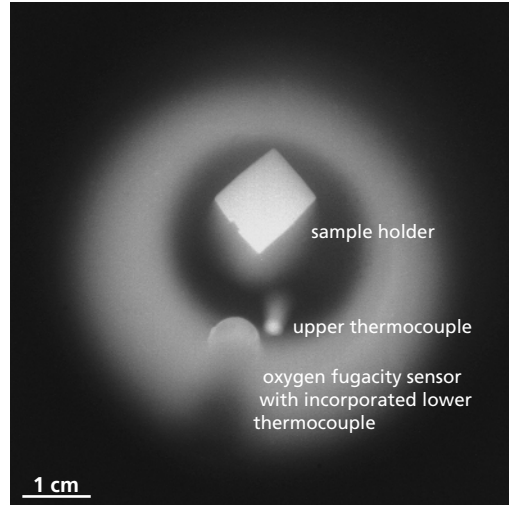


fig 2.4 Sample and sensor assembly in the hot-zone during annealing at 1130°C viewed from the bottom of the furnace tube.

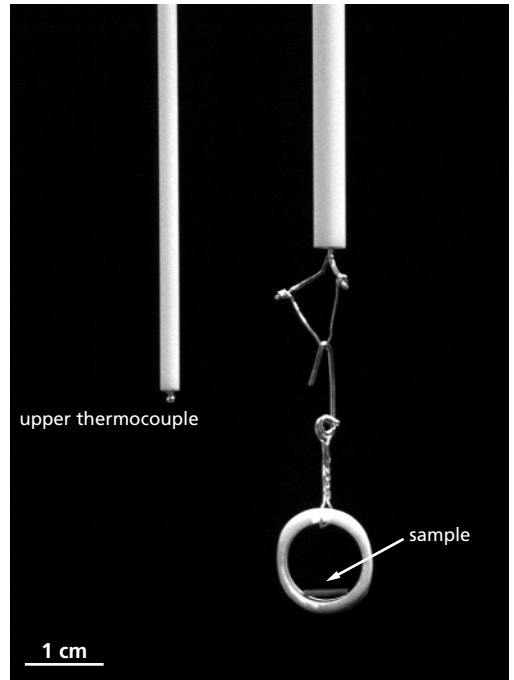


fig 2.5 Upper thermocouple and sample holder assembly attached to the upper lid of the furnace tube. Note that the sample in the specimen holder only touches the holder along its edges.

of the furnace tube. Temperature and oxygen fugacity were monitored by one thermocouple just above and an oxygen fugacity sensor with integrated thermocouple just below the sample assembly (fig 2.4). The output of the sensors was continuously monitored during the experiments and stored in a computer. Data were recorded by a program written by Dr C.J. Peach and Dr

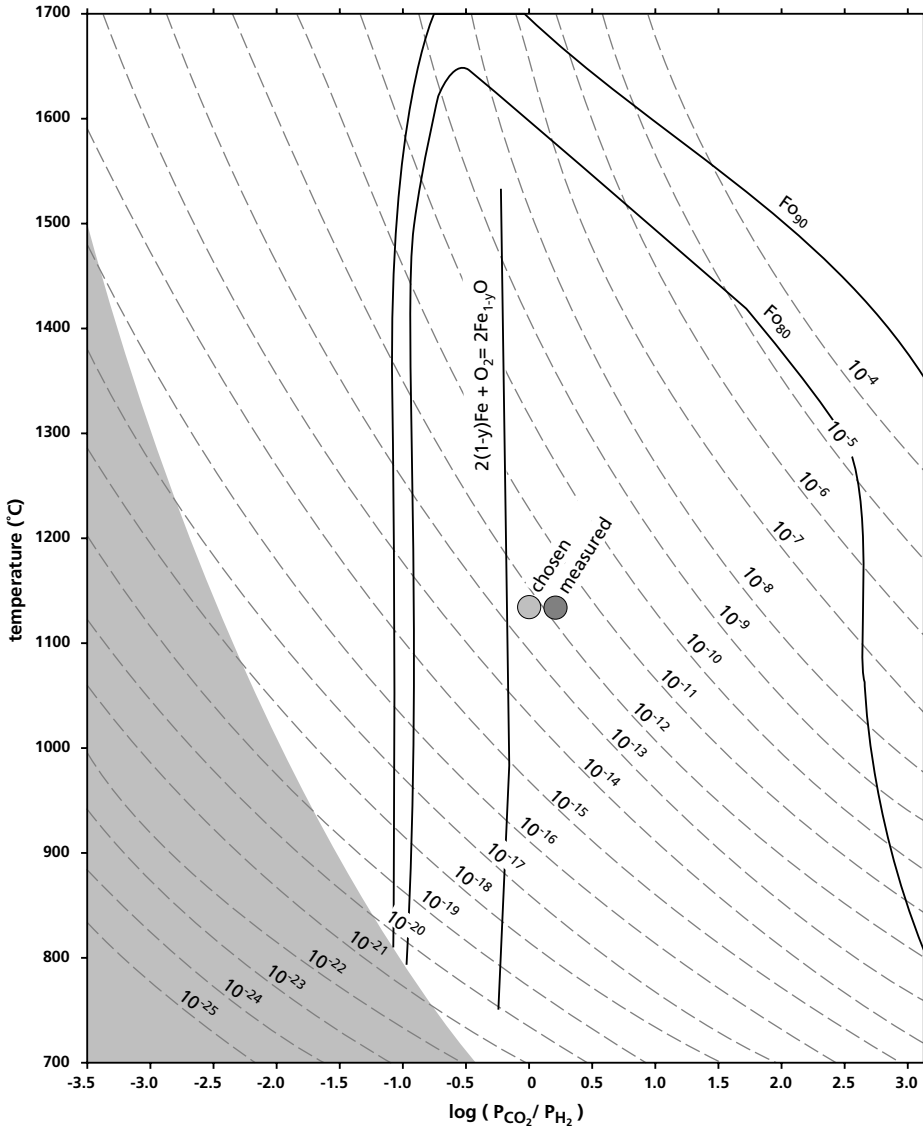


fig 2.6 Relationship of the oxygen fugacity produced by a CO_2/H_2 -gas mixture with temperature (Muan & Osborn 1965). The stability fields of olivine Fo_{80} and Fo_{90} are indicated (Ricoult 1978) to show the stability range of typical mantle olivine crystals. The oxygen fugacity that is imposed by the solid-state iron-wüstite buffer used in deformation experiments is independent on temperature and corresponds to a gas-mixture: $\log (P_{\text{CO}_2} / P_{\text{H}_2}) = -0.3$ (Huebner 1987). The grey area indicates the field where graphite is stable and may precipitate from the gas (Huebner 1987).

R.D. McDonnell. The samples were placed inside a sample holder formed by a cylinder of pure synthetic forsterite material supplied by Dr R.D. McDonnell (see McDonnell 1997) that was attached to a 4 mm thick ceramic tube by platinum-wires (fig 2.5). The open sample cylinder allowed free access to the gas-mixture ensuring a constant oxygen fugacity. Both the upper thermocouple and the specimen holder were attached to the top lid of the furnace tube that could be removed to insert the specimen. The position of the specimen in the furnace could be modified by moving the 4 mm tube through clamps in the top lid.

Deformation experiments were performed with the oxygen fugacity limited by a Fe jacket close to the Fe-FeO buffer. Therefore, for the annealing experiments the gas mixture of 50% CO₂ and 50% H₂ was chosen to approach this oxygen fugacity during annealing while maintaining a maximum possible flow rate of 70 ml/minute (fig 2.6). The oxygen fugacity that was measured by the fugacity sensor during annealing was slightly higher than that calculated from the gas mixture. It could not be determined whether this anomaly was related to the performance of the oxygen fugacity sensor or to a variation in the gas-flow regulator that was used to prepare the gas-mixture. Both the chosen and measured oxygen fugacity values were close to the iron-wüstite buffer and fell well within the stability field of mantle olivine, so this deviation was neglected.

2.4.2 Experimental procedure

Before inserting the sample, the top lid of the furnace tube was removed and the specimen holder was retracted to the uppermost position just below the lid. Thin slices, approximately 1 x 5 mm, were cut from the deformed cylindrical specimens and inserted in the forsterite sample holder such that contact between the two materials was limited to the edge of the specimens. After closing the furnace tube, the gas-flow was established while the specimen was located in the upper end of the tube at a temperature below 200°C. When the temperature and oxygen fugacity were stable, the sample was gently lowered into the hot-zone at approximately 1 cm/minute. Quenching of the sample after annealing was performed by extracting the sample holder 30 cm out of the hot-zone (fig 2.3) which resulted in cooling down to 600°C in a few seconds. After initial cooling, the sample assembly was allowed to cool down for 10 minutes before moving the sample to the uppermost position. This procedure avoided damage to the O-rings that sealed the furnace tube.

Deformation, static annealing, and microstructural characterisation of the studied partially molten olivine and olivine-orthopyroxene rocks

3.1 Introduction

In this chapter, the mechanical and microstructural data of the partially molten olivine and olivine-orthopyroxene materials investigated in this study are presented. Two sample sets were used. One consists of some olivine and olivine-orthopyroxene samples from the study of Hitchings *et al.* (1989). The other set is comprised of samples with similar compositions and deformation histories from an experimental study performed in 1991-1992 by Dr M.R. Drury at the Australian National University (ANU) in Canberra. The results of the study of Drury are presented in this chapter and in appendix A where the stress-strain curves are given. A low degree of partial melting has occurred in all samples. Both studies were concerned with the effect of orthopyroxene content on the rheology of olivine-orthopyroxene rocks. The observations of Hitchings *et al.* (1989) indicate that the orthopyroxene content influences the strength of the rock with a minimum strength at 50% orthopyroxene. It is not clear what mechanism was responsible for the observed weakening as it is usually assumed that the mechanical properties of olivine-orthopyroxene rocks are primarily controlled by the weakest and most abundant component, olivine (e.g. Karato & Wu 1993). The study of Drury aimed to determine the mechanisms responsible for the weakening observed by Hitchings *et al.* (1989). In order to correlate mechanical behaviour exhibited by the samples with their microstructure, the microstructural features needed to be characterised in all relevant samples. This limited the number of samples that could be studied in detail using a number of time consuming TEM and SEM techniques. Based on the experimental results, five key samples were selected for which various aspects of the grain-scale deformation and melt-microstructure were investigated. Two deformed samples and the starting material for one of the samples were selected from the study of Hitchings *et al.* (1989). The other two deformed samples were from the study of Drury. The hot-pressed starting material for the latter samples was not available as the experimental procedure consisted of hot-pressing directly followed by deformation. In addition to the deformation experiments, three of these samples were statically annealed in a controlled oxygen

fugacity furnace for durations exceeding 100 hours to investigate the stability of the melt microstructures that developed during deformation.

First the experimental results from both studies are given. In the second section of this chapter a microstructural characterisation of the five selected samples is presented to establish if the cause of the mechanical weakening can be related to a difference in microstructure. In the third section the microstructures of the long-duration statically annealed samples are described. The grain size distribution was estimated on the same SEM forward scattering images that were used for the electron backscatter diffraction pattern (EBSP) crystallographic orientation analysis (see chapter 2)*. Melt content and melt distribution were determined from SEM backscattered electron images. Melt connectivity and possible differences in the grain-scale melt distribution between samples were estimated by measuring the solid-melt dihedral angle distributions on TEM bright field images.

3.2 Deformation experiments

All deformation experiments were performed in a Paterson gas-rig at the Australian National University (ANU) in Canberra. Samples have been prepared from olivine and orthopyroxene crystals that were taken from two spinel lherzolite nodules from Mt. Leura (samples 5072, 5099, 5132, and 5249, (5xxx samples) Hitchings *et al.* (1989)) and Mt. Porndon (samples 6208, 6212, 6213, 6218, 6219, 6220, 6222, and 6223, (62xx samples) Drury) from the Western District volcanics of Victoria, Australia. No basalt powder was added to form the melt phase. The specimens from Hitchings *et al.* (1989) may contain some tungsten-carbide contamination resulting in a grey appearance of the samples, originating from the powder preparation by tungsten-carbide ball milling. Cylindrical ~7 mm wide and 15 mm long samples in iron jackets were initially cold-pressed, followed by hot-pressing at 1200-1230°C and subsequent deformation in multiple stages. The ingredient material for samples 5072, 5099, and 5249 was oven-dried before cold-pressing. The 62xx samples were not dried prior to deformation, except for sample 6220 that was dried at 1200°C for 60 hours before cold-pressing. An IR study on the other 62xx samples indicated that they also were dry (M. Cmíral, personal communication). The specimen preparation is described in detail in Hitchings *et al.* (1989). After deformation, the samples were cut along their length except for sample 5132 that was sectioned from the top of specimen 5249 before deformation. Two petrological thin sections were prepared from each specimen. One was polished for SEM analysis, from the other several TEM grids were prepared and ion beam thinned to perforation. The compositions of the ingredient materials used to make the specimens in both suites of experiments and the experimental details are shown in tables 3.1 and 3.2. The µm-scale melt pockets in sample 5249 that could be analysed with an electron microprobe were silicon-rich and showed compositions in the range 53-55% SiO₂, 19-22% Al₂O₃, 7-9% CaO, 2-7% MgO, and

* All measurements on SEM images were performed on a Macintosh computer using the public domain program NIH Image (developed at the U.S. National Institutes of Health and available on the Internet at <http://rsb.info.nih.gov/nih-image/>).

	olivine 5xxx samples	orthopyroxene 5xxx samples	olivine 62xx samples	orthopyroxene 62xx samples
SiO ₂	40.91	55.99	41.09	56.96
TiO ₂	-	0.09	-	-
Al ₂ O ₃	0.03	2.88	-	2.03
Cr ₂ O ₃	-	0.60	-	0.47
FeO	9.21	5.34	8.47	5.52
MnO	0.13	0.15	-	-
NiO	0.28	0.09	0.41	-
MgO	49.37	34.04	50.03	34.43
CaO	0.07	0.75	-	0.58
Na ₂ O	-	0.09	-	-
<i>Mg/Mg+Fe</i>	<i>90.5</i>	<i>91.9</i>	<i>91.3</i>	<i>91.7</i>
<i>backscatter coefficient</i>	<i>0.1386</i>	<i>0.1350</i>	<i>0.1376</i>	<i>0.1346</i>

table 3.1 Microprobe analyses of the ingredient material for the 5xxx series experiments (data from Hitchings *et al.* 1989) and for the 62xx series experiments (wt%, normalised to 100%).

sample	material	initial grain size fraction (μm)	confining pressure (MPa)	temperature (K)	initial strain rate (s^{-1})	flow stress (MPa)	strain (%)	stress exponent (n)
5072a	olivine	5-10	300	1500	1.3×10^{-5}	194	7.8) 2.7
<i>5072b</i>	olivine	"	300	1500	4.5×10^{-5}	309	5.4	
<i>5072c</i>	olivine	"	300	1500	1.3×10^{-4}	408	7.8) 3.1
<i>5072d</i>	olivine	"	300	1500	4.8×10^{-5}	295	4.3	
5099a	olivine	10-38	300	1500	1.2×10^{-5}	205	6.6) 2.5
<i>5099b</i>	olivine	"	300	1500	4.0×10^{-5}	330	5.3	
<i>5099c</i>	olivine	"	300	1500	1.3×10^{-4}	420	7.0) 4.9
5132	70% olivine 30% enstatite	10-38	300	1484-1490	n.a.	n.a.	n.a.	
5249a	70% olivine 30% enstatite	10-38	300	1500	1.4×10^{-5}	116	7.0) 2.4
<i>5249b</i>	70% olivine 30% enstatite	"	300	1500	4.5×10^{-5}	188	6.5	
<i>5249c</i>	70% olivine 30% enstatite	"	300	1500	1.4×10^{-4}	255	8.3) 3.7
6208	olivine	10-38	300	1473	7.2×10^{-6}	195.4	9.0	
6220	olivine	5-10 (dried)	300	1473	8.2×10^{-6}	179.6	11.0	
6223a	olivine	2-10	300	1573	3.7×10^{-5}	129.6	6.5	
<i>6223b</i>	olivine	"	300	1523	3.5×10^{-5}	181.2	8.6	
<i>6223r</i>	olivine	"	300	1523	relaxation	57.0	1.9	3.1
6212	50% olivine 50% enstatite	10-38	300	1473	6.1×10^{-6}	190.0	4.6	
<i>6213</i>	50% olivine 50% enstatite	"	300	1473	7.2×10^{-6}	172.9	7.7	
6218	70% olivine 30% enstatite	10-38	300	1473	6.8×10^{-6}	174.2	7.7	
<i>6219</i>	70% olivine 30% enstatite	"	300	1473	7.0×10^{-6}	182.5	7.7	
6222a	70% olivine 30% enstatite	10-38	300	1573	3.7×10^{-5}	96.7	6.4	
<i>6222b</i>	70% olivine 30% enstatite	"	300	1523	3.4×10^{-5}	172.6	8.2	

table 3.2 Experimental parameters for both suites of experiments. Sample numbers in *italic* are subsequent deformation steps of the sample in **bold** print at different stress and/or temperature. Samples with numbers 5xxx are from Hitchings *et al.* (1989), samples with numbers 62xx are from the experiments performed by Drury. Parameters for the 5xxx samples are based on the completed strain rate steps and may deviate from the values reported by Hitchings *et al.* (1989) that are taken at 5% strain (for $\dot{\epsilon}=10^{-5} \text{ s}^{-1}$, $T=1500 \text{ K}$) because not all of their specimens clearly reached a steady state.

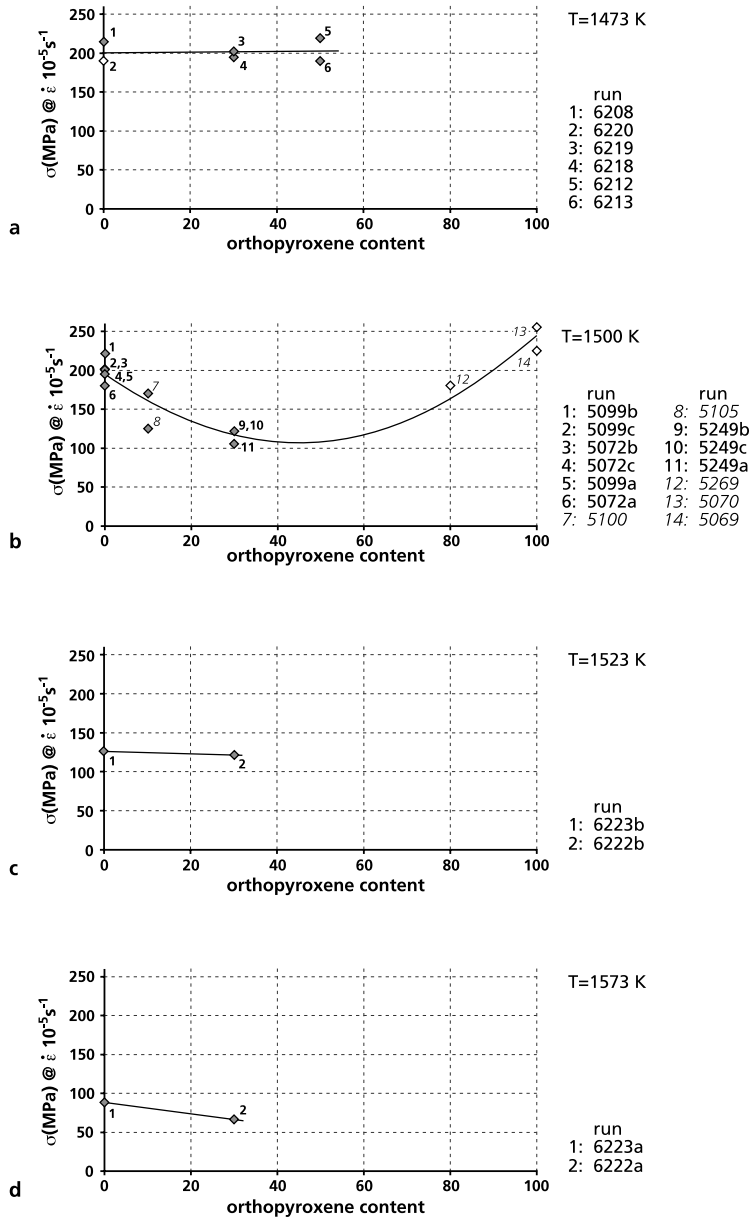


fig 3.1 Flow stress variation with orthopyroxene content in deformation experiments at temperatures 1473 K (a), 1500 K (b), 1523 K (c), and 1573 K (d).

Experimental runs at 1473 K, 1523 K, and 1573 K are performed by Drury (samples 62xx). Experiments at 1500 K are the olivine, olivine-orthopyroxene, and orthopyroxene specimens from Hitchings *et al.* (1989) (samples 5xxx). Samples with numbers in *italic* are additional samples taken from Hitchings *et al.* (1989) and are not included in table 3.2. Strain rate is normalised to 10^{-5} s^{-1} using a stress exponent $n=3.5$ (Bai *et al.* 1991). No temperature normalisation was carried out.

2–5% FeO with the balance made up of alkalis and H₂O (Drury & FitzGerald 1996). Strain rate stepping tests of Hitchings *et al.* (1989) and a relaxation test of Drury showed stress exponents $n \sim 3$, indicating that dislocation creep was the rate-limiting deformation mechanism.

The variation of flow stress with orthopyroxene content is shown in figure 3.1a–d for samples deformed at 1473, 1500, 1523, and 1573 K respectively (for sample numbers see table 3.2). The samples deformed at 1473 K and at 1523 K (experiments performed by Drury) show no apparent influence of orthopyroxene content on flow stress (fig 3.1a, c) and only a slight weakening with increasing orthopyroxene content was observed in samples deformed at 1573 K (fig 3.1d) (experiments performed by Drury). In contrast to the experiments performed by Drury, the 5xxx experiments carried out by Hitchings *et al.* (1989) (fig 3.1b) show a strain rate variation with orthopyroxene content that is indicative for minimum strength at 50% orthopyroxene. A comparison of the strength of the pre-dried olivine sample 6220 deformed at 1473 K (fig 3.1a, open diamond) with the non-dried 62xx samples indicated that if any water was present in the latter samples, its influence was negligible. Activation energies for creep in the olivine-orthopyroxene and olivine materials from the experiments performed by Drury were estimated using two methods (fig 3.2a, b). Two temperature-stepping tests performed at constant strain rate,

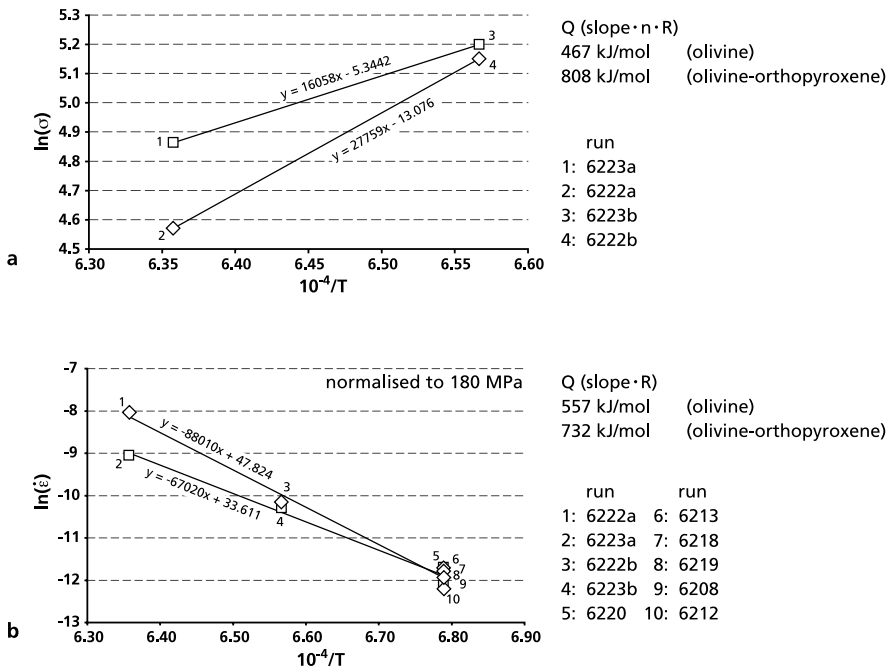


fig 3.2 (a) Activation energy determination from temperature stepping tests with experimental run combinations 6222a, 6222b (olivine-orthopyroxene) and 6223a, 6223b (olivine). (b) Activation energy determination from the strain rate measurements of all 62xx series experiments. The strain rate is normalised to 180 MPa differential stress.

Normalisation and determination of the activation energy Q were carried out using a standard flow law of the form $\dot{\epsilon} = A\sigma^n e^{(-Q/RT)}$ using stress exponent $n=3.5$, where $\dot{\epsilon}$ is strain rate (s^{-1}); σ is applied differential stress (MPa); Q is activation energy (J), R is the gas-constant (J/Kmol), T is temperature (K), and A is a constant.

experiment combinations 6222a, 6222b (olivine-orthopyroxene) and 6223a, 6223b (olivine), yielded activation energies of 808 kJ/mol for the olivine-orthopyroxene sample and 467 kJ/mol for the olivine material (fig 3.2a). Figure 3.2b shows an alternative determination of the creep activation energy using the strain rate variation in all 62xx series experiments with differential stress normalised to 180 MPa. This yielded activation energies of 732 kJ/mol for the olivine-orthopyroxene samples and 557 kJ/mol for the olivine samples.

Comparison of the data presented here (both 5xxx and 62xx samples) with the results of Chopra & Paterson (1984), Mackwell *et al.* (1985), and Karato *et al.* (1986) required that the stress-strain rate data be normalised to 1573K. There is uncertainty in the activation energy for creep of fine-grained olivine. Therefore the data was normalised twice using two possible values. The first normalisation was carried out using the activation energy estimated by Drury & FitzGerald (1998) for dry fine-grained olivine deforming by (weak) [a]-slip: $Q=385$ kJ/mol (fig 3.3a). The second normalisation was carried out using the activation energy for dry fine-grained olivine deforming by (strong) [c]-slip: $Q=535$ kJ/mol (fig 3.3b) (Chopra & Paterson 1984; Drury & FitzGerald 1998). In figure 3.3a olivine samples 5072 and 5099 plot intermediate to the stress-strain rate relations for [a]- and [c]-slip with strength similar to the fine-grained olivine of Karato *et al.* (1986). Samples 6208 (olivine), 6213 (olivine-orthopyroxene), 6219 (olivine-orthopyroxene), and 6220 (olivine) are only slightly weaker. The remaining samples, 5249 (olivine-orthopyroxene), 6222 (olivine-orthopyroxene), and 6223 (olivine) are considerably weaker and exhibit creep strength similar to or even below that of the olivine single crystal [a]-slip experiments of Mackwell *et al.* (1985). The higher activation energies used for figure 3.3b resulted in lower stresses for the present samples while their relative positions remain unchanged, except for the 1573K runs 6222a and 6223a that did not need to be normalised. Here the stress levels of samples 5072, 5099, 6208, 6213, 6219, 6220, and 6223 plot closer to the strength of single crystal [a]-slip with the stresses of samples 5249 and 6222 being below that level.

3.3 Results

3.3.1 Microstructural characterisation of selected deformed samples

Based on the results presented in figures 3.1 and 3.3, five samples were chosen to be studied in detail. Samples 5249 and 5072 were selected for a detailed characterisation as they represented the relatively weak and strong material from the study of Hitchings *et al.* (1989). For comparison, two relatively strong olivine-orthopyroxene materials from the study of Drury, samples 6213 and 6219, were investigated. The composition and deformation history of these samples with 50% and 30% orthopyroxene resembled that of 5249, but the experimental duration was longer (table 3.4) providing a means to check whether or not the microstructure in the shorter duration deformation experiment had reached equilibrium. The partially molten starting material for sample 5249, sample 5132, was also studied to check to what extent the melt microstructure was influenced by the deformation. The starting material for the olivine sample 5072 has not been studied. The olivine and olivine-orthopyroxene samples had similar deformation histories and

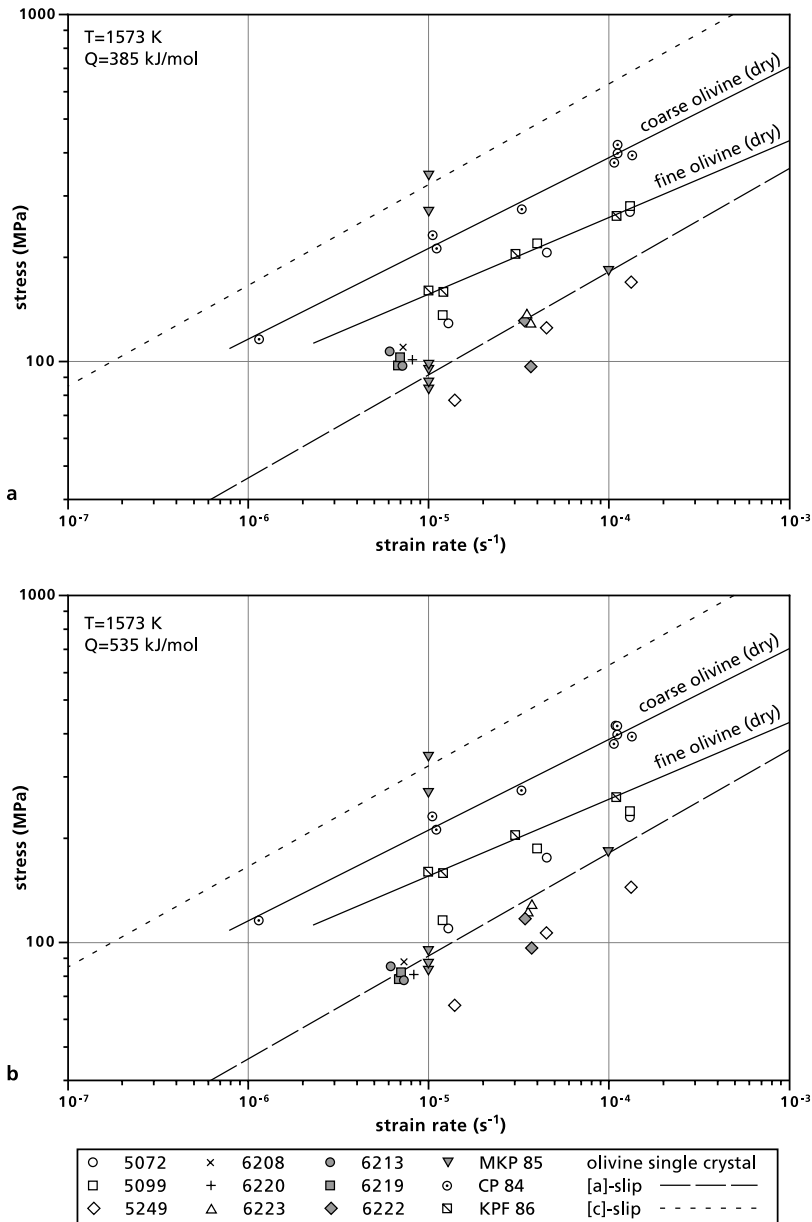


fig 3.3 Strength of the partially molten olivine (5072, 5099, 6208, 6220, 6223) and olivine-orthopyroxene samples (5249, 6213, 6219, 6222) compared to dry olivine experiments (CP84, MKP85, KPF86). Lines depicting the weakest, [a]-slip: (010)[100], and strongest, [c]-slip: (010)[001], dislocation slip systems in olivine single crystals are given as reference. Strength for [a]-slip is based on MKP85; strength for [c]-slip is based on BMK91. All data is normalised to T=1573 K using $n=3.5$ and activation energies for olivine single crystal [a]-slip, $Q=385$ kJ/mol (**a**) and olivine single crystal [c]-slip, $Q=535$ kJ/mol (**b**) (Drury & FitzGerald 1998).

(CP 84, Chopra & Paterson 1984, MKP 85, Mackwell et al. 1985, KPF 86, Karato et al. 1986, BMK91, Bai et al. 1991)

	deformed olivine 5249*	deformed orthopyroxene 5249*	deformed olivine 5072
SiO ₂	41.15	54.41	40.76
TiO ₂	-	0.11	-
Al ₂ O ₃	0.05	4.70	0.08
Cr ₂ O ₃	0.03	0.49	-
FeO	8.68	6.08	9.45
MnO	0.12	0.13	0.15
NiO	0.18	0.16	0.44
MgO	49.72	33.00	49.00
CaO	0.07	0.81	0.10
Na ₂ O	-	0.11	0.01
Mg/Mg+Fe	91.1	90.6	90.2
backscatter coefficient	0.1378	0.1360	0.1392

table 3.3 Microprobe analyses of olivine and orthopyroxene in samples 5072 and 5249 after deformation (wt%, normalised to 100%). (* Data from Hitchings *et al.*(1989)).

exhibited low degrees of *in situ* partial melting during the experiments. The olivine and orthopyroxene composition in two of the deformed samples is given in table 3.3. The origin of the higher Al₂O₃ content in the deformed orthopyroxene in sample 5249 (4.8%, table 3.3) with respect to the ingredient material (2.88%, table 3.1) is not clear, but the difference in composition

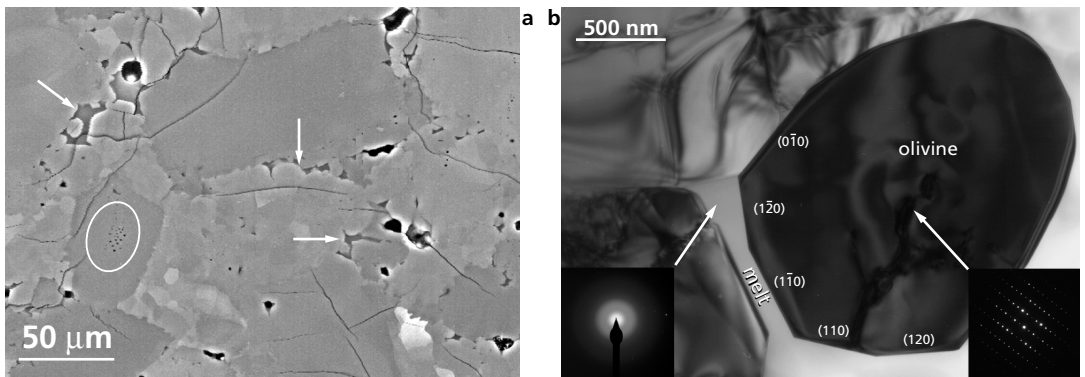


fig 3.4 (a) Backscatter SEM image of the hot-pressed starting material for sample 5249, sample 5132. Individual phases can be recognised by their respective grey levels (table 3.1, 3.3). Darker grains are orthopyroxene, lighter grains with small brightness variations are olivine, melt pockets are dark grey (arrowed), gas-filled pores are black. Internal pores in enstatite (encircled) indicate early partial melting during hot-pressing (Doukhan *et al.* 1993; Falloon *et al.* 1999).

(b) TEM bright field image of a melt body in sample 5132. The distinguishing features between amorphous solidified melt and crystalline olivine are indicated.

-1- Inside the olivine crystals both crystal defects and bending of crystal lattice planes produce diffraction contrast, which is absent in the melt body.

-2- The crystalline nature of the dark olivine crystal is illustrated by flat crystal faces (indexed) in contact with the melt phase. Its diffraction pattern (right inset) shows a regular array of bright spots caused by elastic scattering in the crystal.

-3- Diffraction in the melt phase (left inset) is limited to a number of diffuse rings caused by inelastic scattering around the central spot without evidence for a regular atomic structure.

sample	experimental duration (min.)	overall / local melt content
5132	n.a.	1.0 % (+1.5% gas-filled pores)
5249	177	1.1 / 5.0 %
6213	575	0.8 / 6.0 %
6219	710	0.9 / 5.0 %
5072	145	0.8 / 3.0 %

table 3.4 Experimental duration of the deformation experiments and produced melt fraction (area%). Specimen 5132 also contained 1.5% residual gas-filled porosity after hot-pressing. As the local melt content is variable within the samples, both the overall melt content and a measure of locally observed higher melt fractions are given.

led Hitchings *et al.* (1989) to suggest that a different ingredient material was accidentally analysed.

Residual gas-filled porosity in sample 5132 and the melt content in all samples were determined from binary images. These binary images were obtained from SEM backscatter electron images by isolating the image intensity levels specific for gas-filled pores and the melt phase using the public domain program NIH Image on an Apple Macintosh computer. Features to distinguish the melt phase on SEM backscattered electron images and TEM bright field images

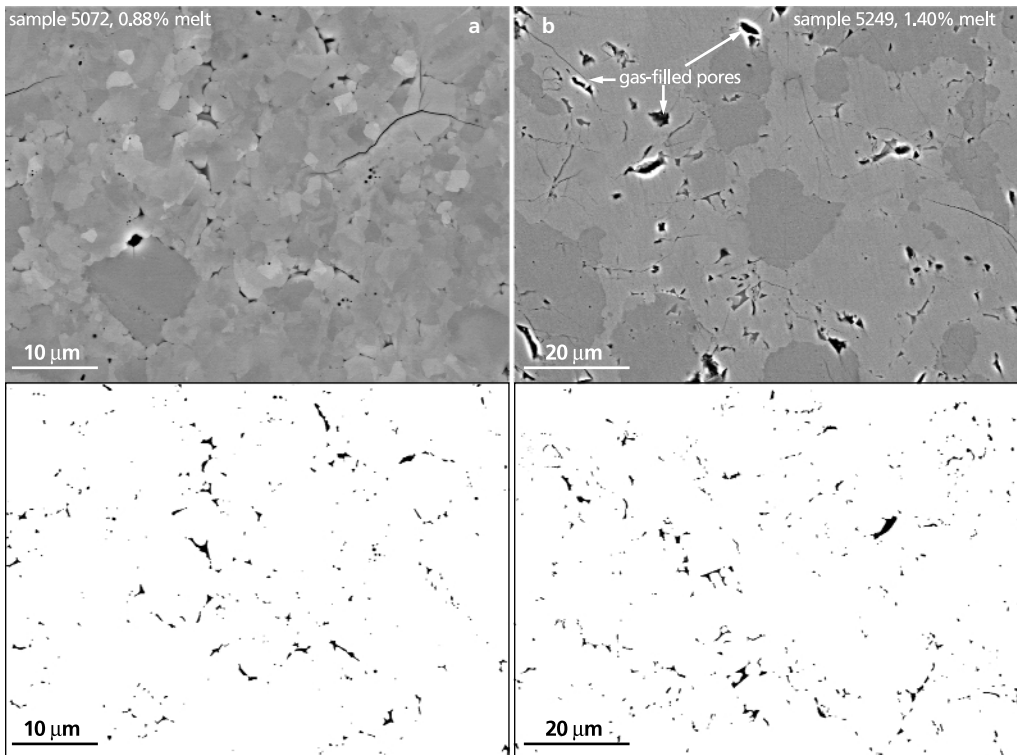


fig 3.5 Examples of the melt distribution in samples 5072 (olivine) (a) and 5249 (olivine-orthopyroxene) (b). Upper images are backscatter SEM images, lower images are binary images only showing the melt phase. Compression is horizontal.

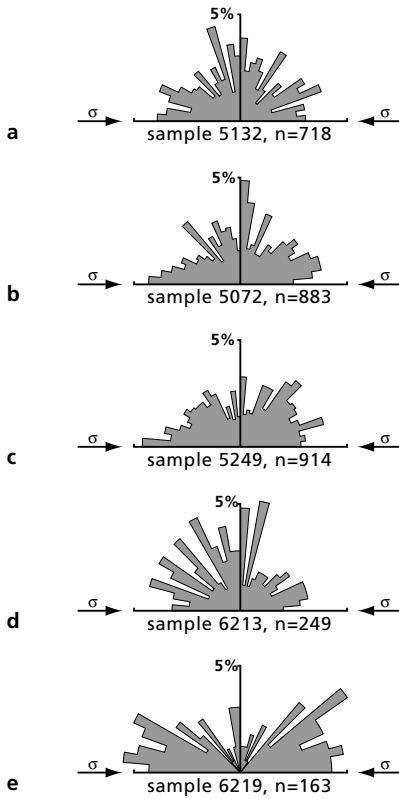


fig 3.6 Rose diagrams depicting the angle between the longest axis of elongated melt occurrences and the compression direction in samples 5132 (a), 5072 (b), 5249 (c), 6213 (d), and 6219 (e). Melt bodies with cross-sectional areas smaller than $0.05 \mu\text{m}^2$ were excluded from the orientation analysis as these are composed of only three or fewer image pixels which limited the number of possible orientations.

the scale of the individual images. Locally, areas with higher melt contents were associated with smaller grain size, similar to the hot-pressed material. The binary images were also used to measure the size of the melt occurrences and the orientation of elongated melt bodies with respect to the compression direction. Melt bodies were represented by ellipses for which the angle between the longest axis and the compression direction was determined (fig 3.6). In specimens 5132 (fig 3.6a) and 6213 (fig 3.6d), no preferential orientation of the melt body with respect to the compression direction was observed. In the other specimens, 5072 (fig 3.6b), 5249 (fig 3.6c), and 6219 (fig 3.6e), some alignment of melt bodies parallel to the compression direction was present. The cross-sectional area of melt pockets in all five samples is shown in figure 3.7. The smallest melt bodies inferred from SEM images had the size of single pixels, which corresponded to 0.01-

are illustrated in figure 3.4. Figure 3.4a shows the microstructure of sample 5132, the starting material for experiment 5249, which was thought to be similar to the starting material of the other two olivine-orthopyroxene samples (samples 6213 and 6219). Residual gas-filled porosity after hot-pressing was less than 2%. The hot-pressed material contained irregular-shaped, large ($20\text{-}50 \mu\text{m}$) grains and fine-grained ($<5 \mu\text{m}$) areas associated with melt concentrations. The melt content varied from 2 to 5% in the fine-grained regions to less than 1% in areas where few small grains were present (table 3.4). Note the small pores inside one orthopyroxene crystal (Fig. 3.4a, encircled) that indicated the occurrence of (early) partial melting during hot-pressing (Doukhan *et al.* 1993). The melt phase formed patches at three- or more grain intersections that appeared isolated in cross-section and some melt layers along grain interfaces. In the fine-grained areas with higher melt content flat low-index crystal faces formed many crystal-melt interfaces. TEM analysis indicated that $\{010\}$, $\{110\}$, $\{011\}$, $\{210\}$ and $\{120\}$ faces were common (fig 3.4b). Other crystal-melt contacts tended to be continuously curved.

Typical melt distributions in the olivine and olivine-orthopyroxene samples after deformation are illustrated in figure 3.5. The overall melt microstructure was similar in all deformed samples, independent of experimental duration (table 3.4). The melt distribution was not homogeneous on

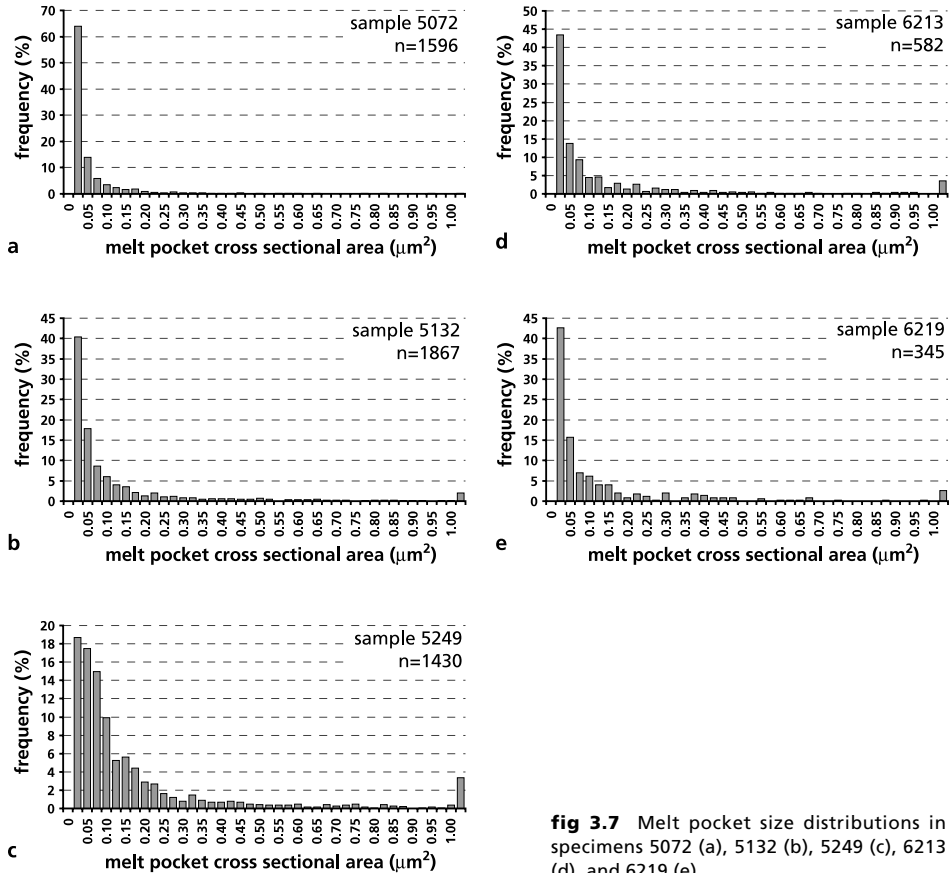


fig 3.7 Melt pocket size distributions in specimens 5072 (a), 5132 (b), 5249 (c), 6213 (d), and 6219 (e).

$0.05 \mu\text{m}^2$ for the different magnifications used. The cross-sectional area of the majority of the melt pockets was smaller than $0.2 \mu\text{m}^2$.

Table 3.2 shows the grain size fractions that were used for the preparation of each sample. The grain size distributions in the hot-pressed and deformed samples (fig 3.8, table 3.5) has been measured using the mean linear intercept method on SEM orientation contrast images of polished specimens. These images were the same as those on which the crystallographic fabric was measured, thus allowing for accurate identification of any subgrains. A correction factor of 1.5, assuming that spheres can represent the grains, was applied to account for the sectioning effect (Gifkins 1970). Two- to three-hundred olivine and fifty to one-hundred orthopyroxene grains were measured in each sample. Grain size after deformation in the olivine-orthopyroxene samples varied between 20 and $50 \mu\text{m}$ for large elongated original grains and 2 and $7 \mu\text{m}$ for the equidimensional recrystallized grains. The grain size in sample 5072 after deformation ranged from 0.5 to $16 \mu\text{m}$. The grain size distributions were lognormal, therefore the median grain size will be used throughout this thesis. The orthopyroxene grain size in the starting material 5132 was

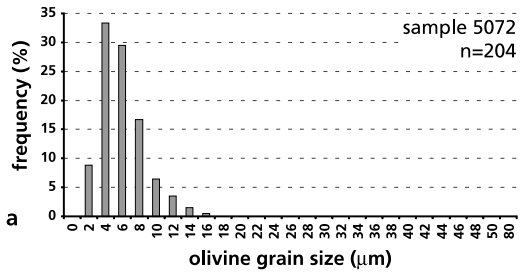
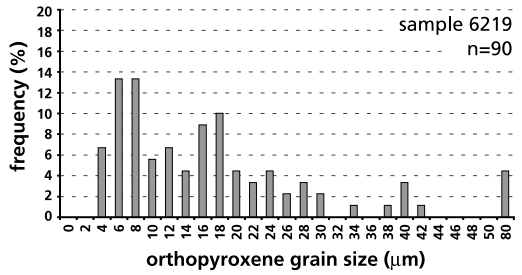
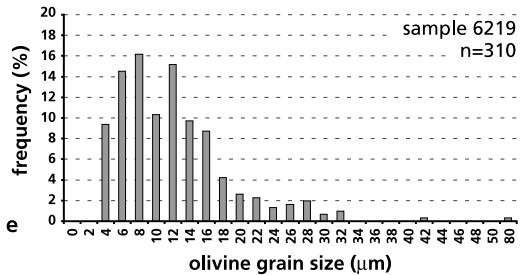
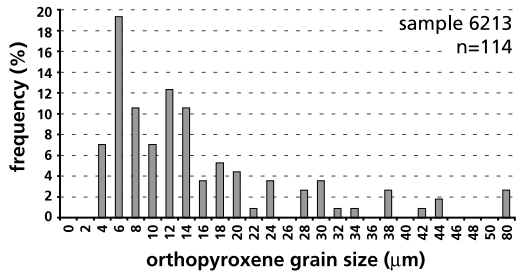
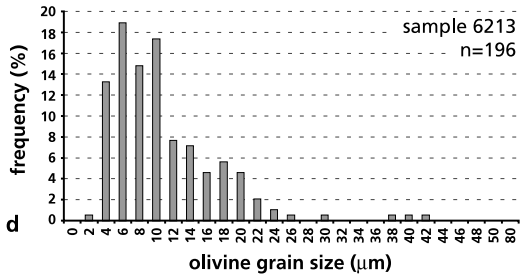
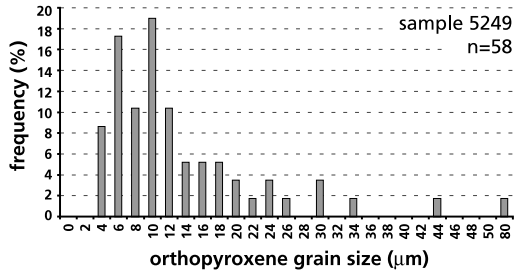
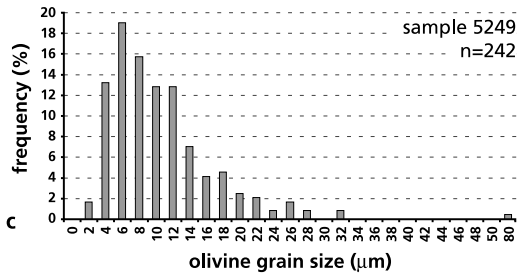
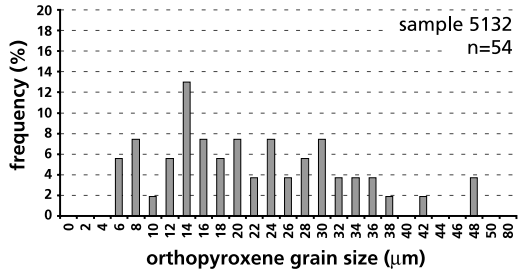
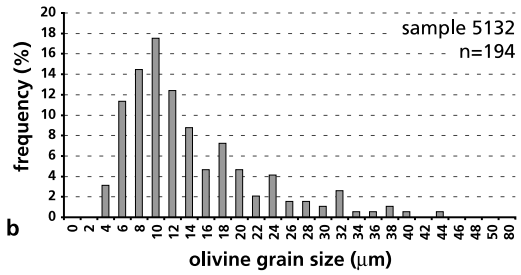


fig 3.8 Olivine and orthopyroxene grain size distributions measured with the mean linear intercept method along lines parallel to the compression direction on forward scattered SEM images, sample 5132 (a), 5072 (b), 5249 (c), 6213 (d), and 6219 (e).



sample	olivine median grain size	olivine grain size range	orthopyroxene median grain size	orthopyroxene grain size range
5072	4.5 μm	0.5 – 16 μm	n.a.	n.a.
5132	10.4 μm	2 – 44 μm	18.8 μm	6 – 50 μm
5249	8.1 μm	2 – 32 μm	9.2 μm	4 – 44 μm
6213	8.2 μm	2 – 42 μm	10.9 μm	4 – 44 μm
6219	9.9 μm	4 – 42 μm	14.1 μm	4 – 42 μm

table 3.5 Median grain size and grain size range in the studied samples.

equally distributed over the whole grain size range. In samples 6213 and 6219 two different grain size domains could be distinguished. Within the matrix with a median grain size of 8 to 10 μm (table 3.5), elongated large, 0.5 to 2.5 mm long, grain aggregates occurred. These elongated aggregates were preferentially oriented perpendicular to the compression axis and were comprised

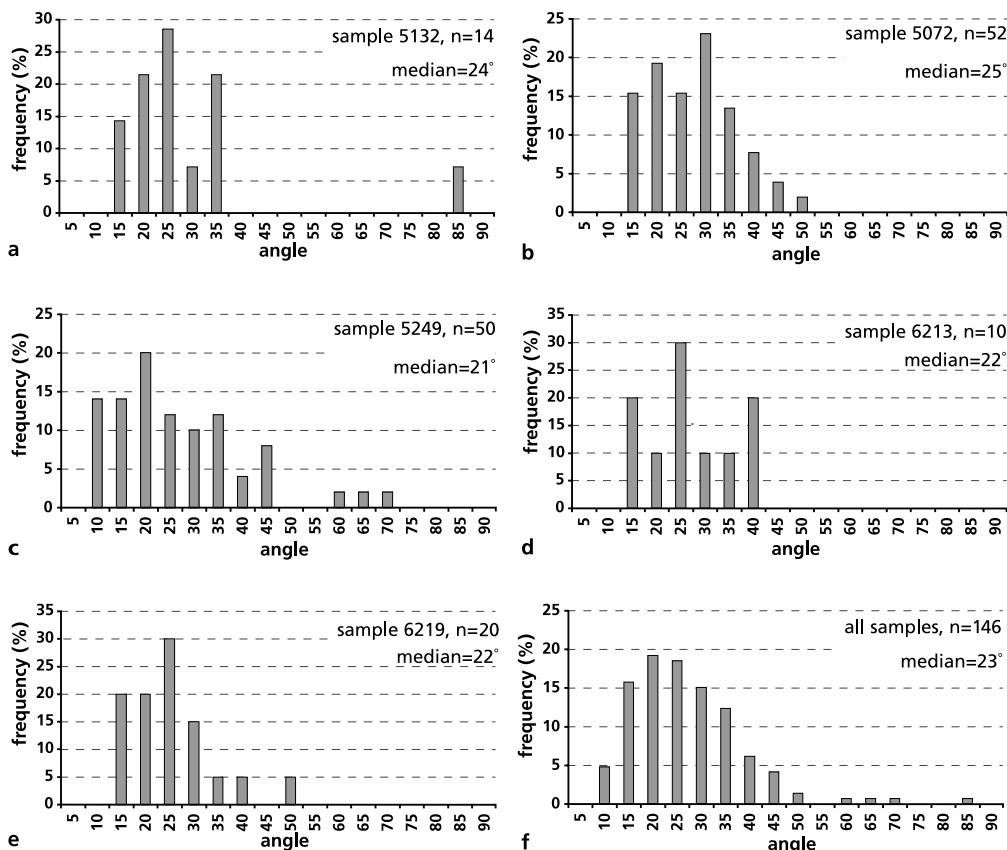


fig 3.9 Dihedral angle distributions determined on TEM images in samples 5132 (a), 5072 (b), 5249 (c), 6213 (d), 6219 (e), and a compilation of all dihedral angle measurements (f).

of small olivine and orthopyroxene grains that showed a gradual increase in grain size from $< 1 \mu\text{m}$ to a maximum of $8 \mu\text{m}$ in sample 6213 and $25 \mu\text{m}$ in sample 6219. The olivine-orthopyroxene content in both domains was equal to the starting distribution, 50%-50% and 70%-30% respectively. During deformation the grain size decreased slightly (see 5249 vs. 5132). Light microscopy revealed undulatory extinction and subgrain development in the larger grains in all samples indicating that deformation involved dislocation creep and dynamic recrystallization. This was confirmed by the increase of the fraction of small grains and reduction of the fraction of large grains.

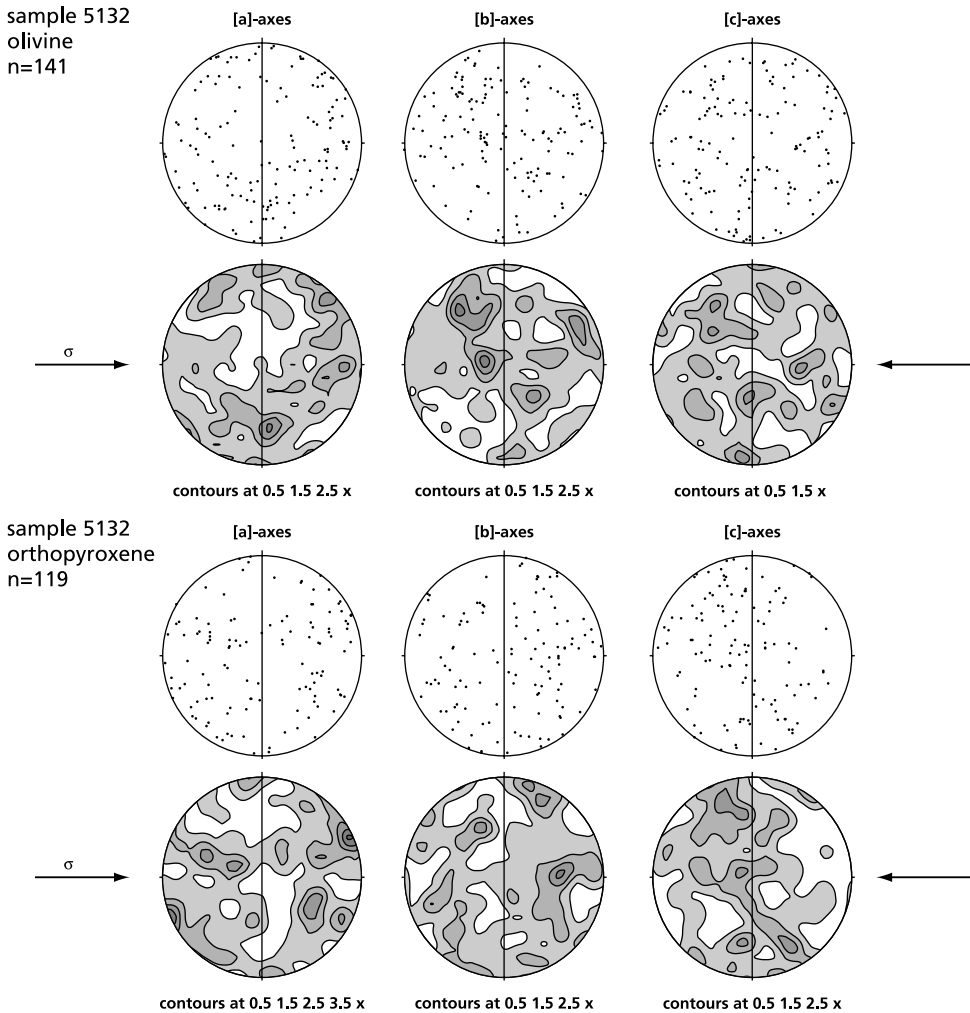


fig 3.10a EBSP crystallographic orientation measurements of olivine and orthopyroxene in sample 5132 (hot-pressed).

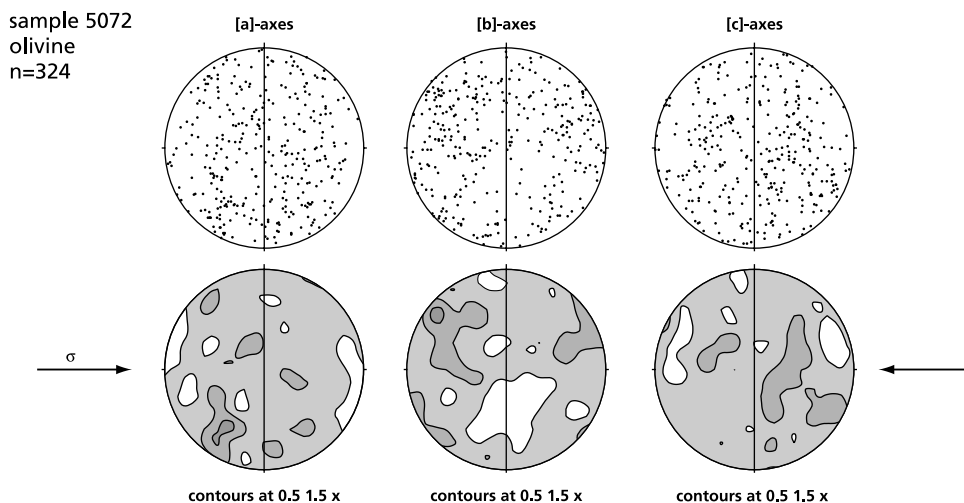


fig 3.10b EBSD crystallographic orientation measurements of olivine in sample 5072 (deformed).

Dihedral angle measurements were done in the transmission electron microscope as scanning electron microscope imaging limited the accuracy of dihedral angle measurements due to lower resolution of the SEM and the unknown sectioning effect, which tends to overestimate the dihedral angles (Cmíral *et al.* 1998). These uncertainties were avoided in the TEM where specimen tilting allowed orientation of solid-melt contacts in the thin electron-transparent sections parallel to the electron beam. The dihedral angle distributions are presented in figure 3.9. The median dihedral angle in the starting material and the deformed specimens ranged from 21° to 25° . When all dihedral angle measurements were combined, the median olivine-melt dihedral angle was 23° (fig 3.9f).

EBSF crystallographic fabric analysis of both olivine and orthopyroxene was performed on four of the samples, the undeformed starting material, 5132 and the deformed samples 5072, 5249 and 6213. The resulting plots are shown in figure 3.10a-d. No clear crystallographic preferred orientation could be discerned in the olivine crystallographic distribution in sample 5132, the starting material for sample 5249 (fig 3.10a). The orthopyroxene distribution however was not random. The [c]-axes showed a distinct girdle distribution perpendicular to the compression direction and the [a]-axes showed a (weak) point maximum near the compression axis. The b-axis distribution appeared random. During deformation, the olivine grains developed a weak crystallographic preferred orientation in all samples. In sample 5072 (fig 3.10b) a broad olivine [a]-axis girdle formed perpendicular to the compression direction, together with weak [b]-axis point maxima parallel to the compression axis. The [c]-axis distribution remained random. The olivine grains in the olivine-orthopyroxene samples (fig 3.10c, d) formed similar fabrics, a broad girdle distribution of the [a]-axes perpendicular to the compression direction and a [b]-axis point maximum parallel to the compression direction. In both olivine-orthopyroxene samples, the [c]-

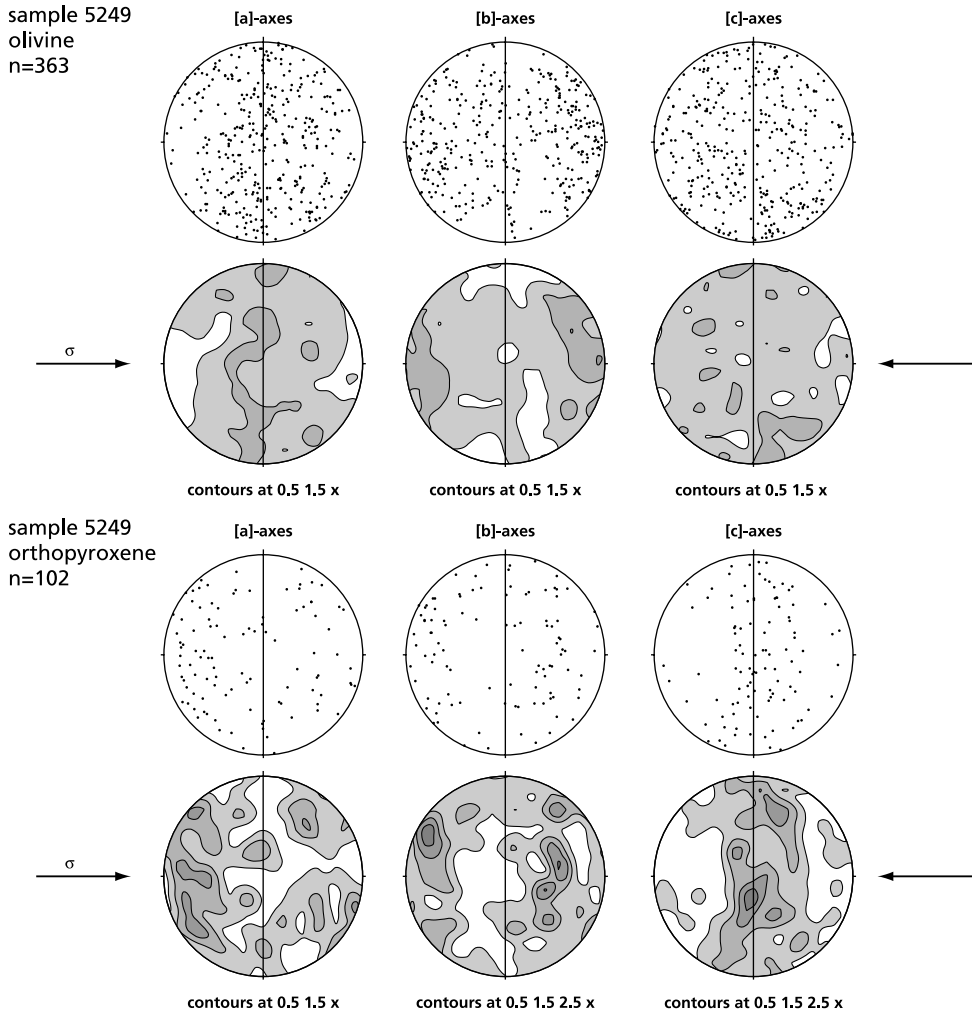


fig 3.10c EBSD crystallographic orientation measurements of olivine and orthopyroxene in sample 5249 (deformed).

axes do not show a clear fabric. The orthopyroxene fabric in the olivine–orthopyroxene samples resembled that of the starting material with a distinct [c]-axis girdle perpendicular to the compression direction. In sample 5249 (fig 3.10c), the orthopyroxene [a]-axes formed a point maximum close to the compression direction. The orthopyroxene [a]-axes in sample 6213 (fig 3.10d) and the [b]-axes in both 5249 and 6213 appeared random.

Next to the overall crystallographic fabric, the grain neighbour misorientation was analysed from the same EBSD dataset for the olivine sample 5072 (fig 3.11a) and olivine–orthopyroxene samples 5249 (fig 3.11b) and 6213 (fig 3.11c). The misorientation was calculated using an Excel

spreadsheet written by Dr T.F. Fliervoet (personal communication) that allowed for calculation of both the misorientation and the rotation axis to accommodate this misorientation. When subgrains in adjacent grains resulted in multiple misorientation calculations of the same grain pair, these subgrain duplicates were omitted. To provide a reference for the determination of the presence of anomalous grain boundary misorientations with respect to a random distribution, an uncorrelated misorientation distribution was determined in each sample by calculating the misorientation for a large set of randomly chosen grain pairs from each sample (fig 3.11). This uncorrelated distribution was characterised by a highly skewed distribution that ranged from 0° to

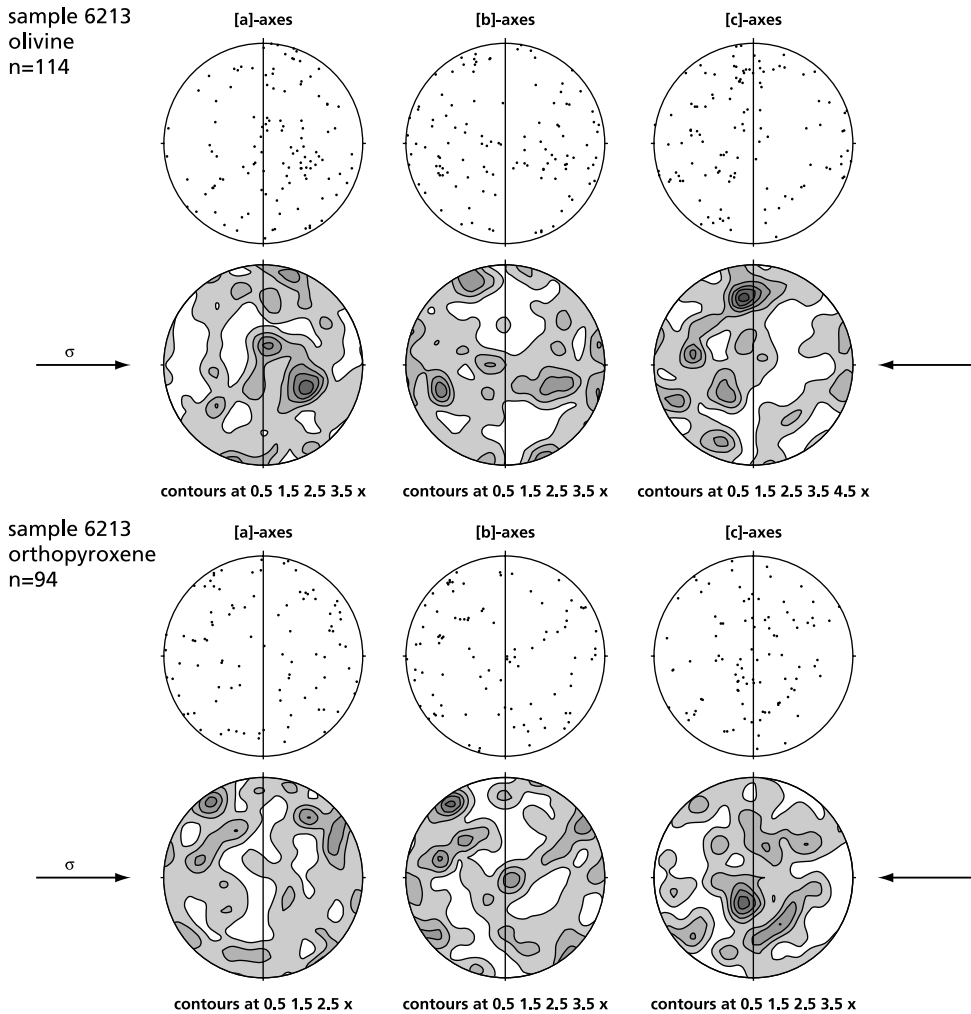


fig 3.10d EBSD crystallographic orientation measurements of olivine and orthopyroxene in sample 6213 (deformed).

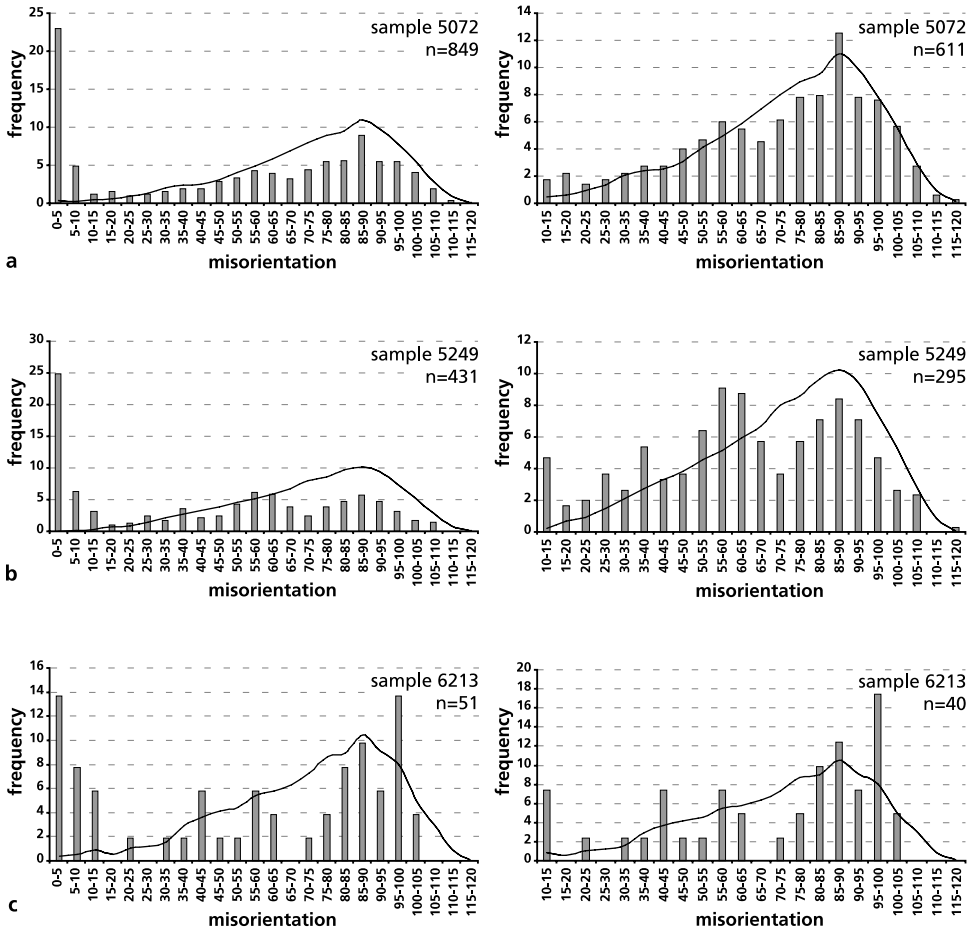


fig 3.11 Olivine grain boundary misorientation distribution calculated from EBSD measurements of samples 5072 (a), 5249 (b), and 6213 (c). The left diagrams show all grain boundary misorientation measurements, including low-angle subgrain boundaries. In the right diagrams, all misorientations below 10° are omitted and the remaining measurements are normalised to 100%. The curves represent uncorrelated grain boundary misorientation distributions using >30000 arbitrary grain pairs in sample 5072, >40000 arbitrary grain pairs in sample 5249, and >7800 arbitrary grain pairs in sample 6213.

120° with a maximum at 90° . Misorientations above 120° do not occur in the plots as they can always be represented by smaller rotations around a different axis (Grimmer 1980; Fliervoet *et al.* 1999).

All measured grain boundary misorientation distributions deviated from the uncorrelated distribution for grain misorientations below 10° (fig 3.11). The high frequency of misorientation angles below 10° is matched by a lower frequency of the higher angle misorientations to values below the uncorrelated distribution. Therefore the misorientation distributions are also calculated for the interval 10° – 120° to allow comparison with the uncorrelated distribution. The higher

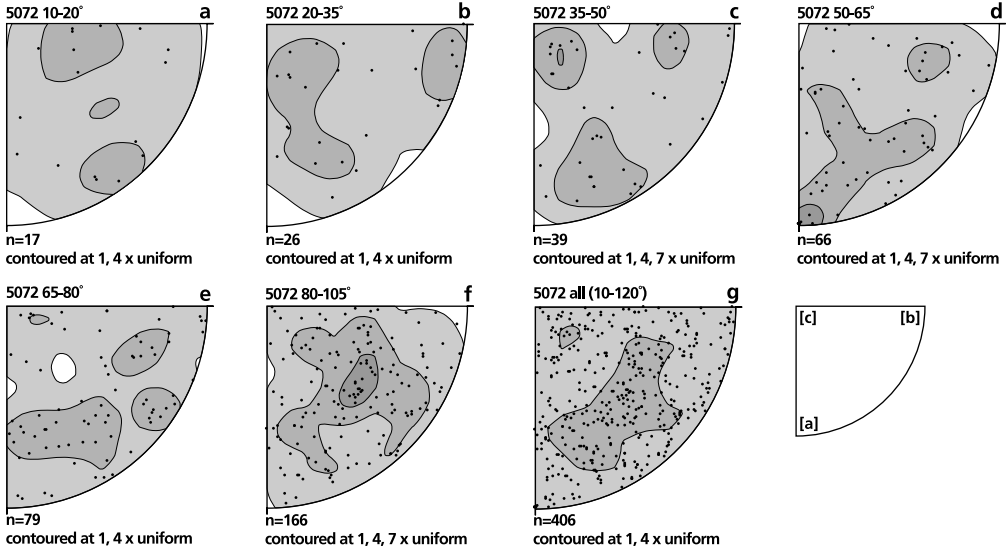


fig 3.12 Rotation axes that accommodate grain misorientations in sample 5072 measured using EBSP. The axes are subdivided into classes and plotted in inverse pole figures: (a) 10°-20°, (b) 20°-35°, (c) 35°-50°, (d) 50°-65°, (e) 65°-80°, (f) 80°-105°, and (g) all misorientations larger than 10°.

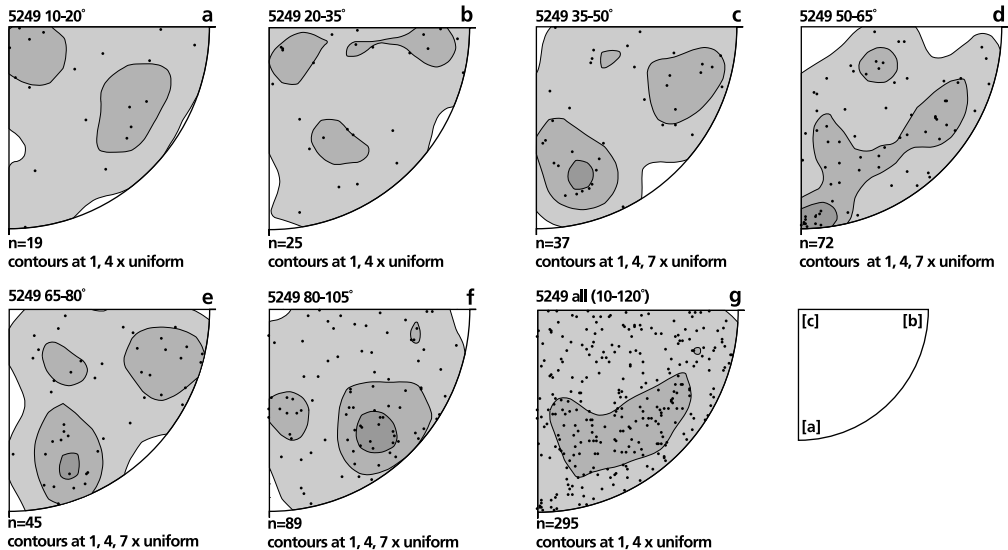


fig 3.13 Rotation axes that accommodate grain misorientations in sample 5249 measured using EBSP. The axes are subdivided into classes and plotted in inverse pole figures: (a) 10°-20°, (b) 20°-35°, (c) 35°-50°, (d) 50°-65°, (e) 65°-80°, (f) 80°-105°, and (g) all misorientations larger than 10°.

sample	annealing duration (hours)	annealing temperature (°C)	oxygen fugacity (atm)
5072_1	306	1132	1.5×10^{-12}
5249_1	219	1131	2.0×10^{-12}
6219_2	136	1131	1.8×10^{-12}

table 3.6 Experimental parameters for the annealing experiments

angle misorientations were concentrated around 90° , with an anomaly around 60° . This deviation was weak in sample 5072, but in sample 5249 the number of misorientations in this range exceeded the peak at 90° . The limited number of olivine-olivine grain boundaries in sample 6213 hampered comparison with samples 5072 and 5249. The large peak of misorientations below 10° that was prominent in samples

5072 and 5249 (fig 3.11a, b) was less pronounced in sample 6213 (fig 3.11c). The small peak at 60° misorientation in sample 6213 (fig 3.11c) correlated to the 60° misorientation maxima observed in samples 5072 and 5249, but remained lower than the maximum in the other olivine-orthopyroxene sample (5249, fig 3.11b).

Based on the misorientation distribution, rotation axes that describe the misorientations between olivine grains in samples 5072 and 5249 were subdivided into classes for different ranges of misorientation (fig 3.12a-f, 3.13a-f). Grain combinations with misorientations smaller than 10° were considered to be subgrains and are discussed in chapter 4. In the subsets, no preferential orientation was observed for the rotation axes in the misorientation ranges 10° - 20° (fig 3.12a, 3.13a), 20° - 35° (fig 3.12b, 3.13b), 35° - 50° (fig 3.12c, 3.13c), and 65° - 80° (fig 3.12e, 3.13e). The 80° - 105° plots (fig 3.10f and 3.11f) show the expected distribution away from the primary axes (Faul & FitzGerald 1999; Fliervoet *et al.* 1999). In contrast to the other misorientations, the axes that accommodate rotations between 50° and 65° show a (weak) maximum near the [a]-axis (fig 3.12d and 3.13d). The inverse pole figures in figures 3.12g and 3.13g show all rotation axes for misorientations larger than 10° . In these compilation plots, the rotation axes were equally distributed.

3.3.2 Melt microstructures after annealing

Long-duration annealing experiments were performed on rectangular slabs ($\sim 4 \times 8 \times 1$ mm) that were cut from the centre of three of the deformed samples, samples 5072, 5249 and 6219. Annealing was performed to establish whether or not the melt microstructures that were formed

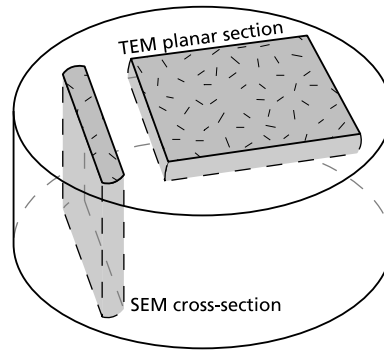


fig 3.14 Schematic drawing of the orientation of the annealed samples after embedding in resin. The top of the sample was polished and coated with carbon for SEM imaging. A $30 \mu\text{m}$ thin section was subsequently made from the planar section from which standard TEM samples were prepared by ion-beam thinning.

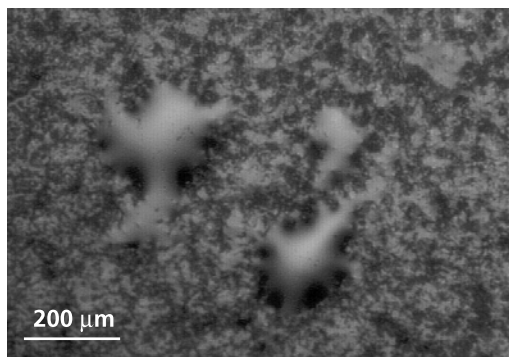


fig 3.15 Reflected light micrograph of the surface of sample 5072_1 after 306 hours annealing. Two large (~200 μm) melt droplets are visible in the centre of the image. All light grey areas are melt partly covering the darker olivine grains.

annealing was performed with a reflected light microscope. The samples were subsequently embedded in resin, sectioned and polished to prepare both cross-section SEM and plan-view TEM specimens (fig 3.14).

During annealing, the colour of the samples changed from the original dark grey-green to bright green. Reflected light microscopy showed smooth irregular shaped melt droplets on the surface (fig 3.15). In cross-section, the microstructure of all samples was dominated by the presence of irregular shaped gas-filled pores together with melt bodies. The distribution of the pores differed between the olivine and olivine-orthopyroxene materials. In the olivine material, sample 5072_1, a 20-30 μm thick layer at the surface of the sample was free of gas-filled pores and showed a connected network of melt layers and larger melt bodies. In the interior of the sample the pores were evenly distributed (fig 3.16). In the olivine-orthopyroxene materials some small pores were present in olivine areas, but the majority of gas- and melt-filled pores were concentrated along olivine-orthopyroxene interphase boundaries (fig 3.17). In contrast to sample 5072_1 no pore-free rim was present and gas-filled pores associated with orthopyroxene grains also occurred near the

during deformation were stable. The experimental parameters are presented in table 3.6. In order to allow the melt microstructure to respond to the annealing conditions, it was necessary to re-melt the glass phase that formed during the deformation experiments while preventing significant additional melting during annealing. The difference in confining pressure between the deformation runs and the annealing experiments implied a decrease in melting temperature. However, the melting temperature of the olivine-orthopyroxene aggregates at atmospheric pressure was not exactly known. Initial experiments showed that a temperature of 1130°C was suitable. Preliminary examination of the samples after

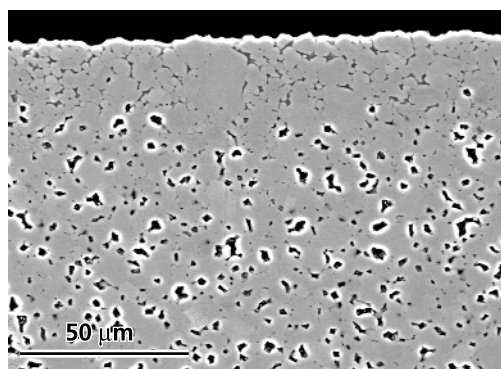


fig 3.16 Backscatter SEM image illustrating the melt and pore distribution in the olivine sample (cross-section of sample 5072_1 after 306 hours annealing, the original compression direction is perpendicular to the paper). Light grey areas are olivine, darker grey areas are melt. Black patches with bright rims are gas-filled pores. The melt phase is dispersed equally throughout the sample, both in completely melt-filled pores and along the edge of gas-filled pores. The latter occurrences are obscured in the image due to the bright rim. A 20-30 μm thick pore-free rim occurs along the surface of the specimen.

surface of the samples. Adjacent to gas-filled pores, 100–300 nm thick melt layers were common (fig 3.18 (arrowed)). Smooth melt-blobs on top of the samples, analogous to those found with reflected light microscopy, were associated with clusters of gas-filled pores (fig 3.19). The melt content was measured from binary images (similar to those presented in fig 3.5) that were obtained from backscatter SEM images. During the annealing experiments, the melt fraction increased in all samples. The total of retained melt and empty pores was 7 to 10% with large local differences. In sample 5072_1 the overall melt content after annealing was 3.9% with an additional gas-filled pore volume of 5.4%. The local melt content was variable between 3 and 7% and the gas-filled pore volume locally varied between 1 to 7%. In sample 5249_1 the total melt fraction was 7.2% with an additional gas-filled pore volume of 2.5%. The local melt fraction varied from 1.5 to 9% and the gas-filled pore volume locally ranged from 1 to 3.5%. In sample 6219_2 the fraction melt- versus gas-filled pores could not be determined on all SEM images, but estimates from two images indicated a distribution of melt-versus gas-filled pores similar to sample 5249_1. The total melt- and gas-filled pore volume in sample 6219_2 was 7.4%. Light microscopy observations (fig 3.15) showed that melt was localised

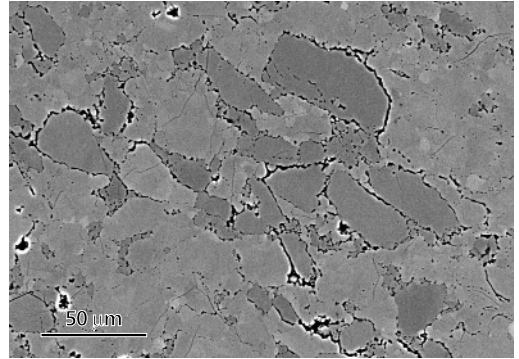


fig 3.17 Backscatter SEM image illustrating the melt and pore distribution in the olivine-orthopyroxene samples (cross-section of sample 6219_2 after 136 hours annealing, the original compression direction is perpendicular to the paper). The darker grains are orthopyroxene crystals, which have most of the gas and melt-filled pores associated with them. Orthopyroxene-free areas (e.g. in the lower left of the micrograph) exhibit low porosity and melt content similar to the olivine regions in the deformed samples (e.g. fig 3.5). The contrast was enhanced to distinguish the olivine from the orthopyroxene grains. Due to this enhancement, the melt phase appears black and cannot be discriminated from gas-filled pores.

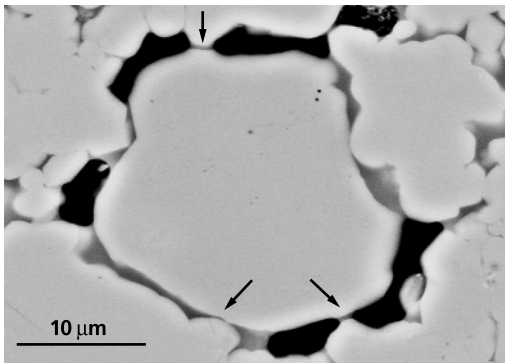


fig 3.18 Backscatter SEM image of an olivine crystal in sample 5249_1. Around the grain, gas-filled pores occur adjacent to 100–300 nm thick melt layers (arrowed).

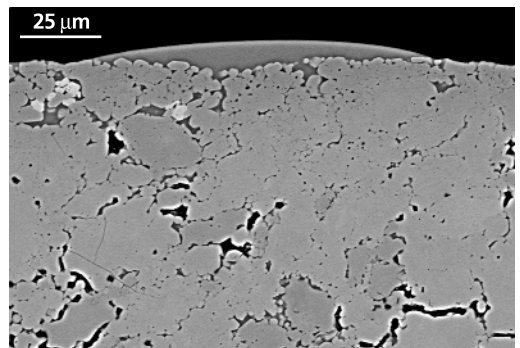


fig 3.19 Backscatter SEM image of a melt droplet on top of sample 5249_1. Melt-filled pores connect the droplet with a cluster of gas-filled pores deeper in the sample.

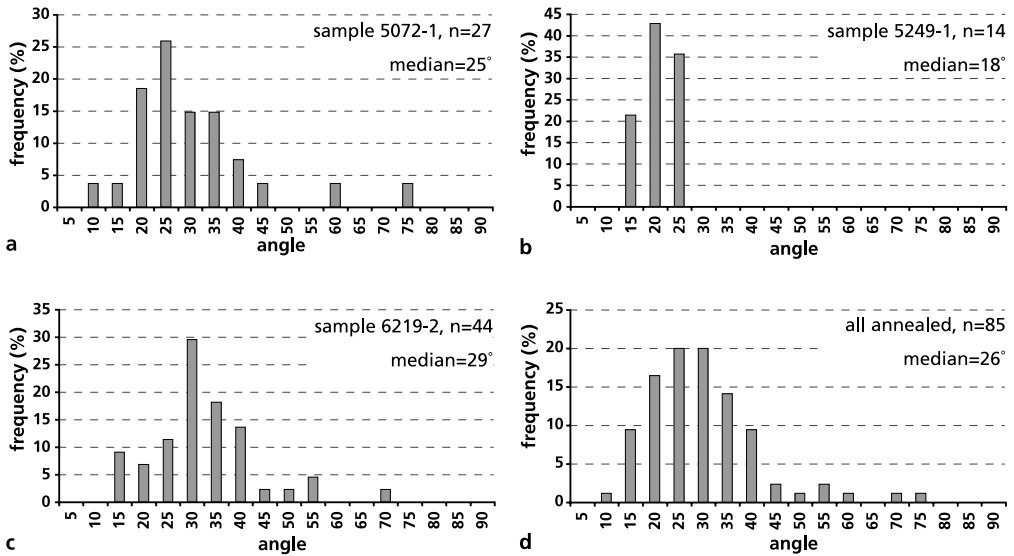


fig 3.20 Dihedral angle distributions in the annealed specimens measured on TEM images, 5072_1 (a), 5249_1 (b), 6219_2 (c), and all measurements in the annealed samples (d).

in distinct droplets on the surface of the annealed specimens. Because of the inhomogeneous melt distribution on the surface of the specimens it was not possible to correlate the gas-filled pore volume measured on cross-sections with the extruded melt volume.

TEM dihedral angle measurements were performed on planar sections (fig 3.14). The orientation perpendicular to the SEM sections was chosen to be able to produce several TEM sample-grids, although the exact distance of the specimen to the original sample surface was lost. The olivine-melt dihedral angle distribution after annealing is presented in figure 3.20. The median dihedral angle for the individual samples ranged from 18° to 29° with the median dihedral angle for all annealed samples being 26°, which is similar to the dihedral angle in the deformed samples.

3.4 Discussion

3.4.1 Mechanical data

The olivine-orthopyroxene rocks from the presented experimental studies showed a different rheological response to increasing orthopyroxene content. The study of Hitchings *et al.* (1989) shows that the olivine samples (5072, 5099) deform with strength indicative for the operation of both [a]- and [c]-slip, while the behaviour of the olivine-orthopyroxene material (5249) is suggestive for deformation controlled by weaker [a]-slip (fig 3.3). The weak mechanical behaviour of sample 5249 suggested that an additional weak deformation mechanism became operational and replaced the harder dislocation [c]-slip mechanism, a process proposed earlier by Hirth & Kohlstedt (1995b). In the limited number of experiments performed by Drury that are reported here, this weakening with increasing orthopyroxene content could not be reproduced. The additional weaker mechanism apparently was not activated in the lower temperature ($T=1473$ K) samples of Drury and only limited weakening was observed with increasing orthopyroxene content in the higher temperature ($T=1573$ K) runs. This raised the question as to what deformation mechanisms had been activated in both series of experiments.

Daines & Kohlstedt (1996) report strength variations with orthopyroxene content in olivine-orthopyroxene materials similar to the results of Hitchings *et al.* (1989). Their results together with the data presented in figure 3.1b suggest that maximisation of the olivine-orthopyroxene interphase area leads to weakening of the rocks. This is a possibility when the deformation behaviour is controlled by grain boundary processes that are enhanced along olivine-orthopyroxene grain boundaries with respect to olivine-olivine grain boundaries. However, both studies (Hitchings *et al.* 1989; Daines & Kohlstedt 1996) show stress exponents close to 3, indicating that intracrystalline deformation is important. And although the stress exponent was only determined in one of the 62xx experiments (sample 6223, $n=3.1$), the similarity in deformation conditions for the 62xx series experiments suggested that deformation of the other 62xx samples was also accommodated by intracrystalline deformation mechanisms. Therefore, it is not clear how any enhancement of grain boundary processes along olivine-orthopyroxene grain interfaces would result in weakening of the samples from Hitchings *et al.* (1989) and Daines & Kohlstedt (1996) while no effect is observed in Drury's experiments and in a recent study by Mackwell *et al.* (1999).

A clue to the active deformation mechanism may be provided by the activation energies (fig 3.2, 3.3) for the olivine and olivine-orthopyroxene samples of Drury. Both activation energy determinations for the olivine samples showed an activation energy that is comparable to the value reported by Drury and FitzGerald (1998) for olivine [c]-slip as rate-limiting deformation mechanism. The activation energies for the olivine-orthopyroxene rocks were considerably higher and were not consistent with deformation rate-limited by olivine [a]-slip. Despite this difference in activation energy, the mechanical behaviour of the olivine-orthopyroxene samples 6213 and 6219 was very similar to the behaviour of single-phase olivine samples 6208, 6220, and 6223. Higher activation energies in the olivine-orthopyroxene material may originate from additional partial melting during the higher (1573 K) temperature step of the experiment

(Kohlstedt & Zimmerman 1996). However, this cannot be verified as the subsequent experimental step for these samples involved deformation at lower temperature (1523 K), thus obliterating the high-temperature melt microstructure by crystallisation equivalent to quench crystallisation. Similarly the formation of partial melt can also influence the resulting activation energy in the olivine samples, thus incorrectly suggesting the operation of olivine [c]-slip as rate-limiting deformation mechanism. The above considerations indicate that indirect evidence for the active mechanism during deformation, such as the stress exponent and activation energies, may not correctly identify the active deformation mechanisms. Additional active deformation mechanisms can alter rheological parameters while remaining unrecognized.

3.4.2 Microstructures and melt distribution

The analyses showed that most microstructural features in the deformed samples were similar. The melt content and distribution, solid-melt dihedral angles and grain size distributions were comparable except for the smaller grain size in sample 5072. The dihedral angles average around 25°, which is well below the 60° connectivity threshold (Waff & Bulau 1979; Toramaru & Fujii 1986; Faul 1997), indicating that the grain edge tubes were interconnected in all samples. These values are in good agreement with the olivine-melt dihedral angle measurements of Bussod & Christie (1991) that have also been made on TEM images. Cmíral *et al.* (1998) however, report dihedral angles in olivine-basalt samples being between 1° and 10° after annealing at high temperature and pressure for several days. This discrepancy may be caused by the very long experimental duration of the samples of Cmíral *et al.* (1998), the difference in experimental history or a difference in melt composition. The first possibility is considered unlikely as no change in dihedral angle distribution was observed within the olivine-orthopyroxene samples that were held at the experimental conditions for increasingly longer times, from the undeformed hot-pressed material (5132) to samples 5249 (177 minutes), 6213 (575 min.) and 6219 (710 min.) (table 3.4). The absence of a progressive change in dihedral angle distribution from the hot-pressed material to the longest deformation run also indicates that the distribution already reaches equilibrium during hot-pressing and is not significantly influenced by subsequent deformation.

The long-duration annealing experiments reported here were performed to further establish the stability of the melt microstructure, but the unexpected development of gas-filled pores during annealing precluded a straightforward comparison with the melt microstructure in the deformed samples. The reason for the colour change from dark grey-green in the hot-pressed and deformed specimens to bright (olivine-) green in the annealed specimens is not clear. It may be related to a difference in actual oxygen fugacity between the deformation and annealing experiments or changes in parameters as grain size, porosity, and olivine-orthopyroxene ratio, which can influence the specimen colour (Drury, personal communication). Another possibility is the possible presence of carbon, iron or tungsten-carbide particles that originate from sample preparation in the deformed samples.

The formation of gas-filled pores during annealing may be related to the hot-pressing procedure. Initially the samples were not intended to be annealed at atmospheric pressure. Therefore no attempt was made to extract the air from the powder aggregate during hot-pressing,

which may have resulted in dissolution of nitrogen gas at high pressure into the developing melt phase as the atmospheric oxygen would react with the iron sample jacket. Upon annealing and partial re-melting of the samples at atmospheric pressure, the gas was released from the melt phase, expanded and expelled the melt from the sample to form the melt droplets on top of the samples. Despite the development of gas-filled pores, the stability of melt-filled triple junctions and the occurrence of 100–300 nm thick melt layers adjacent to gas-filled pores along two-grain boundaries (fig 3.18) indicates that the annealed samples can be used to assess the stability of details of the melt microstructure that formed during deformation. The similarity of the dihedral angle distributions in the deformed samples prior to annealing and after annealing supports the conclusion that the dihedral angle distributions have already attained equilibrium during the short deformation runs. Therefore, the difference between the small dihedral angles ($<10^\circ$) observed by Cmíral *et al.* (1998) and the larger ($\sim 25^\circ$) dihedral angles presented in figure 3.20 is probably related to a difference in melt composition. The silica-rich melt phase in the samples presented here is produced during *in situ* partial melting and its composition is not exactly known, whereas the chemistry of the melt phase in the samples of Cmíral *et al.* (1998) consists of added oxide-derived sintered powder with basaltic composition.

3.4.3 Crystallographic preferred orientation

The development of (weak) olivine crystallographic preferred orientations in all samples indicated that dislocation creep accommodated a significant fraction of the deformation, which is consistent with the stress exponents summarised in table 3.2. While no olivine crystallographic preferred orientation was recognised in the starting material, the orthopyroxene grains did exhibit a clear texture. As this was already present in the starting material (fig 3.8b), it must have been introduced before or during hot-pressing and is most likely the result from the elongated shape of the orthopyroxene crystals after grinding (e.g. fig 3.4a, 3.17). Enstatite has good cleavage along $\{210\}$ and perfect cleavage along $\{100\}$ (Tröger 1979). This probably resulted in elongated fragments during crushing, which were compacted in a preferred orientation during the initial cold-pressing of the samples. The dominant slip system in enstatite is $(100)[001]$ with minor $(100)[010]$ slip (Skrotzki 1994). As the $[a]$ -axis distribution showed a maximum near the compression direction, the slip plane was oriented at high angles to the compression direction. This texture will reduce the participation of orthopyroxene deformation to the general deformation of the materials, which supports the idea that the sample rheology was controlled by the olivine component.

3.4.4 Implications for mechanical properties

Important differences between the samples are the variation in local melt content and the grain misorientation distribution. The local melt content was 3% in the olivine and may be as high as 5–6% in the olivine-orthopyroxene materials. The latter melt concentration was higher than the critical value of 4 to 5%, above which an abrupt weakening is observed in partially molten rocks (Hirth & Kohlstedt 1995a, b). The combination of such local melt concentrations with melt layers in contact with specific low-index crystal faces may lead to the formation of localised melt-rich

zones in olivine–orthopyroxene rocks containing aligned melt layers. If such a microstructure formed during deformation at $T=1500$ K it could have caused the weakening in sample 5249 with respect to sample 5072. However, similar high local melt contents also occurred in the other olivine–orthopyroxene samples and the weakening with increased orthopyroxene content did not occur in the lower temperature (1473 K) samples 6213 and 6219. An alternative weakening mechanism of olivine–orthopyroxene materials with respect to olivine samples is suggested by the melt distribution in the annealed samples. Where melting is equally dispersed in the olivine sample, melting in the olivine–orthopyroxene materials occurs preferentially along the olivine–orthopyroxene grain boundaries. Although similar thick melt layers around orthopyroxene crystals have not been found in the deformed specimens, melting probably occurred at the same sites and was subsequently redistributed. The localisation of melt generation along olivine–orthopyroxene boundaries may thus facilitate grain boundary sliding although the effect will be reduced as the elongated orthopyroxene crystals are preferentially oriented perpendicular to the compression direction.

Another microstructural difference between samples 5072 and 5249 was the olivine grain boundary misorientation distribution. Within the latter sample a distinct peak occurred at a misorientation angle of 60° with rotation axes near the [a]-axis (figures 3.9–3.11). A small number of the 60° misorientations determined in these samples may be attributed to misindexing of EBSD patterns around the [a]-axis in adjacent subgrains, which can result in apparent 60° rotations (Fliervoet *et al.* 1999). This is considered unlikely because each computed indexing solution of the EBSD patterns was examined individually. The cause for the occurrence of excess 60° misorientations in sample 5249 is not clear. It could not solely be attributed to the presence of orthopyroxene because the misorientation distribution in another olivine–orthopyroxene sample (sample 6213, fig 3.9c) was similar to that in sample 5072. Furthermore, Faul & FitzGerald (1999) also find a similar preferential grain boundary misorientation of 60° around the [a]-axis in partially molten olivine–basalt aggregates. They attribute this to the presence of a CSL (coincident site lattice) boundary for the oxygen sub-lattice that corresponds to the $\{011\}$ twin boundaries that occur in olivine (‘t Hart 1978; Deer *et al.* 1992). Such twin boundaries can be stabilised in forsterite by the incorporation of Ca atoms along the boundary (‘t Hart 1978). The presence of additional Ca derived from the orthopyroxene grains may then explain the preferential occurrence of twin boundaries in the olivine–orthopyroxene sample with respect to the olivine material, but it is not clear how this could weaken the rock.

3.5 Conclusions

The mechanical data of two studies on olivine–orthopyroxene rocks reveal a clear difference in mechanical response of the samples to orthopyroxene content. A general microstructural characterisation yields no conclusive evidence for the origin of this rheological difference. The weak olivine–orthopyroxene material (5249) exhibits several features that are different from the strong olivine sample (5072) and may provide an explanation for the relative weakness. However,

as it was suggested that the weakening is related to the presence of orthopyroxene (Hitchings *et al.* 1989), it should also have occurred in other olivine–orthopyroxene samples, which is not supported by the observations. It is plausible that the variations in strength amongst the samples are related partly to (local) variations in melt content and to the occurrence of zones of high melt content.

In addition to the characterisation presented in this chapter, the intracrystalline deformation features as well as the grain boundary melt microstructure need to be analysed in detail in order to evaluate the active deformation mechanisms that control the rheology of the partially molten olivine and olivine–orthopyroxene materials. The results obtained from the annealing experiments indicate that, although there were complications, the specimens may be used to test the stability of individual features of the microstructure. Variations in rheology may be produced by differences in the micron- to nanometer-scale distribution of melt along grain boundaries or to differences in the intragranular deformation mechanisms. These aspects are investigated in the next three chapters of this thesis.

Intracrystalline deformation microstructures in partially molten olivine and olivine-orthopyroxene rocks deformed in the dislocation creep field

4.1 Introduction

In this chapter, the intragranular deformation structures of two of the experimentally deformed materials from the study of Hitchings *et al.* (1989) are investigated, sample 5072 (olivine) and sample 5249 (70% olivine - 30% orthopyroxene). These two samples were chosen because they represented the stronger and weaker materials analysed in chapter 3 (see fig 3.3). The stronger material, sample 5072, deformed with flow strength intermediate to the weakest, [a]-slip: (010)[100] and strongest, [c]-slip: (010)[001], dislocation slip systems in olivine single crystals (fig 3.3). The weaker material, sample 5249, deformed with flow strength similar to olivine single crystal [a]-slip. From the analysis presented in chapter 3, it was concluded that the observed strength differences between samples 5072 and 5249 could not be explained by differences in bulk melt content, crystallographic preferred orientation or grain size distribution.

The contrast in strength of both samples suggested that the activated dislocation slip systems that accommodated deformation in the two samples might be different. If intracrystalline deformation in sample 5072 occurred by a combination of [a]-slip and [c]-slip, the weakness of sample 5249 could be attributed to inactivity of the hardest dislocation slip system ([c]-slip). Since both samples exhibited low degrees of partial melting, the weakness of sample 5249 with respect to sample 5072 could be explained by the replacement of the [c]-slip deformation mechanism in sample 5249 by melt-enhanced grain boundary processes as proposed by Hirth & Kohlstedt (1995b). If such a difference in active dislocation slip system was responsible for the strength difference, dislocations in the weak and strong sample were expected to exhibit different microstructures and/or Burgers vectors.

In order to test whether or not intracrystalline deformation in samples 5249 and 5072 was accommodated by different olivine dislocation slip systems, the olivine dislocation microstructure has been investigated in detail in both samples and compared to the results from oriented single crystal experiments. The densities of free dislocations with Burgers vectors $\mathbf{b}=[a]$ and $\mathbf{b}=[c]$ were measured as number of dislocations per unit area to determine the relative importance of both

types of dislocations. It is recognised that dislocations associated with the harder slip system are more difficult to move and may be preferentially retained in deformed grains. The presence of such residual ‘strong’ dislocations, however was not shown in olivine single crystals deformed along the weak $[101]_c$ -orientation (Bai & Kohlstedt 1992) and is therefore not expected to affect the relative densities of $\mathbf{b}=[a]$ and $\mathbf{b}=[c]$ dislocations. The rotation axes that describe the misorientation between subgrains were measured to determine the nature of the dislocations that make up the subgrain boundaries.

4.2 Background

The development of dislocation microstructures in experimentally deformed olivine has been extensively studied in single crystals using SEM and light microscopy (e.g. Durham & Goetze 1977a, b; Darot & Gueguen 1981; Bai & Kohlstedt 1992) and TEM (e.g. Phakey *et al.* 1972; Gueguen & Darot 1982; Bai *et al.* 1991). In these experiments, one crystal axis of the deformed sample is oriented perpendicular to the compression direction with the other two crystal axes at an angle of 45° . These orientations are commonly described by referring to a cubic reference lattice as $[110]_c$, $[101]_c$ and $[011]_c$ (fig 4.1) (Durham & Goetze 1977a; Bai & Kohlstedt 1992). Because intracrystalline deformation in olivine is mainly accommodated by dislocations with Burgers vectors $\mathbf{b}=[a]$ and $\mathbf{b}=[c]$ and dislocation slip occurs primarily on the $\{100\}$, $\{010\}$ and $\{001\}$ planes (e.g. Zeuch & Green 1984), specific slip systems can be activated depending on the orientation of the sample.

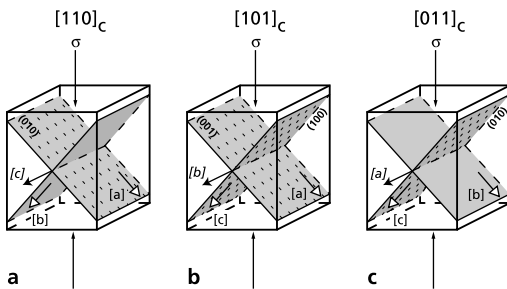


fig 4.1 Diagrams showing the orientation of olivine crystal axes with respect to the compression direction in single crystal experiments for the cubic $[110]_c$ (a), $[101]_c$ (b) and $[011]_c$ (c) directions. Orientation $[110]_c$ enables $(010)[100]$ slip, orientation $[101]_c$ enables both $(100)[001]$ and $(001)[100]$ slip and orientation $[011]_c$ enables $(010)[001]$ slip.

The fastest and easiest method to determine the dislocation microstructure in olivine is by analysing the traces of dislocations on decorated specimens using either optical microscopy or SEM imaging. The advantage of this technique is that relatively large areas can be analysed quickly, although the Burgers vectors of dislocations cannot be determined with light microscopy or from SEM images. This is usually overcome by taking the line direction of dislocations to be indicative for either edge or screw dislocations assuming that dislocation slip in the oriented single crystal samples is restricted to a limited number of expected glide planes with high theoretical Schmid's factors (Darot & Gueguen 1981). The shape and distribution of the dislocations on

selected crystal faces of oriented samples then allows determination of the slip system (Durham & Goetze 1977b). These results, however should be interpreted with care. When the compression direction is not oriented exactly perpendicular to the direction of the inactive burgers vectors, significant deformation may occur on additional slip systems (Darot & Gueguen 1981; Gueguen & Darot 1982). Such deviations in the orientation can for example be caused by the presence of (developing) subgrain boundaries that can accommodate lattice rotations of several degrees. This introduces errors in the interpretation of the dislocations present. Gueguen and Darot (1982) for example, show that in both $[110]_c$ and $[011]_c$ oriented samples long straight dislocations with line direction $[001]$ occur which are often interpreted to be $\mathbf{b}=[a]$ edge dislocations. TEM observations however show that in their samples these are actually $\mathbf{b}=[c]$ screw dislocations (Gueguen and Darot 1982). The distinction can only be made by determining the Burgers vectors using transmission electron microscopy.

$[110]_c$	$[101]_c$	$[011]_c$
The main slip system is $(010)[100]$ with common occurrence of $[100]$ tilt walls ^(1,2,4,5) . The dominant free dislocations are $[100]$ edge dislocations ^(1,5) that are curved. $[001]$ Dislocations also occur, but $[100]$ dislocations are 2-3 orders of magnitude more numerous ⁽⁴⁾	Two main slip systems: $(001)[100]$ and $(100)[001]$. Additional glide planes are: (011) , (021) , (031) and (010) ⁽⁴⁾ . Both $[100]$ and $[001]$ screw dislocations are present ^(1,2,3,4,5) with densities in the same order of magnitude ⁽⁴⁾ . No extensive subgrain boundary formation occurs ^(2,3) , but (010) twist walls are present ⁽⁴⁾	The main slip system is $(010)[001]$ ^(2,4) with additional activation of the (001) glide plane ⁽⁴⁾ . Both $[100]$ and $[001]$ dislocations occur with straight $[001]$ screw dislocations being dominant ^(1,2,5,6) . Numerous twist walls occur in the (010) plane ^(2,4,5)
fastest creep rates ⁽⁴⁾	Intermediate creep rates ⁽⁴⁾	Slowest creep rates ⁽⁴⁾

table 4.1 Summary of observed dislocation structures in oriented single crystal experiments. (1) Phakey *et al.* (1972), (2) Durham *et al.* (1977b), (3) Kohlstedt *et al.* (1980), (4) Darot & Gueguen (1981), (5) Gueguen & Darot (1982), (6) Bai & Kohlstedt (1992).

Descriptions of dislocation microstructures that typically form in single crystals for the different compression directions are summarised in table 4.1. Difficulties in accurately orienting the samples with respect to the compression direction are illustrated by the activation of the $(010)[100]$ slip system in $[011]_c$ oriented samples in which the resolved shear stress in the $[100]$ direction should be zero (Darot & Gueguen 1981). Single crystals that have been deformed with the compression direction outside the major crystallographic planes show an intermediate dislocation structure that is characterised by both free $\mathbf{b}=[a]$ and $\mathbf{b}=[c]$ dislocations and numerous tilt walls in (100) planes (Durham & Goetze 1977b; Kirby & Wegner 1977; Zeuch & Green 1984). This microstructure is also found in natural and experimentally deformed polycrystalline aggregates (Green & Radcliffe 1972; Buiskool Toxopeus & Boland 1976; Boland & Buiskool Toxopeus 1977). The dislocation line direction for dislocations with Burgers vector $\mathbf{b}=[a]$ in the

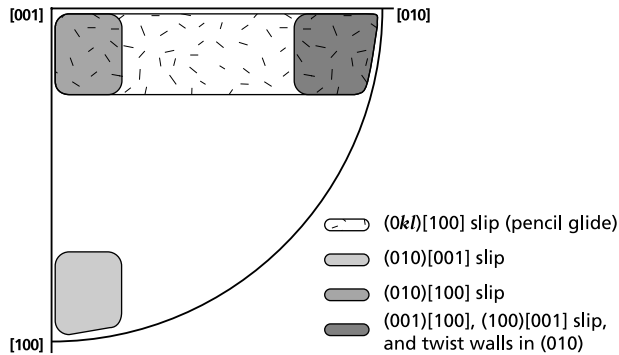


fig 4.2 Inverse pole figure of the expected rotation axes orientations for the most common slip systems in olivine.

latter tilt walls can deviate from the [010] and [001] directions (Zeuch & Green 1984) due to slip on prism planes. Extrapolating the dislocation creep data of olivine single crystals to polycrystalline aggregates where the grains have random orientations and all slip systems are activated indicates that bulk deformation should be rate-controlled by the hardest slip system when dislocation creep is the only deformation mechanism operating. This may change when a lattice preferred orientation has developed. A common natural fabric in mylonitic upper mantle rocks is characterised by a preferential [a]-axis orientation parallel to the stretching lineation with the [b]-axis perpendicular to the foliation. Assuming the σ_1 -direction to be at an angle of 45° to the foliation, a situation comparable to the $[110]_c$ orientation, a dislocation microstructure dominated by (010)[100] slip, the weakest slip system, can be expected (Bai & Kohlstedt, 1992). Likewise, the activation of specific slip systems is expected to produce distinct crystallographic preferred orientations and grain misorientation relations. The rotation axes that accommodate these misorientations give an indication of the active slip system during deformation (fig 4.2, table 4.2) (Poirier 1975; Darot & Gueguen 1981; Fliervoet & White 1995; Lloyd *et al.* 1997). If the hypothesis that the strongest slip system (010)[001] is not the rate-limiting deformation mechanism in sample 5249, but is relieved by grain boundary processes and intracrystalline deformation is accommodated only by (010)[100] slip, it can be expected that the rotation axes between subgrains plot near the [c]-axis in an inverse pole figure (fig 4.2).

subgrain boundary	burgers vector	primary dislocation slip plane	dislocation line direction	expected rotation axis
tilt wall in (001)	[001]	(010)	[100]	[100]
tilt wall in (001)	[001]	(100)	[010]	[010]
tilt wall in (100)	[100]	(010)	[001]	[001]
tilt wall in (100)	[100]	(001)	[010]	[010]
tilt wall in (100)	[100]	{011}	<011>	<011>
tilt wall in (100)	[100]	{031}	<013>	<013>
twist wall in (010)	[100]&[001]	(010)	[100]&[001]	[010]

table 4.2 Expected configurations for the most common subgrain boundaries in olivine.

4.3 Applied analytical methods

The dislocation microstructures were studied with a combination of SEM and TEM techniques. SEM-EBSP analysis was applied to measure the misorientation and the associated rotation axis between subgrain pairs. Adjacent grains that had a misorientation lower than 10° were considered to be subgrains in this analysis (Hull 1975). The measurement error in the determination of the orientation of the rotation axes is highly dependent on the amount of rotation. Measurement of the orientation of rotation axes accommodating misorientations less than 2° can produce errors of 20° – 30° in the orientation determination, whereas the measurement error for the orientation decreases to $\sim 10^\circ$ and less for misorientations exceeding 10° (Prior 1999). Despite this large experimental error, the orientation distribution of the rotation axes can still be used to extract the dislocation slip system that produced the subgrain boundary because the number of potential (subgrain) rotation axes produced by dislocation slip in olivine is limited (fig 4.2). Straightforward identification of adjacent subgrains in SEM forward scattering imaging was hampered by the strong dependence of the contrast or grey-level on its crystallographic orientation. The contrast can vary strongly with only minor variations in grain orientations and the resulting contrast difference between grains may actually be lower than between adjacent subgrains (fig 4.3). Initial selection of subgrain pairs inside larger crystals was based on the often smoothly curved shape of the subgrain boundary (fig 4.3) and confirmed with EBSP measurements by monitoring the change of the diffraction patterns when moving the electron beam over the boundary. An Excel spreadsheet, written by Dr T.F. Fliervoet (personal communication), was used to calculate the misorientation of adjacent subgrains and the corresponding rotation axes. The shape and Burgers vectors \mathbf{b} of individual dislocations and subgrain boundaries in the grains were analysed with TEM weak beam dark field imaging. This imaging method allowed for the measurement of the total dislocation density together with the determination of the fraction of free dislocations with $\mathbf{b}=[a]$ and $\mathbf{b}=[c]$ Burgers vectors respectively as described below. Weak beam dark field images are by their nature very sensitive to the orientation of the studied crystal and high dislocation densities and subgrain boundaries accommodate rotations of the crystal lattice. Therefore, images of crystals that are bent or contain one or more subgrain boundaries cannot be ideal in the whole image. The (in)visibility of dislocations in standard dark field imaging can be described with invisibility criteria for both edge and screw

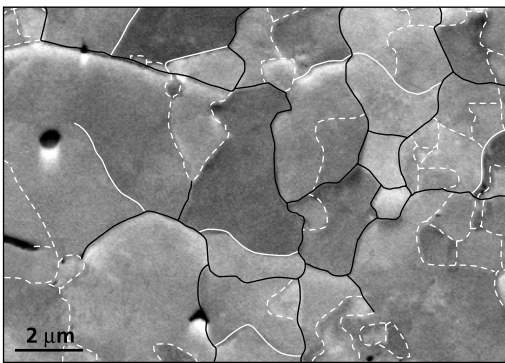


fig 4.3 SEM orientation contrast image illustrating the (sub)grain structure within sample 5072. (Sub)grains whose orientations were determined are outlined. Black lines are grain boundaries, white lines are subgrain boundaries. Misorientations of boundaries that are marked with dashed lines were not determined. Note that the contrast change at subgrain boundaries may be higher than at high angle grain boundaries.

dislocations and subgrain boundaries in the grains were analysed with TEM weak beam dark field imaging. This imaging method allowed for the measurement of the total dislocation density together with the determination of the fraction of free dislocations with $\mathbf{b}=[a]$ and $\mathbf{b}=[c]$ Burgers vectors respectively as described below. Weak beam dark field images are by their nature very sensitive to the orientation of the studied crystal and high dislocation densities and subgrain boundaries accommodate rotations of the crystal lattice. Therefore, images of crystals that are bent or contain one or more subgrain boundaries cannot be ideal in the whole image.

The (in)visibility of dislocations in standard dark field imaging can be described with invisibility criteria for both edge and screw

dislocations assuming a two-beam diffraction condition (e.g. McLaren 1991). The contrast of dislocations in TEM images arises from diffraction on the lattice planes that are distorted by the dislocation. For pure screw dislocations all planes parallel to \mathbf{b} are undistorted. Therefore, all electron beams that are diffracted by planes parallel to \mathbf{b} show no image contrast for the screw dislocation. With \mathbf{g} being the operating diffraction vector (which corresponds to the diffracted beam used), \mathbf{b} the Burgers vector of the dislocation, and \mathbf{u} a unit vector parallel to the dislocation line direction, the invisibility criterion is $\mathbf{g} \cdot \mathbf{b} = 0$. For pure edge dislocations, only lattice planes perpendicular to the dislocation line direction will be undistorted and edge dislocations will be invisible in images that are formed using electron beams diffracted from these planes. The invisibility criterion for edge dislocations can be expressed as $\mathbf{g} \cdot (\mathbf{b} \times \mathbf{u}) = 0$ (Howie & Whelan 1962; McLaren 1991). Using these two invisibility criteria, imaging conditions can be determined in which only dislocations with the Burgers vectors of interest are visible, while other dislocations remain invisible. As the olivine crystals in the studied samples have random orientations and the major crystal axes often lie beyond the tilting range of the specimen holder, the latter criterion greatly limits the actual number of olivine grains in which dark field dislocation analysis can be done.

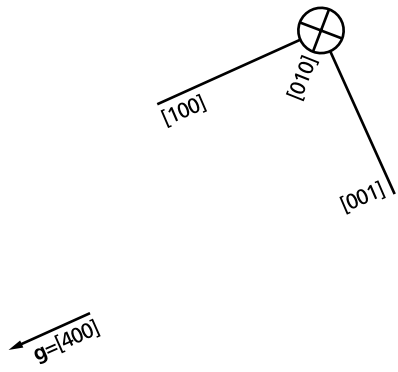
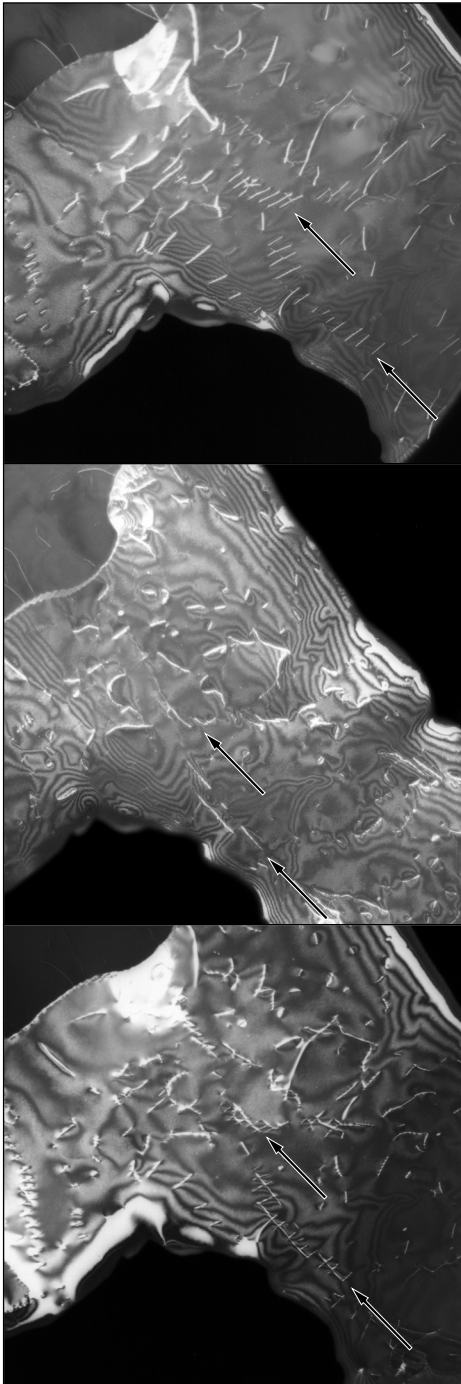
The image contrast of edge dislocations in standard dark field imaging when $\mathbf{g} \cdot \mathbf{b} = 0$ and $\mathbf{g} \cdot (\mathbf{b} \times \mathbf{u}) \neq 0$ is dependent on the deviation from the Bragg diffraction angle. When this deviation is zero or very small (with the crystal near the ideal reflecting orientation), appreciable contrast arises from the $\mathbf{g} \cdot (\mathbf{b} \times \mathbf{u}) \neq 0$ condition and edge dislocations are clearly visible. If the deviation from the Bragg diffraction angle increases, as is the case for weak beam imaging, the contribution of the $\mathbf{g} \cdot (\mathbf{b} \times \mathbf{u})$ term to the image contrast becomes negligible (McLaren 1991). In weak beam dark field imaging conditions, the $\mathbf{g} \cdot \mathbf{b} = 0$ condition for invisibility is also applicable for edge dislocations, even when the value of $\mathbf{g} \cdot (\mathbf{b} \times \mathbf{u}) \neq 0$ is large. The weak beam dark field imaging technique now allows the determination of the Burgers vector while the dislocation line direction can be used to determine the edge or screw character of the dislocations.

The intensity of the diffracted beams for a given lattice plane is dependent on the atom

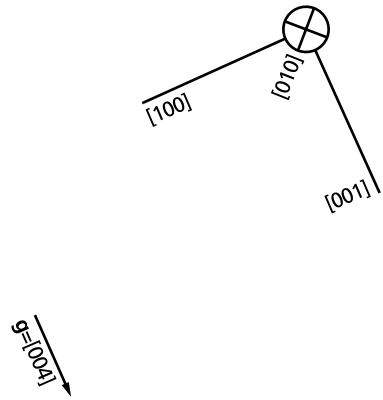
reflection (<i>hkl</i>)	intensity	reflection (<i>hkl</i>)	intensity	reflection (<i>hkl</i>)	intensity
004	35.9	021	20.0	170	13.4
062	30.8	400	19.2	404	11.9
130	24.4	240	18.2	211	11.7
222	24.1	322	17.7	133	11.5
112	23.1	122	17.2	210	11.5
131	20.6	043	13.4		
140	20.5	020	13.4		

table 4.3 Reflections used for weak beam dark field imaging with their relative intensities. The structure factors are calculated using a computer program based on the polynomials from Doyle & Turner (1968).

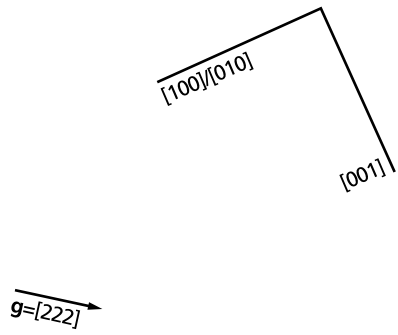
fig 4.4 TEM weak beam dark field images of the dislocation microstructure in an olivine grain in sample 5072. Bending of the crystal lattice locally changes the diffraction conditions away from the weak beam condition and gives rise to the brighter areas. Several twist wall segments are present (arrowed) that consist of long $\mathbf{b}=[c]$ screw dislocations with perpendicular shorter $\mathbf{b}=[a]$ screw dislocations (a) $\mathbf{g}=[400]$, (b) $\mathbf{g}=[004]$, (c) $\mathbf{g}=[222]$.



a



b



1 μm

c

arrangement of the diffracting plane and can be expressed by a structure factor (e.g. Edington 1975; McLaren 1991). Structure factors for electron diffraction on specific lattice planes in olivine have been calculated using a computer program that was written by John FitzGerald (Australian National University) and adapted for Macintosh computers by David Mainprice (University of

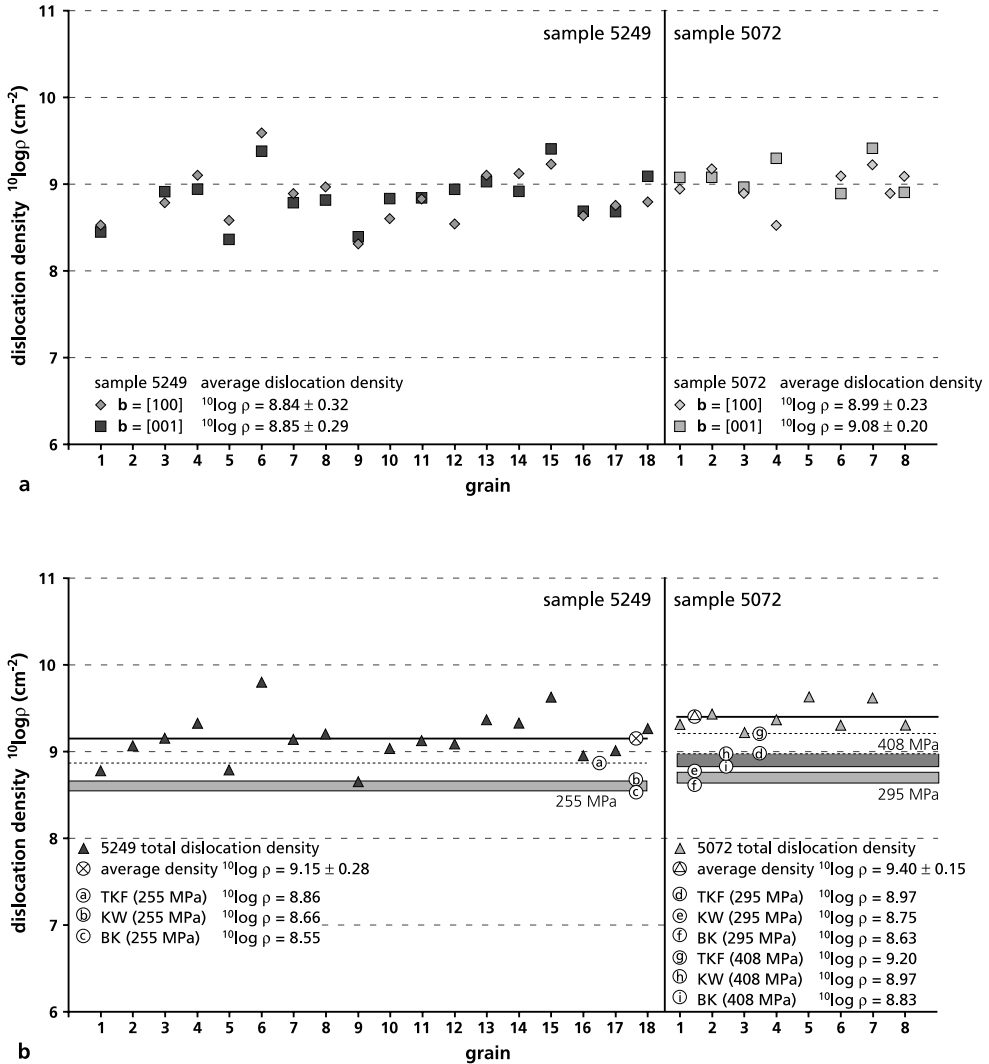


fig 4.5 (a) Dislocation densities in samples 5072 and 5249 for individual grains, subdivided in **b**=[100], **b**=[001]. (b) Average dislocation densities in samples 5072 and 5249. The shaded fields indicate the range of dislocation density estimates determined using the stress-dislocation density calibrations of Kohlstedt & Weathers (1980) (KW) and Bai & Kohlstedt (1992) (BK) for the applied differential stresses of 255 MPa for sample 5249 and 408 and 295 MPa for sample 5072. The dislocation densities calculated using the calibration of Toriumi *et al.* (1984) (TKF) are indicated by the dotted lines and not included in the shaded areas because the measurement method is not clear.

Montpellier). Table 4.3 shows the reflections with the highest structure factors that have been used for Burgers vector determination. Orienting individual crystals in the microscope is a time consuming process and mechanical considerations limit the number of zone axes that can be reached by tilting the specimen. Therefore, where possible, the grains were oriented along a zone axis that contained strong reflections of (hko) , (okl) and (hkl) character. This permitted subsequent imaging of dislocations with $\mathbf{b}=[a]$, $\mathbf{b}=[c]$, and all dislocations present without having to reorient the crystal along another zone axis. A drawback of this approach is that the small rotations between different images prohibit the accurate determination of the dislocation line directions. Instead, the dislocation line direction in the images was compared with the projected trace of the main crystal axes to estimate the line direction and place constraints on the screw or edge character of the dislocations.

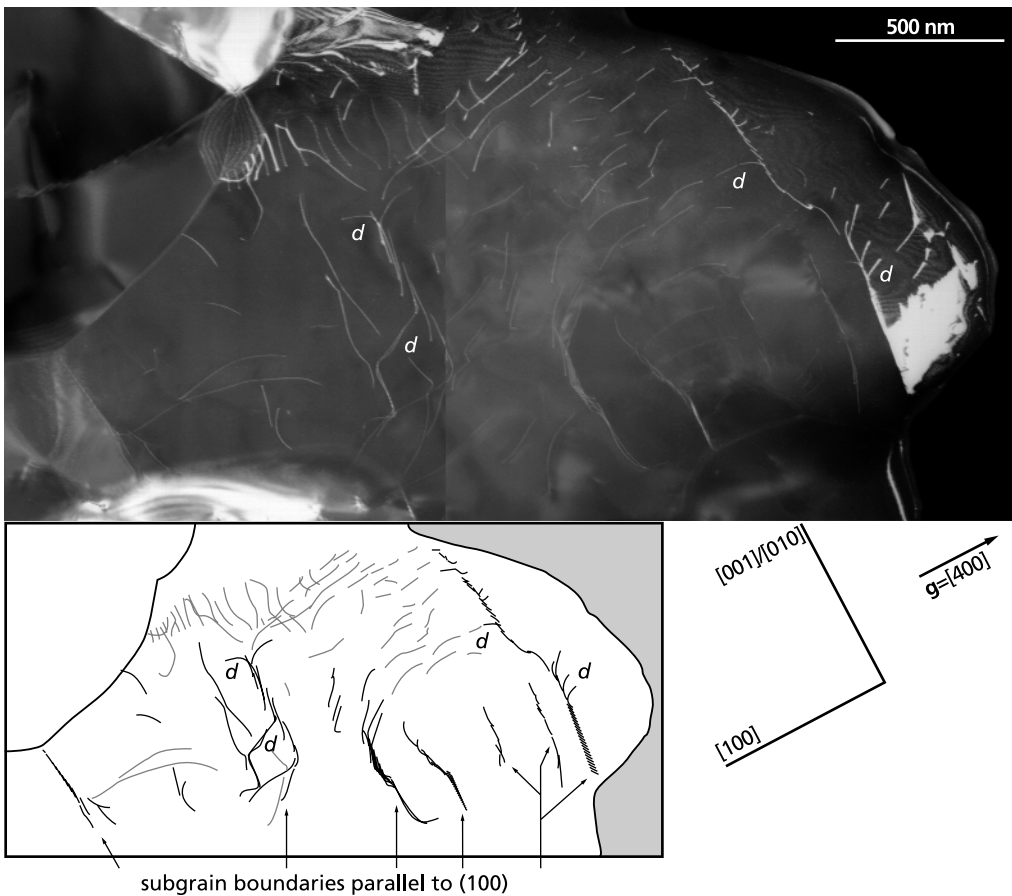


fig 4.6 TEM weak beam dark field image showing the presence of tilt walls composed of $\mathbf{b}=[100]$ dislocations parallel to the (100) plane (the $[100]$ organisation of Durham *et al.* (1977b)) in sample 5072, longer $\mathbf{b}=[a]$ screw dislocations (d) locally connect to the tilt walls. $\mathbf{g}=[400]$.

4.4 Results

The dislocation microstructure within individual olivine grains was imaged with weak beam dark field microscopy. Where possible, images were obtained using three different \mathbf{g} conditions from a single zone axis. In order to check the validity of the interpretation of the Burgers vectors of the dislocations, this procedure was repeated along another zone axis for some grains. The resulting images are illustrated in fig 4.4. In fig 4.4a, only $\mathbf{b}=[a]$ dislocations are imaged, in fig 4.4b only $\mathbf{b}=[c]$ dislocations and fig 4.4c shows all the dislocations that are present. The projected line direction of the $\mathbf{b}=[a]$ dislocations was parallel to $[100]$, suggesting that these dislocations were screw dislocations. The $\mathbf{b}=[c]$ dislocations with projected line directions parallel to $[001]$ or $[100]$ were interpreted to be screw and edge dislocations respectively. In fig 4.4c the $\mathbf{b}=[a]$ and $\mathbf{b}=[c]$ screw dislocations combined to form fragments of twist walls (arrowed) that intersected the foil parallel to the $[001]$ direction.

Free dislocations had both $\mathbf{b}=[a]$ and $\mathbf{b}=[c]$ burgers vectors and free dislocation densities varied an order of magnitude between grains within the samples, therefore the results are presented for individual grains in fig 4.5a. Within grains the density of $\mathbf{b}=[a]$ and $\mathbf{b}=[c]$ dislocations was similar and both grains in which $\mathbf{b}=[a]$ dislocations were dominant as grains in which $\mathbf{b}=[c]$ dislocations were dominant occur. The average dislocation densities in samples 5072 and 5249 were $2.7 \times 10^9 \text{ cm}^{-2}$ and $1.8 \times 10^9 \text{ cm}^{-2}$ respectively (fig 4.5b). In both samples, several types of subgrain boundaries were present. Long $\mathbf{b}=[a]$ screw dislocations merged into subgrain boundaries in the (100) plane where they formed tilt walls (fig 4.6, 4.7). Similarly $\mathbf{b}=[c]$ screw dislocations were connected to $\mathbf{b}=[c]$ tilt walls that formed in the (001) plane (fig 4.8). In the centre of this image part of a twist wall composed of $\mathbf{b}=[a]$ and $\mathbf{b}=[c]$ screw dislocations can be recognised in contact with the tilt wall. Such interactions of tilt and twist walls were common. Figure 4.9 illustrates a junction of a $\mathbf{b}=[c]$ tilt wall with a twist wall. Interactions of perpendicular subgrain boundaries produced rectangular subgrains (fig 4.10). The boundaries that produced this substructure were oriented along the (100) and (001) planes and were composed of combinations of both edge and screw dislocations. Note that although the subgrain boundaries are perpendicular, no four-fold junction occurred, but rather two closely

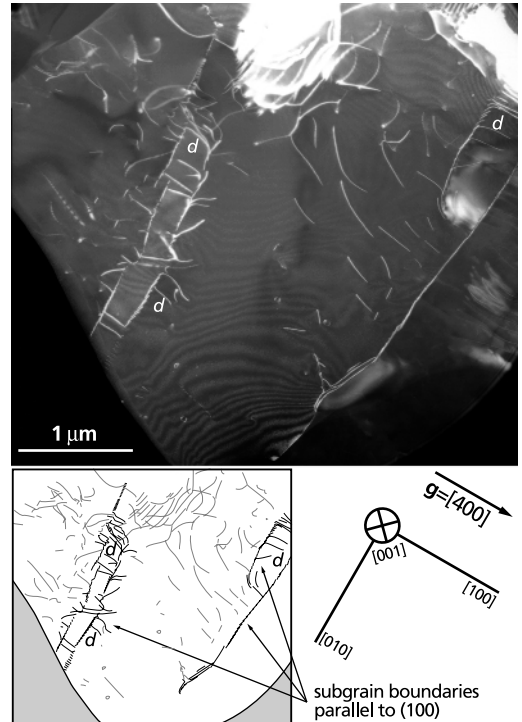


fig 4.7 TEM weak beam dark field image showing the presence of tilt walls composed of $\mathbf{b}=[100]$ dislocations parallel to the (100) plane ($[100]$ organisation) in sample 5249, longer $\mathbf{b}=[a]$ screw dislocations (d) locally connect to the tilt walls. $\mathbf{g}=[400]$.

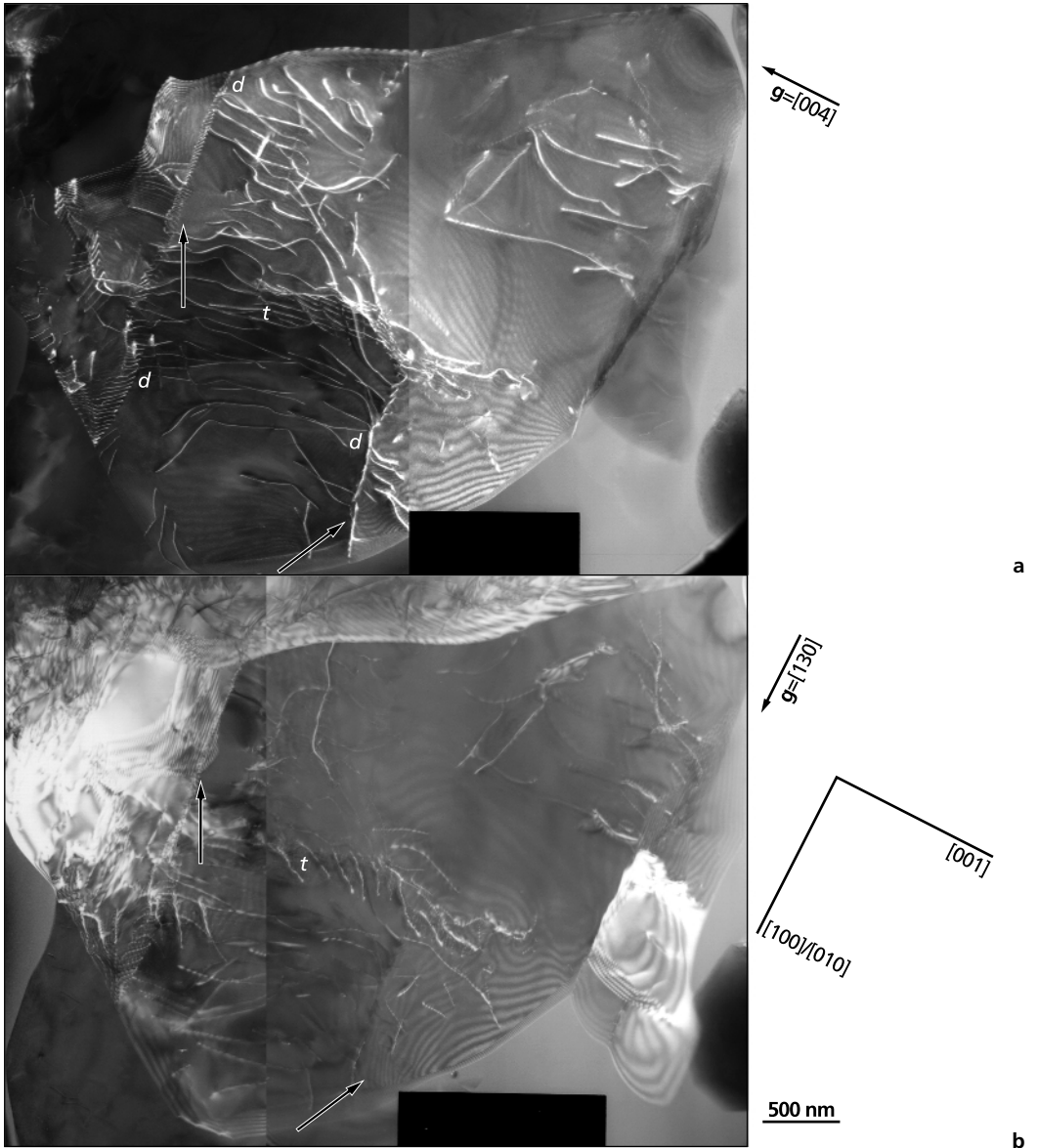


fig 4.8 TEM weak beam dark field image showing the presence of tilt walls composed of $\mathbf{b}=[001]$ dislocations parallel to the (001) plane ([001] organisation of Zeuch & Green (1984) in sample 5249 (a) $\mathbf{g}=[004]$, (b) $\mathbf{g}=[130]$). Locally long dislocation loops (*d*) with $\mathbf{b}=[c]$ connect to the tilt walls (arrowed). In the centre of the image, a twist wall (*t*) is in contact with one of the tilt walls.

spaced three-grain junctions with a connecting subgrain boundary at an intermediate orientation. No preference for a specific type of subgrain boundary was found in either sample. The presence of long curved dislocations parallel to $[100]$ with $\mathbf{b}=[c]$ in the (010) plane, indicated activation of the hard $(010)[001]$ slip system (fig 4.10). Dislocation densities were not measured in the long-duration annealing samples, but free dislocation densities were still high with abundant subgrain boundaries after annealing.

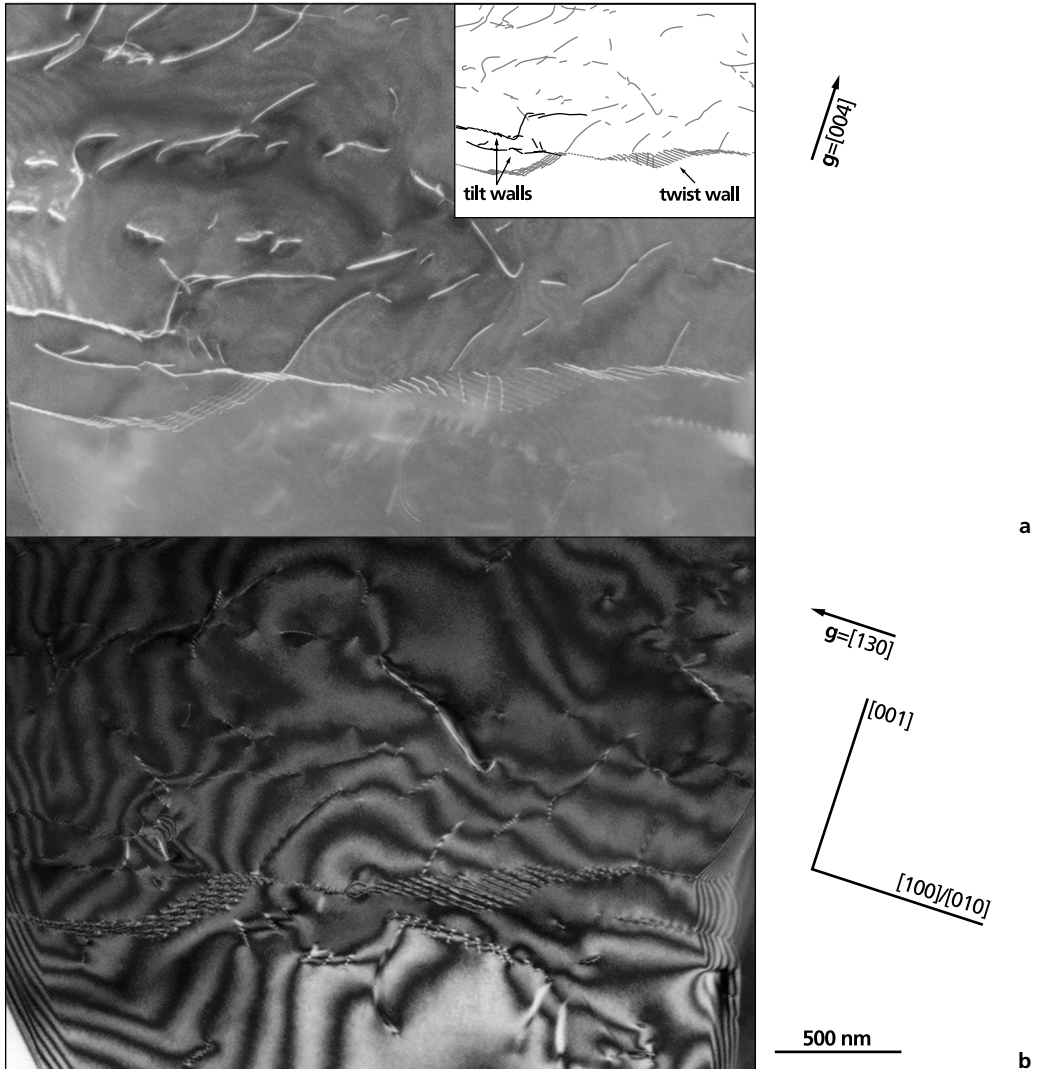


fig 4.9 TEM weak beam dark field image of an interaction between a $\mathbf{b}=[c]$ tilt wall with a twist wall consisting of $\mathbf{b}=[a]$ and $\mathbf{b}=[c]$ dislocations. (a) $\mathbf{g}=[004]$, (b) $\mathbf{g}=[130]$ (sample 5249).

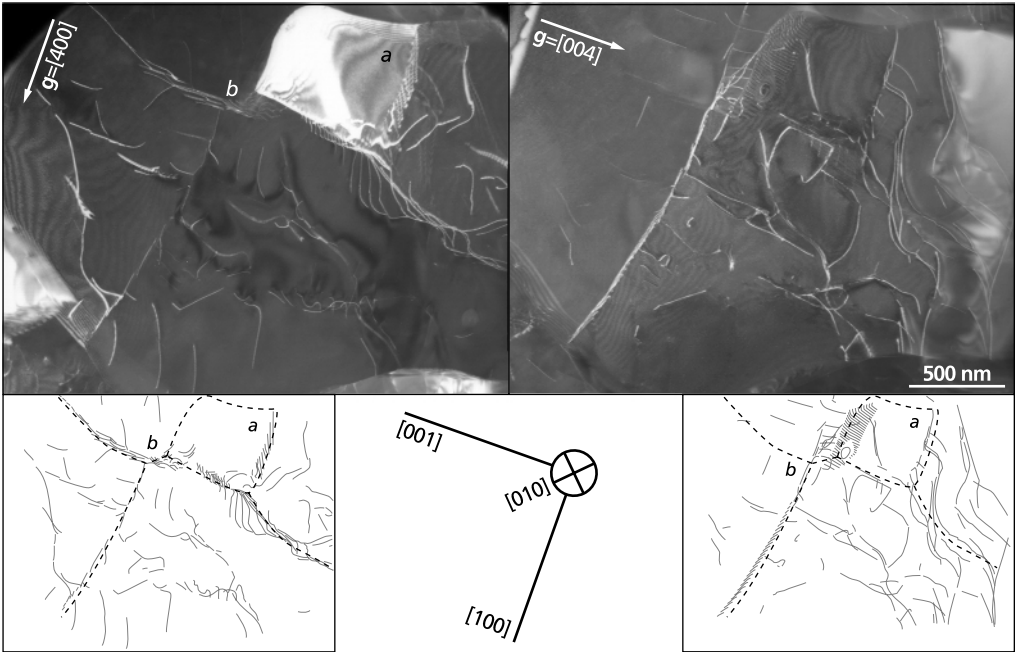


fig 4.10 TEM weak beam dark field image of a rectangular subgrain structure (a) in sample 5249. Two perpendicular subgrain boundary junctions are connected by a subgrain boundary with intermediate orientation (b) The subgrain boundaries are marked with a dotted line in both insets.

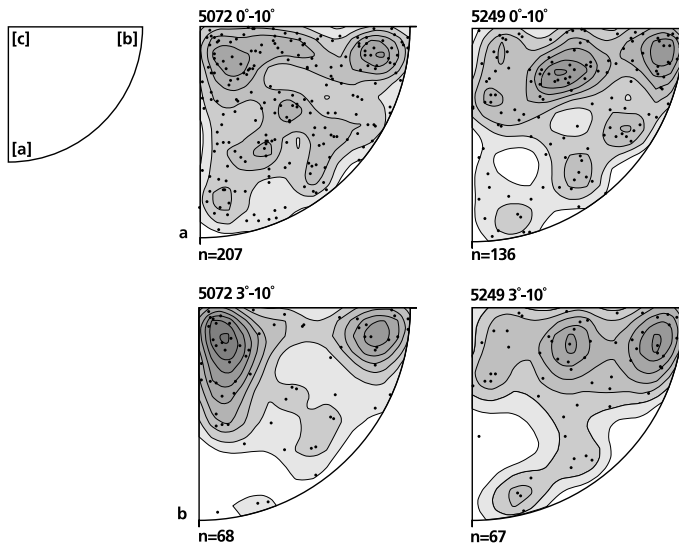


fig 4.11 Inverse pole figure of (subgrain) rotation axes with misorientations less than 10°, subdivided in classes (a) 0°-10° and (b) 3°-10°. (Contours at 0.5-1.5-2.5-3.5-4.5-5.5-6.5-7.5-8.5 x uniform)

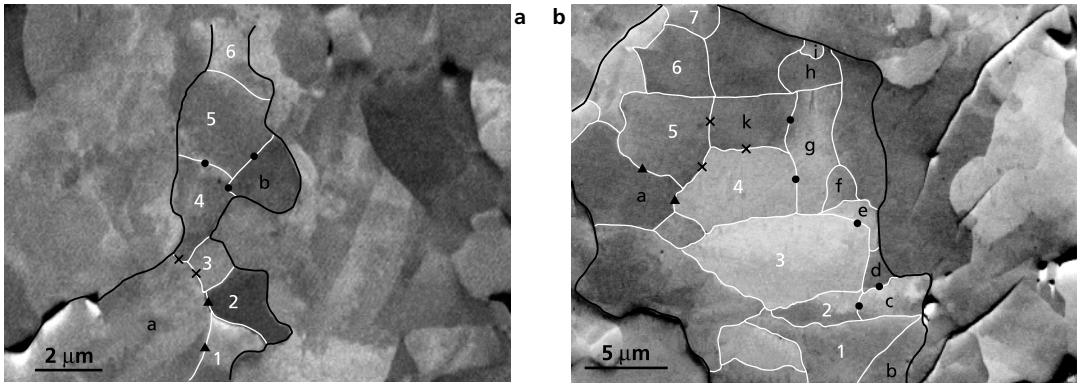


fig 4.12 SEM orientation contrast image illustrating the subgrain microstructure within grains. Black lines outline individual crystals, subgrain boundaries are indicated by white lines. (a) sample 5072, (b) sample 5249. The orientations of the subgrains indicated with numbers and letters were measured with EBSD and used in figures 4.13 and 4.15. For explanation about the numbers, letters, and symbols (circle, triangle and cross) that mark some subgrain boundaries refer to figures 4.13 and 4.15. The compression direction is horizontal.

The EBSD determination of the orientation distribution of the rotation axes for misorientations 0° - 10° is presented in figure 4.11a. Because the small misorientation angles may introduce large uncertainties in the calculation of the orientation of the rotation axes (Prior 1999), the orientation distributions were also investigated for the misorientation intervals 1° - 10° , 2° - 10° , and 3° - 10° , subsequently omitting rotation axes for misorientations smaller than 1° , 2° , and 3° . This procedure was applied to test whether or not the distribution was altered by the errors from the smallest misorientations. Omission of the rotation axes with the lowest misorientations resulted in a decrease in scatter, but between these plots no obvious difference in orientation distribution was present. The resulting orientation distribution is illustrated for rotations in the 3° - 10° interval in figure 4.11b. Subgrain rotation axes in sample 5072 clustered near the $[001]$ direction with a spread towards $[100]$ and showed a second maximum near $[010]$. The rotation axes in sample 5249 were distributed in a broad girdle parallel to the (100) plane with minor maxima close to the $[021]$ and $[010]$ directions.

To illustrate the development of the subgrain microstructure within larger olivine crystals involving progressive rotation of adjacent subgrains, one grain containing a series of subgrains that stretched across the grain was selected in each sample (fig 4.12). The misorientation that was accommodated by the subgrains is shown by the progressive rotation of the principal crystal axes (fig 4.13). In fig 4.13a (sample 5072) the $[100]$ and $[010]$ axes show progressive rotation across the host grain whereas the $[001]$ axes of the subgrains plot in a cluster. A similar pattern is visible in figure 4.13b (sample 5249) where the $[100]$ and $[010]$ axes also show progressive rotation, which was absent for the $[001]$ axes. In both grains, the $[010]$ axes were subparallel to the compression direction. The traces of the major crystal planes within the individual subgrains are plotted in figure 4.14 and showed a relation with the orientation of the subgrain boundaries. The rotation axes that describe the individual rotations were calculated from the EBSD measurements (fig 4.15). Despite the large uncertainty in the orientation determination of the rotation axes for the

subgrains with small misorientations, the scattering of rotation axes in these plots indicated that subgrain formation within the grains did not involve a single rotation axis. Within the measurement error, the rotation axes of adjacent subgrain boundaries sometimes showed similar orientations (fig 4.12, 4.15). These clusters of boundaries divided the deformed olivine grain into segments that contained related subgrain boundaries with similar rotation axes.

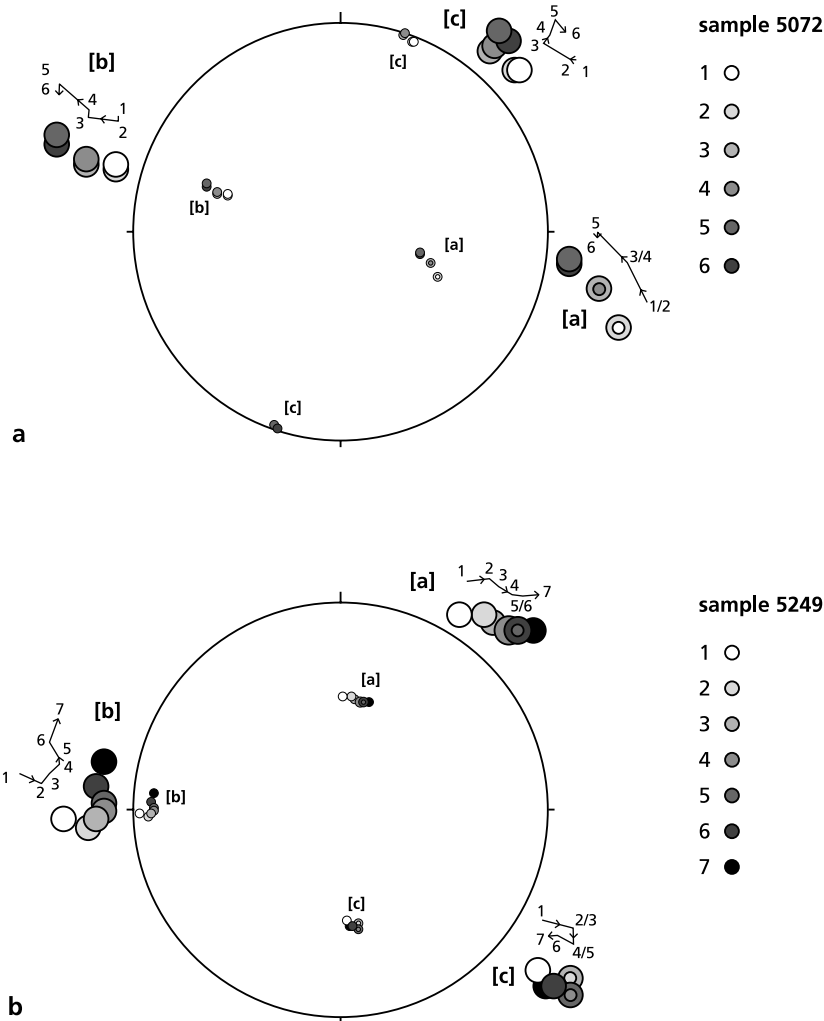


fig 4.13 Stereographic projection of the crystal axes of the two series of subgrains denoted with numbers that stretch across individual olivine crystals in figure 4.12. The subgrains marked with letters in figure 4.12 lie besides the chosen transect across the crystals and are not included in the projections. Figure 4.13a corresponds to figure 4.12a (sample 5072), figure 4.13b corresponds to figure 4.12b (sample 5249). The compression direction is horizontal.

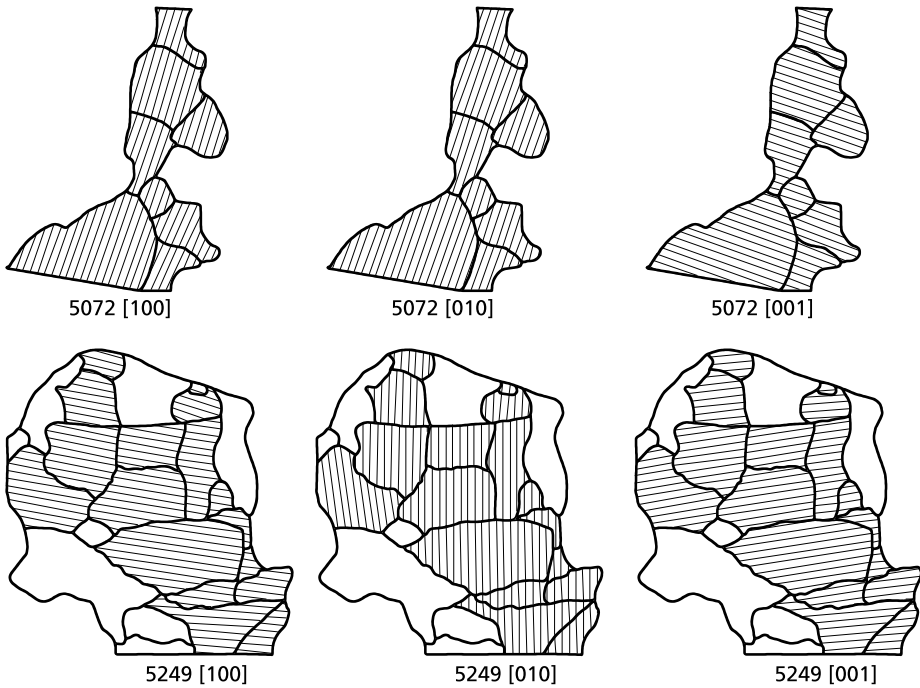


fig 4.14 Line drawings of the grains in figure 4.12 showing the trace of the principal crystal lattice planes within the subgrains. Upper drawings correspond to figure 4.12a (sample 5072), lower drawings correspond to figure 4.12b (sample 5249).

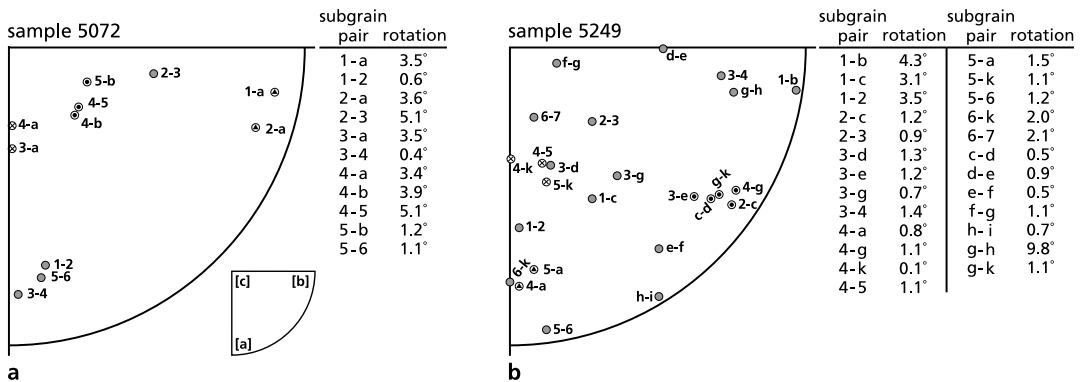


fig 4.15 Inverse pole figure of all rotation axes that accommodate misorientations between adjacent subgrains in the grains shown in figure 4.12. Subgrain pairs are indicated by the letters and numbers used in figure 4.12. Figure 4.15a corresponds to figure 4.12a (sample 5072), figure 4.15b corresponds to figure 4.12b (sample 5249). Adjacent subgrain boundaries with similar rotation axes are indicated with symbols inside the markers (circle, triangle and cross) that correspond to the symbols on the subgrain boundaries in figure 4.12.

4.5 Discussion

Two approaches were followed to establish the active dislocation slip systems in samples 5072 and 5249. The first method involved direct observations of individual dislocations and subgrain walls using TEM weak beam dark field imaging. The fraction of dislocations with either Burgers vector $\mathbf{b}=[a]$ or $\mathbf{b}=[c]$ provided insight into the relative importance of the different slip systems, while the method also allowed for the analysis of the types of dislocations in subgrain boundaries. Second was the indirect approach of measuring subgrain rotations in the SEM that are indicative for the crystallographic nature of the subgrain boundaries that accommodate the lattice misorientation. Because the line direction of individual dislocations was not determined in the randomly cut grains in the TEM foils, the line direction of the projected dislocations was compared with the projected orientation of the major crystal axes. For the dislocations that were parallel to these axes the screw or edge character was readily inferred. However, many dislocations, both free and in subgrain boundaries, were observed to make a distinct angle with these axes. The weak beam dark field imaging technique used does not allow discrimination of the character of these dislocations. Part of these oblique dislocations are likely to be $[100]$ edge dislocations that lie in the (100) plane with line directions in $\langle okl \rangle$ orientations (pencil glide, Raleigh (1968)) with others being of mixed edge-screw character.

The densities of both $\mathbf{b}=[a]$ and $\mathbf{b}=[c]$ dislocations were variable within the samples where some grains preferentially exhibited $\mathbf{b}=[c]$ dislocations whereas in other grains the $\mathbf{b}=[a]$ dislocations dominated. This may be related to the activation of specific slip systems for different crystal orientations with respect to the compression direction, in analogy with the activation of selected slip systems in single crystal experiments. In accordance with the results of Bai & Kohlstedt (1992), who found that the dislocation density is independent of the activated slip system, the overall $\mathbf{b}=[a]$ and $\mathbf{b}=[c]$ dislocation densities were similar both in sample 5072 and in sample 5249 (fig 4.5a), with the density in sample 5072 being somewhat higher. The higher dislocation density in sample 5072 can be related to the higher stress level during deformation. An unknown fraction of the dislocations in both samples may be geometrically necessary dislocations as the number of linearly independent slip systems in olivine is less than 5 (Durham & Goetze 1977b) and the Von Mises criterion that is required for homogeneous deformation solely accommodated by dislocation slip (Von Mises 1928; Paterson 1969), is not satisfied in olivine.

Comparison of the observed dislocation density with the single-crystal dislocation density-stress calibrations of Toriumi *et al.* (1984), Kohlstedt & Weathers (1980), and Bai & Kohlstedt (1992) requires that the measure for dislocation density can be compared. There are two common expressions for dislocation density, number of dislocations per unit area and dislocation line length per unit volume. For randomly oriented dislocations the number per unit area is exactly half the density measured as dislocation line length per unit volume (Kohlstedt & Weathers 1980). In the present study, dislocation densities were measured on TEM micrographs as number of dislocations per unit area. The same method was used by Kohlstedt & Weathers (1980). Bai & Kohlstedt (1992) defined the dislocation density as dislocation line length per unit volume, but actually measured the number of dislocations per unit area of a decorated thin section as these expressions

of the dislocation density are equivalent when dislocations are straight and oriented mainly perpendicular to the surface. In the study of Toriumi *et al.* (1984) the measurement technique is not mentioned other than that the dislocation densities were measured on decorated thin sections (see Karato *et al.* 1980). Because of the different measurement techniques, the measured dislocation densities were compared to dislocation densities calculated using the calibrations of Kohlstedt & Weathers (1980) and Bai & Kohlstedt (1992) (fig 4.5b).

The total dislocation densities in both samples were consistently higher than the densities predicted from single crystal experiments (shaded areas in fig 4.5b) (Kohlstedt & Weathers 1980; Bai & Kohlstedt 1992). From the stress-strain curve for sample 5249 in appendix A, it was concluded that the sample had reached a steady-state flow-stress, so it is unlikely that the higher dislocation density was related to initial strain hardening. The stability of the dislocation density is also supported by the study of Durham & Goetze (1977b) where the dislocation density in olivine stabilised after 1-2% strain, while the experimental steps of samples 5072 and 5249 exceeded 5% strain. The stress-strain curve for sample 5072 is unfortunately not available, but all tests in the study of Hitchings *et al.* (1989) were conducted until a quasi-steady state flow-stress was achieved. The higher dislocation densities in both samples with respect to single crystal data may point to a difference in the development of the dislocation microstructure between the single crystal experiments used to calibrate the stress-density relationship and polycrystals (Zeuch & Green 1984). If this difference originates from the interaction between adjacent grains in a polycrystal, extrapolation of single crystal dislocation data to polycrystalline aggregates may be invalid. A possible cause for the difference in dislocation density is the additional formation of geometrically necessary dislocations in the polycrystalline material that form to accommodate both deformation imposed by adjacent grains and small amounts of grain boundary sliding (Ashby 1970; Gifkins 1976). Similar relatively high dislocation densities have been reported in polycrystalline calcite with respect to calcite single crystals (De Bresser 1996). The deviation from dislocation densities predicted from single crystal calibrations was seen to increase with decreasing grain size. Such data is not available for olivine, but indications that grain size plays a role in the resulting dislocation density are discussed by Twiss (1986). This may be supported by the data of Zeuch & Green (1979) that are presented by Kohlstedt & Weathers (1980) (their fig. 2), considering that the stress estimates of Zeuch & Green (1979) are likely to be overestimated by a factor 3 to 7 (Green & Borch 1989; Van der Wal *et al.* 1993). Adjusting the flow stress accordingly would result in dislocation densities for the polycrystals that are relatively higher than the single crystal densities. This increase in dislocation density in polycrystals with respect to single crystals may relate to a Hall-Petch type relationship or to the interaction of geometrically necessary and statistically stored dislocations in polycrystals as discussed by De Bresser (1996).

In the interpretation of the relatively high dislocation densities, the multi-stage history of sample 5072 has to be taken into account. The development of the dislocation microstructure with progressive deformation at higher stress conditions has been extensively studied and it is shown that the existing dislocation microstructure will usually be obliterated within 1% additional strain (e.g. Durham & Goetze 1977b; Kohlstedt & Weathers 1980). However, the response of the dislocation microstructure to annealing or subsequent deformation at lower stress levels at similar

temperatures is not uniform. In most cases the dislocation distribution homogenises and the density decreases during annealing (Goetze & Kohlstedt 1973; Ricoult 1979; Kohlstedt *et al.* 1980; Karato & Ogawa 1982; Karato *et al.* 1993). In some cases however, annealing has little or no effect on the dislocation density (Bai & Kohlstedt 1992) and 5% to 10% additional strain may be required to obtain effective recovery (Toriumi *et al.* 1984). This is supported by the occurrence of numerous subgrain boundaries and high dislocation densities that survived the long-duration annealing experiments of samples 5249 and 5072 reported in chapter 3. Furthermore, during initial stages of annealing additional closely spaced tilt walls may form parallel to the (100) and (001) planes (Ricoult 1979; Gueguen & Darot 1982; Bai & Kohlstedt 1992). The effect of subsequent deformation steps at similar temperatures but lower stress levels on the dislocation density is not known. The study of Ross *et al.* (1980) indicates that subgrain structures that form at high stress only adapt slowly to lower stress conditions. However, the use of a Griggs-rig type deformation apparatus introduces uncertainties in the stress determination (Green & Borch 1989), which may give rise to additional unrecognised deformation of the sample during unloading and decompression as witnessed by an increase in dislocation density during annealing (Zeuch & Green 1984). Because the adaptation of the dislocation microstructure to subsequent lower stress conditions is not well constrained, it is not sure whether or not high dislocation densities from previous high stress experiments may survive deformation at lower stress. Therefore, the dislocation structure that was observed in sample 5249 is likely to reflect only the final situation. But sample 5072 experienced a deformation step of 408 MPa before the final 295 MPa deformation step and it can not be excluded that the observed dislocation microstructure has retained remnants of this higher stress deformation step. However, even if the microstructure in sample 5072 was preserved from the high-stress deformation stage, the dislocation densities in both samples were higher than expected from single crystal data.

Comparison of the observed distribution of free dislocations with results from oriented single crystal studies is difficult. Although the identity of individual dislocations could be determined, comparison of the resulting dislocation microstructure was hampered by the sectioning of dislocations in the randomly cut crystals in thin TEM foils. Tilting of individual crystals to orientations corresponding to the orientations in single crystal studies is often possible, but the remaining truncated dislocation line length in thin foils from the polycrystalline specimens is limited. This precludes direct application of the shape and length criteria of dislocations on chosen crystal planes that are used in the characterisation of the dislocation microstructure in oriented single crystal studies (Phakey *et al.* 1972; Durham & Goetze 1977a, b; Darot & Gueguen 1981; Gueguen & Darot 1982; Bai & Kohlstedt 1992). More reliable indicators for the activated slip systems were the subgrain walls that formed during deformation. Because the number of possible subgrain configurations in olivine is limited, the orientation of a subgrain wall combined with the Burgers vector and projected line direction of the individual dislocations are sufficient to identify the crystallographic character of the subgrain boundary. Similar to the free dislocation distribution, the subgrain boundary structures in both samples were variable in individual grains. Examples of subgrain boundaries that are produced by all of the different slip systems depicted in fig 4.2 were found in both samples. The simple subgrain boundary morphologies of the [100]

organisation (Durham *et al.* 1977b; Zeuch & Green 1984; Bai & Kohlstedt 1992) and the similar [001] organisation (Zeuch & Green 1984; Bai & Kohlstedt 1992) were occasionally observed in the samples (fig 4.6, 4.7, 4.8), but did not appear to be the dominant subgrain boundary structures in the studied areas. More commonly found were subgrain boundaries that consisted of combinations of edge and screw dislocations with both Burgers vectors $\mathbf{b}=[a]$ and $\mathbf{b}=[c]$ and twist walls in the (010) plane. Conclusions about the relative abundance of each type of subgrain boundary, however should not be based on TEM observations because the area that could be studied with this technique was limited and the variability between the individual grains was high.

In summary, the TEM results show evidence for the activation of all of the earlier reported dislocation slip systems in olivine, including the weak [a]: (010)[100] and strong [c]: (010)[001] dislocation slip systems in both samples. The occurrence of similar dislocation microstructures in samples 5072 and 5249 indicate that the same slip systems were operating in both samples and no preference for a specific dislocation slip system could be shown for either sample.

In order to estimate the relative activity of the different slip systems, data on the subgrain development throughout the sample is required. As TEM imaging only provided local examples of the dislocation microstructure, EBSD data obtained in the SEM was used to determine the orientation distribution of rotation axes between subgrains. Comparison of the observed orientation of the rotation axes between subgrains with the expected rotation-axis orientation for selected types of subgrain boundaries (table 4.2, fig 4.2) provided indirect evidence for the activity of specific slip systems. If the strength difference between samples 5072 and 5249 was caused by the activation of different dislocation slip systems it was expected that sample 5072 would show evidence for significant activity of the hardest slip system (010)[001]. This slip system produces rotation axes parallel to [100], while the dislocation microstructure in sample 5249 would be dominated by slip of the weakest slip system (010)[100] with rotation axes parallel to [001]. This hypothesis is not supported by the results. The orientation distribution of the subgrain rotation axes in sample 5072 showed maxima near [001] and [010] (fig 4.11). The strong maximum near [001] indicates that slip along the weak (010)[100] slip system was important, while the minor concentration of rotation axes close to the [010] direction may have been produced by tilt walls of the intermediate strength (100)[001] and (001)[100] slip systems or twist walls in the (010) plane. The girdle distribution of the rotation axes in the (100) plane in sample 5249 is indicative for activation of the (okl)[100] slip system (pencil glide) which included (010)[100] slip. Two preferential orientations can be recognised within the girdle. The rotation axis maximum that occurred near [021] suggests the presence of tilt walls of $\mathbf{b}=[a]$ dislocations in {012} prism planes and the maximum near [010] may originate from the intermediate strength (100)[001] and (001)[100] slip systems or twist walls in the (010) plane, similar to sample 5072. The evidence for the activation of the hard (010)[001] slip system in both samples, as provided by the TEM analysis, could explain the spread of the orientation data towards the [100] direction in figure 4.11 although no preferential orientation of rotation axes close to [100] was found with the SEM EBSD measurements. The occurrence of many rotation axes in apparently random orientations in both samples suggests that although there was a preference for certain orientations, many subgrain boundaries had intermediate orientations and may consist of dislocations of mixed edge-screw character.

The orientation variation of subgrain rotation axes was also present within single grains. From figures 4.13 and 4.15 it is clear that although the principal crystal axes show a consistent cumulative rotation in a transect across the crystals, dislocation slip systems were not activated homogeneously within grains and areas can be recognised where a single dislocation slip system was dominant and resulted locally in a uniform rotation axis. This implies that in a polycrystal, the activation of specific slip systems in the grains is not controlled only by the orientation with respect to the compression direction, but also on local stresses imposed by adjacent grains. This response is different from the activation of well-defined slip systems controlled by the compression direction in single crystal experiments. Minor variations in the initial crystal orientation with respect to the compression direction or variations in the local stress field caused by adjacent grains must produce regions in which different slip systems are activated. Subsequently clusters of subgrains with common rotation axes form within each of these regions. As a consequence, different areas within crystals in a polycrystalline aggregate will exhibit different strength during deformation depending on the neighbouring grains. This may be a cause for the strength of many polycrystalline aggregates to be intermediate to the end-member slip systems activated in single crystal experiments (see chapter 3, fig 3.3).

The scatter in the orientation of rotation axes determined in the SEM can be correlated with the variability of the dislocation microstructure as observed in the TEM. Particular dislocation microstructures are often confined to individual grains or adjacent subgrains and can greatly differ from the adjacent grains. This indicates that the orientation of the crystals with respect to the compression direction has only limited effect on the activation of specific dislocation slip systems in the individual grains in both samples. SEM measurements indicate a difference in the abundance of some rotation axis orientations. In sample 5072 rotation axes orientations show a maximum near $[001]$ indicating slip by $[100]$ dislocations on the (010) plane whereas rotation axes in sample 5249 show a maximum near $[021]$ suggesting dominant $[100]$ slip on prism planes. Intermediate strength dislocation creep involving slip along $(100)[001]$ and $(001)[100]$ and the formation of (010) twist walls occurs in similar magnitude in both samples. The observation that the weak $[a]$ -slip system is dominant in the stronger sample 5072 while it is only a minor slip system in the weaker sample 5249, is in contrast with the hypothesis proposed by Hirth & Kohlstedt (1995b) that the observed weakening of partially molten olivine-bearing rocks to a strength similar to single crystal $[a]$ -slip (such as sample 5249) is caused by the replacement of the hard $[c]$ -slip system by melt-enhanced grain boundary processes.

4.6 Conclusions

Deformation of the polycrystalline olivine (5072) and olivine-orthopyroxene (5249) aggregates in the dislocation creep field results in the formation of a non-uniform dislocation microstructure. Evidence was found of simultaneous activation of different dislocation slip systems in both samples, including the strongest and weakest olivine slip systems. The average density of $\mathbf{b}=[a]$ and $\mathbf{b}=[c]$ dislocations is comparable within the samples and both the dominant dislocation type

and crystallographic character of subgrain boundaries are highly variable, even within individual grains. The occurrence of different slip systems partitioned into different areas of deformed grains indicates that interactions with the adjacent grains have a larger influence on the activation of specific slip system than the externally imposed compression direction.

The main difference between the two samples is indicated by the orientation distribution of rotation axes that describe the rotation between low-angle boundaries. This points to a difference in activated slip systems in the two samples with the dominant slip systems being weak $(010)[100]$ slip in sample 5072 and intermediate strength $(okl)[100]$ slip in sample 5249. The activation of these slip systems together with the occurrence of similar densities of $\mathbf{b}=[a]$ and $\mathbf{b}=[c]$ dislocations in both samples does not provide an explanation for the observed strength differences between the two samples. The hypothesis that the strength differences between samples 5072 and 5249 is caused by the inactivation of the hard $[c]$ -slip deformation mechanism in sample 5249, in accordance with the weakening mechanism proposed by Hirth & Kohlstedt (1995b), is not supported by the observed dislocation microstructures.

It is concluded that the intracrystalline deformation processes considered in this chapter are not responsible for the strength differences between these partially molten rocks and that the rheological differences are likely to be related to processes along the grain boundaries.

Evidence for stable grain boundary melt films in experimentally deformed olivine-orthopyroxene rocks^{*}

5.1 Introduction

In nature, partially molten rocks are associated with a number of geologically important processes like the formation of granitic material (migmatization), volcanism, and melting beneath mid-ocean ridges. Next to these well-established occurrences, small amounts of partial melt may also cause the zone of low seismic velocities and attenuation of seismic waves in the upper mantle (Gutenberg 1954; Press 1959; Anderson & Spetzler 1970; Schmeling 1985; Green & Falloon 1998). If the observed attenuation and velocity decrease is caused by the presence of a melt phase, it is also possible that the viscosity of this layer is lower than that of the over- and underlying melt-free mantle regions. The layer can then act as decoupling horizon between the overlying plate motions and the underlying convecting mantle (Press 1959). Many experimental and theoretical studies have been conducted to establish the formation and distribution of the melt phase in a partially molten rock (e.g. Bulau *et al.* 1979; Seifert *et al.* 1982; Cooper & Kohlstedt 1986; Toramaru & Fujii 1986; Bussod & Christie 1991; Waff & Faul 1992; Faul 1997; Cmíral *et al.* 1998).

Studies that have concentrated on the rheological effect of the melt in partially molten materials have shown that as soon as the melt fraction exceeds about 4%, the strength of the rocks may decrease by an order of magnitude in both the dislocation and the diffusion creep field. This is attributed to complete wetting of a critical number of grain boundaries enabling easy grain boundary sliding (Pharr & Ashby 1983; Hirth & Kohlstedt 1995a, b; Bai *et al.* 1997). From studies of the connectivity of the melt phase in partially molten rocks, however, it follows that a fully interconnected melt network is already present at melt fractions below 1% (Waff & Bulau 1979; Von Bargen & Waff 1986; Bussod & Christie 1991) and that effective extraction of melt from the rock is established at 2–3% melt (Faul 1997). This may set a maximum melt content that can be retained within the host rock during partial melting in the upper mantle and although the strength reduction is not so profound as in materials with more than 4% melt, rocks with 2–3% melt

^{*} Most of the results presented in this chapter are published in:

De Kloe, R., Drury, M.R., Van Roermund, H.L.M. (2000). Evidence for stable grain boundary melt films in experimentally deformed olivine-orthopyroxene rocks. *Phys. Chem. Minerals* 27: 480-494.

exhibit a factor 3 to 5 increase in creep rate when compared to melt-free materials (Hirth & Kohlstedt 1995b). This lowers the strength of partially molten olivine polycrystals deforming in the dislocation creep regime to the level of the weakest olivine slip system, [a]-slip (010)[100] (Hirth & Kohlstedt 1995b). The exact mechanism that is responsible for this weakening is not known, but the observed reduction in strength suggests that the hardest olivine dislocation slip system, [c]-slip (010)[001], is replaced by another mechanism. A likely mechanism for the observed weakening is an enhancement of grain boundary processes, such as grain boundary sliding and grain boundary diffusion due to the presence of minor amounts of melt.

In this chapter the occurrence of melt along olivine-olivine grain boundaries is investigated in two samples from the study of Hitchings *et al.* (1989), samples 5072 and 5249 and two olivine-orthopyroxene samples from the suite of experiments carried out by Drury, samples 6213 and 6219 (see chapter 3). After deformation, samples 5072, 5249, and 6219 were statically annealed for 306, 219, and 136 hours respectively to assess the stability of the melt occurrences (see chapters 2 and 3). The term melt film is used in this chapter to describe films less than 5 nm thick. The physical properties of such films may be different to bulk melt because of the interaction of the surface forces from the adjacent crystal surfaces (Clarke *et al.* 1993; Hess 1994). Melt occurrences along grain boundaries with thickness larger than 5 nm and physical properties similar to bulk melt are called melt layers (see also Cmíral *et al.* 1998).

5.2 Background

The samples from Hitchings *et al.* (1989) are experimentally deformed partially molten olivine (sample 5072) and olivine-orthopyroxene (sample 5249) rocks with ~1% melt. The partially molten olivine sample exhibits a strength (chapter 3, fig 3.3) comparable to 'dry' fine-grained polycrystalline olivine (Karato *et al.* 1986), whereas sample 5249 is relatively weak and deforms with strength somewhat below that of olivine single crystals deforming by [a]-slip (chapter 3, fig 3.3). In a previous study on sample 5249, Drury & FitzGerald (1996) found some chemical evidence for the presence of nm-scale ultrathin films along grain boundaries of material that resembles the melt in the larger melt pockets. They inferred that the detected Ca-Al enrichment along the grain boundaries represents ultrathin 1-2 nm thick melt films with a composition similar to the melt in larger pockets. If such films are absent in the olivine material (sample 5072), their presence in sample 5249 could explain the weakening of the olivine-orthopyroxene material. Because Drury & FitzGerald (1996) analysed the grain boundary regions with an elongated electron probe with a size of 300 x 25 nm, they could not exclude the possibility that the Ca and Al enrichment was distributed within a wider zone along the grain boundary. In this study, a wider range of TEM techniques was used to determine if the chemical signature at the grain boundaries is definitely related to the occurrence of melt films or to solid state impurity segregation.

Based on the 1-6 μm separation of melt pockets in the recrystallized areas in sample 5249, equilibration times of 30-360 min were estimated (Drury & FitzGerald 1996) where the experimental duration was only 177 min. Therefore, it is possible that the microstructures had not

yet attained structural equilibrium. To test whether the observed structures in sample 5249 are transient, grain boundary microstructures are also studied in two samples that have been subjected to the elevated P-T conditions for longer times (samples 6213, 6219). These two samples are chosen because their composition and deformation histories are similar to 5249, although it should be noted that they have the same strength as single-phase olivine polycrystals (chapter 3, fig 3.3). In addition, the occurrence of thin melt films has also been investigated in the hot-pressed undeformed starting material (sample 5132) of one of the experimental runs (sample 5249). The deformation procedure of samples 6213 and 6219 consisted of a continuous process of hot-pressing and deformation. Therefore, the hot-pressed starting material for these two samples was not available for investigation. The electron microscopy techniques used in the analyses of olivine-olivine grain boundaries and the procedure for the long-duration annealing experiments are described in chapter 2. Details on the deformation experiments and a microstructural characterisation of all studied samples are given in chapter 3.

5.3 Results

In this section, the results are described by technique. The imaging produced comparable results for each of the three deformed samples. For each technique examples are shown from any of the olivine-orthopyroxene samples. Similar results have been obtained on the olivine sample 5072. Each technique has its own characteristics and allows different aspects of the melt microstructure to be studied. The techniques are ordered from structure-based to chemistry-based.

5.3.1 Diffuse dark field imaging

The μm -scale distribution of the melt phase in melt rich areas could be readily imaged using diffuse dark field imaging. Figure 5.1 illustrates the distribution of the amorphous phase in a melt-rich area in sample 5249. It shows three different types of melt occurrences: a triple junction, a four-grain junction, and a 300 nm thick melt layer next to a flat face. At higher magnifications, DDF images show bright lines emerging from the tip of melt pockets into grain boundaries (fig 5.2). This indicates the presence of an amorphous phase. The imaged width of this amorphous grain boundary film is approximately 3 nm. Similar features are observed in 120° triple junctions that are not associated with μm -scale melt bodies. Figure 5.3 shows a bright field image of such a triple

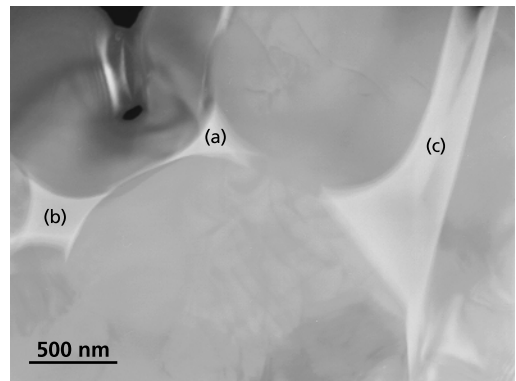


fig 5.1 TEM DDF image of three different types of melt pockets in sample 5249: (a) triple junction (b) four-grain junction (c) melt layer.

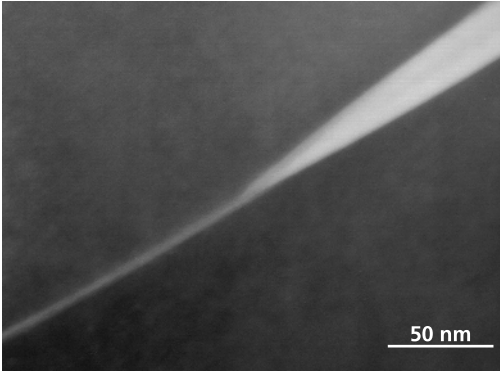


fig 5.2 TEM DDF image of the tip of a melt pocket illustrating the continuation of the melt phase as a thin film of amorphous material along the grain boundary. (sample 6219).

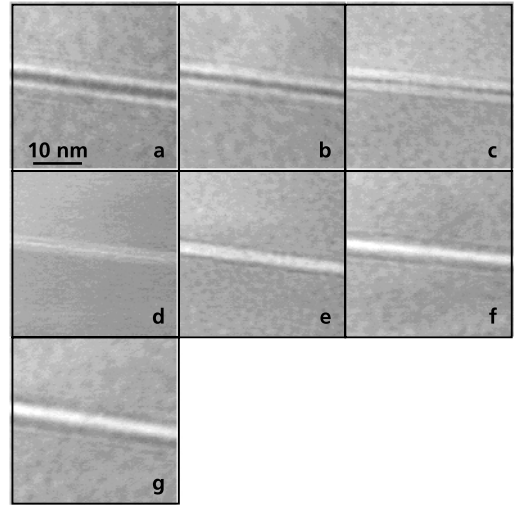


fig 5.5 Through-focus series Fresnel fringe images from a straight olivine-olivine grain boundary in sample 5249 oriented parallel to the electron beam. Defocus: a) -2300 nm; b) -1540 nm; c) -768 nm; d) 0 nm; e) 768 nm; f) 1540 nm; g) 2300 nm.

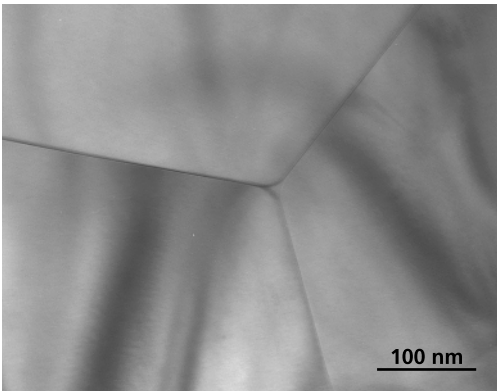


fig 5.3 Bright field TEM image of a well-equilibrated olivine triple grain junction that contains a small 10 nm wide melt tube along the intersection (sample 6219).

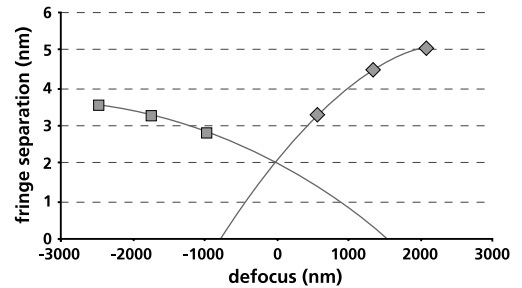


fig 5.6 Reconstruction of the thickness of the intergranular phase using the Fresnel fringe separation measurements in figure 5.5.

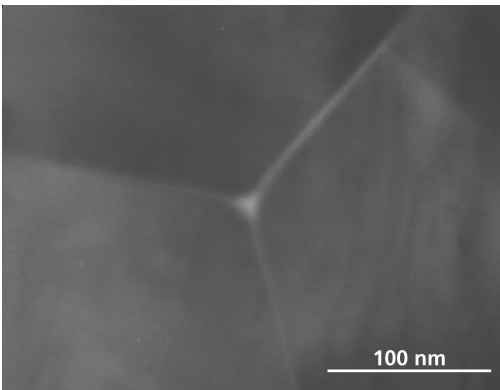


fig 5.4 TEM DDF image of the grain junction in figure 5.3. The amorphous character of the melt tube in the centre is confirmed by its higher intensity in the diffuse dark field image. Bright lines emerging from the melt-filled triple junction indicate the presence of thin amorphous films along the grain boundaries.

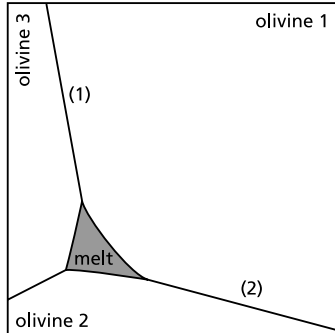
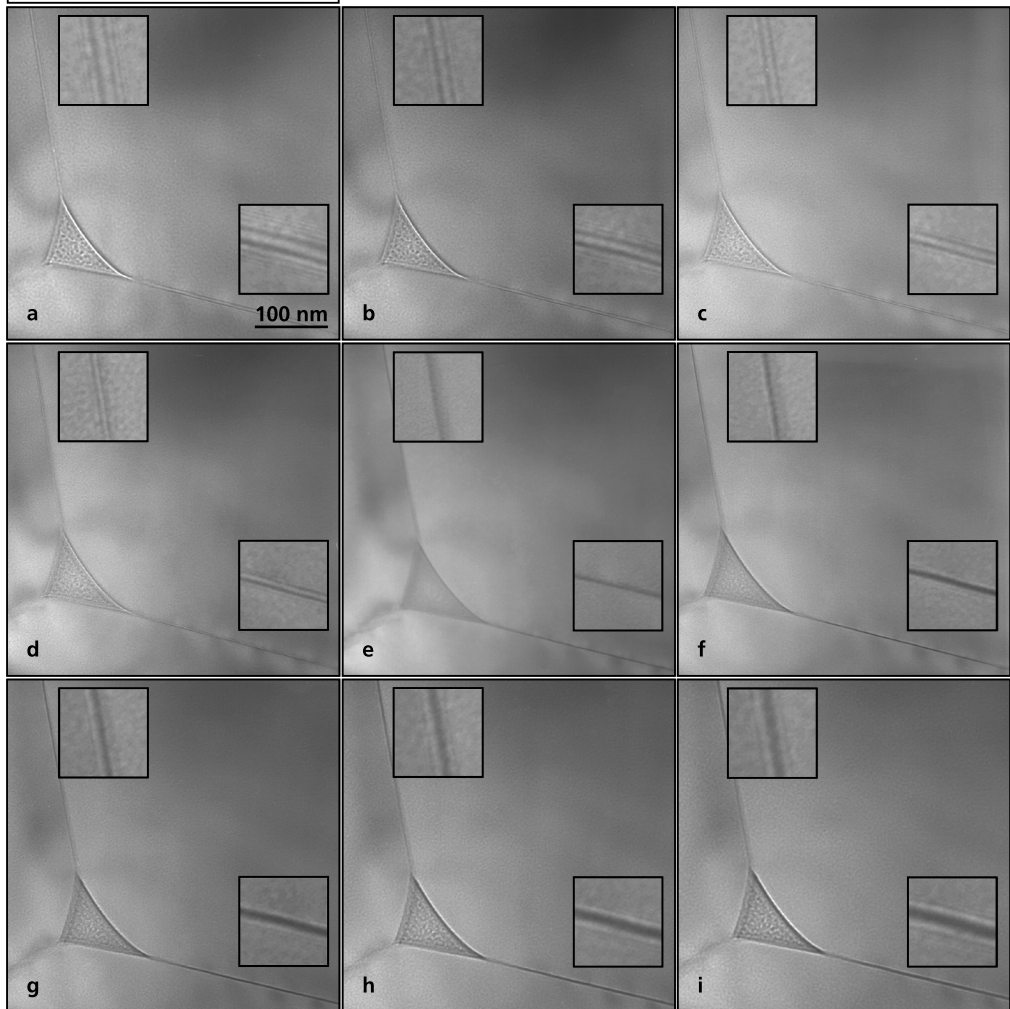


fig 5.7 Through focus series Fresnel fringe images from two straight olivine grain boundaries and a melt filled triple junction tube in sample 6219_2 (annealed for 136 hours). Reconstruction of the fringe separation to zero defocus indicated a film thickness of ~ 1 nm along grain interfaces (1) and (2). Note that along the olivine grain interfaces a double set of fringes is visible, where only one set of fringes is present along the crystal-melt interface. Defocus: a) -3070 nm; b) -2300 nm; c) -1540 nm; d) -768 nm; e) 0 nm; f) 768 nm; g) 1540 nm; h) 2300 nm; i) 3070 nm.



junction. The DDF image of the same area (fig 5.4) shows evidence for the presence of a 10 nm wide patch of amorphous material at the junction and thin films along the grain boundaries. The difference in imaged film width in this image is caused by the orientation of the grain boundaries that are not perfectly aligned parallel to the incident electron beam. The imaged grain boundary width on the diffuse dark field images is 2–3 nm.

5.3.2 Fresnel fringe imaging

Fresnel fringe images have been obtained at single grain boundaries and triple junctions that could be oriented parallel to the electron beam. In the small images (fig 5.5a–g), a through-focus series of a detail of one of the grain boundaries is given. The symmetric set of fringes indicates the presence of two parallel interfaces. When the fringe separation is plotted against defocus, the distance between the two interfaces can be reconstructed for zero defocus (fig 5.6). In these images, the extrapolation of the fringe separation to zero defocus results in a minimum distance of 2 nm between the two interfaces. This indicates the presence of an intergranular phase with a thickness of 2 nm. In 13 other series of FFI images in all the samples, the fringe separation varied between 1 and 2.5 nm. The compilation of FFI images in figure 5.7 indicates the presence of ultrathin grain boundary films along grain interfaces in sample 6219_2 after 136 hours annealing.

5.3.3 High resolution lattice fringe imaging

The imaging conditions that have to be met to image a possible intergranular phase while producing lattice fringes in both adjacent grains simultaneously, limit the number of grain boundaries that can be imaged. Most grain boundaries in olivine are curved and not parallel to a zone axis, which prohibits the imaging of multiple lattice fringes. Due to this curvature, thin films can often only be imaged over a small part of the grain boundary. The lattice fringe images in figure 5.8 have been taken from a single grain boundary while holding the specimen at a fixed

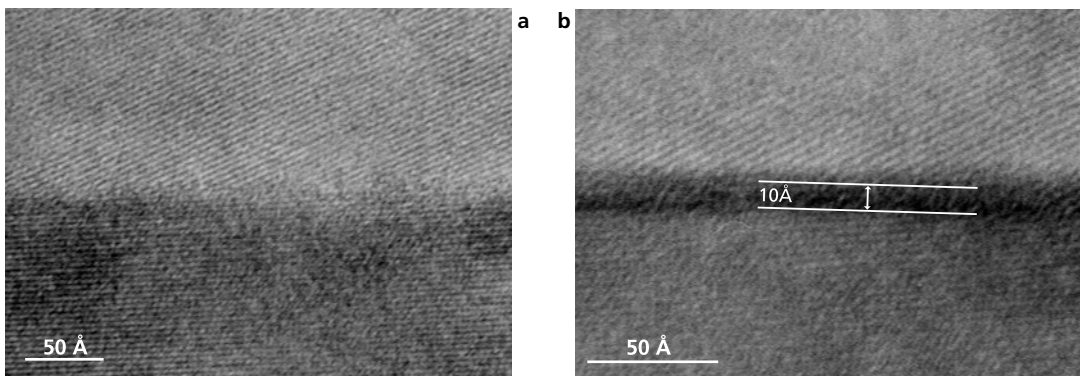


fig 5.8 Lattice fringe images of an irregular olivine-olivine grain boundary in sample 6219. Fringes in the upper grain are 3.9 Å (021) fringes, fringes in lower grain are 3.5 Å (111) fringes. Sample orientation in the TEM is the same for both images. In a) the fringes touch and locally overlap slightly along the grain boundary, indicating that the grain boundary is not parallel to the electron beam. This obscures the possible presence of an intergranular film along the grain boundary. In b) part of the same grain boundary is vertical and shows a 10 Å amorphous film.

orientation. Because the grain boundary interface is not planar, the grain boundary is slightly tilted with respect to the beam in figure 5.8a. This causes the fringes to overlap at the interface, thus obscuring any amorphous intergranular phase. Figure 5.8b shows another part of the same grain boundary and at the grain contact the fringes are now separated by a 1 nm thin film of amorphous material. When the grain boundary interface is (sub)parallel to a low-index crystal plane, the boundary can be planar. Observed film thickness along such boundaries appears to be constant (fig 5.9). Observed film thickness in high-resolution lattice fringe images of the deformed samples varies between 0.6 and 2.5 nm. Similar film widths were observed in the specimens after long-duration annealing (fig 5.10).

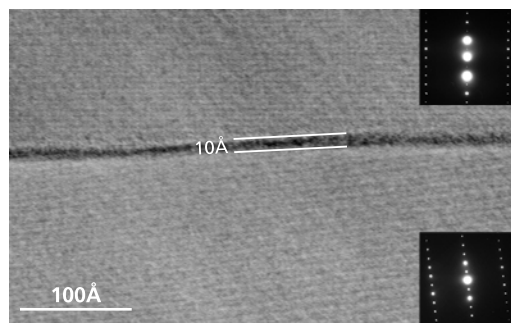


fig 5.9 Lattice fringe image of a vertical olivine-olivine grain boundary in sample 5249. The grain boundary is subparallel to the 5.1 Å (020) fringes in the upper grain, fringes in lower grain are 10.2 Å (010) fringes. A continuous 10 Å wide amorphous film is present along the whole boundary.

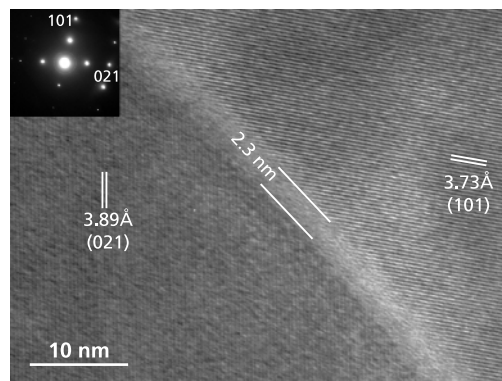


fig 5.10 Lattice fringe image of an olivine-olivine grain boundary in sample 5072_1 (annealed for 306 hours). Fringes in the grain on the left correspond to 3.89 Å (021) planes, fringes in the crystal on the right correspond to 3.73 Å (101) planes. Along the grain interface a 2.3 nm wide amorphous film is present.

5.3.4 EDX

EDX analyses have been performed both in the starting material for sample 5249 and in the four deformed samples. When a grain boundary region is analysed, two analyses of the adjacent olivine crystals are also made. This is because the additional signal that is derived from the grain boundary region is very small and cannot be reliably quantified. The easiest way to detect the small differences is by visual comparison of the spectra from the grain boundary region and the spectra from the adjacent olivine crystals. Figure 5.11 shows typical EDX spectra that are collected in an olivine grain and in a melt pocket. The amorphous phase is rich in Si, Al and Ca, whereas Mg and Fe are present in minor amounts. In the olivine, Ca and Al are not present above the detection limit of the EDX system.

Grain boundary analyses using a 3 nm spot size in the deformed samples show spectra comparable to those from the adjacent olivine but with small Al and Ca peaks and a slightly higher Si content (fig 5.12). When the spot is positioned directly next to the grain boundary, no Ca and Al is detected. For comparison, figure 5.13 shows the element intensities vs. sample thickness for the major elements of the grain boundary and olivine analyses, respectively. Because

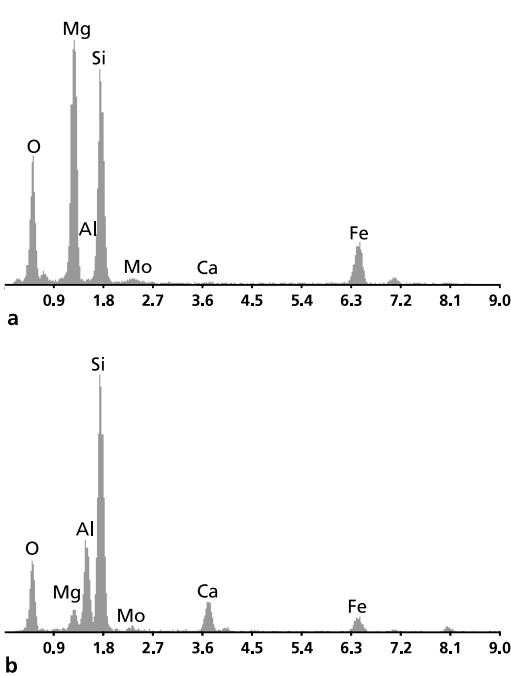


fig 5.11 a) Typical EDX spectrum for olivine, Al and Ca are not present in detectable amounts. The small Mo peak is the result from sample contamination during carbon coating. b) EDX spectrum of a larger melt pocket. The melt analyses are characterised by clear Al, Si, and Ca peaks with minor amounts of Mg and Fe.

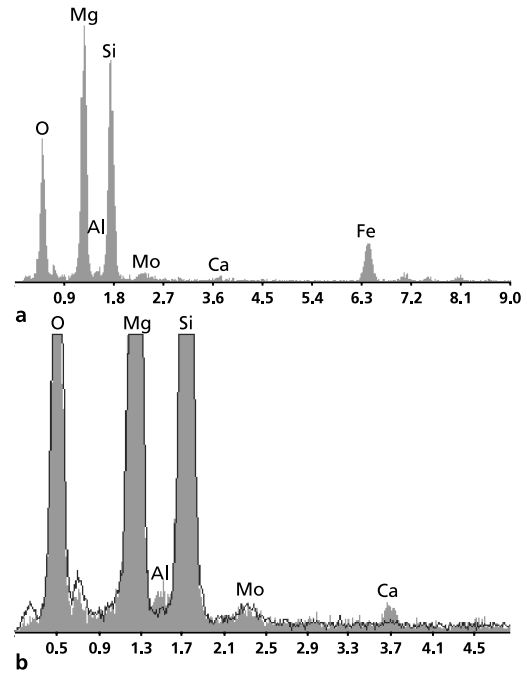


fig 5.12 a) EDX spectrum of a grain boundary analysis with small Al and Ca peaks. In b) the grain boundary analysis is superimposed on the spectrum of the adjacent olivine grain to illustrate the additional presence of Al and Ca in the grain boundary.

the difference is so small, the unprocessed X-ray intensity data are used here to avoid any additional errors related to the quantification procedure. There is no apparent difference in the intensities of O and Fe, but a small deviation is present for the Mg and Si intensity data of the grain boundary and olivine grain analyses, respectively. This minor difference in Mg and Si signal was not observed in the undeformed starting material. Individual spot analyses, however, show occasional Al and Ca enrichments on some grain boundaries. Figure 5.14 shows a triple junction with one grain boundary containing the Al and Ca enrichment, whereas the other grain boundaries appear free of an intergranular phase.

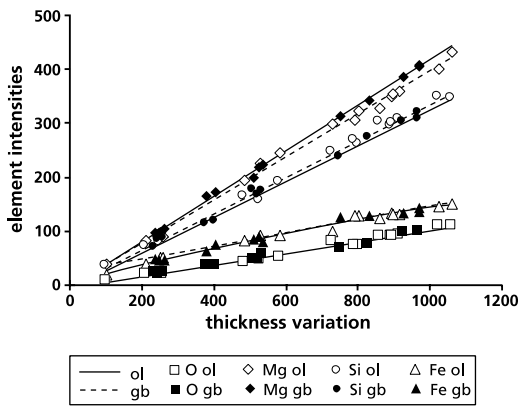


fig 5.13 X-ray intensities of the major elements plotted against specimen thickness. The arbitrary thickness scale is based on the total measured X-ray intensity per unit time for each analysis and is not quantified.

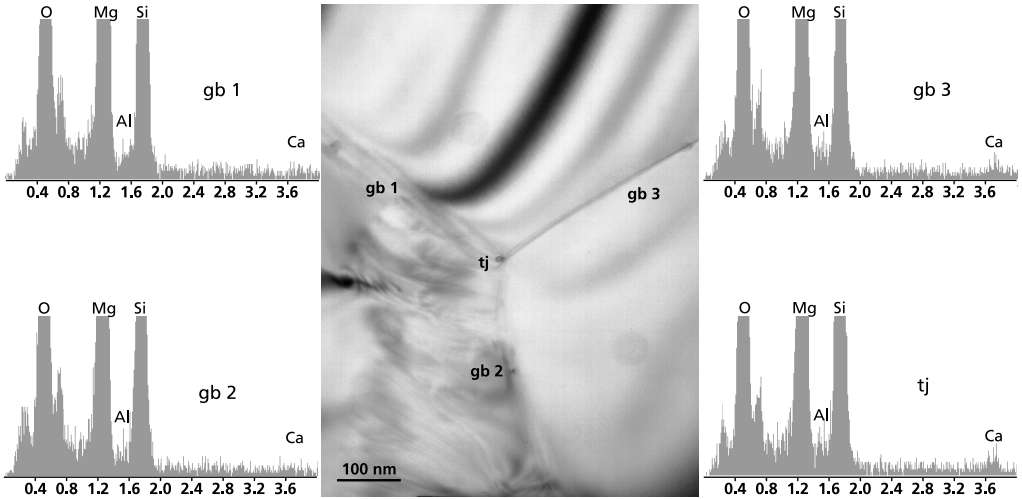


fig 5.14 EDX analyses of three olivine-olivine grain boundaries and the triple junction in between in the starting material of sample 5249, 5132. On the right the spectra for one of the grain boundaries (gb3) and of the triple junction (tj) show evidence for the presence of Al and Ca. This (slight) Al and Ca enrichment is absent in the spectra of the other two grain boundaries (gb1, gb2) on the left.

The Al and Ca intensities are too low to plot against specimen thickness in the same figure as the major elements. When the Al and Ca intensities from sample 5249 are plotted, the analyses from grain boundary areas, melt pockets and olivine crystals form linear trends (fig 5.15). For the grain boundary analyses the Ca/Al intensity ratio is 0.59, for the melt pocket analyses 0.26 and the olivine crystals show a Ca/Al intensity ratio of 0.03. A single analysis of a triple junction yields a Ca/Al ratio intermediate to the grain boundary and melt pocket analyses.

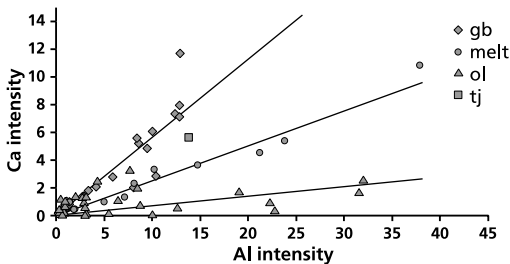


fig 5.15 Plot of the Ca and Al X-ray intensities in olivine crystals (ol), grain boundaries (gb), melt pockets (melt) and one triple junction (tj) in sample 5249. The intensity range is due to the varying specimen thickness for the different analyses.

5.3.5 Energy filtering imaging

The depletion of Mg with respect to Si along the grain boundaries was confirmed using energy filtering imaging on an area in sample 5249. Figure 5.16a shows the EFI image using the Mg signal. The image shows three olivine crystals enclosing a melt-filled triple grain junction. The melt pocket can be recognised by the low Mg signal. A faint dark line emerges from this melt pocket along the grain boundary of olivine grains 1 and 2 (fig 5.16a). The other grain boundaries are not oriented parallel to the electron beam. Similar images prepared from the Si, Fe, Ca and Al

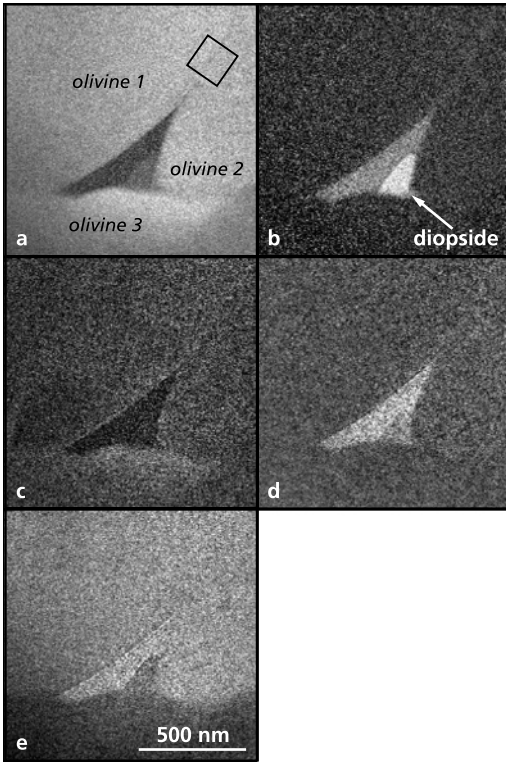


fig 5.16 Energy filtering images of three olivine crystals surrounding a melt pocket in sample 5249. Inside the melt pocket a diopside crystal is present (fig 5.16 b). a) Mg jump ratio image b) Ca element map c) Fe jump ratio image d) Al jump ratio image e) Si jump ratio image.

signal (fig 5.16b-e) show the Ca and Al enrichment of the melt phase and the Si and Fe depletion that goes along with the Mg depletion in the melt pocket. The Ca and Al concentrations along the grain boundary were too low to be imaged by this method. The integration of Mg intensity profiles taken perpendicular to boundary 1-2 shows a depression of the Mg signal along the grain boundary (fig 5.17) with a width of 7.5 nm. As the grain boundary is slightly curved, this depression illustrates the maximum width of a grain boundary interphase with deviating composition. In the Ca image a diopside crystal can be recognised as a bright phase inside the melt pocket (fig 5.16b).

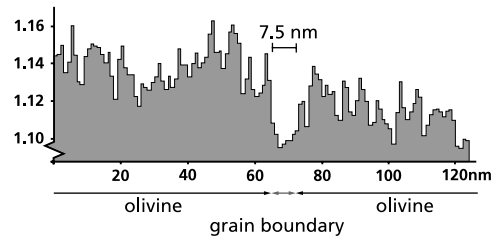


fig 5.17 Integrated Mg intensity profile perpendicular to boundary 1-2 (area within square on fig 5.16a). The gradual decrease in intensity to the right is related to thinning of the sample area.

5.4 Discussion

The techniques that are applied in this work give information about the structure and chemistry of the grain boundary region. The analytical methods to obtain chemical information include EDX and EFI. These methods have been applied only to olivine-olivine grain boundaries because the compositional difference between the olivine and the orthopyroxene crystals would make a direct interpretation of the grain boundary chemistry impossible. If the grain boundary regions contain an ultrathin film, an EDX spectrum obtained with a 3 nm spot can be expected to be a mixture of an olivine and a melt spectrum (Kohlstedt 1990), which makes quantification difficult. The EDX results show that along the grain boundary in the deformed samples there is enrichment in Al and Ca and an increased Si/Mg ratio. This would be expected if the grain

boundary phase has a composition similar to the melt in the larger triple junctions. There are indications, however, that the grain boundary composition is not the same as the melt composition. The Al/Ca intensity ratio (fig 5.15) from analyses of both occurrences indicates that grain boundary areas have a relatively higher Ca content. The origin of this discrepancy is not clear. Occasional diopside crystals observed in some melt pockets (fig 5.16b) and quench modification of the melt may account for the difference. Another explanation could be element volatilisation. During analysis it was attempted to minimise the volatilisation of elements in the target area, but the Al and Ca concentrations are near the detection limit of the EDX system used and it was hard to tell whether the EDX signal changed during spectrum acquisition.

Also the Si enrichment has to be interpreted with care. When other elements disappear from the target area, Si is left behind and may cause an increase in Si content in the analysis (Champness & Devenish 1990). If this caused the change in Mg/Si ratio, it is expected to occur in all grain boundary analyses. However, in the starting material for sample 5249, sample 5132, many grain boundaries did not show evidence for such Si enrichment, which implies that the Mg/Si ratio changes along grain boundaries are not analytical artefacts. This is supported by the Mg depletion detected along an olivine-olivine grain boundary by EFI. With this method, no element loss is expected as the images are obtained at low magnification with a defocused electron beam. Although EDX cannot give information about the structure of the occurrence, a maximum width of the Ca-Al enrichment can be deduced from the used spot size of 3 nm. Only analyses that were positioned exactly onto the grain boundary showed evidence for the intergranular phase. This confines the Al-Ca enrichment to a zone less than ± 3 nm wide along the grain boundary, which is in agreement with the width of the Mg depletion observed with EFI.

All imaging techniques based on the structural differences of the amorphous grain boundary films supported the presence of a thin intergranular phase, as indicated by the chemical methods. These techniques have been extensively used in grain boundary studies in ceramics (e.g., Cinibulk *et al.* 1993b). Although they are more powerful in direct imaging, they are also more 'vulnerable' to contamination and imaging artefacts. The easiest (and fastest) methods are diffuse dark field and Fresnel fringe imaging. As shown, these techniques reveal the presence of an amorphous phase along the grain boundaries and give a good indication of the scale of the features of interest. However, artefacts that can be introduced during specimen preparation are easily misinterpreted as being ultrathin grain boundary films. The resulting images can be explained by preferential etching of grain boundaries that results in a grain boundary groove filled with amorphous material produced during ion beam thinning or carbon coating (Rasmussen *et al.* 1989). Positive discrimination between artefacts and grain boundary films when using DDF or FFI has to be done by supplementary chemical analysis. Unequivocal evidence of the presence of a grain boundary film can only be obtained using the last technique: high-resolution or lattice fringe electron microscopy. This technique can give direct information about the relationship between the adjacent crystals and may visualise the exact width of a grain boundary interphase.

In summary, the easiest way to check for the presence of a grain boundary phase is by using EDX analyses. This technique can be applied to most grain boundaries and then confirmed with a limited number of high-resolution electron microscopy images. The chemical and structural

imaging techniques are complementary. Taken together, these methods indicate that there are ~ 1 nm thick amorphous films along some olivine–olivine grain boundaries in the undeformed starting material and along all analysed olivine–olivine grain boundaries in the deformed olivine–orthopyroxene and olivine samples.

These observations confirm the hypothesis postulated by Drury & FitzGerald (1996) that the observed Ca and Al signals along olivine–olivine grain boundaries in olivine–orthopyroxene materials represent ultrathin nm-scale melt films. Similarly, Cmíral (1998) and Cmíral *et al.* (1998) have found chemical evidence for the presence of ultrathin melt films along grain boundaries in olivine samples with added basalt that were annealed for several hundred hours. However, in two earlier studies by Vaughan *et al.* (1982) and Kohlstedt (1990) no direct evidence was found to support the presence of such ultrathin melt films. Both studies were concerned with olivine–olivine grain boundaries in the same isostatically hot-pressed olivine–basalt samples. Vaughan *et al.* (1982) used TEM imaging techniques similar to those applied in this work and Kohlstedt (1990) reports the results of EDX analyses of the olivine–olivine grain boundaries. Although the diffuse scattering and phase contrast images from Vaughan *et al.* (1982) do not exclude the possibility that films thinner than 2 nm are present, this is not supported by TEM lattice fringe imaging. These images (figures 5 and 12 from Vaughan *et al.* (1982)) show irregular grain boundary interfaces with lattice fringes that locally touch each other or slightly overlap at the interface. No amorphous material can be recognised along the grain boundary. The images illustrate one of the major problems in the direct imaging of possible grain boundary films along olivine–olivine grain boundaries that was also encountered in the present study. These grain boundaries are not parallel to low-index crystallographic planes and even at the high magnifications of the micrographs it is clear that the grain boundaries are not planar. Additional chemical analyses of the grain boundaries by Kohlstedt (1990) provided no evidence for the presence of a grain boundary interphase in this olivine–basalt material.

The added melt fraction in the samples studied by Vaughan *et al.* (1982) and Kohlstedt (1990) consisted of 10 μm grains of a natural basalt with known composition. A consequence of the *in situ* melting in the present samples is that the source grains for the melt and the final melt composition are not exactly known. It is expected that the majority of the Al and Ca in the melt in the olivine–orthopyroxene samples is derived from the orthopyroxene crystals. This is supported by the observation of Al-free orthopyroxene rims and recrystallized orthopyroxene grains in sample 5249 (Drury & FitzGerald 1996) and the presence of rounded melt-filled pores in the centre of some orthopyroxene crystals (see chapter 3, fig 3.4a) which indicates partial melting (Doukhan *et al.* 1993; Falloon *et al.* 1999). However, it cannot be excluded that small fragments of spinel or clinopyroxene remained in the starting powders after mineral separation and produced melt during hot-pressing. The latter would also provide a possible source for the Al and Ca occurrence in the olivine sample 5072.

The composition of the melt in a partially molten rock has a pronounced effect on the melt distribution (Kohlstedt 1990). Therefore compositional differences of the melt phase in the olivine–orthopyroxene materials studied here and the olivine–basalt samples studied by Vaughan *et al.* (1982) and Kohlstedt (1990) may prevent the formation of grain boundary films in the latter

samples. Although this is a distinct possibility it does not account for the detection of Ca and Al along grain boundaries in similar olivine-basalt materials studied by Cmíral (1998) and Cmíral *et al.* (1998). It cannot be excluded that films were actually present in the samples of Kohlstedt (1990) but remained undetected. A possible reason could be rapid element loss during irradiation or difficulties in the exact positioning of the electron beam on the grain boundary.

The occurrence of films in samples 6213 and 6219 which were held at P-T conditions longer than the estimated equilibration times together with the observation of thin films after long-duration annealing, suggests that the films are stable. Most of the melt pockets present at three intersecting olivine-olivine high-angle grain boundaries are bounded by at least one crystallographically controlled flat face (e.g., chapter 3, fig 3.4b), similar to the microstructures described by Faul (1997) and Cmíral (1998). When flat faces are absent, the microstructure that is developed shows continuously curving crystal-melt interfaces and 120° angles between the straight grain boundaries (fig 5.3), which points to the grain boundary structure being in structural equilibrium. Other experimental work, however, indicates that microstructural equilibrium is achieved only after 2-3 weeks at 1300-1400°C for the larger-scale melt microstructures like triple grain junctions at the intersection of three high-angle grain boundaries and wide low-aspect ratio melt layers along grain boundaries (Faul 1997). The chemical identification of melt films along grain boundaries in static long-duration experiments on olivine-basalt samples by Cmíral (1998) and Cmíral *et al.* (1998) is also strong evidence that melt films are a stable feature of the microstructure. The absence of the intergranular films along many grain boundaries in the starting material for sample 5249 suggests that either hot-pressing was too short to form films along all olivine-olivine grain boundaries or that the formation and distribution of the films is actively promoted by deformation.

In the olivine-orthopyroxene rocks studied, the composition points to the films being either a melt product from the initial Al and Ca bearing orthopyroxene, or derived from the melting of spinel or clinopyroxene impurities that might have been present before hot-pressing. A contribution from the segregation of impurities from the cores of olivine grains into the grain boundaries upon heating and deformation is also possible. The presence of a Si-enriched phase along the olivine-olivine grain boundaries suggests a similarity with the ultrathin films in Si_3N_4 ceramics. In these ceramics, the grains are coated with a thin rim of oxidised material, SiO_2 (Kleebe *et al.* 1994b) and this layer, together with the sintering aids, forms a thin melt film upon hot-pressing. This mechanism implies that the films form during hot-pressing of the olivine-olivine samples. This is not supported by the EDX analyses of the starting material, where many grain boundaries are melt-free. It also does not explain the presence of higher concentrations of Al and Ca along the grain boundaries. Alternatively, stress-induced kinetic decomposition has been proposed by Wolfenstine & Kohlstedt (1994) as a mechanism to form grain boundary films. Grain boundaries at high angles to the principal stress become enriched in SiO_2 and a Mg and Fe enrichment occurs at the 'relaxed' grain boundaries. The EDX analyses do not support this mechanism in the samples studied here. The Si enrichment has been found on all grain boundaries in the deformed material independent of the orientation with respect to the maximum compressive stress. Furthermore, it does not give an explanation for the occurrence of excess Al

and Ca along the grain boundaries at a ratio different from that in the larger melt pockets. The occurrence of the excess Ca with respect to Al in the grain boundaries when compared to the melt in larger pockets might be caused by preferential diffusion of Ca from the melt pockets or segregation of Ca impurity atoms from the olivine interiors onto the grain boundaries. However, the latter mechanism cannot be verified, as it is not possible to analyse the trace amounts of Ca in olivine in the TEM, and the interaction volume during microprobe analysis is too large to allow for the detection of Ca concentration differences in the core and rims of the olivine grains.

It is proposed that relaxation of the interface tension of certain olivine–olivine grain boundaries is the driving force in the formation of thin melt films during the static part of the experiments. Deformation can subsequently distribute the films by grain boundary sliding and subgrain rotation recrystallization. When grain boundary sliding occurs in a partially molten rock, it is feasible that upon sliding an adsorbed melt layer is ‘dragged’ along the boundary. With subgrain rotation, it is likely that the growing crystallographic misfit along the subgrain boundary facilitates diffusion or infiltration of the melt phase into the subgrain boundary, thus forming a film or layer with deviating composition along the newly formed grain boundaries.

What is the effect of these films on the rheological behaviour of mantle rocks? Within each of the studied samples, the overall melt content is the same, ~1%, but locally the melt content may be as high as 5 vol%. Experiments on olivine samples with similar melt contents showed that the creep rate is three to five times higher than in melt-free samples (Hirth & Kohlstedt 1995b). A similar weakening is observed between samples 5072 and 5249 that were deformed in the dislocation creep field, although both contain a small melt volume. If this strength difference were related to the unique occurrence of ultrathin melt films in the olivine–orthopyroxene material, then films should be absent in the olivine samples. Melt films, however, are found in all studied samples and the longer duration olivine–orthopyroxene runs (samples 6213, 6219) deform with strength similar to the fine-grained olivine deformed at the same conditions. A possible cause for the different mechanical behaviour is that the melt phase and the grain boundary films in the studied samples are of different composition. Such compositional variation will affect the viscosity and the kinetics of diffusion through the melt phase (Bottinga & Weill 1972) and provided that diffusion through the melt phase contributes significantly to the deformation, differences in melt composition may account for the differences in mechanical behaviour. Hitchings *et al.* (1989) attributed the observed weakening in sample 5249 with respect to the olivine samples to the presence of orthopyroxene, although the study of Mackwell (1991) indicates that enstatite would be stronger than olivine in the dislocation creep regime at 1200–1250 °C. This suggests that the addition of orthopyroxene could actually increase the strength of an olivine–orthopyroxene aggregate, which has recently been confirmed by Mackwell *et al.* (1999). The weak olivine–orthopyroxene sample 5249 has similar strength to fine-grained olivine samples containing 3–5% basalt (Hirth & Kohlstedt 1995b). This suggests that this olivine–orthopyroxene sample may be affected by melt weakening. The occurrence of melt films in both strong and weak samples implies that the presence of grain boundary films does not influence the strength of these samples. Any melt-induced weakening must therefore be related to the larger scale melt network of tubes and layers.

It should be noted that grain boundary melt films are likely to be present in the nominally melt-free samples of many experimental studies on olivine. Hirth & Kohlstedt (1995a), for example, mention the presence of 0.5–1 vol% melt in their nominally melt free samples, which compares to the melt fraction in the current samples. To determine to what extent grain boundary melt films influence olivine rheology, data on completely melt-free samples are required. McDonnell *et al.* (1999) synthesised melt free forsterite_(97.5%)-enstatite_(2.5%) rocks and found their samples to be 1 to 2 orders of magnitude stronger than the extrapolated strength of synthetic samples manufactured from natural powders (Fo₉₀) deforming by diffusion creep. This strength difference could be related to the effect of FeO (McDonnell *et al.* 1999) or may possibly be explained by the weakening effect of melt films in the Fo₉₀ samples of Karato *et al.* (1986).

5.5 Conclusions

The grain boundary structure of olivine-olivine grain boundaries in experimentally deformed olivine and olivine-orthopyroxene rocks has been investigated. Along the grain boundaries a chemically distinguishable phase occurs in the form of ultrathin, 1–3 nm thick films of amorphous material with a composition comparable to the melt phase found in larger pockets. These grain boundary films completely wet the olivine-olivine grain boundaries in the deformed rocks and may influence the deformation behaviour of the samples by enhancing grain boundary diffusion and grain boundary sliding. In the undeformed material the films are not present along all boundaries. Either they need more time to develop than the available 1 hour during hot-pressing, or deformation is required to distribute the films. The occurrence of films in samples heated longer than the estimated equilibration time and in samples after 136 to 306 hours annealing, implies that melt films are stable in these samples.

The presence of melt films apparently does not significantly influence the strength of the olivine and olivine-orthopyroxene samples investigated in this study, although it is possible that samples containing melt films (i.e. all samples from this study) are weaker than completely melt-free material. The weakening observed in one olivine-orthopyroxene sample may therefore be attributed to the effects of the larger, micrometer-scale melt network. However, it cannot be excluded that, if differences in grain boundary film composition affect the kinetics of grain boundary diffusion, films do influence rheology.

Subgrain controlled melt topology in experimentally deformed upper mantle rocks

6.1 Introduction

The melt phase in partially molten rocks is primarily distributed in tubes along intersections of three or more grains, as layers or isolated melt bodies along grain boundaries, and in larger melt interserts between several grains (e.g. Vaughan *et al.* 1982; Bussod & Christie 1991; Beeman and Kohlstedt 1993; Faul *et al.* 1994; Jin *et al.* 1994). The melt in a partially molten rock influences processes such as diffusion and chemical alteration of the host rock during melt transport and thereby causes weakening of the host rock depending on the amount of melt that can be attained in the rocks and its distribution. Dihedral angle measurements indicate that a fully interconnected melt network forms in olivine at melt fractions below 1% (Waff & Bulau 1979; Bussod & Christie 1991; Von Bargen & Waff 1986), although it is estimated that effective extraction of the melt from the host rock may not occur until the melt fraction exceeds 2–3% (Faul 1997). Therefore, small fractions of a partial melt can be retained in the host rock, providing fast diffusion pathways along the grain edges. The efficiency of diffusion through the melt network depends on the distance that diffusing species must travel along virtually dry grain boundaries between adjacent melt bodies. In the case of a melt distribution primarily along grain edges, the spacing of the melt bodies is determined by the grain size. Considering the enhancement of grain boundary kinetics in the presence of a fluid phase (e.g. Watson 1991; Kohlstedt & Zimmerman 1996), any additional stable melt occurrence along grain interfaces is expected to significantly affect the rheology of partially molten rocks.

The ultrathin melt films along high angle grain boundaries that were characterised in chapter 5 (Drury & FitzGerald 1996; Cmíral *et al.* 1998; De Kloe *et al.* 2000) represent one type of melt feature that may occur along high angle grain boundaries. Another type of sub-micrometer scale melt body, which occurs at the intersection of subgrain boundaries with high angle grain boundaries, has also been recognised. This second type of melt body has occasionally been reported (Cooper & Kohlstedt 1982; Drury & FitzGerald 1996; Cmíral *et al.* 1998), but the overall influence of subgrain boundaries on the melt distribution in polycrystals has not been considered in detail. However, the association of melt occurrences with dislocation microstructures implies that these melt bodies can play an important role during deformation. The melt pocket separation along high angle grain boundaries, independent of the grain size, would be greatly reduced by the presence of a secondary sub-micron scale melt network associated with subgrain boundaries.

In this chapter, the occurrence and morphology of such subgrain boundary melt bodies is investigated in the undeformed starting material of sample 5249, sample 5132 (olivine-orthopyroxene) and in three of the deformed samples, 5072 (olivine), 5249 (olivine-orthopyroxene), and sample 6219 (olivine-orthopyroxene), to assess whether or not the observed strength differences reported in chapter 3 may be related to differences in the subgrain-related melt microstructures in these samples. The stability of the observed melt features was tested by analysing samples 5072_1, 5249_1, and 6219_2 after annealing in a controlled atmosphere furnace operating at atmospheric pressure for 306, 219, and 136 hours, respectively. The designation subgrain is used for recognisable crystal parts, separated by dislocation arrays that may accommodate crystallographic misorientations up to 10° . Grain boundaries with higher misorientation and lacking a dislocation array will be referred to as high-angle grain boundaries (Hull 1975; White 1976).

6.2 Imaging and measurement techniques

The sub-micrometer scale melt features associated with dislocation structures were imaged with a Philips CM200FEG transmission electron microscope using conventional bright field imaging and weak beam dark field imaging (see chapter 2). The morphology of the melt bodies in contact with subgrain boundaries and individual dislocations was characterised by measuring the size of the melt pockets and the solid-melt dihedral angle at the melt-subgrain boundary intersection on bright field electron micrographs. In order to allow accurate measurement of these features, it was attempted to orient both the subgrain boundary and the adjacent high angle grain boundary parallel to the electron beam. The influence of crystallographic misfit, accommodated by subgrain boundaries, on the shape of associated melt pockets was investigated by determining the subgrain misorientation angle.

Crystallographic misorientation measurements were performed using convergent beam electron diffraction patterns (Steeds & Morniroli 1992), recorded with a low camera-length of 253 mm (see appendix C and fig 6.9). The convergent beam diffraction mode coupled with the low camera-length, when compared to the 1000 mm used for standard diffraction patterns, allowed for the imaging of Kikuchi-bands similar to those present in electron backscatter patterns (EBSP) in the SEM (Steeds and Morniroli 1992). The shape and symmetry of these Kikuchi patterns can be used for the exact determination of the orientation and location of the centre of a zone-axis (Randle 1992). By orienting an olivine crystal parallel to a low-index zone-axis on one side of a subgrain boundary and subsequently collecting CBED patterns on both sides of the subgrain boundary, the shift and rotation of the Kikuchi patterns over the subgrain boundary could be determined. The resulting patterns were scanned into a computer and the shift and rotation of the pattern centre, with respect to a fixed reference point on the micrographs, was measured. With the known camera-length, the shift and rotation of the centre of the patterns in the two images were used to calculate the minimum rotation angle between the two crystal parts. The accuracy of this measurement technique was estimated to be on the order of 0.5° . Details of the method are given in appendix C.

6.3 Results

Backscattered SEM imaging of the deformed samples showed a melt microstructure that was characterised by small tubes along triple junctions, larger melt interconnects in recrystallised areas and some melt volumes along grain boundaries (fig 6.1). Triangular melt pockets in the SEM images (fig 6.1, 6.2) were commonly found at junctions of three or more grains. Locally elongated

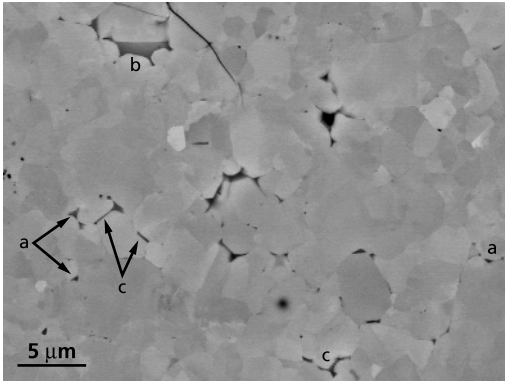


fig 6.1 SEM backscatter image of the melt distribution in sample 5072 (a) triangular melt tubes in triple grain junctions (b) melt interconnect extending along several grains (c) melt layers at grain interfaces.

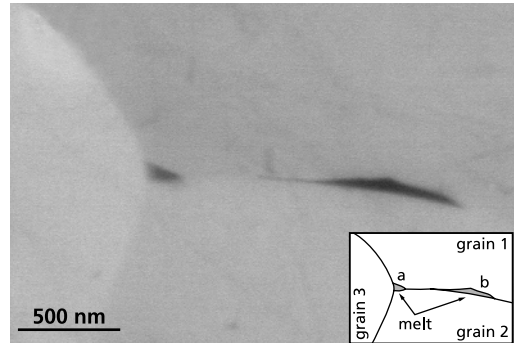


fig 6.2 SEM backscatter image of two types of triangular melt pockets in sample 6219 (a) melt tube in triple junction (b) elongated triangular melt pocket along the boundary between two grains.

triangular melt bodies were also observed along grain interfaces (fig 6.2). Their shape suggested that they were influenced by a planar feature within the adjacent olivine crystal. Because the internal structure of such “indented” olivine grains is not visible with SEM backscatter imaging of polished specimens, these features were studied with transmission electron microscopy. TEM imaging revealed that elongated triangular melt bodies along grain interfaces, similar to those observed with scanning electron microscopy (e.g. fig 6.2), occurred at the intersection of dislocation arrays or subgrain

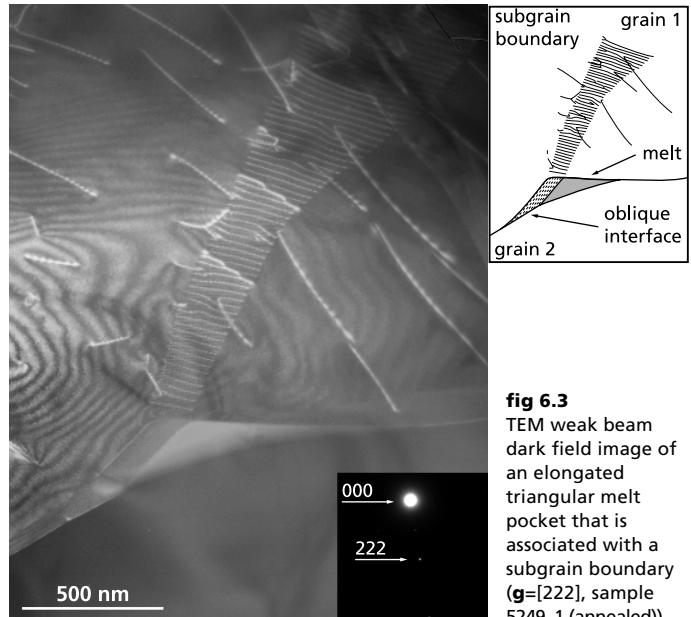


fig 6.3 TEM weak beam dark field image of an elongated triangular melt pocket that is associated with a subgrain boundary ($\mathbf{g}=[222]$, sample 5249_1 (annealed)).

boundaries with high-angle grain boundaries, away from a melt-filled triple junction (fig 6.3). The melt formed a cusp at the subgrain boundary contact while the opposite interface of the triangular melt pocket remained unaffected (fig 6.3). The size of these subgrain boundary melt bodies was highly variable and data on the morphology of these melt occurrences in both

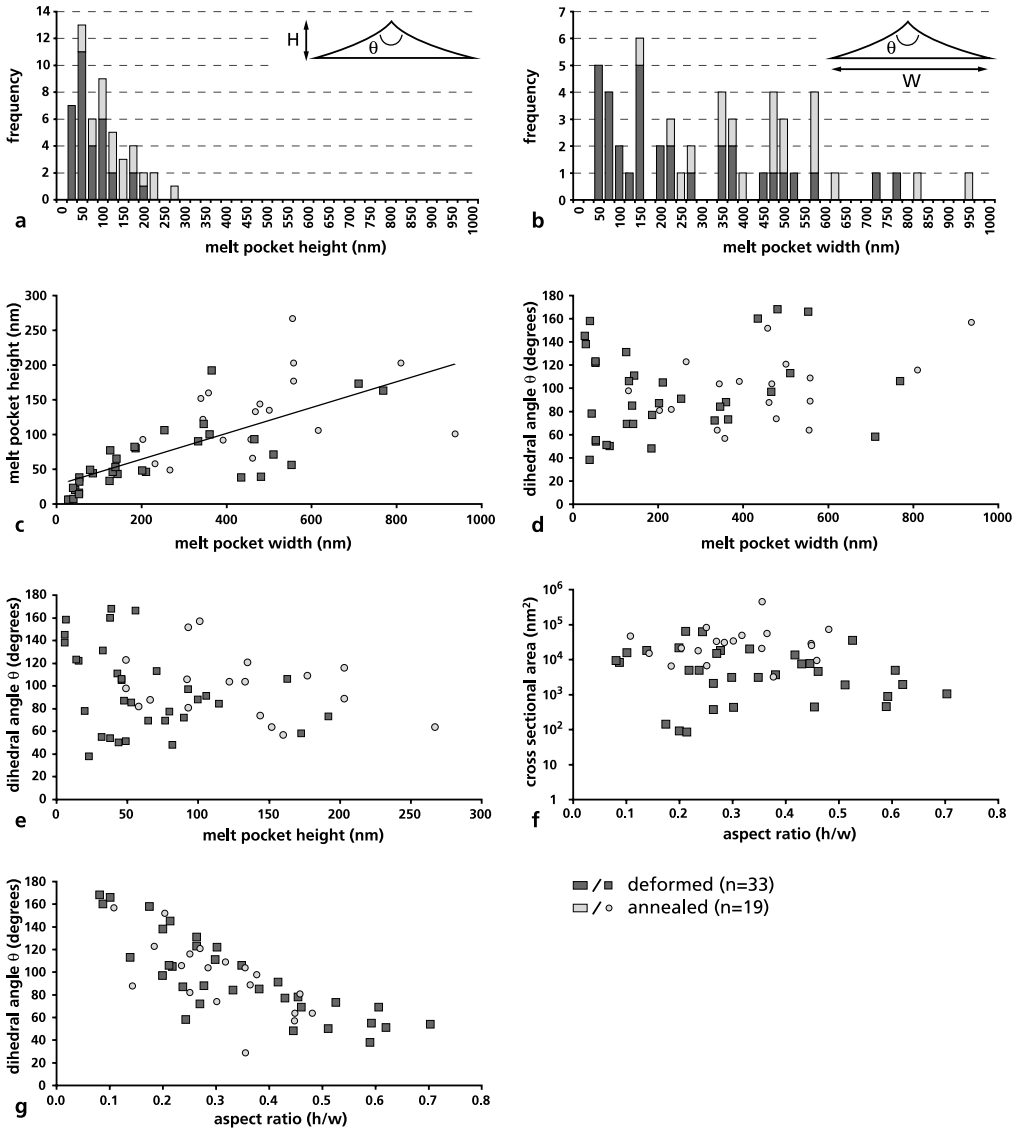


fig 6.4 Characteristics of the subgrain boundary melt bodies in both deformed (dark symbols) and annealed specimens (light symbols). (a) frequency distribution of the height of the melt pockets (b) frequency distribution of the width of the melt pockets (c) melt pocket height vs. width (d) dihedral angle θ vs. melt pocket width (e) dihedral angle θ vs. melt pocket height (f) cross sectional area vs. melt pocket aspect ratio (g) dihedral angle θ vs. melt pocket aspect ratio.

deformed and annealed specimens are presented in figure 6.4. The accuracy of the melt pocket size measurements depended on the magnification of the micrographs on which they were measured but measurement errors were estimated to average around 10 nm. The cross-sectional area was determined by approximating the subgrain boundary melt bodies by triangles and using the measured height and width to calculate the area. Dihedral angle measurements are accurate within 10° .

The height of the subgrain boundary melt bodies in cross-section was typically on the order of 100 nm (fig 6.4a) whereas the width measured along the base of the subgrain boundary melt bodies ranged from 15 nm to $1\ \mu\text{m}$ (fig 6.4b). In general, the height of the melt bodies increased with the width (fig 6.4c). The size of the subgrain boundary melt bodies was not related to the dihedral angle at the subgrain boundary-melt intersections (fig 6.4d, e) and no relation between the aspect ratio and the cross-sectional area of the subgrain boundary melt bodies was observed in any of the samples (fig 6.4f). The aspect ratio (height/width), or elongation, of the subgrain boundary melt pockets did show a relation to the dihedral angle at the subgrain boundary-melt intersection (fig 6.4g) with the aspect ratio decreasing, or the elongation of the melt pockets increasing, with increasing dihedral angle. Overall, the subgrain boundary melt pockets in annealed samples have characteristics similar to those in the deformed materials, but tended to be slightly larger. In addition to the occurrence of

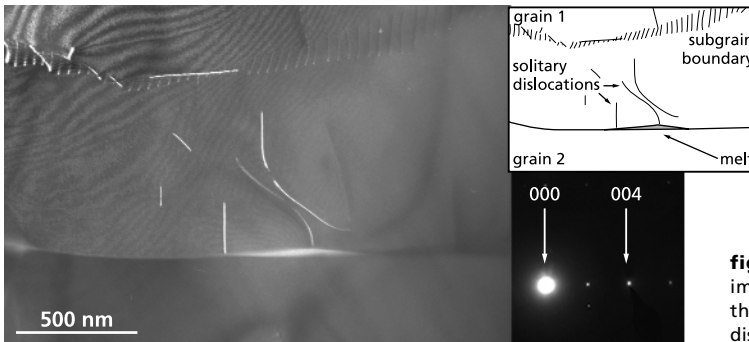


fig 6.5 TEM weak beam dark field image of an elongated melt pocket that is associated with a solitary dislocation ($\mathbf{g}=[004]$, sample 5249).

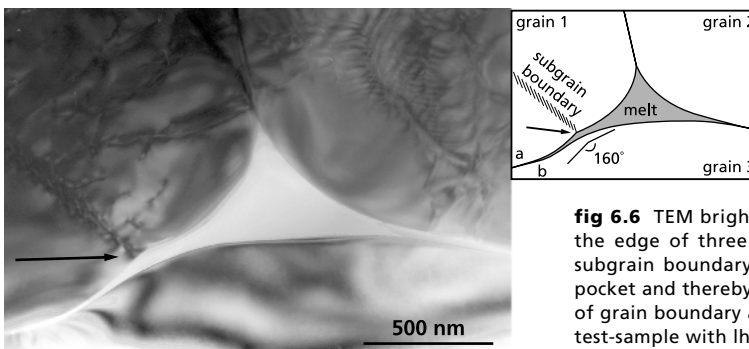


fig 6.6 TEM bright field image of a melt body along the edge of three olivine grains. On the left side a subgrain boundary is visible that intersects the melt pocket and thereby enables additional wetting of part of grain boundary a-b. This example was taken from a test-sample with Iherzolite composition (sample 5598) that was not studied in further detail.

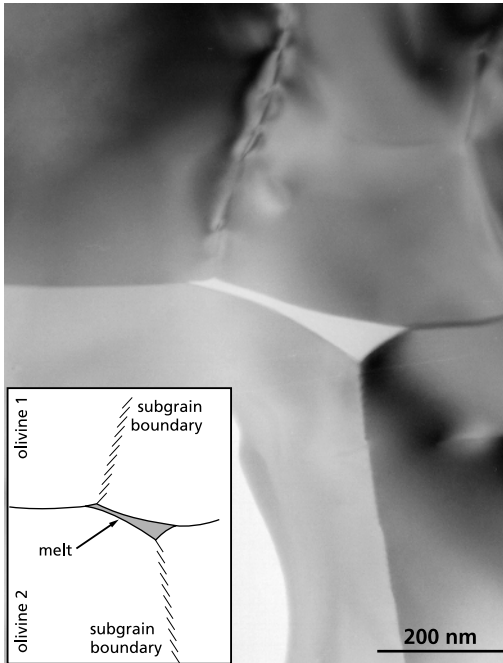


fig 6.7 TEM bright field image of a melt pocket associated with two subgrain boundaries extending into adjacent olivine grains (sample 5072).

The observed dihedral angles at such melt–subgrain boundary intersections were not affected by the size of the triple junction melt pockets in contact with the subgrain boundaries. Because the location of the elongated melt bodies along high angle grain boundaries depended on the presence of subgrain boundaries, melt bodies associated with subgrain boundaries from adjacent olivine crystals also occurred. Figure 6.7 shows a melt body that was associated with two subgrain boundaries from opposite olivine grains. The shape of the melt volume suggested that it was formed by the merging of two (~ 100 nm and ~ 200 nm wide respectively) triangular melt bodies, similar to the one shown in figure 6.3. Similarly, elongated melt bodies associated with closely spaced subgrain boundaries within a single olivine crystal were observed to form 10 to 30 nm thick melt layers along high angle grain boundaries (fig 6.8).

elongated triangular melt bodies at the intersection of subgrain boundaries, or dislocation arrays, with high-angle grain boundaries, occasional isolated melt pockets also occurred where individual dislocations intersected high angle grain boundaries (fig 6.5).

The shape of the larger triple junction melt tubes and melt layers were also affected by the presence of a subgrain boundary–high angle grain boundary intersection. Figure 6.6 shows three olivine crystals with a triangular melt pocket at the triple junction. In one of the grains a dislocation array, defining a subgrain boundary, was present that intersected the melt pocket (arrowed). The melt formed a cusp at the subgrain boundary, thereby forming a dihedral angle of 160° at the melt–subgrain boundary contact. The occurrence of the subgrain boundary resulted in the melt extending further along the high-angle grain boundary, producing a 20 nm thick melt layer along part of that boundary.

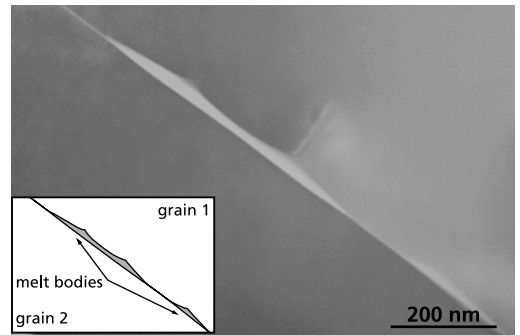


fig 6.8 TEM diffuse dark field image showing three closely spaced subgrain boundary melt pockets along a high angle olivine-olivine grain boundary. The spacing between the upper two melt pockets is so small that they have merged (sample 6219).

As the dihedral angle and thus the connectivity of the melt phase in a partially molten rock is determined by the interfacial energies (e.g. Kingery *et al.* 1976; Bulau *et al.* 1979; Watson 1982; Cooper & Kohlstedt 1986; Toramaru & Fujii 1986; McKenzie 1989; Wanamaker & Kohlstedt 1991), the misorientation of subgrain boundaries would also influence the shape of any associated melt bodies because the energy of subgrain boundaries increases with misorientation (Read & Shockley 1950). To establish the influence of the subgrain misorientation on the dihedral angle, the misorientation was measured using convergent beam electron diffraction patterns (CBED) (Appendix C). The accuracy of the CBED method used was tested on two subgrain boundaries. In figure 6.9 two parts of an olivine crystal are separated by a composite subgrain boundary that is composed of three lower misorientation tilt walls. The presence of several subgrain boundaries prohibited ideal weak beam conditions in the whole image, therefore it is not known whether the subgrain boundaries were composed of $\mathbf{b}=[a]$ or $\mathbf{b}=[c]$ dislocations. The spacing of the dislocations in subgrain boundaries a, b, and c was 63 nm, 24 nm, and 33 nm respectively.

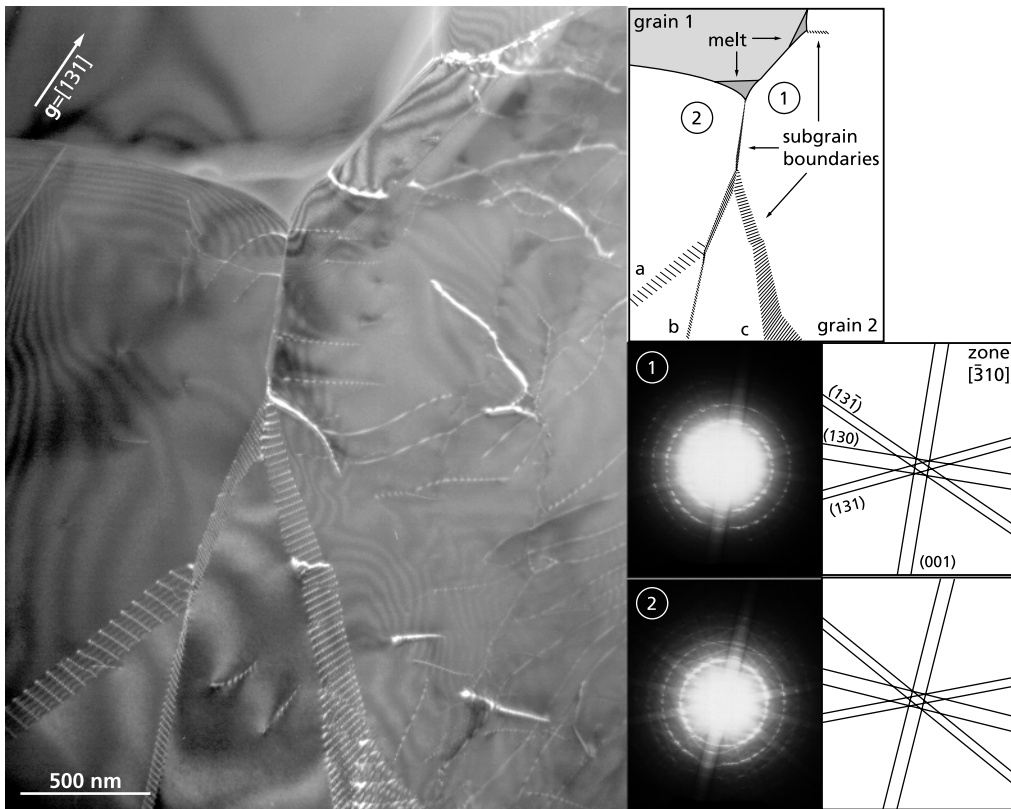


fig 6.9 TEM weak beam dark field image of subgrain boundaries that are associated with a melt pocket ($\mathbf{g}=[131]$) along a high angle grain boundary. The three subgrain boundaries in the lower part of the micrograph combine near the melt pocket and accommodate the combined rotation of 2.3° . The small rotation and displacement of the convergent beam electron diffraction patterns taken along the zone $[310]$ (inset) illustrate the total misorientation of 2.3° (sample 5072_1, annealed).

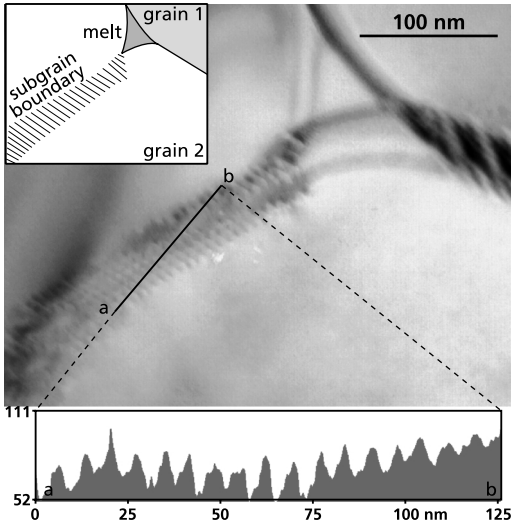


fig 6.10 TEM bright field image of a subgrain boundary in contact with a melt body. The fringe pattern represents the dislocation microstructure of the boundary. The fringe or dislocation spacing was determined using the intensity profile along the line indicated in the micrograph. The average fringe spacing is 6.9 nm.

and three annealed samples (olivine 5072_2, olivine-orthopyroxene 5249_1, and olivine-orthopyroxene 6219_2) (fig 6.12). Cooper & Kohlstedt (1982) estimated the interface energies for the olivine-melt interface and two common types of tilt walls composed of either $\mathbf{b}=[a]$ or $\mathbf{b}=[c]$ dislocations with line direction $[010]$. These estimates were used to determine the dihedral angle - subgrain misorientation relation for a partially molten olivine rock that is shown as a shaded area in the graphs (fig 6.12). The dashed curves plotted in figure 6.12 depict calculated misorientation-dihedral angle relationships for different solid-liquid interface energies and will be addressed in the discussion. Measured misorientations in all specimens ranged from $\phi=0.2^\circ$ to $\phi=11.6^\circ$, although the latter misorientation has not been included in figure 6.12 as it was not clear if that boundary could still be considered as a subgrain boundary (see also fig 6.16a, b). In the undeformed olivine-orthopyroxene starting material, sample 5132,

Assuming continuous rotation along the subgrain segments, this corresponded to 0.4° , 1.1° , and 0.8° with a total misorientation of 2.3° for $\mathbf{b}=[a]$ dislocations and 0.5° , 1.4° , and 1.0° with a total misorientation of 2.9° for $\mathbf{b}=[c]$ dislocations. CBED analysis of the misorientation over the composite boundary yielded a rotation of 2.3° (fig 6.9). A single subgrain boundary composed of $\mathbf{b}=[c]$ dislocations is shown in figure 6.10. The dislocations had an average spacing of 6.9 nm. This corresponded to a misorientation of 5.0° . Measurement of the rotation over the same boundary using CBED patterns resulted in a misorientation of 5.4° . From these analyses, an error of 0.5° was estimated for the CBED measurements.

The relation between subgrain misorientation and subgrain-melt dihedral angle (fig 6.11) was measured in the hot-pressed material (olivine-orthopyroxene 5132), two deformed samples (olivine 5072, olivine-orthopyroxene 5249)

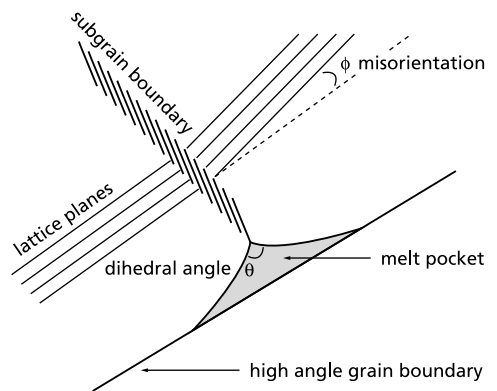


fig 6.11 Schematic drawing of a subgrain boundary with an associated melt body. The measured parameters, the crystallographic misorientation across the subgrain misorientation and the solid-melt dihedral angle are indicated.

the misorientations ranged from 0.8° to 8.7° . All solid-melt dihedral angles larger than 80° were associated with subgrain boundaries with misorientations lower than 3° , whereas smaller dihedral angles were associated with misorientations that ranged from 0.9° to 8.7° (fig 6.12b). The dihedral

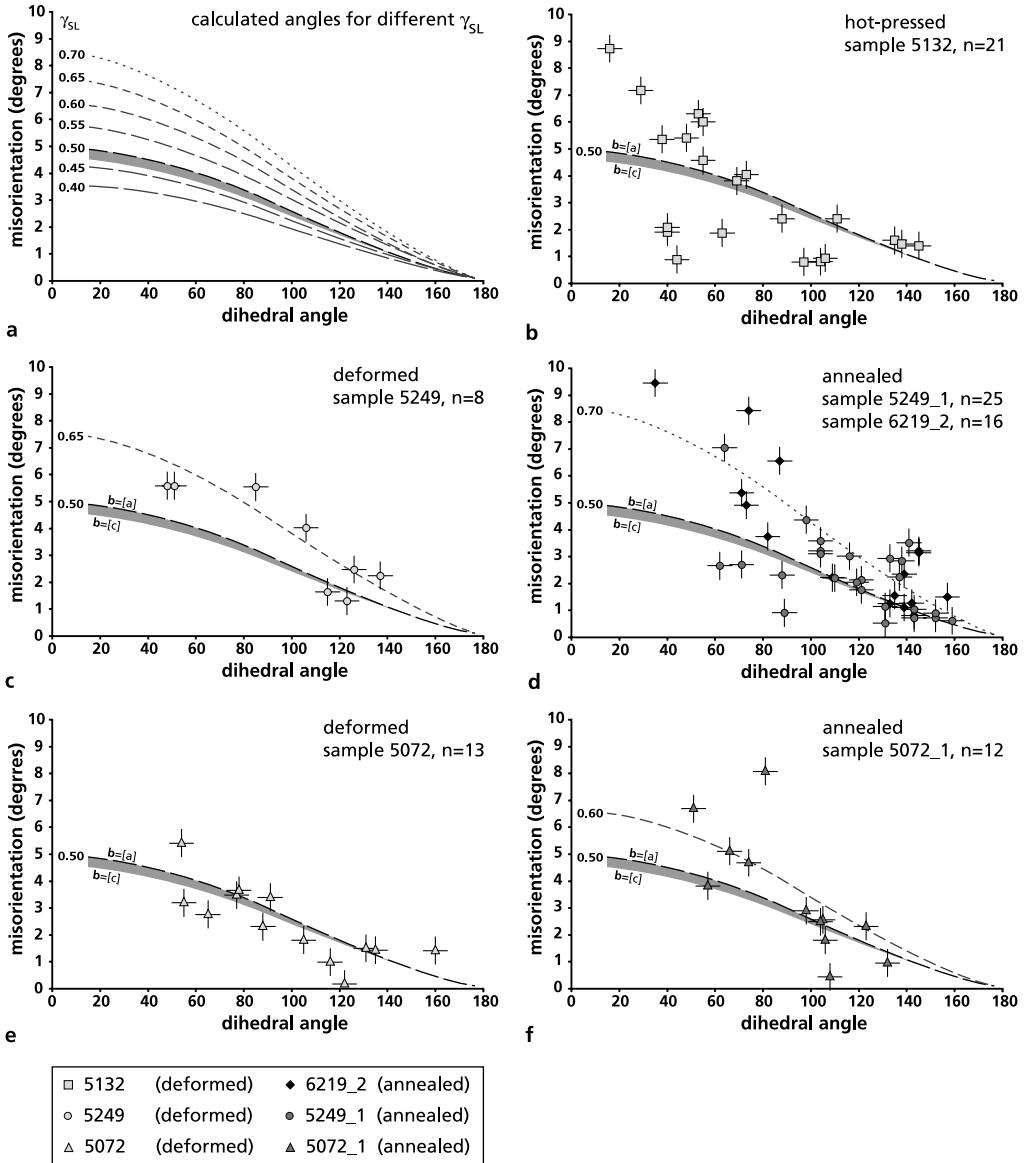


fig 6.12 Subgrain boundary misorientation measurements versus the solid-melt dihedral angle at the subgrain-melt intersection. The curves in (a) depict predicted misorientation-dihedral angle relationships for arbitrary values of the interface energy γ_{SL} . The shaded curve is based on the interface energy estimates for tilt boundaries that consist of either $b=[a]$ or $b=[c]$ dislocations with line direction $[010]$ from Cooper & Kohlstedt (1982). (b) sample 5132 (c) sample 5249 (d) samples 5249_1 & 6219_2 (annealed) (e) sample 5072 (f) sample 5072_1 (annealed).

angles in the deformed olivine-orthopyroxene specimen, sample 5249, ranged from 48° to 137° and consistently decreased with increasing misorientation (fig 6.12c). Most of the measurements in figure 6.12c plotted above the shaded curve that is based on the energy estimates from Cooper & Kohlstedt (1982). In the olivine material, sample 5072, the measured dihedral angles ranged from 55° to 160° and also showed a consistent decrease with increasing misorientation (fig 6.12e). In contrast to the measurements from sample 5249, the measurements plotted close to the shaded curve. Long-duration annealing of fragments of the deformed samples (see chapters 2 and 3) produced a larger scatter in the misorientation-dihedral angle plots (fig 6.12d, f), but the general trend of decreasing dihedral angle with increasing misorientation remained both in the olivine-orthopyroxene samples (fig 6.12d) and in the olivine sample (fig 6.12f). Overall, the cross-sectional shape of the melt bodies changed from elongated with aspect ratios 1:10 for subgrain boundaries with mis-orientations smaller than 2° to more equi-dimensional with aspect ratios 1:2 when the misorientation over the subgrain boundary exceeded 4° (see fig 6.4, 6.12).

In addition to the melt occurrences around grains, occasional nm-scale melt bodies associated with subgrains have been observed inside olivine crystals in the hot-pressed starting material. These melt bodies were related to intersections of three subgrain boundaries with misorientations

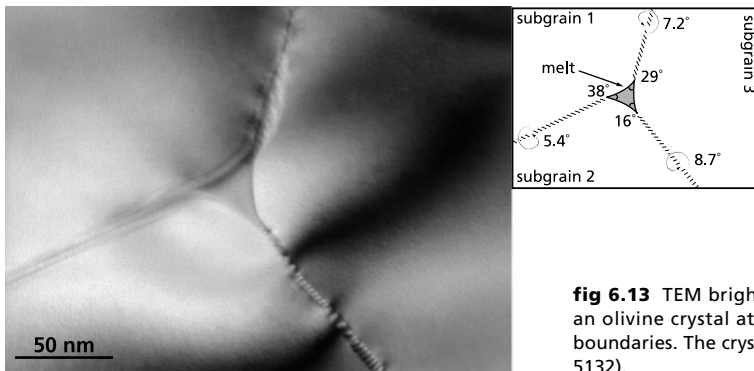


fig 6.13 TEM bright field image of a melt body inside an olivine crystal at the intersection of three subgrain boundaries. The crystal-melt contacts are curved (sample 5132).

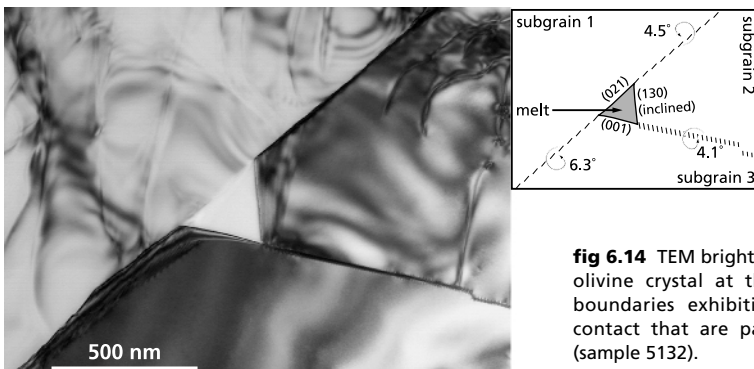


fig 6.14 TEM bright field image of a melt body inside an olivine crystal at the intersection of three subgrain boundaries exhibiting flat faces at the crystal-melt contact that are parallel to low-index crystal planes (sample 5132).

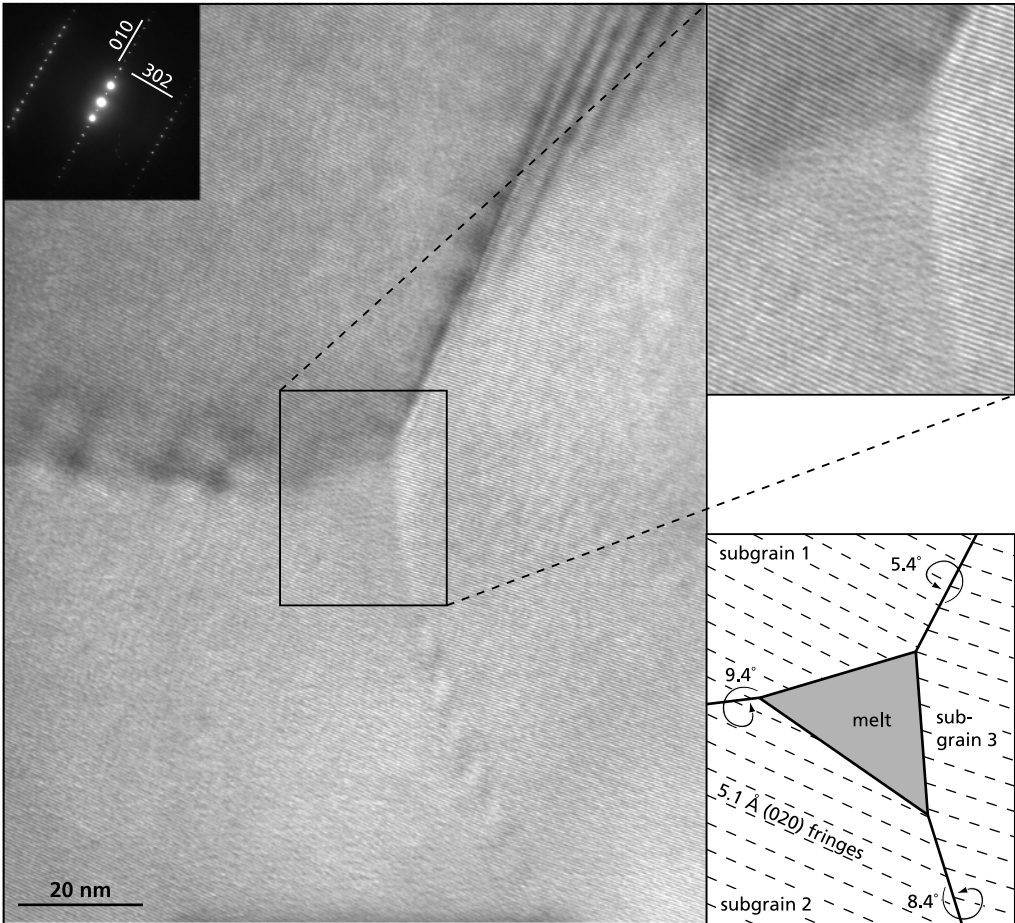


fig 6.15 TEM high resolution lattice fringe image of a melt body inside an olivine crystal in sample 6219_2 after 136 hour annealing. Fringes in all subgrains are 5.1 Å (020) fringes. The subgrain boundaries are not vertical in the entire image. Where the subgrain boundaries are inclined, the overlapping lattice fringes give rise to Moiré fringes.

exceeding 4° . The morphology of these melt volumes inside grains was similar to the melt pockets at the intersections of three high-angle grain boundaries. The internal melt bodies showed either continuously curving crystal melt interfaces (fig 6.13) or exhibited planar interfaces parallel to specific low-index crystal planes that commonly form flat faces in contact with melt (Drury & Van Roermund 1989; Jung & Waff 1998), in this case (001), (021) and (130) (fig 6.14). The diameter of the observed melt bodies ranged from 20 to 200 nm. Such melt occurrences at the intersection of three subgrain boundaries inside an olivine crystal have not been found in the deformed samples, although a similar melt body was found in the olivine-orthopyroxene sample 6219_2 that was deformed and subsequently annealed for 136 hours (fig 6.15).

A more complicated microstructure that occurs at the intersection of several subgrain boundaries inside olivine crystals is shown in figure 6.16a. In this micrograph, two melt pockets

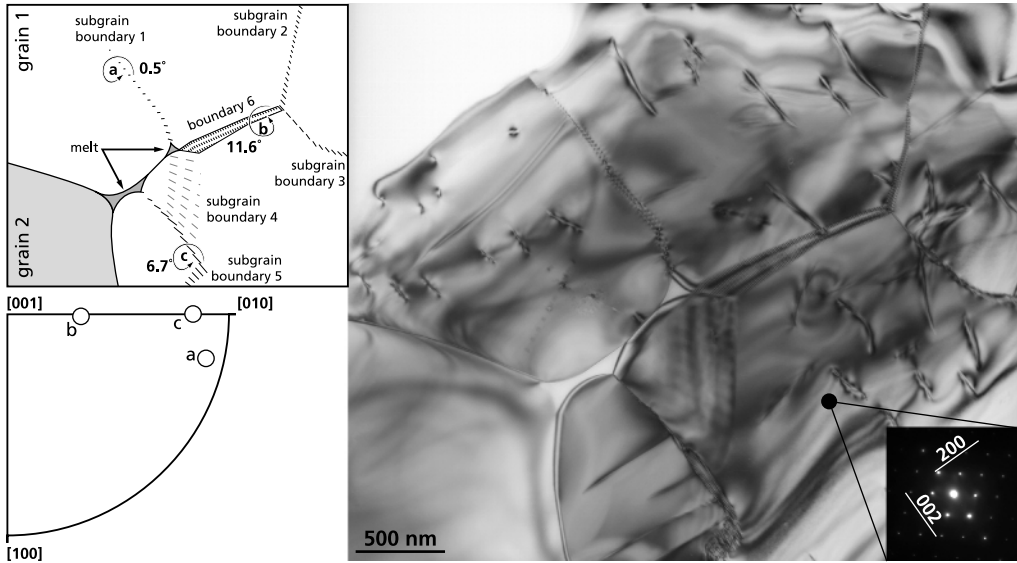


fig 6.16 a TEM bright field image of melt bodies incorporated within a single olivine grain. The orientations of the rotation axes of the three (subgrain) boundaries that are in contact with the melt bodies are given in an inverse pole figure. The misorientations of these three boundaries are indicated in the drawing. For discussion see text (sample 5072_1 (annealed)).

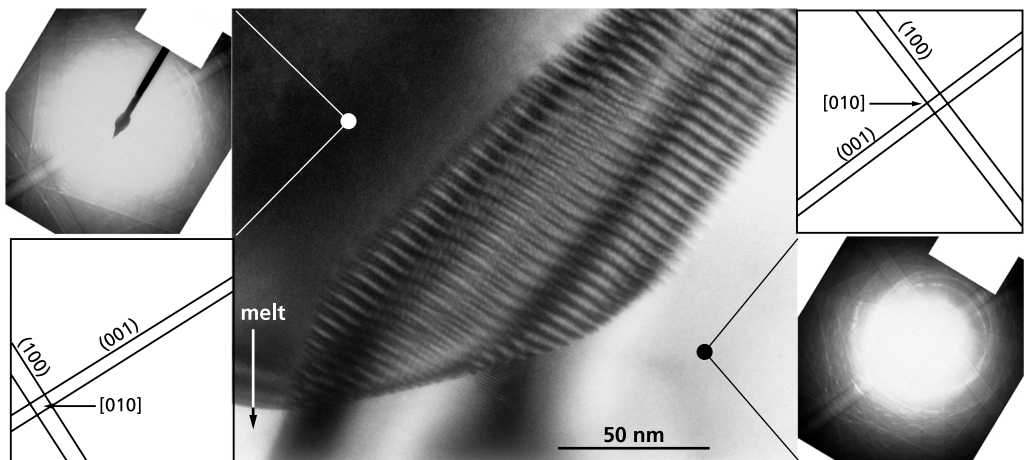


fig 6.16 b Detail of the fringe pattern of boundary 6 from figure 6.16a. The misorientation of 11.6° over the boundary is illustrated by the shift of the centre of the CBED patterns (sample 5072_1 (annealed)).

are enclosed within a single olivine crystal that also contained a number of subgrain boundaries. Both melt bodies have one or more subgrain boundaries associated with them and the shape of the smaller triangular melt body on the right, that is bounded by boundaries 1 and 6 and one high angle boundary, suggested that it formed inside the olivine grain at the intersection of three subgrain boundaries. This microstructure was further characterised by determining the misorientations and rotation axes of the three subgrain boundaries that intersected with both melt bodies (see drawing in figure 6.16a). Boundary 6 accommodated the largest rotation, 11.6° , with subgrain boundaries 1 and 5 accommodating 0.5° and 6.7° respectively. The rotation axes for subgrain boundaries 1 and 5 and boundary 6 were calculated using the method outlined in chapter 3 and appendix C and are given in the inverse pole figure in figure 6.16a. The axes for subgrain boundary 1 (a) and subgrain boundary 5 (c) indicated that they either consist of dislocations of the $(001)[100]$ or $(100)[001]$ slip systems or that they were twist walls in the (010) plane, whereas the rotation axis for boundary 6 (b) indicated slip of the $(0kl)[100]$ slip system (see fig 4.2 in chapter 4). In subgrain boundaries 1 to 5, dislocation arrays were recognised, but the internal structure of boundary 6 was not clear (fig 6.16b). The imaged width of boundary 6 on the micrograph suggested that it was close to the (010) plane. Because of the large misorientation it was uncertain whether boundary 6 was a subgrain boundary or should be considered as a new high angle grain boundary that intersected with subgrain boundaries 2 and 3 in the 120° triple junction on the right. From the bright field TEM micrograph in figure 6.16b it is not possible to distinguish if the fringes represent a dislocation array or if they were a Moiré interference pattern. A detail of the fringe pattern of boundary 6 is shown in figure 6.16b. The pattern was characterised by evenly distributed fringes with 4.7 nm spacing that were split both at the margins of the boundary and in the

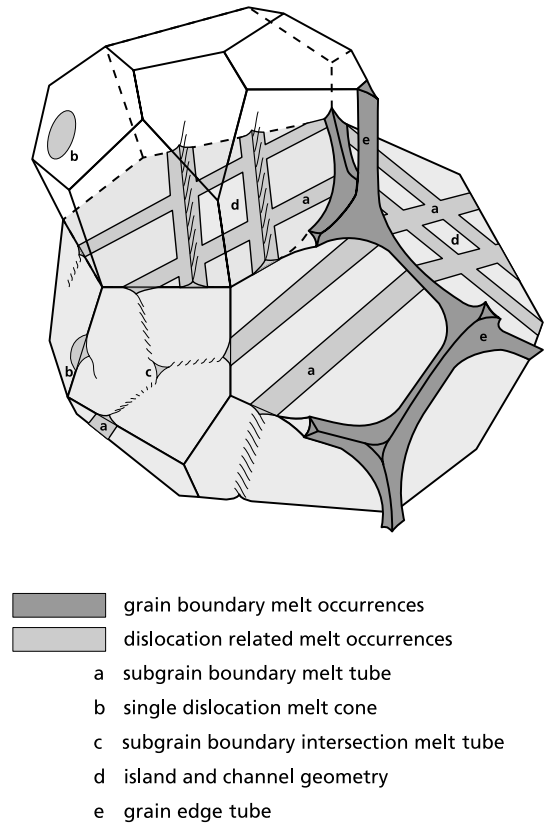


fig 6.17 Schematic representation of the dislocation-related melt microstructures at the grain scale, (a) subgrain boundary melt tubes, (b) melt cone at isolated dislocations, (c) melt tube into the grain along a subgrain boundary triple junction, (d) overlapping subgrain boundary melt tubes forming an island and channel geometry at grain interfaces (e) grain edge melt tube

centre where the fringes formed a cross-over pattern. If the pattern is an image of primary dislocations, the fringes would account for a rotation of 5.8° by $\mathbf{b}=[a]$ dislocations or 7.3° for $\mathbf{b}=[c]$ dislocations. The actual rotation over this subgrain boundary is 11.6° which implies that either a second set of dislocations is present, but out of contrast, or the fringes are images of a regular set of secondary dislocations. Rotational Moiré fringes perpendicular to the boundary would be produced by the interference of lattice fringes parallel to the boundary (Edington 1975), in this case the (001) lattice fringes. These make an angle of 5.9° across the boundary and could produce fringes with a separation of 5.8 nm. Although this is larger than the observed fringe spacing of 4.7 nm and the complexity of the pattern suggests that the fringe pattern was not formed by interference of two sets of parallel fringes it can not be excluded that the pattern is a Moiré pattern.

6.4 Discussion

In partially molten rocks with low melt fractions, the melt phase is highly dispersed in the system. Most melt resides in grain edge tubes and in larger melt interserts (Bussod & Christie 1991; Faul *et al.* 1994; Cmíral 1998) and also in ultrathin melt films that may cover the grain boundaries (Cmíral *et al.* 1998; De Kloe *et al.* 2000 / Chapter 5). In addition to these occurrences, melt was also found in nm-scale pockets along grain boundaries. These melt pockets were related to the occurrence of intracrystalline defects such as subgrain boundaries and individual dislocations. When an intracrystalline defect in the olivine crystal lattice intersected the grain surface in contact with an existing triple junction melt tube or melt layer, the geometry of that larger melt body was also affected.

The melt occurrences that are reported in this chapter were observed in cross-section. However, where these triangular melt bodies are related to planar features as subgrain boundaries, they are likely to form melt tubes that outline the traces of subgrain boundaries along the surface of the olivine grains. The subgrain boundary melt tubes produce a nm-scale melt network around individual olivine grains while isolated melt bodies can be present where individual dislocations intersect the olivine surface. The different types of observed melt occurrences are illustrated schematically in figure 6.17.

6.4.1 Morphology of subgrain boundary melt tubes

The cross-sectional shape of melt tubes along the subgrain boundaries is determined by the balance between the solid-liquid interface energy γ_{SL} and the subgrain interface energy γ_{SG} . In this analysis, it is assumed as a first approximation that the solid-liquid interface energy is isotropic. The dihedral angle θ at the melt-subgrain boundary intersection is given by

$$\gamma_{SG} = 2\gamma_{SL} \cos \frac{\theta}{2} \quad [1]$$

Cooper & Kohlstedt (1982) estimated the subgrain interface energy in olivine as function of their misorientations using [eq. 2].

In general:

$$\gamma_{SG}(\phi) = \gamma_{SG}^0 \phi (A_0 - \ln \phi) \quad (\phi \text{ in radians, Read \& Shockley (1950)}) \quad [2]$$

$$A_0 = 1 + \ln \frac{b}{2\pi r_0} \quad [3]$$

In the equation 2 the total energy (both elastic and core energy) for individual dislocations is included in the A_0 -term [eq. 3] with r_0 being the critical radius down to which the elastic strain energy must be integrated to give the total energy of the dislocations in the boundary (Cooper & Kohlstedt 1982). Because the strain energy for individual dislocation cores is not known for olivine, Cooper & Kohlstedt (1982) used $b/r_0=4$ ($A_0=0.55$) as a first-order approximation to calculate the subgrain interface energy of two common types of tilt walls (composed of $\mathbf{b}=[a]$ or $\mathbf{b}=[c]$ dislocations with line direction $[010]$) [eq. 4, 5]. Their experimental results on subgrain boundaries with misorientations below 2° supported these estimates.

$$\mathbf{b}=[a] \quad \gamma_{SG}(\phi) = 3.84\phi(0.55 - \ln \phi) \quad [4]$$

$$\mathbf{b}=[c] \quad \gamma_{SG}(\phi) = 4.05\phi(0.55 - \ln \phi) \quad [5]$$

With increasing subgrain misorientation, dislocation spacing decreases until the strain fields of the individual dislocations interact (Hull 1975) and the equation is no longer valid. Hull (1975) estimated that the individual identity of dislocations is lost when the dislocation spacing decreases below ~ 5 lattice planes. The spacing for which the strain fields of individual dislocation interact to the extent that the individual identity of the dislocations is lost is not known for olivine. Assuming that a spacing of 5 lattice planes is also applicable for olivine, this would result in dislocation spacings of 2.3 or 3 nm for tilt walls consisting of $\mathbf{b}=[a]$ or $\mathbf{b}=[c]$ dislocations respectively and maximum subgrain rotations of $\sim 11^\circ$ which corresponds to the largest (subgrain) boundary rotation that was measured in this study.

The solid-liquid interface energy for the olivine-basalt systems, γ_{SL} , has been estimated by Cooper & Kohlstedt (1982) to be 0.5 ± 0.2 J/m². Using this value, the misorientation-dihedral angle relationships for two common subgrain boundaries in olivine were calculated. The results are plotted in figure 6.12 to provide a reference for the measurements reported in this study although most of these measurements show misorientations exceeding 2° . The additional curves in figure 6.12a were calculated using arbitrary values for the solid-liquid interface energy for tilt walls composed of $\mathbf{b}=[a]$ dislocations with line direction $[010]$. The melt microstructure in the undeformed hot-pressed olivine-orthopyroxene sample (sample 5132) which was held at high temperature for 1 hour apparently is not yet in equilibrium given the scatter in the dihedral angle-misorientation plot (fig 6.12b). After deformation the scatter is reduced and the dihedral angle and misorientation measurements in the olivine-orthopyroxene sample (5249) plotted above the

$\gamma_{SL}=0.5$ reference curve and can be described by the curve using $\gamma_{SL}=0.65\pm 0.2$ J/m² (fig 6.12c). The measurements in the deformed olivine sample (5072) on the other hand were in good agreement with the data of Cooper & Kohlstedt (1982), indicating a solid-liquid interface energy $\gamma_{SL}=0.5\pm 0.2$ J/m² (fig 6.12e). Long-duration annealing of the olivine and olivine-orthopyroxene samples resulted again in an increased scatter of the data points similar to the hot-pressed material with the measurements of the olivine-orthopyroxene materials on average plotting somewhat higher than those of the olivine sample (fig 6.12d, f). The reduced amount of scatter in the results of the deformed specimens suggests that active deformation promotes equilibration of the melt tube morphology as described by equations [1] and [2], while unstressed annealing enables a variation of melt tube shapes to develop. However, it can not be excluded that the differences in data scatter are caused by the limited dataset .

As in both the olivine and olivine-orthopyroxene materials the misorientation-dihedral angle has only been measured in the olivine grains, which exhibit the same solid-solid interface energy relationship for subgrain boundaries, any differences in the dihedral angle-misorientation relationship are likely to be caused by differences in the solid-liquid interface energy due to compositional differences of the melt phase. This difference in interface energy results in a change in melt tube shape. The results presented in this chapter show that at the same misorientation, subgrain boundary melt tubes in the deformed olivine sample exhibit smaller dihedral angles and thus have a higher aspect ratio than those in the deformed olivine-orthopyroxene rocks. This implies that the melt transport in partially molten rocks is not only governed by the size and distribution of the melt tubes, the stress conditions and the viscosity of the melt phase (Rutter 1997), but that the shape and thus connectivity of melt tubes is also influenced by the chemistry of a melt phase that migrates through the rock. Reliable quantification of the melt phase composition in the small melt pockets was not possible, which is illustrated by the range of melt compositions in sample 5249 reported by Drury & FitzGerald (1996) (see also Appendix B). The uncertainty of the melt composition makes it difficult to verify whether the melt composition actually did vary between the samples. Studies on the influence of contaminants on the grain boundary melt film thickness in Si₃N₄ ceramics show however that even minor concentrations of impurity elements, for example less than 500 ppm Ca²⁺, can have a measurable effect on the equilibrium thickness of the melt films (Bruley *et al.* 1994; Tanaka *et al.* 1994a, b) by modifying the silica network structure. Therefore, it is feasible that (minor) variations in the concentration of the constituents of the melt phase have a significant effect on the solid-melt interface energy and thereby on the (sub)grain boundary melt tube morphology.

From the estimates of the subgrain interface energy (eq. [4, 5]) it follows that subgrain boundaries with misorientations exceeding $\sim 4.3^\circ$ for $\mathbf{b}=[a]$ dislocations and $\sim 3.9^\circ$ for $\mathbf{b}=[c]$ dislocations exhibit an interface energy that is similar to or higher than that of a high-angle grain boundary which is estimated to be $\gamma_{SS}=0.9\pm 0.35$ J/m² (Cooper & Kohlstedt 1982). The solid-liquid dihedral angle for subgrain boundaries with such misorientations is estimated to be $\sim 50^\circ$ (eq. [1], fig 6.12). Therefore, when the misorientation of a subgrain boundary exceeds $\sim 4^\circ$, the connectivity considerations of melt tubes along grain edges which are based on interface energies (eq. [1]) may also be applied to intersections of such high-misorientation subgrain boundaries (e.g.

fig 6.13, 6.14, 6.15). The measurements reported here show that subgrain boundaries with misorientations exceeding 4° and dihedral angles smaller than the 60° connectivity threshold (Toramaru & Fujii 1986) occur frequently. This implies that the formation of melt tubes along the intersection of subgrain boundaries with misorientations higher than 4° may be a common process in partially molten rocks.

6.4.2 Distribution of defect related melt occurrences

The subgrain size and thus the spacing between adjacent subgrain melt tubes is controlled by the differential stress level during deformation (e.g. Raleigh & Kirby 1970; Green & Radcliffe 1972; Twiss 1977). The flattened shape of the subgrain boundary melt pockets decreases the solid-solid contact area between adjacent olivine grains. Merging of adjacent melt tubes may occasionally occur in areas with smaller subgrains (fig 6.8), but complete wetting of grain interfaces would require an overall subgrain melt tube spacing of $\sim 1 \mu\text{m}$. Taking into account the possibility of interfering subgrain melt tubes from adjacent grains, this indicates a subgrain size of $\sim 2 \mu\text{m}$. This would require differential stresses exceeding 245 MPa based on the calibration of Van der Wal (1993), which are not feasible in the asthenospheric upper mantle. However, experimental evidence exists that small subgrains may develop in olivine during deformation under low differential stress when the (001)[100] slip system is activated (Darot & Gueguen 1981, 10 μm subgrains at $\sigma=8$ MPa) or during the initial stages of annealing, (Ricoult 1979; Bai & Kohlstedt 1992). In these studies it is concluded that free dislocations that are formed during deformation when the (001)[100] slip system (a-slip) is activated get rearranged into low-misorientation subgrain boundaries. This configuration with small subgrains is likely to be stable as subgrain coarsening in olivine has been found to be a slow process (Ricoult 1978).

Considering that the maximum width of subgrain boundary melt tubes occurs at the smallest misorientations, merging of subgrain boundary melt tubes can occur during annealing and thus produce melt layers with a typical thickness of 20 nm. This will significantly alter the melt microstructure when deformation ceases. Another consideration is the possible occurrence of the process of dynamical wetting as reported by Jin *et al.* (1994). They show the formation of melt layers along olivine grain boundaries upon deformation where melt migrates from the triple junction network into grain boundaries. A relationship of the melt redistribution with the active deformation mechanism was suggested and decoration of the dislocations in the olivine-orthopyroxene samples indicated that intracrystalline deformation was an important mechanism. However, a direct relationship of the occurrence of the melt layers with the dislocation microstructure was not shown by Jin *et al.* (1994).

The amount of melt that is accommodated in the subgrain boundary melt tubes is limited and does not represent a significant fraction of the total melt content in fine grained rocks once that exceeds 1%. Table 6.1 shows a first order approximation of the volume fraction of melt that could fill all available subgrain boundary tubes for several possible configurations together with the fraction of grain surface area that will be covered by the melt phase. This was calculated using cubic grains that contain planar parallel subgrain boundaries, e.g. subgrain boundaries in the (100) plane in olivine (fig 6.18). The small grain sizes and melt tube

grain size (μm)	subgrain size (μm)	melt tube width (nm)	melt tube height (nm)	volume fraction subgrain melt	subgrain melt covered surface
10	2	300	100	0.3 %	15.0 %
20	4	400	125	0.1 %	10.0 %
50	10	500	175	0.04 %	5.0 %
500	40	1000	300	0.003 %	2.4 %
1000	80	300	100	0.0001 %	0.4 %
1000	80	1000	300	0.0007 %	1.2 %
1000	15	300	100	0.0004 %	2.0 %
1000	15	1000	300	0.004 %	6.6 %

table 6.1 Melt volume fractions in subgrain boundary tubes for different (sub)grain size and melt tube configurations.

dimensions are representative for the experimental samples, The larger (sub)grain sizes are estimates for upper mantle conditions (Stocker & Ashby 1973). Estimates of differential stresses in the asthenosphere range from 1 to 10 MPa (Nicholas 1978). Using the stress-subgrain size relation for a ‘wet’ olivine rheology (Van der Wal 1993) this corresponds to subgrain sizes from 15 to 80 μm , similar to those reported in natural rocks (Suhr 1993). Assuming a melt tube width of 300 to 1000 nm, 0.4 to 6.6 % of the grain interface could be covered with melt. From these estimates it is clear that the total melt fraction that is present in grain edge tubes and melt layers will not be influenced by the very small melt fraction that is accommodated in the subgrain boundary tubes. The occurrence of such minute melt fractions in a stable natural configuration has been proposed by Spiegelman & Elliot (1993). They estimated the presence of residual porosities $\phi \sim <10^{-4}$ in the asthenosphere based on the partitioning of radiometric decay products of the uranium series in extruded basalts.

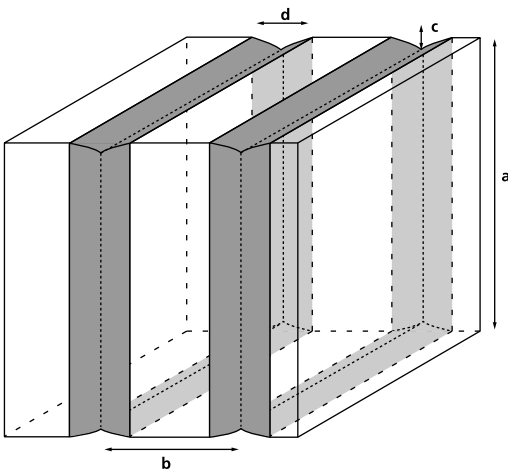
6.4.3 Implications for the deformation of partially molten olivine-orthopyroxene rocks.

This study has focussed on determining the distribution of very small amounts of melt and the factors that control the melt distribution at the grain scale in experimentally deformed olivine and olivine-orthopyroxene rocks. The significance of the presence of subgrain boundary melt tubes has yet to be established. Melt occurrences could be formed by at least three different mechanisms. First is the infiltration of melt from melt tubes and layers that exist along grain edges into the subgrain boundary intersections at grain interfaces. This implies that a percolating grain boundary network has to be established before wetting of grain interfaces occurs. Such melt infiltration was recently recognised in natural mantle rocks by Dijkstra *et al.* (2000a), who report melt impregnation into lithospheric shear zones with a pre-existing high-stress microstructure. The infiltration mechanism provides a way to fill continuous subgrain boundary tubes with a melt phase that may have originated from a remote source, but the formation of isolated melt occurrences associated with individual dislocations is not explained.

A second source of origin is by de-wetting of the grain interface (e.g. removal of a melt film or layer) into discrete bubbles and tubes that are preferentially associated with dislocations. While it is feasible that this process occurs at some grain interfaces, the observation of the stable occurrence

of melt layers (Faul *et al.* 1994) and melt films (Hess 1994; Drury & FitzGerald 1996; De Kloe *et al.* 2000 / Chapter 5) along olivine grain boundaries implies that the interface energy at many grain interfaces is effectively lowered by the presence of a melt phase. The presence of melt along grain interfaces therefore minimises the driving force for de-wetting of olivine grain interfaces and de-wetting is not considered to be of major importance in partially molten olivine-orthopyroxene rocks. A third possible source of origin of subgrain boundary melt tubes is *in situ* melting at sites where dislocations intersect with a high angle grain boundary or at subgrain boundary intersections inside olivine crystals. With temperatures near or above the melting point, the core of dislocations can be considered as a separate phase with thermodynamic properties distinguishable from the surrounding crystal (Glicksman & Vold 1972). When such heterophase dislocations are organised in a subgrain wall and the distorted cores of these dislocations merge at the intersection with a high angle grain boundary, a nanometer scale melt tube or melt film can be formed. This latter mechanism may be responsible for the initiation of the subgrain boundary melt tubes and in particular for the formation of melt tubes along subgrain boundary intersection inside olivine grains. Once a number of subgrain boundary melt tubes is formed and has become interconnected, the melt from different sites can mix as described in the first mechanism as the microstructure matures.

When a subgrain boundary melt network is established, the most important effect on the rheology of partially molten olivine-orthopyroxene rocks is expected to be the availability of fast diffusion paths. When deformation occurs by dislocation creep accompanied by dynamic

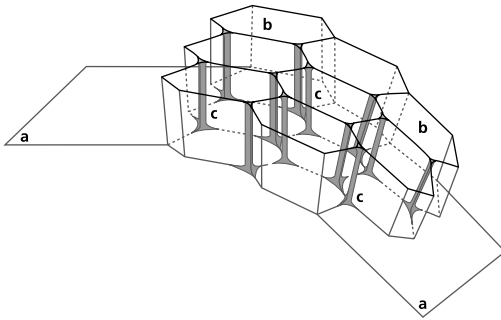


- a grain size
- b subgrain size
- c melt tube height
- d melt tube width

fig 6.18 Schematic drawing of the square grain-subgrain boundary configuration that was used to calculate subgrain boundary-related melt content.

recrystallisation involving subgrain rotation, a dynamic melt microstructure evolves at the scale of single grains where the spacing between adjacent melt tubes is determined by the subgrain size. The subgrain boundary melt tubes decrease the distance that diffusing atomic species must travel along virtually dry grain boundaries between the melt volumes at grain edges. Eventually, a decrease in subgrain size may result in the complete wetting of the grain interface in the form of melt layers by merging of adjacent or opposite subgrain boundary melt tubes.

Together with decreasing subgrain size, the process of dynamical wetting (Jin *et al.* 1994) can be responsible for the wetting of a large fraction of the interface area in mylonitic shearzones where active grain size reduction occurs in the presence of a melt phase (e.g. Kelemen & Dick 1995). The extensive formation of melt layers along olivine grain



- a level in the deforming olivine crystal in contact with the outermost subgrains
- b high-misorientation ($>4^\circ$) subgrains in the rim of a deforming olivine crystal
- c melt tubes along subgrain boundary intersections

fig 6.19 Schematic representation of melt infiltration into the rim of a larger deforming olivine crystal through subgrain boundary intersections.

boundaries is especially feasible in mylonite zones where the olivine [a]-axes are preferentially oriented parallel to the lineation and the (010) planes parallel to the foliation, which is a common fabric in upper mantle rocks (e.g. Kern *et al.* 1996). As the subgrain boundaries parallel to the (100) plane are common in mantle olivine (Mercier 1985), this configuration introduces an alignment of the elongated base of subgrain boundary melt tubes along the (010) faces. This can promote the formation of melt layers along grain boundaries that lie in the shear plane by merging of the subgrain boundary melt tubes, thereby causing significant weakening of the deforming rocks parallel to the foliation and providing a mechanism for shear localisation in the presence of a melt phase. The preferential formation of melt layers along (010) faces is supported by experimental studies (e.g. Waff & Faul 1992; Daines & Kohlstedt 1997; Jung & Waff 1998). Additional weakening of mylonitic rocks in the presence of a melt phase may occur in situations where olivine grains are developing a core-mantle structure by subgrain rotation and melt tubes extend into olivine crystals along the intersection of subgrain boundaries. If the mantle of such a grain contains subgrains with misorientations higher than 4° , melt may penetrate into the deforming grain and form a weaker layer that separates these outer subgrains from the host grain (fig 6.19). This can facilitate further rotation of the outer subgrains to individual grains. Besides the mechanical significance, the infiltration of a melt phase into an olivine crystal will also enhance the exchange of ions between the melt phase and the deforming olivine crystals. This will speed up any chemical re-equilibration of the deforming grains with an infiltrating melt phase to the ambient P-T conditions.

In addition to the possibility of forming continuous melt layers along grain interfaces, the presence of subgrain boundary controlled melt tubes along grain interfaces also provides enhanced diffusion along interfaces by establishing an island and channel microstructure (fig 6.17) (e.g. Raj 1982; Spiers & Schutjens 1990; Spiers *et al.* 1990). In a polycrystalline aggregate these subgrain melt tubes at interfaces form a network that divides the grain surface into parts where the grains remain in solid contact separated by melt covered areas. The orientation of the subgrain boundary melt tubes is independent in adjacent grains, hence interfaces of two grains hosting subgrain boundary melt tubes can have an interface melt distribution ranging from parallel melt tubes to a square island and channel structure (fig 6.17). The diffusivities in (basaltic) silicate melts are several orders of magnitude faster than lattice or grain boundary diffusion (Chakraborty *et al.* 1997; Farver *et al.* 1994; Hofman 1980; Houlier *et al.* 1988). Therefore, the establishment of an island

and channel microstructure along grain interfaces by subgrain boundary melt tubes can greatly promote the solution-precipitation type deformation mechanisms that occur in partially molten rocks (Dell'Angelo *et al.* 1987). Although the location of the melt tubes is dynamic with an evolving subgrain microstructure, melt tubes will remain to provide continuous pathways for efficient material transport away from the stressed interfaces as long as there are subgrain boundary-high angle grain boundary intersections.

The effect that the melt tubes have on mobility of both the grain boundaries and the subgrain boundaries is not clear. Drury & Van Roermund (1989) have suggested that the presence of a melt phase along olivine grain boundaries results in the formation of euhedral grain boundaries. This indicates that the movement of grain boundaries is effectively limited by the precipitation on the growing grain. If a melt pocket would either enhance or restrict grain boundary migration, bulging is expected to occur respectively at or next to the site of a melt tube, but an effect of the presence of subgrain boundary melt pockets on grain boundary migration was not noticed. The absence of differences in apparent grain boundary mobility at the site of melt tubes and the adjacent virtually dry grain boundaries could also be explained by the presence of ultrathin melt films along the whole length of the grain boundary (Drury & FitzGerald 1996; Cmíral 1998; De Kloe *et al.* 2000 / chapter 5) which provides a continuous veneer of amorphous material along the grain boundary.

Next to the effect of the secondary melt network on the deformation behaviour of the deforming partially molten rock is its effect on the extraction of the melt phase from the host-rock. Drawing an analogy to the results from Faul (1997), where he shows that even the larger melt tubes along grain edges are insufficient to provide a network to effectively extract the melt, it is unlikely that the individual subgrain melt tubes have a noticeable effect on the percolation properties of the rock. When merging of the tubes occurs and significant areas of grain boundaries become wetted as described earlier, this can change. A possible scenario for the development of the melt microstructure during deformation of a partially molten rock, going from an undeformed rock to a high-strain shear zone, could be as follows. When partial melting starts to occur in upper mantle rocks grain size is still relatively large. Intragranular deformation by dislocation motion is the major deformation mechanism. Upon melting a narrow spaced melt network based on the dislocation microstructure forms along the grain interfaces together with thin grain boundary films. This promotes diffusion processes and may enhance (dynamic) recrystallisation involving subgrain rotation, especially when melt infiltration along subgrain boundary intersections occurs. Alternatively, the formation of melt occurrences along grain interfaces enables strain partitioning into zones where melting occurs or where a crystallographic preferred orientation is present. When melting continues and the melt fraction increases, grain size reduces and intragranular deformation mechanisms are replaced by grain boundary processes hosted by the larger melt tubes and melt layers. Finally internal cohesion is lost, grain boundary sliding becomes possible and a dramatic weakening occurs.

6.5 Conclusions

A melt microstructure that is governed by the occurrence of subgrain boundaries and individual dislocations is identified along grain interfaces in deformed olivine and olivine-orthopyroxene rocks. These melt occurrences are complementary to the melt tubes and layers along grain edges while requiring less than 0.1 vol% melt to be completely filled with melt for typical mantle (sub)grain sizes. Elongated triangular melt tubes with typical dimensions smaller than 100 x 500 nm (height x width) form along intersections of subgrain boundaries with high angle grain boundaries. The triangular section of these melt tubes is related to the misorientation that is accommodated by the subgrain boundaries. This causes the cross-sectional shape of these melt tubes to become more equidimensional when the solid-melt dihedral angle decreases with increasing subgrain misorientation. As the solid-melt dihedral angle decreases with increasing subgrain misorientation, infiltration of melt into deforming olivine grains is possible along intersections of subgrains with misorientations exceeding 4° . The subgrain related melt microstructure in the olivine material (5072) resembles that in the olivine-orthopyroxene material (5249) except that the relation between the subgrain misorientation and the solid-melt dihedral angle at the subgrain boundary suggests that the solid-liquid interface energy in the olivine-orthopyroxene system is higher than in the olivine system. Long-duration annealing of the deformed samples showed the stability of the melt occurrences along grain interfaces. The occurrence of subgrain related melt bodies along grain interfaces enables a dynamic island-channel grain boundary structure and the formation of melt layers at high stress, thereby providing a mechanism for melt-induced weakening in deep lithospheric shearzones impregnated by melt.

Summary and implications of the melt and deformation microstructures on the rheology of partially molten mantle rocks

7.1 Introduction

The research presented in this thesis considered the melt and deformation microstructures in experimentally deformed partially molten olivine and olivine-orthopyroxene rocks. The aims of the study were to characterise the geometry and stability of grain-scale melt occurrences and to identify the deformation processes that determined the mechanical behaviour of olivine and olivine-orthopyroxene rocks in the presence of small amounts of melt (~1 vol%). Distinct strength differences were observed between the samples, with in some cases olivine-orthopyroxene materials being weaker than olivine samples, whereas in other cases both types of materials exhibited similar strength. These differences in rheological behaviour were used as a basis to select specific parts of the microstructure for detailed examination. The detailed studies have been described in previous chapters.

In this concluding chapter, first the results of the microstructural characterisation of the materials presented in this thesis are summarised and an attempt is made to identify the cause of the differences in rheological behaviour between the investigated samples. Then some implications of the observed melt and deformation microstructures for the interpretation of experimental deformation data of partially molten rocks are discussed together with the possible application of the results to natural processes. Finally, general conclusions are drawn and lines of research are proposed to address some unresolved issues.

7.2 Melt and deformation microstructures reported in this thesis

7.2.1 Melt microstructures

The analysis of the morphology and distribution of melt bodies in partially molten olivine-orthopyroxene materials resulted in the identification and characterisation of two types of sub-micrometer melt occurrences along olivine grain interfaces. These interface melt bodies occur in

addition to the well-established grain edge tubes and larger melt inserts identified in earlier studies on partially molten rocks (e.g. Waff & Bulau 1979, 1982; Vaughan *et al.* 1982; Beeman & Kohlstedt 1993; Faul *et al.* 1994; Cmíral *et al.* 1998). The presence of the first type of nanometer-scale melt occurrence was already indicated by Drury & FitzGerald (1996) who reported chemical indications for the occurrence of ultrathin films with “melt-like” composition along olivine-olivine grain boundaries in sample 5249. Their interpretation, that the chemical signal represented a thin melt film, is supported by this study from the results of several dedicated TEM techniques (chapter 5). Ultrathin amorphous films (1–3 nm) were detected along all investigated olivine-olivine grain interfaces in the deformed and annealed olivine and olivine-orthopyroxene specimens. The chemistry of the grain boundary films resembled that of the melt phase in large pockets, but some detected compositional differences (e.g. different Al-Ca ratio, fig 5.15) and the small dimensions of the films suggest that the films could have a different source and properties than the melt phase in larger pockets and should strictly be described as ultrathin amorphous films. The stability of the thin films was validated by their occurrence in samples deformed for longer duration (samples 6213, 6219; fig 5.7, 5.10) than the sample studied by Drury & FitzGerald (1996) (sample 5249) and in subsequent long-duration static annealing experiments. In the hot-pressed starting material for one of the samples, grain boundary melt films were detected along some but not all olivine-olivine interfaces (fig 5.14). The absence of films along some interfaces in the hot-pressed material is similar to the observations by Cmíral (1998) and Cmíral *et al.* (1998) that melt films occur along many, but not all olivine grain interfaces in both deformed and statically annealed olivine-basalt materials. These observations suggest that deformation may actively promote the formation and distribution of ultrathin melt films along olivine-olivine grain boundaries.

The second type of sub-micrometer melt occurrences was found at intersections of subgrain boundaries and individual dislocations with grain boundaries (chapter 6). These melt occurrences consisted of continuous melt tubes with typical dimensions smaller than 100 x 500 nm (height x width) that occurred along intersections between subgrain boundaries and high angle boundaries. The cross-sectional shape of these melt tubes was related to the misorientation accommodated by the subgrain, with melt tubes becoming more equidimensional as subgrain misorientation increases (fig 6.12). The association of melt tubes with subgrain boundaries implies that the geometry of the melt tube network along grain interfaces is controlled by the subgrain microstructure and because subgrain spacing is mainly controlled by differential stress, the geometry is also affected by the differential stress during deformation (Twiss 1977; White 1979a). Ultimately, the dependence of the distribution of these melt tubes on the subgrain configuration may result in the creation of 20–100 nm thick continuous melt layers along grain interfaces. Melt layers may form when the spacing between subgrain melt tubes decreases with decreasing subgrain size, thus allowing adjacent melt channels to coalesce. Similar melt layers are commonly observed in experimental partially molten olivine-bearing rocks and can significantly affect the mechanical properties of such rocks (Faul *et al.* 1994; Hirth & Kohlstedt 1995a)

Analysis of the cross-sectional shape of the subgrain melt tubes in relation to the subgrain misorientation indicated that the dihedral angle-misorientation relationship (fig 6.12) in the

olivine sample for misorientations less than $\sim 4^\circ$ could be described using the interface energy estimate of 0.5 J/m^2 determined by Cooper & Kohlstedt (1982). The dihedral angle–misorientation measurements in the olivine–orthopyroxene material suggested a higher olivine–melt interface energy of 0.65 J/m^2 . Long-duration annealing resulted in a larger scatter of the dihedral angles as function of the misorientation, but the general trend of decreasing dihedral angles with increasing subgrain misorientation remained.

Dihedral angles less than 60° occurred at melt tubes associated with high misorientation ($\theta > 4^\circ$) subgrains. For misorientations higher than 4° , the subgrain–melt dihedral angle appeared to be independent of the subgrain misorientation. In addition to the subgrain melt tubes along grain interfaces, melt tubes were also occasionally observed inside deformed olivine crystals, where the intersection of three subgrain boundaries, with misorientations exceeding 4° , allowed the melt phase to infiltrate the grain (fig 6.13–15). The diameter of such intragranular melt tubes along subgrain intersections ranged in size from 20 nm to 200 nm. These observations indicate that the transition from a low-angle to a high-angle olivine boundary in terms of the formation of melt tubes along (sub)grain edges occurs at $\sim 4^\circ$.

7.2.2 Deformation microstructures

The second goal of the research presented this thesis, in addition to the identification and characterisation of the sub-micrometer scale melt occurrences along grain interfaces, was to investigate how (very) small melt volumes may have affected the mechanical properties of partially molten olivine–orthopyroxene rocks that were deformed in the dislocation creep field. Weakening due to the presence of a melt phase is generally assumed to be related to enhanced grain boundary processes such as faster diffusion along otherwise melt-free grain edges and grain interfaces and the reduction of load-bearing solid–solid contact area (see table 7.1). Variations in the (local) melt fraction and factors that affect the melt distribution, such as grain size distribution and crystallographic preferred orientations (CPO) of the minerals, are therefore likely to affect the mechanical response of a partially molten rock to an applied stress.

An extensive analysis of the grain size distribution, crystallographic orientations, melt content, and melt distribution was carried out on a number of selected samples with special emphasis on two specimens from the study of Hitchings *et al.* (1989), the (stronger) olivine sample 5072 and (weaker) olivine–orthopyroxene sample 5249 (chapter 3). The microstructures showed little difference between the single-phase olivine material and the olivine–orthopyroxene materials except for the smaller grain size in sample 5072 and of course the presence of orthopyroxene in the two-phase materials, which exhibited a crystallographic preferred orientation (CPO) that was probably initiated during hot-pressing. The orthopyroxene CPO showed [c]-axes in a girdle perpendicular to the compression direction together with a (weak) point maximum of [a]-axes parallel to the compression direction (fig 3.10). The olivine grains in both the olivine and olivine–orthopyroxene samples developed a weak CPO during deformation, indicating that (a significant part of) the deformation was accommodated by a dislocation creep mechanism. The main microstructural differences between samples 5072 and 5249 concerned the amount of local melt in fine grained regions and a larger amount of 60° olivine grain misorientations in sample 5249 (fig

3.11). The local melt concentrations in the olivine-orthopyroxene material, sample 5249, tended to contain more melt than those in the olivine material, sample 5072 and a larger fraction of the total melt content in sample 5249 was contained in the larger melt bodies (fig 3.7).

In addition to the intergranular melt and deformation microstructures, the intragranular deformation structures were analysed (chapter 4). The creep strength during deformation provided indirect evidence that deformation of the weaker olivine-orthopyroxene material may have been accommodated by dislocation creep rate-limited by the weak olivine (010)[100] dislocation slip system, [a]-slip. The stronger material showed creep strength intermediate to olivine single crystal [a]-slip, (010)[100] and [c]-slip, (010)[001] (fig 3.3). In order to establish whether or not the difference in creep strength was related to differences in activated dislocation slip systems, the presence and relative amounts of dislocations with Burgers vectors $\mathbf{b}=[a]$ and $\mathbf{b}=[c]$ were determined in two selected samples using TEM dark field imaging. Taking into account that the fraction of the sample that could be studied by TEM imaging was limited, dislocation microstructures in both samples appeared similar and showed evidence for activation of slip systems involving dislocations with both $\mathbf{b}=[a]$ and $\mathbf{b}=[c]$ Burgers vectors. Densities of dislocations with Burgers vectors $\mathbf{b}=[a]$ and $\mathbf{b}=[c]$ were highly variable in individual grains and no preference for a single slip system could be inferred from the TEM analysis (fig 4.5).

The simultaneous activation of the [100](010) and [001](010) dislocation slip systems in both samples was confirmed with an analysis of subgrain rotation axes in the SEM using EBSP. The EBSP analysis showed a wide spread in the orientation of subgrain rotation axes, in agreement with the variations observed with TEM. The distribution of the orientation of subgrain rotation axes, however, was different in the studied samples and indicated that subgrain boundaries related to the weak [100](010) slip system were more abundant in the strong material while slip along the intermediate strength [100]{*okl*} slip systems were more abundant in the weaker material (fig 4.11). The spread in orientation of subgrain rotation axes was also observed in the EBSP analysis of subgrain populations within individual olivine grains. While a range of subgrain rotation axes occurred within crystals, clusters of adjacent subgrain boundaries exhibited similar rotation axes, indicating activation of different slip systems within domains of the deforming crystals (fig 4.15). To conclude, the analysis of intracrystalline deformation microstructures indicated differences in the relative abundance of subgrain boundaries related to specific slip systems, but did not confirm the hypothesis that [a]-slip was the only active dislocation slip system in the weaker material.

7.2.3 Deformation mechanisms

Details of the melt (chapters 3, 5, and 6) and deformation microstructures (chapters 3 and 4) of partially molten olivine-orthopyroxene rocks have been investigated in this thesis in an attempt to identify the processes that caused the differences in rheological behaviour between the samples from the study of Hitchings *et al.* (1989) and the study performed by Drury reported in chapter 3. In each chapter some minor microstructural differences were observed, but the analysis of details of the melt and deformation microstructures did not provide an unequivocal indication for the cause of the rheological differences of the two sets of olivine-orthopyroxene rocks. In this section, the observed microstructural differences will be related to possible associated

deformation mechanisms and the cause for the differences in mechanical properties is discussed.

The study of the intracrystalline deformation structures in samples 5072 and 5249 indicated that, while the olivine crystallographic orientation distribution was similar, the same olivine dislocation slip systems were activated, only in different magnitudes. Together with the observation that localised activation of specific slip systems occurs in larger olivine grains, it is concluded that the dislocation microstructure is critically dependent on the local environment defined by grain size and grain shape. Variations in the local activation of specific slip systems may then result in a different bulk mechanical response.

A ubiquitous presence of small amounts of melt along grain interfaces was shown by the analysis of melt occurrences in all studied materials, but the role of the presence of a small melt fraction on the rheological behaviour remains unclear. The grain-scale melt microstructures were very similar in both sample sets, with continuous ultrathin melt films along olivine grain interfaces and subgrain related melt tubes occurring in all samples. The low strength of the olivine-orthopyroxene samples could not be attributed to the presence of thin amorphous films, because films were present in the stronger olivine samples as well (De Kloe *et al.* 2000 / chapter 5). A possible cause for strength variations in materials with similar melt content and distribution is a difference in the melt composition (see table 7.1).

Melt composition will directly affect the solid-melt interface energy, resulting in different morphologies of grain edge and subgrain melt tubes (e.g. fig 6.12). The kinetics of the basic solution, precipitation, and diffusion steps involved in 'diffusion creep' along boundaries may also be influenced by melt composition (Visser 1999; see also tables 7.2-7.4 and accompanying discussion). The preferential occurrence of 60° grain misorientations in sample 5249 (fig 3.11) may also be related to variations in the melt composition. 't Hart (1978) shows the stabilisation of olivine twin boundaries with 60° misorientation by adding Ca²⁺-ions. Similar preferential occurrences of 60° olivine grain interfaces in partially molten olivine rocks are reported by Faul & FitzGerald (1999). In their study, the 60° boundaries remain free of melt layers and are interpreted to represent coincident site lattice (CSL) boundaries. A weakening mechanism that is related to this preferred misorientation is therefore unlikely, because CSL boundaries generally have slower diffusion kinetics and higher resistance to grain boundary sliding (see Fliervoet & White 1995 and references therein).

On a larger scale, some differences in the melt distribution were observed between the olivine and olivine-orthopyroxene samples that may partly account for the strength variation. The overall and local melt contents were somewhat higher in the olivine-orthopyroxene sample 5249 when compared to the olivine material, sample 5072. Furthermore, the microstructures in the annealed specimens (fig 3.17) indicate that melting in the olivine-orthopyroxene material occurs primarily along olivine-orthopyroxene interfaces. Although similar melt layers along olivine-orthopyroxene interfaces are absent in the deformed materials, melt may be preferentially produced along olivine-orthopyroxene interfaces before being redistributed in the sample. The higher local melt content and the production of melt along olivine-orthopyroxene interfaces may give rise to more effective grain boundary sliding and strain localisation in the olivine-orthopyroxene samples. However, higher local melt contents do not cause weakening in the

other olivine-orthopyroxene materials. This difference in mechanical response may be related to the average size of the melt bodies. When the melt pockets on average are larger, which is the case in sample 5249 (see figure 3.7), the melt phase will be more concentrated, producing relatively strong areas with very low melt content between the melt-rich zones. The areas with higher melt content are more abundant in samples with higher bulk melt content and the possibility increases that these melt-rich fine-grained zones will interconnect, producing zones with lower strength.

In addition to microstructural indicators, a clue for the difference in mechanical behaviour may be given by the activation energies for creep that were determined from Drury's 62xx olivine and olivine-orthopyroxene experiments reported in chapter 3 (fig 3.1, 3.2). The activation energies estimated for the olivine-orthopyroxene materials from Drury's experiments, 808 kJ/mol and 732 kJ/mol (fig 3.2), are much higher than the activation energies for the olivine material from Drury's experiments, being 467 kJ/mol and 557 kJ/mol. The large difference in activation energy between the olivine and olivine-orthopyroxene materials is interpreted to result from a more rapid increase of melt content in olivine-orthopyroxene materials compared to olivine samples (Kohlstedt & Zimmerman 1996). The weakening due to an increased melt content at high temperature inferred from the high activation energy is consistent with the experimental data compiled by Kelemen *et al.* (1997) that shows a decrease in olivine solid-state viscosity with increasing melt content:

$$\eta_{\text{partial-melt}} = \eta_{\text{melt-free}} e^{(-45\phi)}$$

where $\eta_{\text{partial-melt}}$ is the viscosity of a partially molten olivine material, $\eta_{\text{melt-free}}$ is the viscosity of a melt-free olivine aggregate, and ϕ is the melt fraction.

A dependence of creep strength on the melt content may partly explain the different results obtained from the experiments of Hitchings *et al.* (1989) and those of Drury (reported in chapter 3). Hitchings *et al.* (1989) found that olivine-orthopyroxene material were weaker than olivine samples at 1227°C, while in Drury's experiments olivine-orthopyroxene samples were only weaker than olivine at a higher temperature of 1300°C. As described in chapter 3, the starting materials in the two experimental studies were different. The Hitchings *et al.* (1989) olivine-orthopyroxene samples had a higher CaO, Al₂O₃ bulk composition (table 3.1, 3.3), therefore these materials are expected to produce a higher melt content than Drury's olivine-orthopyroxene samples at the same temperature.

In summary, the melt and deformation microstructures in all samples were very similar. Larger melt bodies were typically related to relatively fine-grained areas. Together with the localised activation of dislocation slip systems, the occurrence of larger melt bodies points to the grain size distribution being an important parameter in the rheological properties. The influence of the melt phase on deformation is expected to be similar in all studied samples and is probably restricted to the enhancement of diffusion along grain interfaces and grain edges and local stress increases due to the reduction of stress supporting solid-solid contacts (see table 7.1). It is concluded that differences in grain size and grain shape distribution together with variations in local melt content

and melt composition may be the factors that caused the different rheological behaviour in the experimentally deformed samples investigated in this thesis.

7.3 Implications of the observed microstructures on the properties and interpretation of partially molten mantle rocks

In the individual chapters and in the previous section on the deformation mechanisms, the discussion has been limited to the materials studied in this thesis. In this section, the implications of the observed melt and deformation microstructures for the interpretation of experimental results on partially molten rocks in general and processes that occur in natural settings where a partial melt is present are discussed.

7.3.1 Dislocation microstructures

Characterisation of the nature of dislocations in deformed polycrystalline olivine materials is not frequently reported because of the time consuming (TEM) analytical techniques involved. In this thesis as well as in the studies of Zeuch & Green (1979) and Karato *et al.* (1986) on the rheology of polycrystalline olivine containing a very small melt fraction, it was found that densities of free dislocations with Burgers vectors $\mathbf{b}=[a]$ and $\mathbf{b}=[c]$ are comparable while dislocation microstructures are highly inhomogeneous between grains. The dislocation microstructure did not show evidence that the presence of a melt fraction reduced the number of dislocation slip systems activated. This implies that external factors such as the direction of the applied differential stress on the polycrystal and the presence of a melt phase are not the only factors that influence the activation of specific dislocation slip systems in individual grains. The creep strength of olivine deforming in the dislocation creep field is typically intermediate to the levels for olivine single crystal [a]- and [c]-slip (fig 3.3). Together with the observation of highly variable dislocation microstructures, this creep strength is indicative for the bulk creep strength of olivine-bearing materials deforming in the dislocation creep field being determined by the average of locally activated slip systems within individual grains rather than by a single particular slip system that is rate-controlling in the whole sample volume. Any occurring intergranular misfits need to be accommodated by grain boundary processes. The influence of grain boundary processes is illustrated by the observation that olivine aggregates (that probably contain a small amount of melt) are generally weaker for smaller grain sizes (fig 3.3; Karato *et al.* 1986; Kohlstedt & Zimmerman 1996). The activation of dislocation slip systems in individual grains would then be influenced by the local environment defined by mineralogy, grain shape, grain size, and also the grain size distribution. The observed dependence of the dislocation microstructure on the local environment precludes a straightforward comparison of the well characterised dislocation microstructure in single crystals (e.g. Durham *et al.* 1977a; Kirby & Wegner 1977; Zeuch & Green 1984; Bai & Kohlstedt 1992) with polycrystals. This implies that creep strength determinations and dislocation microstructures for specific slip systems, based on ideally oriented single crystal experiments, cannot be directly applied to polycrystals to infer the activated slip systems using

<i>Reported melt occurrences in partially molten olivine-bearing rocks:</i>	<i>Proposed melt-related weakening mechanisms</i>
<p>Earlier studies* :</p> <ul style="list-style-type: none"> • Triple junction melt tubes^(e.g.1, 2) • Melt layers (>5 nm thick)^(e.g. 8, 14) • Melt interserts^(14, 15) • Elongated ellipsoidal inclusions along grain interfaces^(9, 13) 	<ul style="list-style-type: none"> • Stress concentration due to a reduction of load bearing solid-solid contact area^(3, 10, 11) • Formation of short circuit diffusion paths along melt filled grain intersections^(3, 4, 5, 10, 11, 12) • Enhancement of diffusion processes along (partly) wetted grain interfaces^(6, 7, 8, 10, 12, 13) • Easy grain boundary sliding along interfaces with melt layers^(5, 7, 8, 11, 12, 13) • (Possible) transition from dislocation creep to grain boundary diffusion creep⁽⁷⁾
<p><i>Additional melt occurrences in partially molten olivine-bearing rocks reported in this thesis:</i></p>	<p><i>Additional melt-related weakening mechanisms proposed in this thesis:</i></p>
<p>This thesis :</p> <ul style="list-style-type: none"> • Melt films (<5 nm thick)[#] • Elongated subgrain melt tubes along grain interfaces • Melt tubes penetrating into deformed olivine crystals along intersections of subgrain with misorientations exceeding 4° 	<ul style="list-style-type: none"> • Enhanced diffusion along olivine grain interfaces due to the presence of continuous thin amorphous films and corresponding increase of the grain boundary width. • Additional short-circuit diffusion through subgrain melt tubes along (stressed) grain interfaces and into deforming crystals. • Melt composition-related subgrain melt tube morphology changes that can influence local stress concentrations. • Melt composition-related variations of diffusion kinetics.

* Waff & Bulau (1979)¹; Vaughan *et al.* (1982)²; Cooper & Kohlstedt (1984a³,b⁴, 1986⁵); Bussod & Christie (1991)⁶; Kohlstedt (1992)⁷; Waff & Faul (1992)⁸; Faul *et al.* (1994)⁹; Hirth & Kohlstedt (1995a¹⁰,b¹¹); Kohlstedt & Zimmerman (1996)¹²; Cmiral (1998)¹³; Cmiral *et al.* (1998)¹⁴; Faul (2000)¹⁵

Indirect (chemical) evidence for the presence of ultrathin amorphous films along grain boundaries in experiments on olivine-bearing rocks has been presented earlier by Drury & FitzGerald (1996) and Cmiral *et al.* (1998)

table 7.1 Summary of reported melt microstructures and melt-related weakening mechanisms complemented by the additional melt occurrences and proposed weakening mechanisms reported in this thesis.

D _i	X _{SiO₂} = 0.45-0.55		
	T=1473 K	T=1523 K	T=1573 K
SiO ₂	10.33	9.5	8.7
TiO ₂	-1	-1	-1.15
MgO	-2.8	-2.72	-3.07
MgAl ₂ O ₄	4	3.5	2.57
FeO	-3.4	-4.19	-4.82
CaO	-1.4	-1.43	-1.77
CaAl ₂ O ₄	7.1	6.09	4.85
Na ₂ O	-7.37	-7.21	-6.86
NaAlO ₂	11.15	10.59	9.98

table 7.2 D_i values for the major components in basaltic melts for temperatures 1473 K, 1523 K, and 1573 K (Bottinga & Weill 1972). Values in *italic print* are not given in Bottinga & Weill (1972) and are estimates based on adjacent values.

components (at%)	Waff & Bulau (1982)	Cmiral <i>et al.</i> (1998)	Cooper & Kohlstedt (1984a)	Kushiro (1986)	Waff & Faul (1992)
	<i>natural basalt (AOBC70)</i>	<i>synthetic basalt</i>	<i>synthetic basalt</i>	<i>olivine tholeiite</i>	<i>natural basalt (76K6)</i>
SiO ₂	52.29	52.90	52.03	47.94	46.85
TiO ₂	2.67	1.93	0.01	0.34	1.80
Al ₂ O ₃	10.46	8.70	8.47	9.41	7.14
MgO	8.35	16.95	13.21	19.36	19.97
FeO	11.83	4.73	9.01	8.82	10.46
CaO	10.76	12.66	14.33	12.63	11.47
Na ₂ O	3.65	2.12	2.94	1.52	2.31

table 7.3 Major elements of the melt compositions from 5 studies on partially molten olivine-bearing materials recalculated to at% and normalised to 100%. D_i values for some minor components (MnO, NiO, K₂O, P₂O₅, Cr₂O₃) are not listed by Bottinga & Weill (1972) and these components are omitted from the viscosity calculations.

calculated viscosity (Pa s)	Waff & Bulau (1982)	Cmiral <i>et al.</i> (1998)	Cooper & Kohlstedt (1984a)	Kushiro (1986)	Waff & Faul (1992)
	<i>natural basalt (AOBC70)</i>	<i>synthetic basalt</i>	<i>synthetic basalt</i>	<i>olivine tholeiite</i>	<i>natural basalt (76K6)</i>
T=1473 K	61.2	43.0	38.5	21.3	13.6
T=1523 K	31.1	23.8	20.7	11.7	7.7
T=1573 K	15.2	11.9	10.4	5.9	4.0
relative diffusion coefficients					
T=1473 K	100	142	159	287	452
T=1523 K	100	131	150	265	401
T=1573 K	100	127	146	259	377

table 7.4 Viscosity estimates for the basaltic compositions given in table 7.3 for temperatures 1473 K, 1523 K, and 1573 K. Corresponding diffusion coefficients are calculated relative to the results of basalt AOBC70 from the study of Waff & Bulau (1982), that are set to 100 for each temperature.

creep strength measurements.

Weakening mechanisms related to small melt fractions in materials deforming in the dislocation creep field that have been proposed include the enhancement of kinetics of diffusional deformation mechanisms by short-circuit diffusion and the replacement of solid-solid load bearing areas with solid-melt interfaces that cannot support a significant shear stress (see table 7.1; Cooper & Kohlstedt 1986; Hirth & Kohlstedt 1995b). Both mechanisms imply that melt-induced weakening involves the (partial) transition of the deformation mechanism from dislocation creep to diffusion controlled mechanisms. However, the melt phase could also have a direct influence on dislocation mobility or diffusion through the development of partially molten dislocation cores similar to the glassy intracrystalline tubes reported by Hacker & Christie (1991). The continued activation of intracrystalline deformation mechanisms in melt-weakened materials deformed in the dislocation creep field is illustrated by stress exponents indicative for dislocation creep ($n \sim 3$) (Beeman & Kohlstedt 1993; Hirth & Kohlstedt 1995b; Bai *et al.* 1997). A possible dislocation related mechanism that can be associated with the presence of a melt phase is an enhanced mobility of dislocations at elevated temperatures. Dislocations in olivine may develop an amorphous phase at their cores, similar to the heterophase dislocations discussed by Glicksman & Vold (1972). The formation of such heterophase dislocations may enable a kind of solution-precipitation process in the dislocation cores, thereby facilitating dislocation movement. Weakening related to such a mechanism would probably depend on the size of the pockets of amorphous material at dislocation cores being small enough (probably at the scale of individual lattice planes) as impurities and larger melt bodies may harden the material by obstructing dislocation movement (Weeks *et al.* 1969; Burton 1975; Knipe & White 1978). If such a solution-precipitation process occurs, it can be anticipated that this will be affected by the anisotropy of olivine and motion enhancement of different types of dislocation may be different.

7.3.2 Melt related effects on rheology in general

An overview of reported melt occurrences and melt-related weakening processes is given in table 7.1. The analysis of the melt distribution reported in chapters 3, 5, and 6 shows that most melt features occur universally in all studied samples. Small differences that may account for different mechanical responses to an imposed stress were observed in the local melt content and the size distribution of melt pockets. Alternatively, several observations pointed to the composition of the melt phase influencing the rheological behaviour of rocks with low melt fractions. This postulated effect of the composition of the melt phase on creep strength points to an important issue in experimental studies on partially molten mantle materials. The composition of the melt phase in rock samples may not be homogenous in experimental samples and studies by Kleebe *et al.* (1992) and Tanaka *et al.* (1994b) on Si_3N_4 ceramics show that the composition of the melt phase has a pronounced effect on the degree of grain boundary wetting and intergranular film thickness.

In many studies it is attempted to approach mantle 'chemical equilibrium' by mixing powders derived from crushed natural olivine crystals with a synthetic or natural basalt with MORB-like chemistry (e.g. Cooper & Kohlstedt 1984b; Riley & Kohlstedt 1991; Waff & Faul 1992; Hirth &

Kohlstedt 1995a). However, there is some controversy about whether or not a melt phase with MORB chemistry should be used to represent the melt phase in the upper mantle. Green & Falloon (1998) concluded that the composition of natural (MORB) basalts is modified by fractionation before eruption and that these are not primary mantle melts and Falloon *et al.* (1999) show that experiments involving *in situ* melting of natural minerals generally fail to equilibrate completely and resulting melt compositions will be different to that of an equilibrated MORB source. Furthermore, natural melt compositions will evolve with continuing depletion of the mantle source rocks (see Green & Falloon (1998) for discussion). There is also experimental evidence that indicates that an initial melt phase at low melt fractions (<1%) may be more Si-rich than MORB (Schiano & Clocchiatti 1994; Baker *et al.* 1995; Raterron *et al.* 1997, 2000), although Falloon *et al.* (1996, 1999) argue that the high silica content may be a non-equilibrium feature. If small variations in the melt composition indeed influence the strength of the studied samples, it is feasible that mantle rheology will vary with melt composition during ongoing partial melting, which is not accounted for in present studies on partially molten mantle materials. Such strength variations would not only affect the source rock, but also the rocks that function as melt conduits and overlying rocks that act as reservoirs.

A first order estimate of the influence of melt composition on mechanical behaviour due to different diffusion properties can be made using the model evaluated by Bottinga & Weill (1972). Their model allows the estimation of the viscosity and therefore of the diffusion velocities through a melt phase as function of its composition. The viscosity of the melt can be approximated by:

$$\ln \eta = \sum_i X_i D_i$$

with X_i the mole fraction of component i and D_i an empirical value associated with component i (Bottinga & Weill 1972). In the viscosity calculations (table 7.4), any Al_2O_3 present in the melt phase was subsequently ascribed to Na_2O (NaAlO_2), CaO (CaAl_2O_4) and MgO (MgAl_2O_4) until all Al_2O_3 was assigned. The parameters for melts with SiO_2 -contents between 45 and 55 at% used in the viscosity calculations are given in table 7.2. Any pressure effects are neglected. After calculating a viscosity estimate, the viscosity can be related to diffusion coefficients for species in the melt phase using the Stokes-Einstein equation:

$$D = \frac{kT}{6\pi\eta r}$$

with D the diffusion coefficient (m^2/s), k the Boltzmann constant (1.4×10^{-23} J/K), T the temperature (K), η the viscosity (poise, $10 \text{ poise} \propto 1 \text{ Pa s}$), and r the radius of a diffusing particle. The effect of melt composition on diffusivity is illustrated using 5 basaltic melt compositions from the studies of Waff & Bulau (1982), Cooper & Kohlstedt (1984a), Kushiro (1986), Waff & Faul (1992), and Cmíral *et al.* (1998) (table 7.3). The resulting viscosities and derived (relative) diffusion coefficients for arbitrary diffusing particles in these melts are listed in table 7.4. From these estimates, it follows that diffusion coefficients in different basaltic melts used in previous studies

on partially molten olivine-bearing rocks may vary by a factor 1.2 to 4.5 for different temperatures and compositions.

Except for diffusion rates through (sub)grain melt tubes, the composition of the grain boundary films may also affect the creep rate accommodated by grain boundary diffusion. The strain rate related to a grain boundary diffusion process depends on the product of the diffusion constant (D) and the effective grain boundary width (δ) (Coble 1963). Changes in film thickness and thus grain boundary width due to compositional variations (Kleebe *et al.* 1992; Tanaka *et al.* 1994b) may therefore greatly influence creep rates. For example, Kleebe *et al.* (1992) showed the intergranular film thickness in various Si_3N_4 ceramics to vary between ~ 0.5 and ~ 3.5 nm depending on the type and concentration of a particular sintering additive. In the extreme case, this would result in a change of grain boundary diffusivity by a factor of ~ 15 . Small variations in melt composition can thus produce significant differences in creep strength in partially molten materials. To conclude, depending on the fraction of the deformation that is accommodated or affected by diffusion through the melt phase, strength differences between deformed partially molten materials may be (partly) explained by variations in melt composition.

The occurrence of stable melt tubes and nm-scale films along grain interfaces in olivine and olivine-orthopyroxene materials deformed at temperatures between 1200°C and 1300°C in this study and the results of Cmíral *et al.* (1998) on olivine-basalt samples, indicates that many previously reported experiments on olivine-bearing rocks in that temperature range will probably be melt-bearing as well. In other studies the presence of a small melt fraction was acknowledged in ‘nominally melt-free samples’ (Karato *et al.* 1986; Hirth & Kohlstedt 1995a, b) but the impact on the rheology was considered to be minimal and the melt content was ignored in the interpretation of the experimental results. Because the presence of a melt phase was either undetected or ignored in previous experimental work on polycrystalline materials without added basalt, it is difficult to assess the influence of such small melt fractions ($<1\%$) on rheology. Comparison of the results from partially molten polycrystals deforming in the dislocation creep field with single crystals may give an indication of the magnitude of the weakening caused by small melt fractions. However, effects due to the enhancement of grain boundary processes and grain to grain interactions will not be represented in single crystal experiments. A straightforward comparison is also hampered by the style of most single crystal experiments that involve orienting the crystals with respect to the compression direction, which is in contrast to the variable grain orientations in polycrystals.

Considering that ultrathin melt films and subgrain melt tubes are abundant in experimental upper mantle materials at temperatures exceeding 1200°C , the strengthening effect proposed by Karato (1986) and Hirth & Kohlstedt (1996) due to the incorporation of any intracrystalline water into a forming melt phase may need to be reconsidered. Karato (1986) estimates that at melt fractions of $\sim 0.1\%$, water is effectively removed from the olivine crystals, which results in strengthening of the rock. However, the rocks in studies that show the weakening effect of water (Chopra & Paterson 1981, 1984) also contain a small to moderate melt fraction which led Chopra & Paterson (1981, 1984) to the conclusion that the water-weakening effect was partly related to grain boundaries rather than intracrystalline processes. Hirth & Kohlstedt (1996) suggest that

while water will preferentially partition into the melt phase, thereby drying out the olivine crystals which can increasing their strength, melting will simultaneously cause a decrease in the viscosity of a partially molten rock by reducing the solid-solid contact area. Viscosity changes at the onset of melting will therefore be a balance between possible water related strengthening and melt-induced weakening. The observation that the presence of water influences the formation of subgrain boundaries (Mackwell *et al.* 1985, Van der Wal 1993) provides an additional mechanism to reduce the solid-solid olivine contacts by the formation of subgrain boundary melt channels. It is proposed that conclusions about the magnitude of water and melt related viscosity changes of partially molten rocks be made with caution as most reported experiments on wet and dry olivine-bearing rocks are likely to contain an unrecognised very small melt fraction that may affect the resulting creep strength.

Direct evidence on the actual melt content and melt distribution in the upper mantle is limited to observations on mantle xenoliths and mantle massifs in orogens. Wirth (1996), Franz & Wirth (1997), and Wirth & Franz (2000) report the presence of ultrathin melt films along grain interfaces in mantle xenoliths, which are interpreted to form due to decompression during uplift. Such films have not been found in orogenic peridotite bodies, but the detection of excess Al along olivine grain boundaries that were free of a melt layer in mantle xenoliths (Waff & Holdren 1981) indicates that ultrathin films may occur in the mantle. Identification of (former) melt microstructures in rocks that are now exposed in mantle massifs is not straightforward. The long geological residence and uplift times at sub-solidus conditions allow a former melt phase to crystallise in the pore-space and obscure the original melt microstructure and composition. In recent observations on mantle rocks in the Othris massif in Greece as well as in the Hilti Massif in Oman, patches of clinopyroxene, orthopyroxene, and plagioclase in between olivine crystals were interpreted to represent remains of a melt-phase that has impregnated the rocks just below the base of the crust (Dijkstra *et al.* 2000a, b). Details of the clinopyroxene-olivine grain interfaces and dihedral angles at olivine-clinopyroxene contacts resemble the olivine-melt contacts observed in the present experimental study. This includes the presence of crystallographically flat olivine faces in contact with intergranular clinopyroxene aggregates and cusps at the intersection of olivine subgrain boundaries with clinopyroxene crystals that resemble the morphology of subgrain melt tubes. These observations indicate that the melt microstructures observed in this study may also occur in partially molten regions of the upper mantle. The presence of subgrain boundary melt tubes in the upper mantle may thus provide pathways to enable melt segregation at the low melt fractions (< 0.1 vol%) that are indicated by isotope fractionation (Asmerom *et al.* 2000). The estimates of maximum melt retention in the partially molten upper mantle are below 4 vol% and it is therefore expected that the extensive weakening associated with higher melt fractions will only occur under special conditions. The inferred melt impregnation into peridotites just below the base of the crust by Dijkstra *et al.* (2000a) may provide an example for a natural setting where melt is accumulating and occupies more than 4 vol%.

7.4 Conclusions

The aim of this thesis was to establish the structure and distribution of the melt phase at the scale of the individual grains and assess the deformation mechanisms that govern rheology in partially molten olivine and olivine-orthopyroxene rocks. The work was carried out using two sets of experimental data on the deformation of partially molten olivine and olivine-orthopyroxene rocks at low melt fractions. The following conclusions can be drawn from the research presented in this thesis:

1. Melt and deformation microstructures were qualitatively very similar in all studied samples and observed differences in the mechanical behaviour between the sample sets could not be unequivocally attributed to specific microstructures or deformation mechanisms. The main differences were related to the melt distribution that tended to form larger melt concentrations and locally zones of high melt content and fine grain size in the olivine-orthopyroxene material with respect to the olivine samples. However, local high melt contents could not be identified as the main cause for the relative weakening of some materials as it did not produce universal weakening of all olivine-orthopyroxene materials studied. It is proposed that the strength differences are related to variations in local melt content as well as differences in melt composition that affect diffusion kinetics through the melt phase, solid-melt dihedral angles, and grain boundary width.
2. Deformation of polycrystalline olivine and olivine-orthopyroxene aggregates produces highly inhomogeneous dislocation microstructures that could not be related to the observed creep strength in two selected samples. In particular, dislocation microstructures in the weaker material did not show evidence for a preferential activation of $\mathbf{b}=[a]$ dislocations. The observation of areas inside larger crystals where subgrain boundaries show common rotation axes indicates that interactions with the adjacent grains have a larger influence on the activation of specific slip system than the externally imposed compression direction. An effect of the presence of a melt phase on the dislocation microstructure could not be shown.
3. In addition to the primary melt network consisting of grain edge melt tubes, melt layers, and larger melt inserts extending along several grain boundaries, two other types of nanometer-scale melt occurrences were identified: amorphous melt films and melt tubes associated with subgrain boundaries.
 - (a) Olivine grain interfaces in both deformed and statically annealed samples contained stable continuous ultrathin (1–3 nm) amorphous films with a composition similar to the melt in the larger grain edge tubes.
 - (b) Elongated melt tubes with typical dimensions of 100 x 500 nm (height x width) were present at intersections of subgrain boundaries with high angle grain boundaries. Their morphology is related to the misorientation accommodated by the subgrain boundaries. This relation results in decreasing subgrain-melt dihedral angles with increasing misorientation. Small variations in the subgrain melt tube morphology between samples

were interpreted to be related to differences in the melt composition. The decrease in dihedral angle in subgrain boundary melt tubes with increasing subgrain misorientation ultimately enables penetration of the melt phase into deforming olivine crystals along intersections of subgrains with misorientations exceeding 4° .

4. The presence of ultrathin melt films and subgrain boundary melt tubes in all studied samples indicates that these melt occurrences may be a universal feature in experimental olivine-bearing rocks deformed at temperatures exceeding 1200°C . This result implies that samples used in previous work on the experimental deformation of olivine-bearing rocks that were thought to be melt-free should actually be considered to be partially molten with very low melt fractions ($<1\%$).
5. It is difficult to assess if the presence of amorphous grain boundary films in olivine rocks has a weakening effect. In the available experimental data, virtually all samples probably have some form of amorphous grain boundary film so there is no data on the strength of film-free polycrystalline aggregates at high temperatures.

7.5 Suggestions for further research

The work presented in this thesis shows that while the mechanical behaviour of (partially molten) olivine-orthopyroxene materials can be readily determined experimentally, the actual microstructural processes that account for the macroscopic response to an applied stress remain uncertain. Furthermore, the effect of the presence and chemistry of small melt fractions on the mechanical behaviour of partially molten materials needs to be addressed, considering the ubiquitous presence of the nanometer-scale melt occurrences that were successfully established in this thesis. Below, some lines of research are proposed that can be attempted to address these issues.

1. The identification of activated intragranular deformation mechanisms in partially molten polycrystalline olivine-orthopyroxene rocks needs more attention. From the results it was concluded that indirect indications for the preferential activation of specific dislocation slip systems can be misleading. While identification of dislocations can be performed with TEM techniques, these methods do not allow determination of the spatial distribution of the dislocation microstructures in the samples. Instead, determination of the relative abundance of activated dislocation slip systems may be done by analysing subgrain misorientation- and rotation axis distributions using SEM EBSD analysis. Using this technique, the possible dependence of the relative abundance of specific dislocation slip systems on grain size and grain size distributions can be verified.
2. The mechanical response of the olivine-orthopyroxene materials to the presence of minor melt fractions could not be established as it was concluded that many olivine-orthopyroxene materials from earlier experimental studies at temperatures exceeding 1200°C are likely to contain small amounts ($<1\%$) of melt. In order to be able to estimate

mechanical weakening due to the presence of a melt phase, confirmed melt-free deformation experiments need to be performed.

3. To be able to perform melt-free experiments, the melt source and the pressure and temperature conditions at which melting first occurs should be established. This would involve determination of the melt source, melt composition, and pressure and temperature conditions at which melting first occurs. The occurrence of Al-Ca-bearing melt in the single-phase olivine materials studied in this thesis suggests that either small fragments of clinopyroxene or spinel were included in the starting powders, or that the Al and Ca impurities in the olivine crystals were effectively expelled to the grain boundaries. To avoid these uncertainties, initial experiments on synthetic high purity olivine-orthopyroxene materials with or without an added melt phase of known composition could be performed.
4. Because the results presented in this thesis suggest that small variations in melt composition may be an important parameter in the mechanical behaviour of partially molten upper mantle rocks, extra attention must be given to the melt composition. To date partially molten olivine-orthopyroxene specimens are often prepared by mixing crushed olivine and orthopyroxene crystals with a (synthetic) melt phase of MORB composition. Other, often assumed to be melt-free, experiments will contain a partial melt that was formed by *in situ* melting which assumedly produces a different composition. Experiments need to be designed to establish a possible rheological effect of the melt composition. This may be done by impregnating pure synthetic forsterite and forsterite-enstatite materials with small amounts of melt (0.5–1.0%) with different compositions followed by deformation. This would also allow chemical detection of a melt film along olivine-orthopyroxene grain interfaces, which was impossible in the materials studied in this thesis.
5. Experiments on materials containing a melt phase with (slightly) different melt compositions may also be used to investigate the possible connection between the apparent independence of the dislocation microstructure on the observed creep strength and the presence and composition of the melt phase.

References

- 't Hart, J. (1978). "The structural morphology of olivine-type minerals. A qualitative and quantitative approach and a comparison of theoretical morphologies with habits of natural and synthetic crystals." Ph.D. thesis, Faculteit der wiskunde en natuurwetenschappen, Rijksuniversiteit Leiden, Leiden. 139 pp.
- Anderson, D. L., Spetzler, H. (1970). "Partial melting and the low-velocity zone." *Phys. Earth Planet. Interiors* 4 p.62-64.
- Anderson, D. L., Sammis, C. (1970). "Partial melting in the upper mantle." *Phys. Earth Planet. Interiors* 3 p.41-50.
- Ashby, M. F. (1970). "The deformation of plastically non-homogeneous materials." *Phil. Mag.* 21 p.399-442.
- Asmerom, Y., Cheng, H., Thomas, R., Hirschmann, M., Edwards R.L. (2000). "Melting of the Earth's lithospheric mantle inferred from protactinium-thorium-uranium isotopic data." *Nature* 406 p.293-296.
- Bai, Q., Mackwell, S.J., Kohlstedt, D.L. (1991). "High-Temperature creep of olivine single crystals 1. Mechanical results for buffered samples." *J. Geophys. Res.* 96 (B2) p.2441-2463.
- Bai, Q., Kohlstedt, D.L. (1992). "High-temperature creep of olivine single crystals, 2. Dislocation structures." *Tectonophysics* 206 p.1-29.
- Bai, Q., Jin, Z.M., Green II, H.W. (1997). "Experimental investigation of the rheology of partially molten peridotite at upper mantle pressure and temperatures. In: Deformation-enhanced fluid transport in the Earth's crust and mantle." Ed.: M. B. Holness. London, Chapman & Hall. p.40-61.
- Baker, M. B., Hirschmann M.M., Ghiorso, M.S., Stolper, E.M. (1995). "Compositions of near-solidus peridotite melts from experiments and thermodynamic calculations." *Nature* 375 p.308-311.
- Beeman, M. L., Kohlstedt, D.L. (1993). "Deformation of fine-grained aggregates of olivine plus melt at high temperatures and pressures." *J. Geophys. Res.* 98 (B4) p.6443-6452.
- Beeré, W. (1975). "A unifying theory of the stability of penetrating liquid phases and sintering pores." *Acta Metall.* 23 p.131-138.
- Bethe, H. A. (1928). "Theorie der Beugung von Elektronen an Kristallen." *Ann. Phys. (Leipzig)* 87 p.55-128.
- Boland, J. N., Buiskool Toxopeus, J.M.A. (1977). "Dislocation deformation mechanisms in peridotite xenoliths in kimberlites." *Contrib. Mineral. Petrol.* 60 p.17-30.
- Bolt, B. A. (1982). "Inside the earth, evidence from earthquakes". W.H. Freeman and company, San Fransisco. 191 pp.
- Bottinga, Y., Weill, D.F. (1972). "The viscosity of magmatic silicate liquids: a model for calculation". *Am. J. Sci.* 272 p.438-475.
- Bruley, J., Tanaka, I., Kleebe, H.J., Ruhle, M. (1994). "Chemistry of grain boundaries in calcia doped silicon nitride studied by spatially resolved electron energy loss spectroscopy." *Anal. Chim. Acta* 297 p.97-108.
- Buiskool Toxopeus, J. M. A., Boland, J.N. (1976). "Several types of natural deformation in olivine, an electron microscopy study." *Tectonophysics* 32 p.209-233.
- Bulau, J. R., Waff, H.S., Tyburczy, J.A. (1979). "Mechanical and thermodynamic constraints on fluid distribution in partial melts." *J. Geophys. Res.* 84 (B11) p.6102-6108.
- Burton, B. (1975). "The interaction of dislocations and inclusions during creep." *Phil. Mag.* 31 p.1289-1294.
- Bussod, G. Y., Christie, J.M. (1991). "Textural development and melt topology in spinel lherzolite experimentally deformed at hypersolidus conditions." *J. Petrology* p.17-39.
- Carter, C. B., Sass, S.L. (1981). "Electron diffraction and microscopy techniques for studying grain-boundary structure." *J. Am. Ceram. Soc.* 64 (6) p.335-345.
- Carter, N. L., Kronenberg, A.K., Ross, J.V., Wiltschko, D.V. (1990). "Control of fluids on deformation of rocks. In: Deformation mechanisms, rheology and tectonics." Ed.: R. J. Knipe, Rutter, E.H., Geological society special publication. 54. p.1-13.
- Chakraborty, S. (1997). "Rates and mechanisms of Fe-Mg interdiffusion in olivine at 980-1300C." *J. Geophys. Res.* 102 (B6) p.12317-12331.
- Champness, P. E., Devenish, R.W. (1990). "Elemental mass loss in silicate minerals during X-ray analysis." *Trans. R. Microsc. Soc.* 1 p.177-180.
- Champness, P. E., Devenish, R.W. (1992). "Radiation damage in silicate minerals: implications for AEM." *Electron Microscopy* 2 (Proc. Xth Eur. Congr. on Electron Microscopy. Granada) p.541-545.
- Chopra, P. N., Paterson, M.S. (1981). "The experimental deformation of dunite." *Tectonophysics* 78 p.453-473.

- Chopra, P. N., Kohlstedt, D.L. (1983).** "The influence of wet basaltic melt on the flow properties of fine grained polycrystalline olivine." *EOS* 64 (18) p.323.
- Chopra, P. N., Paterson, M.S. (1984).** "The role of water in the deformation of dunite." *J. Geophys. Res.* 89 (B9) p.7861-7876.
- Cinibulk, M. K., Kleebe, H.J., Schneider, G.A., Rühle, M. (1993a).** "Amorphous intergranular films in silicon nitride ceramics quenched from high temperatures." *J. Am. Ceram. Soc.* 76 (11) p.2801-2808.
- Cinibulk, M. K., Kleebe, G.A., Rühle, M. (1993b).** "Quantitative comparison of TEM techniques for determining amorphous intergranular film thickness." *J. Am. Ceram. Soc.* 76 (2) p.426-432.
- Clarke, D. R. (1978).** "Determination of grain boundary segregation by combined X-Ray microanalysis and lattice fringe imaging." *SEM* 1 p.77-84.
- Clarke, D. R. (1979a).** "High-Resolution Techniques and Application to Nonoxide Ceramics." *J. Am. Ceram. Soc.* 62 (5-6) p.236-246.
- Clarke, D. R. (1979b).** "On the detection of thin intergranular films by electron microscopy." *Ultramicroscopy* 4 p.33-44.
- Clarke, D. R. (1980).** "Observation of microcracks and thin intergranular films in ceramics by transmission electron microscopy." *J. Am. Ceram. Soc.* 63 (1-2) p.104-106.
- Clarke, D. R. (1985).** "Grain boundaries in polyphase ceramics." *J. de Physique* 46 p.(C4) 51-59.
- Clarke, D. R. (1987).** "On the equilibrium thickness of intergranular glass phases in Ceramic Materials." *J. Am. Ceram. Soc.* 70 (1) p.15-22.
- Clarke, D. R., Shaw, T.M., Philipse, A.P., Horn, R.G. (1993).** "Possible electrical double layer contribution to the equilibrium thickness of intergranular glass films in polycrystalline ceramics." *J. Am. Ceram. Soc.* 76 (5) p.1201-1204.
- Cliff, G., Lorimer, G.W. (1975).** "The quantitative analysis of thin specimens." *J. Microsc.* 103 p.203-207.
- Cmiral, M. (1998).** "Melt distribution in peridotite, an experimental and electron microscopic study." Ph.D. thesis, Department of Earth Sciences, Australian National University, Canberra. 92 pp.
- Cmiral, M., FitzGerald, J.D., Faul, U.H., Green, D.H. (1998).** "A close look at dihedral angles and melt geometry in olivine-basalt aggregates: a TEM study." *Contrib. Miner. Petrol.* 130 p.336-345.
- Coble, R. L. (1963).** "A model for boundary diffusion controlled creep in polycrystalline materials." *J. Appl. Phys.* 34 p.1679-1682.
- Cooper, R. F., Kohlstedt, D.L. (1982).** "Interfacial energies in the olivine-basalt system." *Adv. Earth. Planet. Science* 12 p.217-228.
- Cooper, R. F., Kohlstedt, D.L. (1984a).** "Sintering of olivine and olivine-basalt aggregates." *Phys. Chem. Minerals* 11 p.5-16.
- Cooper, R. F., Kohlstedt, D.L. (1984b).** "Solution-Precipitation enhanced diffusional creep of partially molten olivine-basalt aggregates during hot-pressing." *Tectonophysics* 107 p.207-233.
- Cooper, R. F., Kohlstedt, D.L. (1986).** "Rheology and structure of olivine-basalt partial melts." *J. Geophys. Res.* 91 (B9) p.9315-9323.
- Cooper, R. F., Kohlstedt, D.L., Chyung, C.K. (1989).** "Solution-precipitation enhanced creep in solid-liquid aggregates which displays a non zero dihedral angle." *Acta Metall.* 37 p.1759-1771.
- Daines, M. J., Richter, F.M. (1988).** "An experimental method for directly determining the interconnectivity of melt in a partially molten system." *Geophys. Res. Lett.* 15 (B13) p.1459-1462.
- Daines, M. J., Kohlstedt, D.L. (1996).** "Rheology of olivine-pyroxene aggregates." *EOS* 77 (46) p.F711.
- Daines, M. J., Kohlstedt, D.L. (1997).** "Influence of deformation on melt topology in peridotites." *J. Geophys. Res.* 102 (B5) p.10257-10271.
- Daines, M. J. (1997).** "Melt distribution in partially molten peridotites: implications for permeability and melt migration in the upper mantle." In: *Deformation enhanced fluid transport in the Earth's crust and mantle.* Ed.: M. B. Holness. London, Chapman & Hall. p.62-81.
- Darot, M., Gueguen, Y. (1981).** "High-temperature creep of forsterite single crystals." *J. Geophys. Res.* 86 (B7) p.6219-6234.
- De Bresser, J. H. P. (1996).** "Steady state dislocation densities in experimentally deformed calcite materials: single crystals versus polycrystals." *J. Geophys. Res.* 101 p.22189-22201.

- De Kloe, R., Drury, M.R., Van Roermund, H.L.M. (2000). "Evidence for stable grain boundary melt films in experimentally deformed olivine-orthopyroxene rocks." *Phys. Chem. Minerals* 27 p.480-494.
- De Kloe, J. (2000). "Pellet-plasma interaction in a tokamak". Ph.D.-thesis, FOM-instituut voor Plasmafysica, Nieuwegein. 164 pp.
- Deer, W. A., Howie, R.A., Zussman, J. (1992). "An introduction to the rock-forming minerals, 2nd edition." Longman Scientific and Technical, Harlow, UK. 696 pp.
- Dell'Angelo, L. N., Tullis, J., Yund, R.A. (1987). "Transition from dislocation creep to melt-enhanced diffusion creep in fine-grained granitic aggregates." *Tectonophysics* 139 p.325-332.
- Devenish, R. W., Champness, P.E. (1992). "The rate of mass loss in silicate minerals during X-ray analysis." *Inst. Phys. Conf. Ser.* 130 (Proc. XIIIth ICXOM,) p.233-236.
- Dijkstra, A. H., Drury, M.R., Vissers, R.L.M. (2000a in press). "Structural petrology of plagioclase peridotites in the West Othris Mountains (Greece): Melt impregnation in mantle lithosphere." *J. Petrology* .
- Dijkstra, A. H., Drury, M.R., Frijhoff, R. (2000b in prep). "Geological evidence for melt weakening in natural peridotites: The Hilti Massif, Oman Ophiolite." .
- Doukhan, N., Doukhan, J.C., Ingrin, J., Jaoul, O., Raterron, P. (1993). "Early partial melting in pyroxenes." *Am. Miner.* 78 p.1246-1256.
- Doyle, P. A., Turner, P.S. (1968). "Relativistic Hartree-Fock X-Ray and electron scattering factors." *Acta Cryst.* A24 p.390-397.
- Drury, M. R., Roermund H.L.M. van (1989). "Fluid assisted recrystallization in upper mantle peridotite xenoliths from kimberlites." *J. Petrology.* 30 p.133-152.
- Drury, M. R., FitzGerald, D.F. (1996). "Grain boundary melt films in upper mantle rocks." *Geophys. Res. Lett.* 23 (B7) p.701-704.
- Drury, M. R., FitzGerald, J.D. (1998). "Mantle rheology: insights from laboratory studies of deformation and phase transition." In: *The Earth's Mantle: Composition, structure and evolution.* Ed.: I. Jackson. Cambridge UK, Cambridge University Press. p.503-559.
- Durham, W. B., Goetze, C. (1977a). "Plastic flow of oriented single crystals of olivine -1- mechanical data." *J. Geophys. Res.* 82 (36) p.5737-5753.
- Durham, W. B., Goetze, C. (1977b). "Plastic flow of oriented single crystals of olivine -2- observations and interpretations of the dislocation structures." *J. Geophys. Res.* 82 (36) p.5755-5770.
- Edington, J. W. (1975). "Electron diffraction in the electron microscope." The Macmillan Press LTD, London. 122 pp.
- Edington, J. W. (1976). "Practical electron microscopy in materials science." N.V. Philips' Gloeilampenfabrieken, Eindhoven, 344 pp.
- Egerton, R. F. (1986). "Electron energy-loss spectroscopy in the electron microscope." Plenum press, New York. 410 pp.
- Eibl, O. (1993a). "New method for absorption correction in high-accuracy, quantitative EDX microanalysis in the TEM including low-energy X-ray lines." *Ultramicroscopy* 50 p.179-188.
- Eibl, O. (1993b). "Improved, parameterless, constant-current method for absorption correction in quantitative EDX microanalysis in the TEM." *Ultramicroscopy* 50 p.203-205.
- Falloon, T. J., Green, D.H., O'Neill, H. St C., Ballhaus, C.G. (1996). "Quest for low-degree mantle melts." *Nature* 381 p.285-286.
- Falloon, T. J., Green, D.H., Danyushevsky, Faul, U.H. (1999). "Peridotite melting at 1.0 and 1.5 GPa: an experimental evaluation of techniques using diamond aggregates and mineral mixes for determination of near-solidus melts." *J. Petrology* 40 (9) p.1343-1375.
- Farver, J. R., Yund, R.A., Rubie, D.C. (1994). "Magnesium grain-boundary diffusion in forsterite aggregates at 1000-1300 C and 0.1 MPa to 10 GPa." *J. Geophys. Res.* 99 (B10) p.19809-19819.
- Faul, U. H., Toomey, D.R., Waff, H.S. (1994). "Intergranular basaltic melt is distributed in thin, elongated inclusions." *Geophys. Res. Lett.* 21 (1) p.29-32.
- Faul, U. H. (1997). "Permeability of partially molten upper mantle rocks from experiments and percolation theory." *J. Geophys. Res.* 102 p.10299-10311.
- Faul, U. H., FitzGerald, J.D. (1999). "Grain misorientations in partially molten olivine aggregates: an electron backscatter diffraction study." *Phys. Chem. Minerals* 26 p.187-197.
- Faul, U. H. (2000). "Constraints on the melt distribution in anisotropic polycrystalline aggregates undergoing grain growth." In: *Physics and chemistry of partially molten rocks.* Ed.: N. Bagdassarov, Laporte D., Thompson, A.B. Dordrecht, Kluwer Academic Publishers. 11. p.67-92.

- Fliervoet, T. F., White, S.H. (1995).** "Quartz deformation in a very fine grained quartzo-feldspathic mylonite: A lack of evidence for dominant grain boundary sliding deformation." *J. Struct. Geol.* 17 (8) p.1095-1110.
- Fliervoet, T. F., Drury, M.R., Chopra, P.N. (1999).** "Crystallographic preferred orientations and misorientations in some olivine rocks deformed by diffusion or dislocation creep." *Tectonophysics* 303 p.1-27.
- Franz, L., Wirth, R. (1997).** "Thin intergranular melt films and melt pockets in spinel peridotite xenoliths from the Rhon area (Germany): early stage of melt generation by grain boundary melting." *Contrib. Mineral. Petrol.* 129 p.268-283.
- Fujii, N., Osamura, K., Takahashi, E (1986).** "Effect of water saturation on the distribution of partial melt in the olivine-pyroxene-plagioclase system." *J. Geophys. Res.* 91 (B9) p.9253-9259.
- Gifkins, R. C. (1970).** "Optical microscopy of metals." Elsevier, New York. 208 pp.
- Gifkins, R. C. (1976).** "Grain-Boundary Sliding and its accomodation during Creep and Superplasticity." *Metall. Trans.* A 7A p.1225-1232.
- Glicksman, M. E., Vold, C.L. (1972).** "Heterophase dislocations-an approach towards interpreting high-temperature grain boundary behaviour." *Surface science* 31 p.50-67.
- Goetze, C., Kohlstedt, D.L. (1973).** "Laboratory study of dislocation climb and diffusion in olivine." *J. Geophys. Res.* 78 (B26) p.5961-5971.
- Goetze, C. (1977).** "A brief summary of our present day understanding of the effect of volatiles and partial melt on the mechanical properties of the upper mantle." In: High-pressure research, applications in geophysics. Ed.: M. H. Manghnani, Akimoto, S. New York, Academic Press Inc. p.3-23.
- Goldstein, J. I. (1979).** "Principles of thin film microanalysis. In: *Introduction to analytical electron microscopy.*" Ed.: J. J. Hren, Goldstein, J.I., Joy, D.C. New York and London, Plenum press. p.83-120.
- Grant-Norton, M., Carter, C.B. (1990).** "Interfaces in structural ceramics." *MRS bulletin* (october) p.51-59.
- Green, D. H., Falloon, T.J. (1998).** "Pyrolyte: A Ringwood concept and its current expression." In: *The Earth's Mantle: Composition, Structure, and Evolution.* Ed.: I. Jackson. Cambridge, Cambridge University Press. p.311-378.
- Green, H. W., Radcliffe, S.V. (1972).** "Dislocation mechanisms in olivine and flow in the upper mantle." *Earth Planet. Sci. Lett.* 15 p.239-247.
- Green, H. W., Borch, R.S. (1989).** "A new molten salt cell for precision stress measurement at high pressure." *Eur. J. Mineral.* 1 p.213-219.
- Grimmer, H. (1980).** "A unique description of the relative orientation of neighbouring grains." *Acta Cryst.* A36 p.382-389.
- Grujic, D., Mancktelow, N.S. (1998).** "Melt-bearing shear zones:analogue experiments and comparison with examples from southern Madagascar." *J. Struct. Geol.* 20 (6) p.673-680.
- Gueguen, P. Y., Darot, M. (1982).** "Les dislocations dans la forstérite déformée à haute température." *Phil. Mag.* A 45 (3) p.419-442.
- Gutenberg, B. (1954).** "Low-velocity layers in the Earth's mantle." *Geol. Soc. America Bull.* 65 p.337-348.
- Hacker, B. R., Christie, J.M. (1991).** "Observational evidence for a possible new diffusion path." *Science* 251 p.67-70.
- Hess, P. C. (1994).** "Thermodynamics of thin fluid films." *J. Geophys. Res.* 99 (B4) p.7219-7229.
- Hirth, G., Kohlstedt, D.L. (1995a).** "Experimental constraints on the dynamics of the partially molten upper mantle: deformation in the diffusion creep regime." *J. Geophys. Res.* 100 (B2) p.1981-2001.
- Hirth, G., Kohlstedt, D.L. (1995b).** "Experimental constraints on the dynamics of the partially molten upper mantle 2. Deformation in the dislocation creep regime." *J. Geophys. Res.* 100 (B8) p.15441-15449.
- Hirth, G., Kohlstedt, D.L. (1996).** "Water in the upper mantle: implications for rheology, melt extraction and the evolution of the lithosphere." *Earth Planet. Sci. Lett.* 144 p.93-108.
- Hitchings, R. S., Paterson, M.S., Bitmead, J. (1989).** "Effects of iron and magnetite additions in olivine-pyroxene rheology." *Phys. Earth Planet. Interiors* 55 p.277-291.
- Hofer, F., Warbichler, P. (1996).** "Application of electron spectroscopic imaging in materials science." *Philips electron optics bulletin* 134 p.1-8.

- Hofmann, A. W. (1980). "Diffusion in natural silicate melts: a critical review." In: Physics of magmatic processes. Ed.: R. B. Hargraves. Princeton, New Jersey, Princeton U.P. p.385-417.
- Houlier, B., Jaoul, O., Abel, F., Liebermann, R.C. (1988). "Oxygen and silicon self diffusion in natural olivine at $T = 1300\text{C}$." Phys. Earth Planet. Interiors 50 p.240-250.
- Howie, A., Whelan, M.J. (1962). "Diffraction contrast of electron microscope images of crystal lattice defects III. Results and experimental confirmation of the dynamical theory of dislocation image contrast." Proc. Roy. Soc. Lond. A. 267 p.206-230.
- Huebner, J. S. (1987). "Use of gas mixtures at low pressure to specify oxygen and other fugacities of furnace atmospheres." In: Hydrothermal experimental techniques. Ed.: G. C. Ulmer, Barnes, H.L. New York (NY), John Wiley & Sons. p.20-60.
- Hull, D. (1975). "Introduction to dislocations." Pergamon Press, Oxford. 271 pp.
- Jin, Z. M., Green, H.W., Yi Zhou (1994). "Melt topology in partially molten mantle peridotite during ductile deformation." Nature 372 p.164-167.
- Johnson, K. T., Dick, H.J., Shimizu, N. (1990). "Melting in the oceanic upper mantle: an ion microprobe study of diopsides in abyssal peridotites." J. Geophys. res. 95 (B3) p.2661-2678.
- Jung, H., Waff, H.S. (1998). "Olivine crystallographic control and anisotropic melt distribution in ultramafic partial melts." J. Geophys. Res. 25 (B15) p.2901-2904.
- Jurewicz, S. R., Jurewicz, A.J.G. (1986). "Distribution of apparent angles on random sections with emphasis on dihedral angle measurement." J. Geophys. Res. 91 (B9) p.9277-9282.
- Karato, S., Toriumi, M., Fujii, T. (1980). "Dynamic recrystallization of olivine single crystals during high-temperature creep." Geophys. Res. Lett. 7 (9) p.649-652.
- Karato, S. (1986). "Does partial melting reduce the creep strength of the upper mantle?" Nature 319 p.309-310.
- Karato, S., Rubie, D.C., Yan, H. (1993). "Dislocation recovery in olivine under deep upper mantle conditions: Implications for creep and diffusion." J. Geophys. Res. 98 (B6) p.9761-9768.
- Karato, S., Wu, P. (1993). "Rheology of the upper mantle: a synthesis." Science 260 p.771-778.
- Karato, S. I., Ogawa, M. (1982). "High-pressure recovery of olivine: implications for creep mechanisms and creep activation volume." Phys. Earth Planet. Interiors 28 p.102-117.
- Karato, S. I., Paterson, M.S., FitzGerald, J.D. (1986). "Rheology of synthetic olivine aggregates: influence of grain size and water." J. Geophys. Res. 91 (B8) p.8151-8176.
- Kelemen, P. B., Hitehead, J.A., Aharonov, E., Jordahl, K., A. (1995). "Experiments on flow focussing in soluble porous media, with applications to melt extraction from the mantle." J. Geophys. Res. 100 (B1) p.475-496.
- Kelemen, P. B., Hirth, G., Shimizu, N., Spiegelman, M., Dick, H.J.B. (1997). "A review of melt migration processes in the adiabatically upwelling mantle beneath oceanic spreading ridges." Phil. Trans. R. Soc. Lond. A 355 p.283-318.
- Kern, H., Burlini, L., Ashchepkov, I.V. (1996). "Fabric-related seismic anisotropy in upper-mantle xenoliths: evidence from measurements and calculations." Phys. Earth Planet. Interiors 95 p.195-209.
- Kingery, W. D., Bowen, H.K., Uhlman, D.R. (1976). "Introduction to ceramics." Wiley, New York. 1056 pp.
- Kirby, S. H., Wegner, M.W. (1978). "Dislocation Substructure of mantle-derived olivine as revealed by selective chemical etching and transmission electron microscopy." Phys. Chem. Minerals 3 p.309-330.
- Kleebe, H.-J., Hoffmann, M.J., Rühle, M. (1992). "Influence of secondary phase chemistry on grain boundary film thickness in silicon nitride." Z. Metallk. 83 p.610-617.
- Kleebe, H.-J., Cinibulk, M.K., Tanaka, I., Bruley, J., Vetrano, J.S., Rühle, M. (1994a). "High resolution electron microscopy studies on silicon nitride ceramics." NATO Advanced Study Institute Series, Series E, Applied Sciences 276 p.259-274.
- Kleebe, H. J., Cinibulk, M.K., Cannon, R.M., Rühle, M. (1993). "Statistical analysis of the intergranular film thickness in silicon nitride ceramics." J. Am. Ceram. Soc. 76 (8) p.1969-1977.
- Kleebe, H. J., Bruley, J., Rühle, M. (1994b). "HREM and AEM studies of Yb₂O₃-fluxed Silicon Nitride ceramics with and without CaO addition." J. Eur. Ceram. Soc. 14 p.1-11.
- Knipe, R. J., White, S.H. (1978). "On the deformation of quartz containing bubbles." J. Geol. Soc. Lond. 135 p.313-316.
- Kohlstedt, D. L., Weathers, M.S. (1980). "Deformation-induced microstructures, paleopiezometers, and differential stresses in deeply eroded fault zones." J. Geophys. Res. 85 (B11) p.6269-6285.

- Kohlstedt, D. L., Nichols, H.P.K., Hornack, P. (1980). "The effect of pressure on the rate of dislocation recovery in olivine." *J. Geophys. Res.* 85 (B6) p.3122-3130.
- Kohlstedt, D. L. (1985). *Electron diffraction and weak-beam microscopy*. In: Short course in applications of electron microscopy in the Earth Sciences. Ed.: White J.C., Mineralogical association of Canada. p.31-62.
- Kohlstedt, D. L. (1990). "Chemical analysis of grain boundaries in an olivine-basalt aggregate using high-resolution, analytical electron microscopy." *Geophysical Monograph* 56 p.211-218.
- Kohlstedt, D. L. (1992). "Structure, rheology and permeability of partially molten rocks at low melt fractions." *Geophysical Monograph* 71 p.103-121.
- Kohlstedt, D. L., Zimmerman, M.E. (1996). "Rheology of partially molten mantle rocks." *Annu. Rev. Earth Planet. Sci.* 24 p.41-62.
- Kohlstedt, D. L., bai, Q., Wang, Z.-C, Mai, S. (2000). "Rheology of partially molten rocks. In: *Physics and chemistry of partially molten rocks*." Ed.: N. Bagdassarov, Laporte D., Thompson, A.B. Dordrecht, Kluwer Academic Publishers. 11. p.3-28.
- Kushiro, I. (1986). "Viscosity of partial melts in the upper mantle." *J. Geophys. Res.* 91 (B9) p.9343-9350.
- Laporte, D. (1994). "Wetting behavior of partial melts during crustal anatexis: the distribution of hydrous silicic melts in polycrystalline aggregates of quartz." *Contrib. Mineral. Petrol.* 116 p.486-499.
- Laporte, D., Provost, A. (2000). "The grain-scale distribution of silicate, carbonate and metallosulfide partial melts: a review of theory and experiments. In: *Physics and chemistry of partially molten rocks*." Ed.: N. Bagdassarov, Laporte D., Thompson, A.B. Dordrecht, Kluwer Academic Publishers. 11. p.93-140.
- Li, J., McCartney, M.R., Dunin-Borkowski, R.E., Smith, D.J. (1999). "Determination of mean inner potential of germanium using off-axis electron holography." *Acta Cryst.* A55 p.652-658.
- Lloyd, G. E., Farmer, A.B., Mainprice, D. (1997). "Misorientation analysis and the formation of subgrain and grain boundaries." *Tectonophysics* 279 p.55-78.
- Loretto, M. H. (1984). "Electron beam analysis of materials." Chapman and Hall, London. 210 pp.
- Mackwell, S., Lawlis, J., Bystricky, M. (1999). "Experimental deformation of two-phase aggregates." *Eos* 80 p.S346.
- Mackwell, S. J., Kohlstedt, D.L., Paterson, M.S. (1985). "The role of water in the deformation of olivine single crystals." *J. Geophys. Res.* 90 (B13) p.11319-11333.
- Mackwell, S. J. (1991). "High-temperature rheology of enstatite: implications for creep in the mantle." *Geophys. Res. Lett.* 18 (11) p.2027-2030.
- McDonnell, R. D. (1997). "Deformation of fine-grained synthetic peridotite under wet conditions." Ph.D. thesis, Faculty of Earth Sciences, Utrecht University, 195 pp.
- McDonnell, R. D., Peach, C.J., Spiers, C.J. (1999). "Flow behavior of fine-grained synthetic dunite in the presence of 0.5 wt% H₂O." *J. Geophys. Res.* 104 (B8) p.17823-17845.
- McKenzie, D. P. (1984). "The generation and compaction of partially molten rock." *J. Petrology.* 25 (3) p.713-765.
- McKenzie, D. P. (1987). "The compaction of igneous and sedimentary rocks." *J. geol. Soc. London* 144 p.299-307.
- McKenzie, D. P. (1989). "Some remarks on the movement of small melt fractions in the mantle." *Earth Planet. Sci. Lett.* 95 p.53-72.
- McLaren, A. C. (1991). "Transmission electron microscopy of minerals and rocks." Cambridge University Press, Cambridge. 387 pp.
- Mercier, J. C. C. (1985). "Olivine and Pyroxenes. In: *Preferred orientation in deformed metals and rocks: an introduction to modern texture analysis*." Ed.: H. R. Wenk. London, Academic Press. p.407-430.
- Muan, A., Osborn, E.F. (1965). "Phase equilibria among oxides in steelmaking." Addison-Wesley, Reading, MA. 236 pp.
- Ness, J. N., Stobbs, W.M., Page, T.F. (1986). "A TEM Fresnel diffraction-based method for characterizing thin grain-boundary and interfacial films." *Phil. Mag.* A 54 p.679-702.
- Nicolas, A. (1978). "Stress estimates from structural studies in some mantle peridotites." *Phil. Trans. R. Soc. Lond. A.* 288 p.49-57.
- Paterson, M. S. (1969). "The ductility of rocks." In: *Physics of strength and plasticity*. Ed.: A. S. Argon. Cambridge (Mass), MIT press. p.377-392.
- Peacor, D. R. (1992). "Analytical electron microscopy: X-Ray analysis. In: *Minerals and reactions at the atomic scale: transmission electron microscopy*." Ed.: B. P.R. Washington, Mineralogical society of America. 27. p.113-140.

- Phahey, P., Dollinger, G., Christie, J. (1972). "Transmission electron microscopy of experimentally deformed olivine crystals." Geophysical Monograph 16 p.117-138.
- Pharr, G. M., Ashby, M.F. (1983). "On creep enhanced by a fluid phase." Acta Metall 31 p.129-138.
- Poirier, J.-P. (1975). "On the slip systems of olivine." J. Geophys. Res. 80 (29) p.4059-4061.
- Press, F. (1959). "Some implications on mantle and crustal structure from G-waves and love waves." J. Geophys. Res. 64 (5) p.565-568.
- Prior, D. J., Trimby, P.W., Weber, U.D., Dingley, D.J. (1996). "Orientation contrast imaging of microstructures in rocks using foreshatter detectors in the scanning electron microscope." Mineral. Mag. 60 p.859-869.
- Prior, D. J. (1999). "Problems in determining the misorientation axes for small angular misorientations using electron backscatter diffraction in the SEM." J. Microsc. 195 (3) p.217-225.
- Raj, R. (1981). "Morphology and stability of the glass phase in glass-ceramic systems." J. Am. Ceram. Soc. 64 (5) p.245-248.
- Raj, R. (1982). "Creep in Polycrystalline Aggregates by Matter Transport Through a Liquid Phase." J. Geoph. Res. 87 (B6) p.4731-4739.
- Raleigh, C. B. (1968). "Mechanisms of plastic deformation of olivine." J. Geophys. Res. 73 (14) p.5391-5406.
- Raleigh, C. B., Kirby, S.H. (1970). "Creep in the upper mantle." Mineral. Soc. Amer. Spec. Pap. 3 p.113-121.
- Randle, V. (1992). "Microtexture determination and its applications." The Institute of Metals, London. 174 pp.
- Rasmussen, D. R., Simpson, Y.K., Kilaas, R., Carter, C.B. (1989). "Contrast effects at grooved interfaces." Ultramicroscopy 30 p.52-57.
- Raterron, P., Bussod, G.Y., Doukhan, N., Douhan, J.C. (1997). "Early partial melting in the upper mantle: an A.E.M. study of a lherzolite experimentally annealed at hypersolidus conditions." Tectonophysics 279 p.79-91.
- Raterron, P., Chopra, P., Doukhan, J.C. (2000). "SiO₂ precipitation in olivine: ATEM investigation of two dunites annealed at 300 MPa in hydrous conditions." Earth Planet. Sci. Lett. 180 p.415-423.
- Read, W. T., Shockley, W. (1950). "Dislocation models of crystal grain boundaries." Phys. Rev. 78 (3) p.275-289.
- Ricoult (1979). "Experimental annealing of a natural dunite." Bull. Minéral. 102 p.86-91.
- Ricoult, D. (1978). "Recuit experimental de l'olivine." Ph.D.-thesis, L'Institute des sciences de la nature, L'Universite de Nantes, Nantes. 55 pp.
- Riley, G. N., Kohlstedt, D.L., Richter, F.M. (1990). "Melt migration in a silicate liquid-olivine system: An experimental test of compaction theory." J. Geophys. Res. 17 p.2101-2104.
- Riley, G. N., Kohlstedt, D.L. (1991). "Kinetics of melt migration in upper mantle-type rocks." Earth Planet. Sci. Lett. 105 p.500-521.
- Ross, J. V., Ave Lallemand, H. G., Carter, N.L. (1980). "Stress dependence of recrystallized-grain and subgrain size in olivine." Tectonophysics 70 p.39-61.
- Rutter, E. H. (1997). "The influence of deformation on the extraction of crustal melts: a consideration of the role of melt-assisted granular flow." In: Deformation-enhanced fluid transport in the Earth's crust and mantle. Ed.: M. B. Holness. London, Chapman & Hall. 8. p.82-110.
- Salters, V. J. M., Hart, S.R. (1989). "The hafnium paradox and the role of garnet in the source of mid-ocean-ridge basalts." Nature 342 p.420-422.
- Schiano, P., Clochiatti, R. (1994). "Worldwide occurrence of silica-rich melts in sub-continental and sub-oceanic mantle materials." Nature 368 p.621-624.
- Schmeling, H. (1985). "Partial melt below Iceland: a combined interpretation of seismic and conductivity data." J. Geophys. Res. 90 (B12) p.10105-10116.
- Schmidt, N. H., Olesen, N.O. (1989). "Computer aided determination of crystal-lattice orientation from electron-channeling patterns in the SEM." Can. Mineral 27 p.15-22.
- Seifert, F., Mysen, B.O., Virgo, D. (1982). "Three-dimensional network structure of quenched melts (glass) in the systems SiO₂-NaAlO₂, SiO₂-CaAl₂O₄ and SiO₂-MgAl₂O₄." Am. Mineral. 67 p.696-717.
- Sheridan, P. J. (1989). "Determination of experimental and theoretical KaSi factors for a 200-kV analytical electron microscope." J. Electron Micr. Tech. 11 p.41-61.
- Shimozuru, D. (1963). "The low velocity zone and temperature distribution in the upper mantle of the earth." J. Phys. Earth 11 (1) p.19-24.

- Skrotzki, W. (1994).** "Defect structure and deformation mechanisms in naturally deformed augit and enstatite." *Tectonophysics* 229 p.43-68.
- Smith, C. S. (1964).** "Some elementary principles of polycrystalline microstructure." *Met. Rev.* 9 p.1-48.
- Smith, D. L., Evans, B. (1984).** "Diffusional crack healing in quartz." *J. Geophys. Res.* 89 (B6) p.4125-4135.
- Solomon, S. C. (1972).** "Seismic-wave attenuation and partial melting in the upper mantle of North America." *J. Geophys. Res.* 77 (8) p.1483-1502.
- Spiegelman, M., Elliot, T. (1993).** "Consequences of melt transport for uranium series disequilibrium in young lavas." *Earth Planet. Sci. Lett.* 118 p.1-20.
- Spiers, C. J., Schutjens, P.M.T.M. (1990).** "Densification of crystalline aggregates by fluid phase diffusional creep." In: *Deformation Processes in Minerals, Ceramics and Rocks.* Ed.: D. Barber and P. Meredith. London, Unwin Hyman Ltd. p.334-353.
- Spiers, C. J., Schutjens, P.M.T.M., Brzesowsky, R.H., Peach, C.J., Liezenberg, J.L., Zwart, H.J. (1990).** "Experimental determination of constitutive parameters governing creep of rocksalt by pressure solution." In: *Deformation mechanisms, rheology and tectonics.* Ed.: R. J. Knipe, Rutter, E.H., Geological society special publication. 54. p.215-227.
- Steeds, J. W., Morniroli, J.P. (1992).** "Electron diffraction - SAED & CBED." In: *Minerals and reactions at the atomic scale: Transmission Electron Microscopy.* Ed.: P. R. Buseck. Washington, Mineralogical Society of America. 27. p.37-84.
- Stocker, R. L., Ashby, M.F. (1973).** "On the rheology of the upper mantle." *Rev. Geophys. Space Phys.* 11 p.391-426.
- Suhr, G. (1993).** "Evaluation of upper mantle microstructures in the table mountain massif (Bay of Islands ophiolite)." *J. Struct. Geol.* 15 (11) p.1273-1292.
- Tanaka, I., Bruley, J., Gu, H., Hoffmann, M.J., Kleebe, H.-J., Cannon, R.M., Clarke, D.R., Rühle, M. (1994a).** "Compositions and thicknesses of grain boundary films in Ca-doped silicon nitride ceramics." In: *Tailoring of mechanical properties of Si₃N₄ mechanics.* Ed.: G. P. M.J. Hoffmann, Kluwer Academic Publishers. 276. p.275-289.
- Tanaka, I., Kleebe, H.J., Cinibulk, M.K., Bruley, J., Clarke, D.R., Rühle, M. (1994b).** "Calcium concentration dependence of the intergranular film thickness in silicon nitride." *J. Am. Ceram. Soc.* 77 (4) p.911-914.
- Tatsumi, Y., Fukuyama, H., Kushiro, I. (1983).** "Generation of arc basalt magmas and thermal structure of the mantle wedge in subduction zones." *J. Geophys. Res.* 88 (B7) p.5815-5825.
- Toramaru, A., Fujii, N. (1986).** "Connectivity of melt phase in a partially molten peridotite." *J. Geophys. Res.* 91 (B9) p.9239-9252.
- Toriumi, M., Karato, S.I., Fujii, T. (1984).** "Transient and steady state creep of olivine." In: *Materials Science of the Earth's Interior.* Ed.: I. Sunagawa. Tokyo, Terra Scientific Publishing Company. p.281-300.
- Tröger, W. E. (1979).** "Optical determination of rock-forming minerals, part 1 determinative tables, 4th edition." Schweizerbart'sche verlagsbuchhandlung, Stuttgart. 188 pp.
- Tullis, J., Yund, R., Farver, J. (1993).** "Interaction of deformation, fluid distribution and bulk transport in feldspar aggregates." *EOS* 74 p.611.
- Twiss, R. J. (1977).** "Theory and applicability of a recrystallized grain size paleopiezometer." *Pure Appl. Geophys.* 115 p.227-244.
- Twiss, R. J. (1986).** "Variable sensitivity piezometric equations for dislocation density and subgrain diameter and their relevance to olivine and quartz." *Geophysical Monograph* 36 p.247-261.
- Urai, J. L. (1985).** "Water-enhanced dynamic recrystallization and solution transfer in experimentally deformed carnallite." *Tectonophysics* 120 p.285-317.
- Urai, J. L., Spiers, C.J., Peach, C.J., Franssen, R.C.M.W., Liezenberg, J.L. (1987).** "Deformation mechanisms operating in naturally deformed halite rocks as deduced from microstructural observations." *Geol. Mijnbouw* 66 p.165-176.
- Van Cappellen, E., Van Dyck, D., Van Landuyt, J., Adams, F. (1984).** "A parameterless method to correct for X-ray absorption and fluorescence in thin film microanalysis." *J. de Physique* 45 (2) p.C2-411 C2-414.
- Van Cappellen, E. (1990).** "The parameterless correction method in X-ray microanalysis." *Microscopy, Microanalysis, Microstructures* 1 p.1-22.

- Van Cappellen, E., Doukhan, J.C. (1994). "Quantitative transmission X-ray microanalysis of ionic compounds." *Ultramicroscopy* 53 p.343-349.
- Van der Wal, D. (1993). "Deformation Processes in Mantle Peridotites." Ph.D. thesis, Geologica Ultraiectina, Utrecht University, Utrecht. 180 pp.
- Van der Wal, D., Chopra, P., Drury, M.R., FitzGerald, J. (1993). "Relationships between dynamically recrystallized grain size and deformation conditions in experimentally deformed olivine rocks." *Geophys. Res. Lett.* 20 (14) p.1479-1482.
- Van der Wal, D., Dingley, D.J. (1996). "An introduction to EBSD." *Philips electron optics bulletin* 134 p.19-25.
- Vaughan, P. J., Kohlstedt, D.L. (1982). "Distribution of the glass phase in hot-pressed, olivine-basalt aggregates: an electron microscopy study." *Contrib. Mineral. Petrol.* 81 p.253-261.
- Visser, H. J. M. (1999). "Mass transfer processes in crystalline aggregates containing a fluid phase." Ph.D. thesis, Department of Geology, Utrecht University, Utrecht. 242 pp.
- Von Bargen, N., Waff, H.S. (1986). "Permeabilities, interfacial areas and curvatures of partially molten systems: results of numerical computations of equilibrium microstructures." *J. Geophys. Res.* 91 (B9) p.9261-9276.
- Von Mises, W. (1928). "Mechanik der Plastischen Formänderungen von Kristallen." *Z. Angew. Math. Mech.* 8 p.161.
- Waff, H. S. (1974). "Theoretical considerations of electrical conductivity in a partially molten mantle and implications for geothermometry." *J. Geophys. Res.* 79 (B26) p.4003-4010.
- Waff, H. S., Bulau, J.R. (1979). "Equilibrium fluid distribution in an ultramafic melt under hydrostatic stress conditions." *J. Geophys. Res.* 84 (B11) p.6109-6114.
- Waff, H. S., Holdren jr., G.R. (1981). "The nature of grain boundaries in dunite and lherzolite xenoliths: implications for magma transport in refractory upper mantle material." *J. Geophys. Res.* 86 (B5) p.3677-3683.
- Waff, H. S., Bulau, J.R. (1982). "Experimental determination of near-equilibrium textures in partially molten silicates at high pressures." In: *High pressure research in geophysics*, Adv. Earth Planet. Sci. Ed.: S. Akimoto, Manghnani, M.H. Tokyo, Center for Academic publications. 12. p.229-236.
- Waff, H. S. (1986). "Introduction to special section on partial melting phenomena in Earth and Planetary evolution." *J. Geophys. Res.* 91 (B9) p.9217-9221.
- Waff, H. S., Faul, U.F. (1992). "Effects of crystalline anisotropy on fluid distribution in ultramafic partial melts." *J. Geophys. Res.* 97 (B6) p.9003-9014.
- Wanamaker, B. J., Evans, B. (1985). "Experimental crack healing in olivine." *Geophysical Monograph* 31 p.194-210.
- Wanamaker, B. J., Kohlstedt, D.L. (1991). "The effect of melt composition on the wetting angle between silicate melts and olivine." *Phys. Chem. Minerals* 18 p.26-36.
- Watson, E. B. (1982). "Melt infiltration and magma evolution." *Geology* 10 p.236-240.
- Watson, E. B. (1991). "Diffusion in fluid-bearing and slightly-melted rocks: experimental and numerical approaches illustrated by iron transport in dunite." *Contrib. Mineral. Petrol.* 107 p.417-434.
- Weeks, R. W., pati, S.R., Ashby, M.F., Barrant, P. (1969). "The elastic interactions between a straight dislocation and a bubble or a particle." *Acta Metall.* 17 p.1403-1410.
- White, S. H. (1976). "The effects of strain on microstructures, fabrics, and deformation mechanisms in quartzites." *Phil. Trans. R. Soc. Lond.* A283 p.69-86.
- White, S. H. (1979a). "Grain and sub-grain size variations across a mylonite zone." *Contrib. Mineral. Petrol.* 70 p.193-202.
- White, S. H., Shaw, H.F., Hugget, J.M. (1984). "The use of backscattered electron imaging for the petrographic study of sandstones and shales." *J. Sed. Petrol.* 54 p.487-494.
- Williams, D. B. (1984). "Practical analytical electron microscopy in materials science." Philips Electronic Instruments, Inc. Electron optics publishing group, Mahwah (New Jersey). 153 pp.
- Williams, D. B., Michael, J.R., Goldstein, J.I., Romig, Jr., A.D. (1992). "Definition of the spatial resolution of X-ray microanalysis in thin foils." *Ultramicroscopy* 47 p.121-132.
- Wirth, R. (1996). "Thin amorphous films (1-2 nm) at olivine grain boundaries in mantle xenoliths from San Carlos, Arizona." *Contrib. Mineral. Petrol.* 124 p.44-54.
- Wirth, R., Franz, L. (2000). "Thin amorphous intergranular layers at mineral interfaces in xenoliths: the early stage of melting." In: *Physics and chemistry of partially molten rocks*. Ed.: N. Bagdassarov, Laporte D., Thompson, A.B. Dordrecht, Kluwer Academic Publishers. 11. p.229-268.

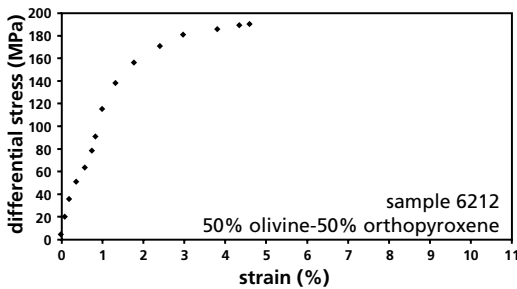
- Wolfenstine, J., Kohlstedt, D.L. (1994).** *"High temperature creep and kinetic decomposition of Ni₂SiO₄."* Phys. chem. Minerals 21 p.234-243.
- Zeuch, D. H., Green, H.W. (1979).** *"Experimental deformation of an anhydrous synthetic dunite."* Bull. Minéral. 102 p.185-187.
- Zeuch, D. H., Green II, H.W. (1984).** *"Experimental deformation of a synthetic dunite at high temperature and pressure. II. Transmission electron microscopy."* Tectonophysics 110 p.263-296.
- Zhang, S., Zimmerman, M., Daines, M.J., Karato, S., Kohlstedt, D.L. (1995).** *"Lattice preferred orientation and melt distribution in experimentally sheared olivine-basalt rocks."* EOS 76 p.281-282.

Appendix A

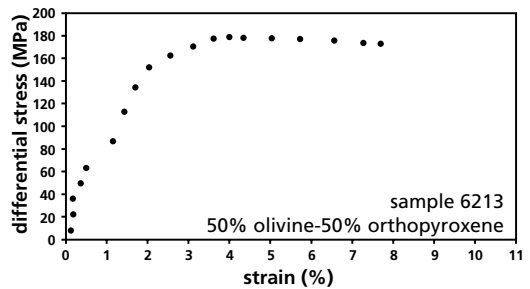
Stress-strain data

In this appendix, the stress-strain curves from all the experiments performed by Drury in 1991-1992 reported in chapter 3 (see table 3.2) are given. From the experiments performed by Hitchings *et al.* (1989) only the stress-strain curve from sample 5249 was available.

Experiments performed by Drury

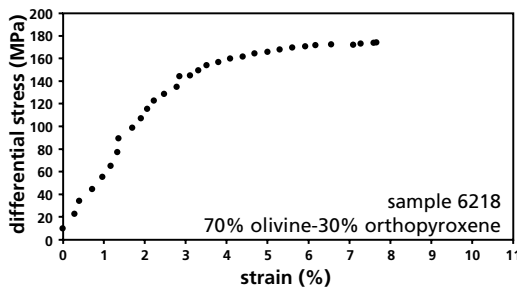


Experiment 6212, $T=1473$ K, $\sigma=190$ MPa.

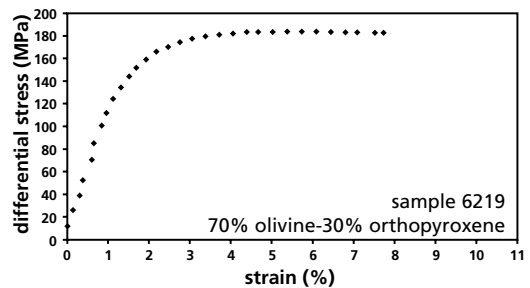


Experiment 6213, $T=1473$ K, $\sigma=173$ MPa.

Experiment 6213 was a subsequent run to experiment 6212 on the same specimen at $T=1473$ K.

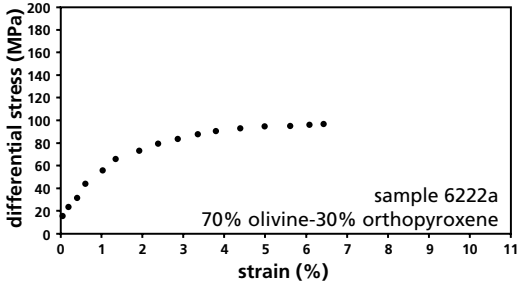


Experiment 6218, $T=1473$ K, $\sigma=174$ MPa.

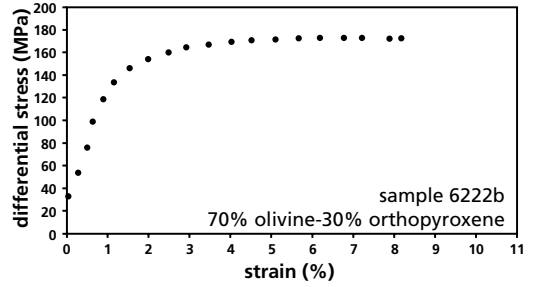


Experiment 6219, $T=1473$ K, $\sigma=183$ MPa.

Experiment 6219 was a subsequent run to experiment 6218 on the same specimen at $T=1473$ K.

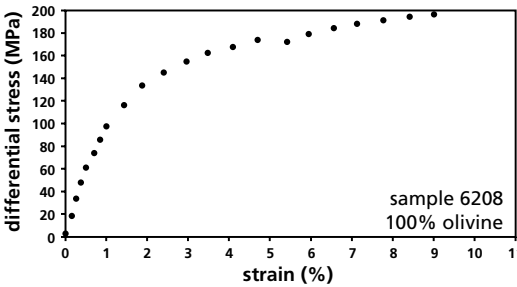


Experiment 6222a, $T=1573$ K, $\sigma=97$ MPa.

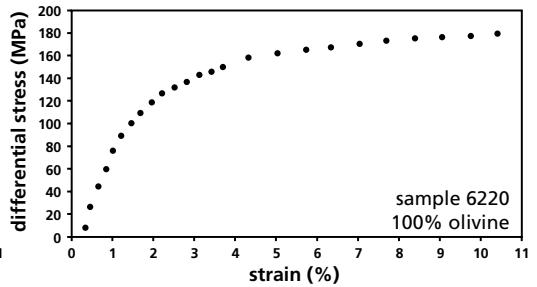


Experiment 6222b, $T=1523$ K, $\sigma=173$ MPa.

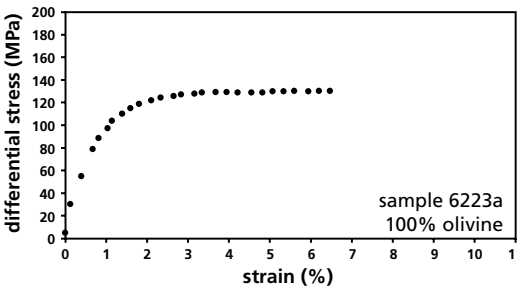
Experiment 6222b was a subsequent run to experiment 6222a on the same specimen, but at lower temperature $T=1523$ K.



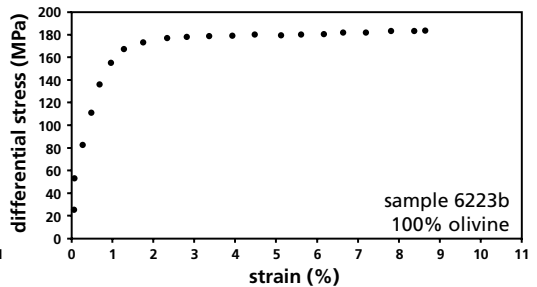
Experiment 6208, $T=1473$ K, $\sigma=195$ MPa.



Experiment 6220, $T=1473$ K, $\sigma=180$ MPa.



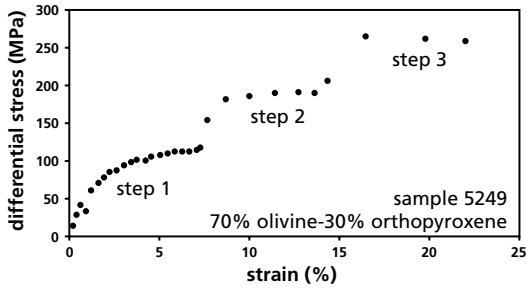
Experiment 6223a, $T=1573$ K, $\sigma=130$ MPa.



Experiment 6223b, $T=1523$ K, $\sigma=181$ MPa.

Experiment 6223b was a subsequent run to experiment 6223a on the same specimen, but at lower temperature $T=1523$ K.

Experiment performed by Hitchings *et al.* (1989)



Stress-strain curves for experiments 5072 and 5099 were not available.

Experiment 5249, $T=1500$ K, $\sigma=116$ MPa (step 1), $\sigma=188$ MPa (step 2), $\sigma=255$ MPa (step 3).

Appendix B

Grain boundary film composition

In this appendix, a method is outlined to obtain an estimate for the composition of the ultrathin amorphous films along olivine grain boundaries reported in chapter 5. The main uncertainty in the quantification of grain boundary analyses, in addition to possible element loss (see chapter 2), concerned the fraction of the EDX signal that was derived from the adjacent olivine crystals as the electron beam used was wider than the grain boundary films (see chapter 5). The large olivine component in grain boundary analyses resulted in very small differences in the EDX signal between the analyses of olivine crystals and the analyses of grain boundaries containing ultrathin amorphous films. Representative olivine and grain boundary analyses can be determined from plots of the measured element X-ray intensity as function of thickness as illustrated in figure 5.13. Below, possible compositions of an amorphous film are calculated using analyses from an olivine grain and the adjacent grain boundary from sample 5249 that plot on the Si and Mg trendlines in figure 5.13 indicating average olivine and grain boundary analyses.

First the sample thickness at the locations of the analyses used for the absorption correction was estimated using the method outlined by Van Cappellen (1984) and the spectra were quantified using the method described in chapter 2 (table B.1). Because the fraction of the EDX signal that is derived from the amorphous grain boundary film is unknown, the grain boundary composition is calculated as function of a superimposed olivine contribution by subtracting incremental amounts of the olivine composition and normalising the resulting calculated compositions to 100% (fig B.1)

	olivine analysis (at%)	grain boundary analysis (at%)
SiO ₂	34.03	35.95
MgO	57.90	54.64
FeO	7.68	8.20
Al ₂ O ₃	0.22	0.56
CaO	0.17	0.65
calculated thickness	23.28 nm	16.96 nm

table B.1 Quantification of adjacent olivine and grain boundary analyses from sample 5249.

In order to estimate the actual grain boundary film composition, the content of one of the components needs to be assumed to determine the olivine fraction in the analysis. Alternatively, the volume of olivine and grain boundary film contributing to the analysis must be analysed (e.g. Kohlstedt 1990). Possible grain boundary film compositions were calculated with SiO₂ and MgO contents based on the composition of the melt in larger pockets (major components normalised to 100%) in sample 5249 that is reported by Drury & FitzGerald (1996), SiO₂: 59.6 at%, MgO: 11.3 at%, Al₂O₃: 14.1 at%, CaO: 10.5 at%, FeO: 4.5 at%, (table B.2). An extreme but unlikely film

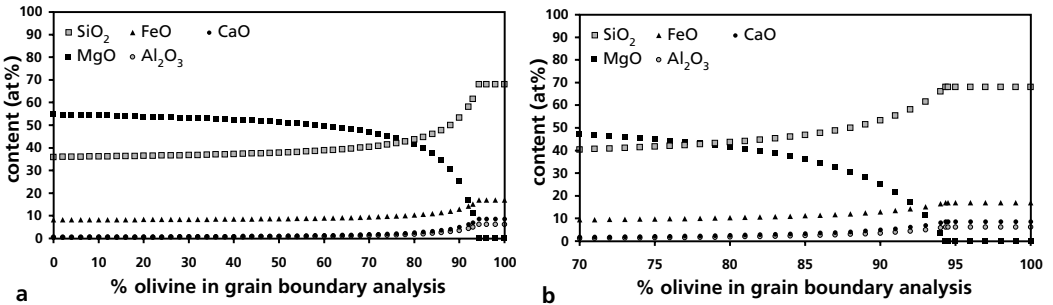


fig B.1 a) Grain boundary film composition with diminishing contribution of olivine-derived signal. b) Enlargement of the graph showing olivine contributions of 70%-100% to the EDX analysis.

composition, as a melt in equilibrium with olivine would not be Mg-free (Beattie 1993), that can be deduced from the graphs in figure B.1 is when the MgO content is completely ascribed to the olivine and the melt phase is MgO-free (table B.2). In the current example, the amorphous grain boundary film generates 5.6% to 7.5% of the EDX signal.

It should be noted that the quality of the film composition estimates is critically dependent on the accuracy of the curve-fitting and background determinations during spectrum processing. This is especially important when only a small fraction of the grain boundary analysis is derived from the amorphous film considering that the calculated composition is automatically normalised to 100% and small variations in major element content dramatically influence the final grain boundary film composition. For example, the high FeO content in the given example may depress a higher actual Al₂O₃ and CaO content (table B.2). Relatively small errors at an early stage of the quantification procedure may therefore lead to substantial errors in the final estimate of the grain boundary film composition. Because of these uncertainties, this quantification method was not used in the thesis.

	grain boundary composition (a) (at%)	grain boundary composition (b) (at%)	MgO-free grain boundary composition (at%)
SiO ₂	59.60	61.44	68.09
MgO	14.43	11.30	0.00
FeO	14.69	15.19	17.01
Al ₂ O ₃	4.81	5.14	6.33
CaO	6.48	6.93	8.57
fraction olivine in grain boundary analysis (%)	92.5	93.0	94.4

table B.2 Possible grain boundary film compositions assuming SiO₂ (a) and MgO (b) contents in the amorphous film to be similar to those in the melt phase in larger pockets in sample 5249 (Drury & FitzGerald 1996). The composition in the last column represents a film composition assuming a completely MgO-free grain boundary phase.

Determination of rotation angle-axis pairs for subgrain misorientations

The method used for the calculation of the subgrain misorientation axes and angles from TEM convergent beam electron diffraction patterns (CBED) is described in this appendix. The mathematical approach followed is similar to the approach used by Faul & FitzGerald (1999) on SEM EBSP data and is based on the pole and line method outlined by Randle (1993) for cubic materials. The misorientation between adjacent subgrains is expressed in a rotation axis - rotation angle pair where the rotation axis between two adjacent (sub)grains is defined as a mutual direction that has the same (Miller) indices in both grains. When one of the grains is taken as a fixed reference frame, the rotation required to bring the crystallographic axes in the second grain into coincidence with the axes in the reference grain defines the misorientation angle. A schematic configuration of the crystal in the TEM, illustrating the directions and angles necessary in the misorientation calculation, is given in figure C.1.

Determination of the misorientation between (sub)grains requires the following steps. First, the (crystallographic) orientation of each (sub)grain must be expressed in parameters that can be derived from the diffraction pattern (see fig C.1). Two perpendicular directions (Z_p and Y_p) expressed in an orthonormal (cubic) crystal reference frame can be extracted from a convergent beam electron diffraction pattern (CBED) containing a (low-index) zone axis. The first direction is the zone-axis (Z_p). The indexed zone-axis is transformed to the orthonormal reference frame with equal units along the axes by multiplication with the olivine crystal parameters ($4.767u_z$, $10.239v_z$, $6.003w_z$). The second direction (Y_p) can be derived from one of the Kikuchi bands. These bands represent the intersection of lattice planes with the plane perpendicular to the zone-axis and the pole to the Kikuchi bands is perpendicular to the zone-axis. The pole (Y_p) to the Kikuchi band (K_u , K_v , K_w) is calculated in the orthonormal reference frame using: $Y_p = (K_u a^*$, $K_v b^*$, $K_w c^*$), with a^* , b^* , and c^* being the reciprocal lattice vectors (McKie & McKie 1986). For olivine this reduces to $\mathbf{N} = (0.2098K_u$, $0.0977K_v$, $0.1666K_w)$. A third perpendicular direction (X_p) parallel to the Kikuchi band is defined by the cross product of the zone-axis (Z_p) and the pole to the Kikuchi band (Y_p). These three orthonormal directions normalised to unit length, define the pattern matrix \mathbf{P} ,

$$\mathbf{P} = \begin{bmatrix} \frac{u_x}{|X_p|} & \frac{v_x}{|X_p|} & \frac{w_x}{|X_p|} \\ \frac{u_y}{|Y_p|} & \frac{v_y}{|Y_p|} & \frac{w_y}{|Y_p|} \\ \frac{u_z}{|Z_p|} & \frac{v_z}{|Z_p|} & \frac{w_z}{|Z_p|} \end{bmatrix}$$

where $|X_p|$, $|Y_p|$, and $|Z_p|$ denote the magnitude of the vectors $[u_x v_x w_x]$, $[u_y v_y w_y]$, and $[u_z v_z w_z]$.

In the second step, the calculated orthonormal set of crystal directions is transposed onto an external reference frame. A rotation matrix $\mathbf{R}_{\text{total}}$ that describes the rotation required to transpose the pattern matrix onto a fixed external reference frame is determined. The transposition involves three subsequent rotations, first \mathbf{R}_z , then \mathbf{R}_y , and finally \mathbf{R}_x ($\mathbf{R}_{\text{total}}=\mathbf{R}_z\mathbf{R}_y\mathbf{R}_x$) with:

$$\mathbf{R}_z = \begin{bmatrix} \cos \gamma & -\sin \gamma & 0 \\ \sin \gamma & \cos \gamma & 0 \\ 0 & 0 & 1 \end{bmatrix} \quad \mathbf{R}_y = \begin{bmatrix} \cos \beta & 0 & \sin \beta \\ 0 & 1 & 0 \\ -\sin \beta & 0 & \cos \beta \end{bmatrix} \quad \mathbf{R}_x = \begin{bmatrix} 1 & 0 & 0 \\ 0 & \cos \alpha & -\sin \alpha \\ 0 & \sin \alpha & \cos \alpha \end{bmatrix}$$

For explanation of the angles α , β , and γ see figure C.1. Multiplication of the resulting rotation matrix $\mathbf{R}_{\text{total}}$ with the pattern matrix \mathbf{P} produces an orientation matrix \mathbf{O} . The orientation matrix describes the relation between the selected orthonormal crystal directions (X_p, Y_p, Z_p), that are the same in both subgrains and the external reference frame based on the TEM negative (X_R, Y_R, Z_R):

$$\mathbf{O}=\mathbf{R}_{\text{total}}\mathbf{P}$$

When such orientation matrices are determined for both adjacent subgrains, the misorientation matrix describing the transposition of one subgrain onto the other is produced by multiplication of the orientation matrices:

$$\mathbf{M}=\mathbf{O}_1^{-1}\mathbf{O}_2$$

From the misorientation matrix \mathbf{M} , which describes the misorientation in the external reference coordinates defined by X_R, Y_R , and Z_R , the rotation axis and the misorientation angle can now be calculated using:

$$\text{rotation axis } V[\text{uvw}]: \quad u=M_{32}-M_{23} \quad v=M_{13}-M_{31} \quad w=M_{21}-M_{12}$$

$$\text{misorientation angle } (\theta): \quad \cos \theta = \frac{M_{11} + M_{22} + M_{33} - 1}{2}$$

The resulting orientation of the rotation axis $V[\text{uvw}]$ is a direction that is common to both the orthonormal crystal and reference coordinate systems and is parallel in both grains. Subsequently, the rotation axis in the orthonormal reference coordinates can be converted to the orthorhombic olivine crystal coordinates by multiplying the rotation axis with a matrix \mathbf{L} :

$V_{\text{orthorhombic}}=\mathbf{L}^{-1}V_{\text{cubic}}$, with the elements of \mathbf{L} being:

$$\mathbf{L} = \begin{pmatrix} a & b \cos \gamma & c \cos \beta \\ 0 & b \sin \gamma & c(\cos \alpha - \cos \beta \cos \gamma) / \sin \gamma \\ 0 & 0 & c\sqrt{1 + 2 \cos \alpha \cos \beta \cos \gamma - \cos^2 \alpha - \cos^2 \beta - \cos^2 \gamma} / \sin \gamma \end{pmatrix}$$

where a, b, c and α, β, γ are the crystal lattice parameters.

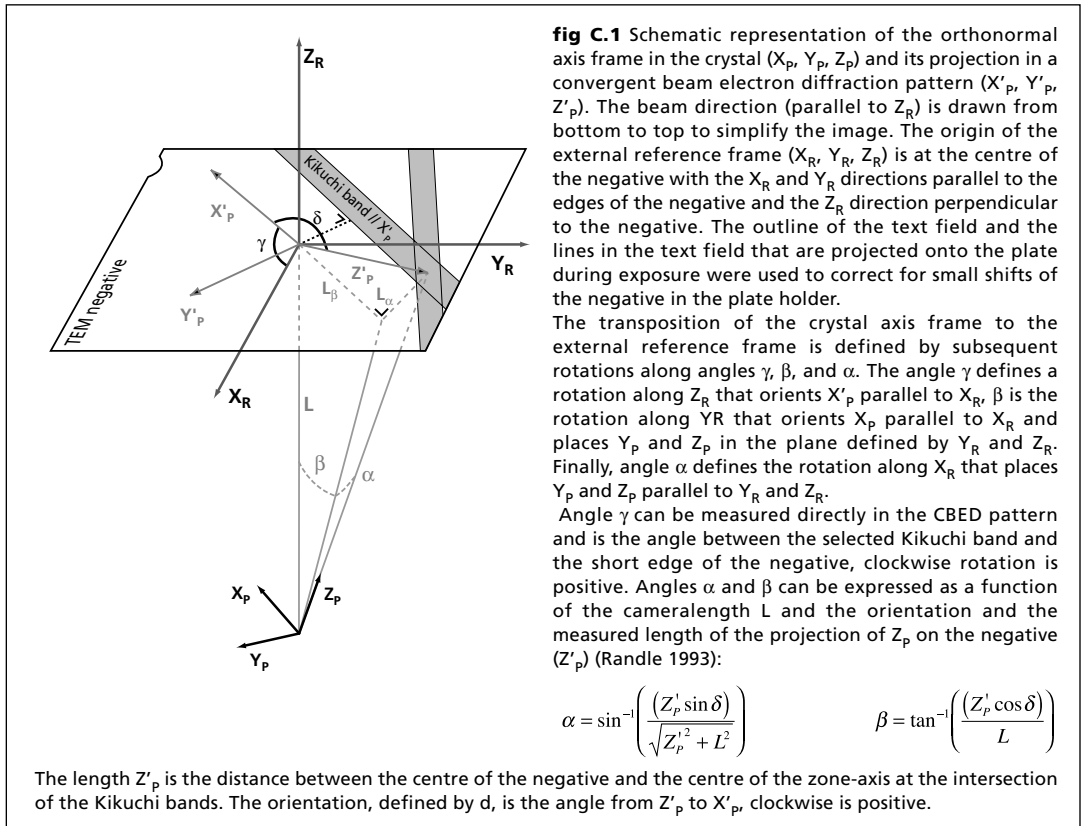
For olivine (Fo_{89}) \mathbf{L} reduces to:

$$\mathbf{L} = \begin{bmatrix} 4.767 & 0 & 0 \\ 0 & 10.239 & 0 \\ 0 & 0 & 6.003 \end{bmatrix} \text{ and } \mathbf{L}^{-1} = \begin{bmatrix} 0.2098 & 0 & 0 \\ 0 & 0.0977 & 0 \\ 0 & 0 & 0.1666 \end{bmatrix}$$

The final step in determining the misorientation angle involves the orthorhombic symmetry of olivine. In the orthorhombic crystal system, each grain can be indexed in four equivalent ways, which results in 16 axis-angle pairs (Faul & FitzGerald 1999). These 16 axis-angle pairs are comprised of four symmetrically equivalent sets with four different rotation angles. The four rotation axis – misorientation angles that correspond to the chosen Miller indices are obtained by multiplying the rotation axis direction with these symmetry matrices:

$$\begin{aligned} \text{a) } & \begin{bmatrix} 1 & 0 & 0 \\ 0 & 1 & 0 \\ 0 & 0 & 1 \end{bmatrix} & \text{b) } & \begin{bmatrix} 1 & 0 & 0 \\ 0 & -1 & 0 \\ 0 & 0 & -1 \end{bmatrix} & \text{c) } & \begin{bmatrix} -1 & 0 & 0 \\ 0 & 1 & 0 \\ 0 & 0 & -1 \end{bmatrix} & \text{d) } & \begin{bmatrix} -1 & 0 & 0 \\ 0 & -1 & 0 \\ 0 & 0 & 1 \end{bmatrix} \end{aligned}$$

Because the studied adjacent grains were subgrains, the rotation axis – misorientation angle pair with the smallest misorientation angle was used.



Dankwoord

Promoveren is een enerverende bezigheid. Het werk dat is gepresenteerd in dit proefschrift is het resultaat van 6 jaar methodisch werken, zoeken naar heel kleine spelden in even zo kleine hooibergjes, veel teleurstellingen, maar ook mooie successen. Bij het begin van mijn promotieonderzoek heb ik niet kunnen voorzien hoeveel tijd en energie er werkelijk gaan zitten in het voltooien van een proefschrift. Behalve de onvermijdelijke wetenschappelijke en organisatorische hobbels die tijdens het werk genomen moesten worden, kostten ook gebeurtenissen in de privé-sfeer veel energie. Ik ben zeer dankbaar voor de motivatie en steun die ik kreeg van mijn begeleiders, collega's en vrienden (in willekeurige volgorde) om door te gaan. Om te voorkomen dat ik mensen vergeet te noemen wil ik hierbij iedereen bedanken die mij heeft geholpen tijdens mijn promotie. Zonder jullie steun was dit boekje er nooit gekomen. Een aantal mensen wil ik echter in het bijzonder noemen.

Al tijdens mijn studie en vooral in de eerste fase van mijn promotieonderzoek heb ik met heel veel plezier studenten begeleid bij verschillende practica en veldwerken. Ik wil dan ook Henko, Rob, Pim, Reinoud, Hans, Jan, Martyn, Stan, Chris, Colin en de student-assistenten van de practica bedanken voor de samenwerking. Dit onderwijs gaf me de gelegenheid om mijn onderzoek even opzij te zetten en enthousiast te kunnen praten over de vele andere aspecten van de geologie. Opmerkingen van studenten als "Ik kon het rif (in de Ardennen, 360 miljoen jaar geleden) zien groeien bij je uitleg bij het practicum paleontologie" en beschuldigingen als "Na dit veldwerk kan ik nooit meer gewoon naar een berg kijken!" na het veldwerk voor 2^e-jaars geofysica studenten gaven me veel voldoening.

Mijn fascinatie voor de elektronenmicroscopie werd gewekt door Martyn en Stan tijdens mijn afstudeeronderzoek, leidde eerst tot een stage bij Exxon Chemical in België en daarna tot dit promotieonderzoek. Het heeft een nieuwe wereld voor mij geopend, bedankt daarvoor! Ik wil Pim, Henk en Theo bij EMSA bedanken voor de faciliteiten en de hulp als één van de instrumenten weer eens een eigen leven ging leiden. Mijn speciale dank gaat ook uit naar Herman die altijd onverbeterlijk positief bleef als er iets mis ging en in veel van mijn resultaten een nieuwe doorbraak meende te herkennen als ik dacht "Dit wordt niks". Meestal had je gelijk. Voor de enige experimenten die ik zelf gedaan heb, ben ik door Martyn aan het werk gezet met geochemiestudent Maarten Nachtegaal. Ik heb er een goede vriend aan overgehouden. Maarten heel veel succes met jouw promotie!

Maar het allerbelangrijkste tijdens een promotie zijn een goede werksfeer en fijne collega's en dat zat wel goed. Tot slot wil ik hier mijn waardering uitspreken voor mijn vrouw Sandra. Je bent geweldig! Je was altijd geïnteresseerd in mijn onderzoek en je vindt het nog steeds niet saai als ik weer eens overloop van enthousiasme voor de geologie.

Curriculum Vitae

Ik* ben geboren op 22 september 1970 in Gameren. In 1988 behaalde ik mijn VWO diploma aan de Rijksscholengemeenschap “Buys Ballot” in Zaltbommel. Van 1988 tot 1994 heb ik Geologie gestudeerd aan de Faculteit Aardwetenschappen van de Universiteit Utrecht met als afstudeerrichting structurele geologie / materiaalkunde. Naast mijn opleiding heb ik het grootste deel van mijn tijd van 1985 tot 1997 besteed aan het werken bij Omroepvereniging “Transmedia” in Zaltbommel. Voor mijn afstuderen heb ik de spanningsverdeling in de “Alpine Fault Zone”, in Nieuw Zeeland onderzocht aan de hand van microstructuren. Als extra studieonderdeel heb ik in 1994 een stage van 3 maanden gedaan bij Exxon Chemical in Machelen, België. In deze twee projecten heb ik veel gewerkt met elektronenmicroscopische technieken. In december 1994 ben ik begonnen aan mijn promotieonderzoek waarin ik mijn fascinatie voor elektronenmicroscopie kon combineren met mijn enthousiasme voor de geologie. Dit onderzoek betrof de identificatie van deformatie-mechanismen en de nanometer-schaal smeltverdeling in partieel gesmolten bovenmantel gesteenten zoals beschreven in dit proefschrift.

* **Peter Antonie de Kloe** (René), **geb.** 22-09-1970 te Gameren, **gehuwd** op vrijdag de 13e november 1998 met Sandra Johanna (Sandra) Bos
zoon van Antonie de Kloe (geb. 17-02-1940 te Gameren) en Pieterella Naaijen
kleinzoon van Joost de Kloe (geb. 23-04-1914 te Gameren) en Mina Cornelia Donker
achterkleinzoon van Willem de Kloe (geb. 27-01-1889 te Gameren) en Jenneke van Steenberg
hij was een zoon van Joost de Kloe (geb. 25-05-1854 te Andel) en Willemijntje Kraaij
hij was een zoon van Jacob de Kloe (geb. 07-09-1824 te Andel) en Leske van Helden
hij was een zoon van Joost de Kloe (geb. 12-03-1777 te Giessen) en Wilhelmina Piek
hij was een zoon van Joost de Kloe (ged. 26-05-1737 te Andel) en Maaijke van Wijngaarden
hij was een zoon van Hardenberg de Kloe (ged. 08-03-1705 te Woudrichem) en zijn 3e vrouw Jenneke Hoeckx
hij was een zoon van Joost de Kloe (ged. 30-01-1670 te Delft) en Pellegrina Stael van Holstijn
hij was een zoon van Isaac du Cloux / de Kloe (ged. 20-04-1642 te Delft) en (Mar)Grietgen Cornelisdr. van Gijsen
hij was een zoon van Daniel du Cloux (mogelijk geb. ca. 1623 te Sedan, Frankrijk) en Maria Dalichamp / Dalichang

Daniel is de oudste bewezen voorvader van de Nederlandse familie De Kloe.

Met dank aan mijn broer Jos voor het uitzoeken van de stamboom van de familie De Kloe (De Kloe, 2000).

